Study on the Point Defects Production and Microstructure Change in Ceria Based Oxides

ソ, プルン

Study on the Point Defects Production and Microstructure Change in Ceria Based Oxides

A dissertation submitted to the department of
Applied Quantum Physics and Nuclear Engineering
in partial fulfilment of the requirements
for the degree of

DOCTOR OF ENGINEERING

By

SEO Pooreun

Graduate School of Engineering
Kyushu University, Fukuoka, Japan
November 2022

Abstract

Ceramic oxide with fluorite structure, such as ceria (CeO_2), has been proposed as a surrogate of nuclear fuels (e.g. UO_2, PuO_2) and transmutation targets because of the excellent radiation resistance. Ceria has a redox effect between two charge states of cerium ions with localized *f* electrons, which induces oxygen vacancies (V_O) to compensate for charge neutrality. Gadolinia (Gd_2O_3) exhibits a bixbyite structure, and it has been doped in UO_2 fuel as a burnable poison due to the large absorption cross-section of thermal neutrons. Gd_2O_3-doped CeO_2 as expressed by $Ce_{1-x}Gd_xO_{2-x/2}$ also produces V_O since the Gd^{3+} substitutes into the Ce^{4+} site. The oxygen deficiency in $Ce_{1-x}Gd_xO_{2-x/2}$ is mainly controlled by the dopant concentration.

Moreover, V_O can be generated by elastic collisions with high-energy electrons by receiving energy above the threshold displacement energy of oxygen atoms. The V_O is a key factor to determine radiation tolerance since it enhances the recombination of interstitials and vacancies. The kinetic behavior of point defects in ceramics is known to depend on their charge states. However, there was only limited research on it since the *in-situ* techniques are needed to gain the production and charge state of point defects in ceramics during irradiation.

In this dissertation, radiation damage in $Ce_{1-x}Gd_xO_{2-x/2}$ was investigated for a wide range of Gd dopant concentrations ($0 \leq x \leq 0.5$). For this purpose, a unique facility of a high voltage electron microscope (HVEM) interfaced with cathodoluminescence (CL) facility at The Ultramicroscopy Research Center of Kyushu University was utilized to examine the production and charge state of point defects *in-situ* under high-energy electron irradiation. Further, microstructure change induced by heavy ion irradiation was studied comprehensively against dopant concentration by x-ray diffraction (XRD) analysis, micro-Raman spectroscopy, and transmission electron microscopy (TEM) to understand the role of oxygen vacancy on the microstructure stability. This dissertation consists of seven chapters.

Chapter 1 described the introduction and research goal of this study. At the end of this chapter, the structure of the dissertation was outlined.

Chapter 2 reviewed the theoretical and experimental background on structure in CeO_2 and $Ce_{1-x}Gd_xO_{2-x/2}$. Displacement damage, energy loss, diffraction analysis for structure evaluation, and CL emission mechanism were described in this chapter.

Chapter 3 explained the experimental methodology for the sample preparation, and the techniques of XRD, Raman spectroscopy, and TEM. Details for the synthesis of $Ce_{1-x}Gd_xO_{2-}$

$_{x/2}$ samples and ion irradiation conditions were described. *In-situ* CL measurement conditions were also described together with the data acquisition procedures.

Chapter 4 described point defect production under in-beam conditions in pure single crystal and polycrystalline ceria using the *in-situ* HVEM-CL technique. The CL spectra were obtained with 400 ~ 1250 keV electrons, and they were fitted into three CL bands. One band was assigned to be the F^+ center which is induced by electron-nuclear elastic collisions, and the other two bands were originated from charge-compensative Ce^{3+} ions caused by V_O formation. Localized atomic configurations between Ce^{3+} ions and charged V_O were suggested according to the CL spectra. The dependence of CL spectra against electron energy and irradiation temperature were also explained by taking the cross-sections of defect production and electronic excitation.

Chapter 5 discussed microstructure and radiation response in $Ce_{1-x}Gd_xO_{2-x/2}$ for a wide range of Gd_2O_3 concentrations ($0 \leq x \leq 0.5$). Microstructure characterization was carried out comprehensively by XRD, micro-Raman spectroscopy, and TEM. The formation of bixbyite structure with V_O ordering was observed for $x \geq 0.2$, associated with the saturation of lattice parameter and micro-strain relaxation. Those microstructure changes with values of x were found to influence the microstructure change induced by 200 MeV Xe ions. Ion track density and size were found to be depressed for samples with $x \geq 0.2$, and this was discussed with the ordering of V_O which attributes to the recovery process of radiation-induced defects.

Chapter 6 described the application of the *in-situ* HVEM-CL technique to $Ce_{1-x}Gd_xO_{2-x/2}$ samples. The CL bands for Ce^{3+}-V_O, Ce^{3+}, and F^+ center were observed from $Ce_{1-x}Gd_xO_{2-x/2}$ as same as pure ceria. The electronic configurations and energy dependence of CL spectra in $Ce_{1-x}Gd_xO_{2-x/2}$ were compared with those of pure ceria. Photon energy shifts and quenching of CL emission were observed in $Ce_{1-x}Gd_xO_{2-x/2}$, and the change was discussed with the generation of V_O induced by Gd_2O_3 doping, and the change of electrical configuration around Ce^{3+} ions and V_O. The band gap energy level of defects in $Ce_{1-x}Gd_xO_{2-x/2}$ was suggested in this chapter.

In chapter 7, all the experimental and simulation works done in the wake of this study are summarized as conclusions together with possible directions for future research.

Acknowledgements

The dissertation was able to be completed thanks to the support of many people, teachers, and institutions. Six years at Kyushu University have been a very valuable experience for me and I would like to express my gratitude to those who have helped me.

I would like to express my sincere gratitude to my supervisor, Prof. Kazuhiro Yasuda. Thanks to the professor's meticulous and accurate guidance, discussion, support, patience, and consideration, this dissertation can be completed. Besides research, he took care of my study abroad life in Japan and gave me warm encouragement and lots of advice whenever I had difficulties. I am very fortunate to have been taught by Prof. Yasuda, and I will continue to live as a good researcher remembering Prof. Yasuda.

I would like to appreciate Prof. Syo Matsumura, who retired in 2022, for giving me a chance to study at Kyushu University in a great environment. I was very impressed with the professor's competence, humility, and support for his students. I appreciate his precious guidance and discussion on this dissertation, as well as his detailed consideration and support for my study abroad life in Japan.

I would like to appreciate my collaborator, Prof. Jean-Marc Costantini at Université Paris-Saclay, CEA-Saclay, France for his valuable cooperation, detailed guidance, and idea to complete this dissertation. Thanks to online and on-site discussions, research collaborations, and encouragement, I could complete this study. The professor's curiosity and passion for research motivated me a lot.

I would like to appreciate Prof. Yasukazu Murakami for providing a great research environment and detailed discussions on this dissertation. His careful consideration and encouragement helped me study at Kyushu University.

I would like to appreciate Asst. Prof. Satoru Yoshioka for his valuable advice and discussion for this dissertation. Thanks to the professor's support, I was able to successfully conduct the experiment and obtain good results.

I would like to thank the co-chairs of this dissertation committee, Prof. Satoshi Hata and Prof. Yaohiro Inagaki.

I would like to express my gratitude to Asst. Prof. Tomokazu Yamamoto, Asst. Prof. Takehiro Tamaoka and all staff members at the Ultramicroscopy Research Center of Kyushu

University for their efforts in the development and maintenance of the electron microscope facilities and their technical support, guidance, and cooperation in using them.

I would like to thank the Center of Advanced Instrumental Analysis of Kyushu University and Asst. Prof. Midori Watanabe for her technical support to use analytical facilities.

I would like to thank Yasuda, Matsumura, and Murakami group members for their various support and cooperation. Sujin Lee gave me a lot of strength by my side. I appreciate alumni and staff members; Dr. AKM Saiful Islam Bhuian, Dr. Md. Majidur Rahman, Dr. Kohei Aso, Dr. Wenhui Yang, Dr. Youngji Cho, Mrs. Atsuko Sato, Mr. Youichiro Kawami for their help and support.

I would like to express my gratitude to Mrs. Hiromi Kumagai and Mrs. Mayumi Matsumoto for their support for comfortable study and research activities.

I would like to express my deep gratitude to my parents, brother, aunt, uncle, Hyunju, and his families, who gave me infinite love, prayer, and support. My friends at Kyushu University, Fukuoka vision church families, Bae's family, and Kkokkyo, I owe a debt of love and prayer to them.

Above all, I praise and thank the almighty God Jesus Christ for guiding and savior of my life. The fear of the Lord is the beginning of wisdom, and knowledge of the Holy One is understanding. Proverbs 9:10.

Table of Contents

List of Figures

List of Tables

List of Abbreviation

BF: Bright-field

CL: Cathodoluminescence

CSDA: Continuous slowing down approximation

E_d: Threshold displacement energy

EELS: Electron energy loss spectroscopy

EPR: Electron-paramagnetic resonance

fcc: Face-centered cubic

HRTEM: High-resolution transmission electron microscopy

HVEM: High-voltage electron microscopy

MOX: Mixed oxide

PKA: Primary knock on atom

PL: Photoluminescence

RE: Rare earth

SAED: Selected area electron diffraction

S_e: Electronic stopping power

SEM: Scanning electron microscope

S_n: Nuclear stopping power

STEM: Scanning transmission electron microscopy

TEM: Transmission electron microscope

URC: Ultramicroscopy Research Center

V_O: Oxygen vacancy

XRD: X-ray diffraction

YSZ: Yttria-stabilized cubic zirconia

ZA: Zone axis

σ_d: Displacement cross-section

Chapter 1

Introduction

A sufficient energy supply is as importance as a fast growing of world population in modern life society demanding safety, mobility and daily comfort life. For this reason, the energy industry has discussed and studied the energy generation and storage systems. To lead these technologies, it is necessary to develop superior materials for energy source applications, such as generation facilities for chemical and photo-physical energy, nuclear reaction energy, and thermomechanical energy. All of those industries need excellent materials, which generate high efficient energy for each environmental condition.

Ceramic oxide is one of the remarkable and fascinated materials, which have high strength, high insulation ability, low thermal expansion, and chemical stability. For those reasons, ceramic oxide has been used safely in many industrial fields, such as energy-supplement devices, auto motives, medical technology, and aerospace. Especially for nuclear applications, magnesia (MgO), sapphire (α-$Al_2O_{3)}$, and yttria-stabilized cubic zirconia (ZrO_2: Y) are promising ceramic materials to be used for the host of inert matrix fuels in nuclear fission reactors, transmutation targets, and functional materials in fusion devices under high-energy particle radiations. They can endure the exposure to extreme environments, for instance, high or low temperatures, and intense radiation. Therefore, it is necessary to understand their physical and chemical characteristics under harsh environment to prevent degradation of physical and chemical properties.

In particular, ceramics are used for nuclear fuel, and they are widely investigated for their safety and reliability. Typically, plutonium oxide (PuO_2) is actively developed for use in mixed oxide (MOX) fuel such as (U, Pu)O_2 for thermal reactors or fast reactor fuel. For the

safe use of MOX fuel, it is necessary to understand the drawbacks caused by the pile-up of damage for a long time. However, it might be hard to handle and study the radiative materials caused by irradiation. Therefore, cerium dioxide or ceria (CeO_2) with a fluorite structure can be considered as a surrogate of PuO_2 to avoid radioactive problems caused by its direct use of it.

Moreover, for the high performance of nuclear reactors to use in long-life power plants, the burnable poison has been used to control the initial reactivity. Fuel utilization has been introduced with additional neutron absorbers in fissile materials. Gadolinium (Gd) is one of the fission products forming solid solutions with uranium dioxide. Gd_2O_3 has been, therefore, used as a dopant for UO_2 fuel in boiling water reactors because Gd isotopes have a large absorption cross-section of 49,000 barns for thermal neutrons with taking the natural abundance of Gd isotopes into consideration [1]. The UO_2-Gd_2O_3 fuel has been used in the boiling water reactor (BWR) type since 1967, and the maximum concentration of Gd_2O_3 is around 4 wt% (i.e. ~6 at% Gd). Recently, the UO_2-Gd_2O_3 fuel is introduced in the pressurized water reactor (PWR) type up to high concentration of Gd_2O_3 around 10 wt% (i.e. ~14 at% Gd).

Nuclear fuel materials are exposed to various radiations such as high-energy fission fragments, high-energy neutrons, α-, β-, and γ-rays generated by nuclear fission reactions in nuclear reactors. Radiation with those high-energy particles has been known to induce the amorphization in ceramics and cause degradation of mechanical properties, and void swelling due to the atomic displacement damage [2]. Irradiation defects resulting from these various radiations form and accumulate in the heating-resisting materials. Also, accumulation of fission products and high-density electron excitation damage are also of importance for the stability of fuels. Detailed knowledge of the point defect production and kinetics are often required for the further understandings of radiation damage in ceramics. For example, electronic excitation is known to affect damage processes, such as the formation and migration of point defects, and

stability of point defect aggregates in ionic and covalently bonded ceramic materials [3–5]. Fission fragments arising from fuels and transmutation targets have high energies of 70 - 100 MeV and induce a high density of electronic excitation in materials. It has been reported that when such high-density electronic excitation is induced during crystallization, columnar irradiation defects called 'ion tracks' form along ion trails [6]. In nuclear fuel, such high-density electronic excitation damage is induced repeatedly to reach 10^4 to 10^5 times for the burn-up of 1% FIMA (% fissioned per initial metal atom). Therefore, evaluation of the ion track formation in the fluorite-structure oxide and the microstructure change due to its overlap is important for understanding the stability of the structure of nuclear reactor fuels and for the development of next-generation fuels.

To understand the basic process of irradiation damage, the threshold displacement energy (E_d) is indispensable physical quantity. Costantini et al. used an electron accelerator to irradiate electrons with a wide range of energies to yttria-stabilized cubic zirconia (YSZ), and anion electron trapping centers (F^+ centers) were investigated by electron spin resonance (EPR) method [7]. From the analysis of the electron-energy dependence of the point defect accumulation process, the value of E_d can be derived by *in-situ* observation in transmission electron microscopy (TEM). Yasunaga et al. irradiated electrons to CeO_2 for various energies by using TEM and observed the formation and growth process of the irradiation defect in-beam state [8,9]. They confirmed that the properties of the dislocation loop depended on the electron energy, and according to the results, they estimated the E_d of Ce and O ions as 44 ~ 58 eV and <33 eV, respectively [9]. Values of E_d in various ceramic materials, such as UO_2 (U: ~40 eV, O: ~20 eV), ThO_2 (Th: 48.5 ~ 61.5 eV, O: 17.5 ~ 100 eV), ZrO_2 (Zr: 54 ~ 68.5 eV, O: 14 ~ 100 eV), were summarized in references [10–12], although the reported values of E_d are not sufficient at the present moment.

Mostly, ceramics includes multielement and their crystal structures content multi-sublattices themselves. The atomic bonds also have ion-covalent bonding which depends on crystal. The electronic valence of point defects can be changed by electronic excitation that influences the migration dynamics and aggregation of point defects [13]. Under radiation irradiation conditions, it is, therefore, necessary to have a general idea of in-beam physical characteristics of defect behaviors.

Electron microscopy is one of the useful techniques to measure radiation damage in materials. High energy electrons generated in an electron microscope, such as a TEM, can be irradiated with a high-flux electron beam to a specimen and produce point defects in a short time. Namely, an *in-situ* TEM experiment has an advantage that one can observe the nucleation and accumulation of defects dynamically. The use of electron irradiation has an additional advantage since the target does not need to be cooled down unlike neutron or high-energy ion irradiation. Unfortunately, the defects recombination occurs during the cooling period, and it is hard to observe its effects *in-situ* right after neutrons/ions irradiation. Therefore, the *in-situ* TEM method has the characteristics of being able to conduct a systematic and precise study on the effects of fission product accumulation in-beam environment and high-density electron excitation.

Optical absorption spectroscopy technique has an advantage to identify the defects in ceramics. Photoluminescence (PL) spectroscopy and UV-visible optical absorption spectroscopy were used to examine the defects in ceramics [14,15]. A photo-induced electron-hole pair indicates the localized defect level at photoexcitation energies within the bandgap energy. In particular, naturally present defects, such as F centers (electron centers) and V centers (hole centers), were demonstrated by PL spectroscopy in alkali halides and oxides [15]. In addition, thermo-stimulated luminescence (TSL) [16], optically stimulated luminescence

(OSL) [17], and radio-luminescence (RL) [18] were also used to identify nature or radiation-induced defects in ceramics.

Cathodoluminescence (CL) spectroscopy is one of the optical absorption techniques, and it has been used for the impurity analysis by using SEM under low-energy electron irradiation (≤ 40 keV). The first observation of discoloration was investigated by Goldstein [19] in alkali halides induced by electron irradiation. For several decades, F centers from oxygen vacancies were examined in various ceramic oxides, such as MgO, Al_2O_3, ZnO, and TiO_2 [20–23].

CL spectroscopy has also been utilized to study the radiation-induced defects. Recently, a study on point defect formation by elastic and inelastic collisions under high-energy electron irradiation was performed in ceramics by using *in-situ* CL spectroscopy under high-energy electron irradiation [24,25]. CL spectra emitted from impurities and F centers in sapphire (α-Al_2O_3), YSZ (ZrO_2:Y), spinel ($MgAl_2O_4$) were detected and revealed its electrical characteristics and formation of defects in-beam condition. It was revealed the point defects formation and aggregation with their charge states under electron irradiation [25].

Radiation response due to multi-particles collisions of electronic and nuclear stopping is also attracted for ceramics leading the annealing of radiation damage due to a synergetic effect. The synergetic effect of elastic (or nuclear) (S_n) and inelastic (or electronic) (S_e) energy loss is a key factor of nanostructure evolution and defect kinetics of ceramics [26,27]. The recovering and expansion delay of the defects due to ionization-induced diffusion and recombination of point defects lead the synergetic effect. These point defects in ceramic influence physical properties, such as thermal conductivity and diffusivity [28]. The kinetic behaviors of point defects are depending on their charge states. Therefore, it is important to understand the charge states of the defects under irradiation conditions, and thereby *in-situ* high

voltage electron microscopy (HVEM)-CL method can be a powerful technique for the radiation damage study in ceramics.

Based on the explanation above, the purpose of this dissertation is to gain insights into the radiation damage in the rare-earth (RE)-doped fluorite structure oxides. In particular, this dissertation has two objectives to elucidate the followings: i) understanding the on-site point defect production and its charge state during electron irradiation, and ii) examination of microstructure evaluation by RE doping and ion irradiation.

The dissertation consists of seven chapters.

Chapter 1 describes the introduction and research goal of this dissertation. At the end of this chapter, the orientation of each chapter is proposed.

Chapter 2 reviews the theoretical and experimental background of physical and chemical characteristics of the main material of Gd_2O_3 doped ceria, and diffraction analysis. Furthermore, fundamental knowledge of displacement damage, energy loss, and cathodoluminescence spectroscopy are described.

Chapter 3 explains experimental methodologies for the sample preparation, measurement, and analysis techniques. The sample preparation complies synthesis procedure, thinning for TEM observation, and ion irradiation. Experimental facility performances and conditions for x-ray diffraction (XRD), Raman spectroscopy, TEM, and *in-situ* HVEM-CL measurement are described with the explanation of data acquisition procedures.

Chapter 4 describes *in-situ* HVEM-CL measurement in pure ceria under electron irradiation by using the HVEM. This technique yields information on the instant Frenkel point defect formation under out-of-equilibrium conditions upon high-energy electron irradiation. CL spectra were obtained from single crystal and polycrystalline samples. Charge states of defects were interpreted by CL profiles and they related to oxygen vacancy localization. Moreover, energy and temperature dependence of CL emission was investigated.

Chapter 5 discusses the microstructure evaluation in Gd_2O_3 doped ceria upon the creation of oxygen vacancies in a wide range of dopant concentrations. Comprehensive microstructure characterization, such as phase, lattice parameter, and microstrain of the samples was carried out by XRD, micro-Raman spectroscopy, and TEM in virgin samples. Moreover, heavy ion radiation-induced microstructure evolution was followed in the same samples by comprehensive microstructure characterization techniques to understand the radiation resistance effect by Gd_2O_3 doping and intrinsic oxygen vacancy creation.

Chapter 6 presents the application of the *in-situ* HVEM-CL technique to the Gd_2O_3 doped ceria samples. Information on charge state and electronic configurations of *in-situ* defects generated during high-energy electron irradiation were investigated in the doped samples. The Gd_2O_3 concentration effect with the creation of oxygen vacancies by doping for CL emission from the defects varying accelerate energies of the HVEM was investigated. At the end of this chapter, the energy levels of defects in the bad gap of the Gd_2O_3 doped ceria were summarized by comparing the pure ceria.

In chapter 7, all the experimental and simulation works done in the wake of this study are summarized as conclusions. Possible directions of research for further understanding of the radiation recovery effect in electron/ion irradiated $Ce_{1-x}Gd_xO_{2-x/2}$ are also highlighted.

Chapter 2

Theoretical and Experimental background

2.1 Introduction

Ceramics are compounds of ionic and covalent bonds of cations and anions, and they are arranged regularly with the periodicity in crystalline solids. To understand the degradation of ceramics under ions and/or electrons irradiation, it often requires the analysis of physical properties under in-beam condition. Also, the background of the reference materials, ceria and Gd_2O_3 doped ceria which are used in this dissertation, need to be introduced especially for the structure and oxygen deficiency by trivalent cation doping. Fundamental knowledge of analytical methods in short and long ranges is important to understand physical and chemical property changes. Moreover, background of radiation dynamics should be introduced with an emphasis on complex displacement mechanism of ceramics with multi sublattices. In this chapter, the background of experimental techniques and fundamental displacement process relevant to this dissertation are described.

2.2 Crystals and ceramics

Crystals have a long-range order in periodic and they can be categorized into six crystal families and seven crystal systems according to the direction and magnitude (Table 2-1) [29,30]. The labels of a, b, c, and α, β, γ in Figure 2-1 are crystallographic axes and angles, respectively. Generally, ceramics are more complex than metals, which are usually contain two or more crystallographic sublattices with a combination of ionic and/or covalent bonds. These bonds give a high elastic modulus and hardness, high melting point, low thermal expansion, and excellent chemical resistance of ceramic materials [31,32]. The crystal structure of ceria (CeO_2),

Table 2-1. Crystal families and systems

Crystal family	Crystal system	Axis system	
Isomeric	Cubic	a = b = c	$\alpha = \beta = \gamma = 90°$
Tetragonal	Tetragonal	a = b ≠ c	$\alpha = \beta = \gamma = 90°$
Hexagonal	Hexagonal	a = b ≠ c	$\alpha = \beta = 90°, \gamma = 120°$
	Trigonal or Rhombohedral	a = b = c	$\alpha = \beta = \gamma \neq 90°$
Orthorhombic	Orthorhombic	a ≠ b ≠ c	$\alpha = \beta = \gamma = 90°$
Monoclinic	Monoclinic	a ≠ b ≠ c	$\alpha = \beta = 90°, \gamma \neq 90°$
Anorthic	Triclinic	a ≠ b ≠ c	$\alpha \neq \beta \neq \gamma \neq 90°$

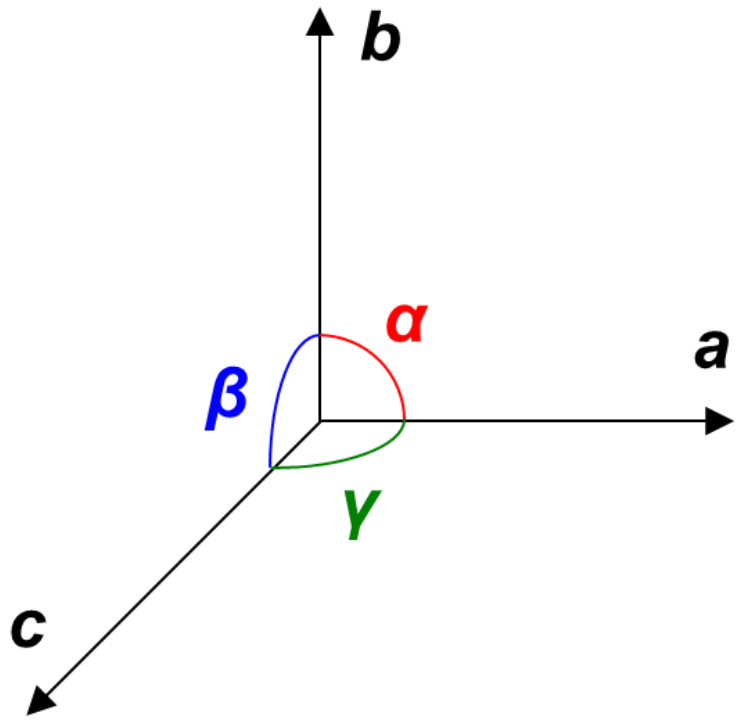

Figure 2-1. Crystallographic axes *a*, *b*, *c* and the angles α, β, γ in positive values.

which is the main compounds investigated in this dissertation, is shown in Figure 2-2 (a). As shown in Figure 2-2 (b), it forms the fluorite structure: the structure and stability of ceria will be discussed in the following section 2.2.1.

2.2.1 Cerium dioxide (CeO_2)

Cerium dioxide or ceria (CeO_2) is one of the prominent materials for a surrogate of PuO_2 and for an inert matrix fuel, such as rock-like oxide fuel [33]. It is noted that most oxide-based nuclear fuels have a fluorite structure. Ceria also possesses a stable cubic fluorite structure under ambient pressure from room temperature to the melting point (2477 °C) [Figure 2-2 (b)].

Ceria produces nature oxygen vacancies due to its non-stoichiometry occurring through the reduction and oxidization of cerium. Under the reducing condition, Ce (IV) is converted into Ce (III), and the reduced ceria is charge-balanced by forming oxygen vacancies. The composition of ceria can be expressed as CeO_{2-x}, where x in CeO_{2-x} represents the oxygen vacancy concentration. The reversible redox reaction in ceria is written in Kröger-Vink notation as below,

$$\mathrm{Ce(IV)} \leftrightarrow \mathrm{Ce(III)}, \tag{2-1}$$

$$2\mathrm{Ce}_{\mathrm{Ce}}^{\times} + \mathrm{O}_{\mathrm{O}}^{\times} \leftrightarrow 2\mathrm{Ce}_{\mathrm{Ce}}^{\prime} + 1/2\mathrm{O}_2(\mathrm{g}) + \mathrm{V}_{\mathrm{O}}^{\cdot\cdot}, \tag{2-2}$$

where the $\mathrm{Ce}_{\mathrm{Ce}}^{\times}$ and $\mathrm{O}_{\mathrm{O}}^{\times}$ are neutrally possessed Ce and O ions in their lattice sites (i.e., Ce^{4+} and O^{2-}), respectively. $\mathrm{Ce}_{\mathrm{Ce}}^{\prime}$ represents a Ce ion at a Ce ion lattice site with a localized mobile electron (i.e., Ce^{3+}), and $\mathrm{V}_{\mathrm{O}}^{\cdot\cdot}$ is positively charged oxygen vacancy (no electron localization). Ceria has a wide band gap energy (~ 6 eV) between 2*p* oxygen valence band and 5*d*, 6*s* cerium conduction band [34,35]. Between these two bands, there is an empty cerium 4*f* band, called $4f^0$ state, which is a narrow localized level in stoichiometric ceria [36]. As the oxygen atom is reduced, an electron is transferred to the empty 4*f* band and it is partially filled, leading the

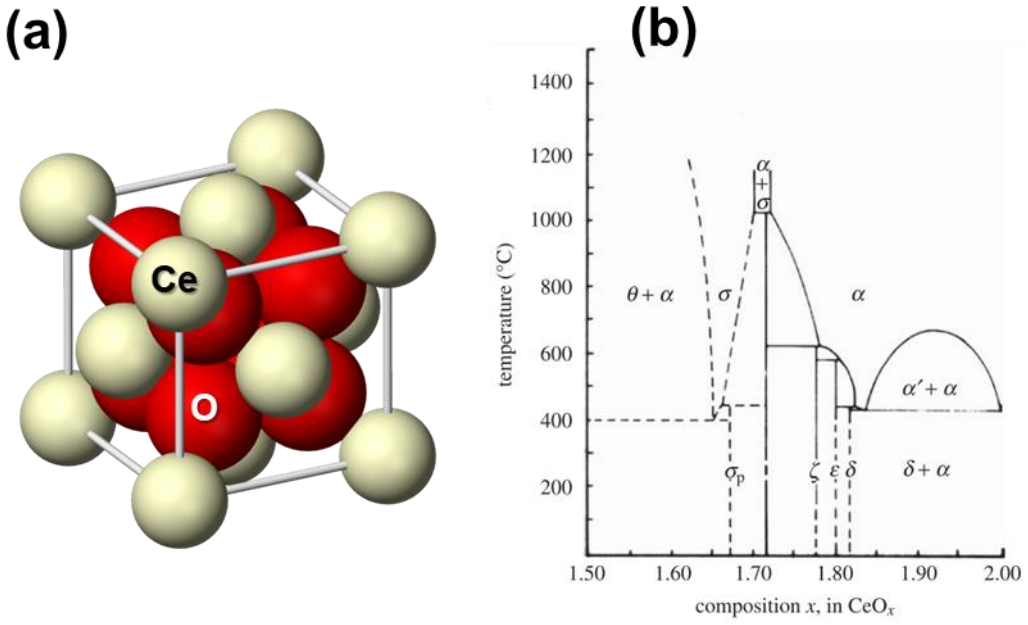

Figure 2-2. (a) Cubic fluorite-type crystal structure and (b) phase diagram of ceria [37].

band splitting into 4*f* full ($4f^1$) and 4*f* empty ($4f^0$) due to spin-orbit coupling of cerium ion [38].

2.2.2 Gd_2O_3 doped CeO_2

Gd_2O_3 doped CeO_2, as expressed by $Ce_{1-x}Gd_xO_{2-x/2}$, is expected to create oxygen vacancies by the substitution of Gd^{3+} into Ce^{4+} site since cations have similar Shannon ionic radius (i.e. Gd^{3+}: 1.053 Å, Ce^{4+}: 0.970 Å). However, due to the different valence states of Gd^{3+} into Ce^{4+} ions [39], a vacancy is created at an oxygen ion site as described by Kröger–Vink notation below,

$$2Ce_{Ce}^{\times} + O_O^{\times} + Gd_2O_3 \rightarrow 2Gd'_{Ce} + V_O^{\cdot\cdot} + 2CeO_2, \qquad (2\text{-}3)$$

where $Ce_{Ce}^{\times}$ and $O_O^{\times}$ represent the neutral charge state of Ce^{4+} on a cerium lattice site and O^{2-} on an oxygen lattice site, respectively. Gd'_{Ce} is a Gd^{3+} ion located at a cerium lattice site with -1 charge, and $V_O^{\cdot\cdot}$ is a vacancy at an oxygen lattice site with +2 charge [40]. In the $Ce_{1-x}Gd_xO_{2-x/2}$ system, the oxygen deficiency is mainly determined by the Gd_2O_3 content [41–43]. Besides, the Gd_2O_3 has a cubic bixbyite (C-type, Ia-3) structure as shown in Figure 2-3 (a) which is close to the fluorite (F-type, Fm-3m) structure. A unit cell of the C-type structure is built from eight-unit cells of the F-type structure, but the C-type structure includes 25% of ordered oxygen vacancies unless the F-type structure [44]. As a consequence of Gd_2O_3 doping, the crystal structure transforms from F-type to the double lattice parameter of C-type ordering oxygen vacancies. Figure 2-3 (b) is a phase diagram of Gd_2O_3 doped ceria examined by different authors. The temperature of ordering (T_{ord}), phase separation (T_{sep}), freezing transition (T_F), cation quenching (T_q), and ordering transition (T^q_{ord}) were evaluated by Monte Carlo (MC) modeling and density function theory (DFT) in $4 \times 4 \times 4$ supercells with 768 lattice sites by Žguns et al [45]. Also, the phase transition from fluorite (F) to C-type (C) was observed by experimental analysis such as XRD [46–48], XAFS [47], and gas analysis [49] at various

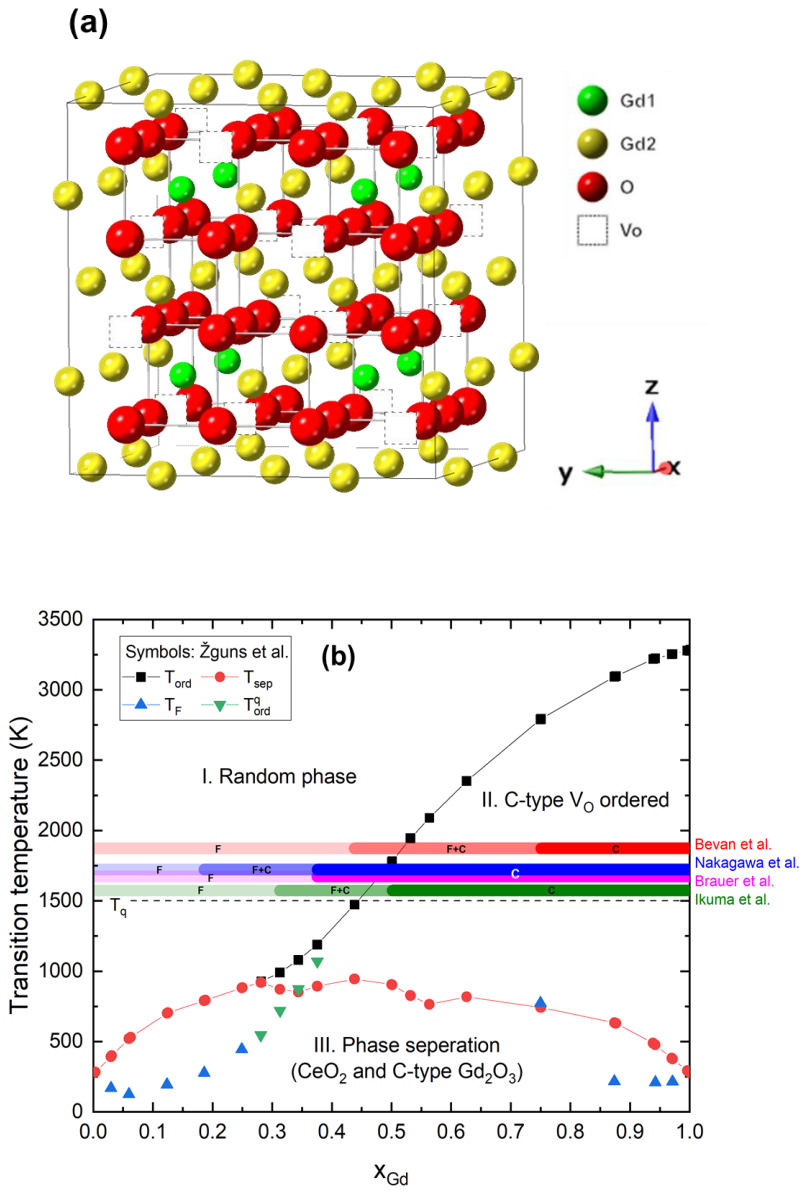

Figure 2-3. (a) Bixbyite (C-type) structure of Gd_2O_3 and (b) phase diagram of Gd_2O_3–CeO_2. Symbols represent the DFT calculation results conducted by Žguns et al. [45]. In the thermodynamic equilibrium, T_{ord} (black) and T_{sep} (red) are temperatures of ordering and phase separation, respectively. The ordering transition was hardly observed for $x_{Gd} < 0.3$, while the vacancy ordering occurred with phase transition for $x_{Gd} \gtrsim 0.3$. Cations were quenched at 1500 K (T_q) and ordering transition (T^q_{ord}) was observed for $0.27 \lesssim x_{Gd} \lesssim 0.4$. Oxygen freezing ($T_F$), which is the rearrangements of vacancies upon cooling are mostly stopped, was observed for $x_{Gd} \lesssim 0.27$ and $\gtrsim$ 0.75. The red, blue, magenta and green horizontal bars represented experimental data of phase transition between fluorite (F) to C-type (C) suggested by Bevan et al. [49], Nakagawa et al. [47], Brauer et al. [46], and Ikuma et al.[48]. F+C is a biphasic region.

quenching temperatures. The fluorite structure started to transform around x_{Gd} = 0.2 ~ 0.5 to the C-type structure but it strongly depends on T_q and analysis methods.

The oxygen vacancy ordering was observed in nano-sized domains formed by the aggregation of dopant Gd^{3+} ions and oxygen vacancies, as observed by electron energy loss spectroscopy (EELS) analysis [50], high-resolution transmission electron microscopy (HRTEM) and the selected area electron diffraction (SAED) patterns [51]. As a consequence of the oxygen vacancy ordering, the disordering is produced by the influence of electrostatic repulsion with oxygen vacancies in the C-type structure, while cations in fluorite keep their perfect cube with 8 coordinated oxygen ions [42]. In particular, it affects the distribution of the interatomic distance between cation-cation pairs rather than cation-oxygen pairs. In addition, the clustering of the dopants with associated oxygen vacancies is increasing with dopant concentration increasing. The clusters reduce the concentration of freely mobile oxygen vacancies that rather decreases conductivity at high concentrations of dopants [51–54].

2.3 X-ray diffraction (XRD) analysis and the Rietveld refinement

X-ray diffraction (XRD) technique helps the understanding of the physical properties of metals, ceramics, polymers, and other solids allowing one to understand the arrangement and distance of lattice planes in a form of crystals. W.H. Bragg and W. L. Bragg interpreted the crystal diffraction by using the wavelength of x-ray, and they expressed it as Bragg's law [Eq. (2-4)].

$$n\lambda = 2d \sin\theta. \qquad (2\text{-}4)$$

When the phase difference between two or more waves is half of the wavelength, the wave is offset and disappears, but when the phase difference is an integer (n) multiple of the wavelength (λ), the amplitude is amplified, and the intensity becomes greater. In Figure 2-4, the distance from A to B is $d \sin\theta$, where d is lattice distance, θ for Bragg's angle, which is

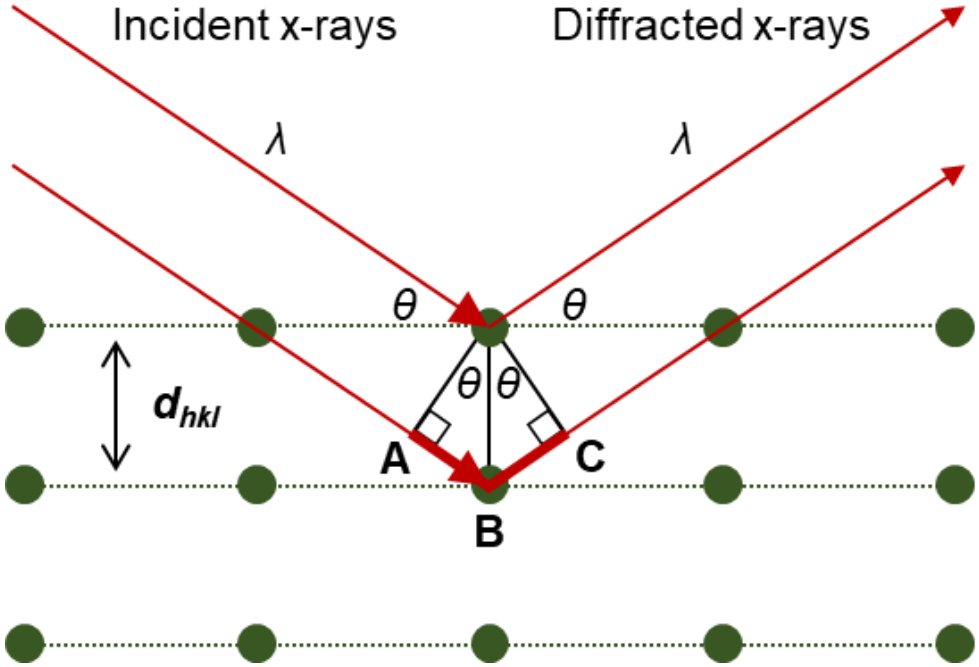

Figure 2-4. Braggs' law reflection

equal to the distance from B to C. Therefore, if AB = BC = $d \sin\theta$ and the following Eq. (2-4) is satisfied, x-rays are strongly diffracted.

In the microcrystalline powder sample, a number of crystalline are combined in random directions. Furthermore, one powder sample consists of more than one phase. In this multi-phase sample, the single Braggs' reflection is hard to examine the crystal structure with high symmetry refinement, since diffracted XRD intensities are overlapped in the XRD patterns. For the multi-phase sample XRD analysis, the Rietveld refinement can be used by fitting Gaussian, Lorentzian, or Pseudo-Voigt profiles using the least-square method, and this method can use for quantitative analysis [55]. The Rietveld refinement is conducted by a computer algorithm and free software programs are typically used for instance Fullprof [56], GSAS [57], and RIETAN [58]. For the operation of Rietveld refinement, it is important to determine crystal structure if the initial structure is known, unless it should be operated by *ab-initio* calculation. Reliable crystal structure models can obtain from the database such as 'Inorganic Crystal Structure Database' [59], 'American Mineralogist Crystal Structure Database' [60], and Crystallography Open Database [61].

The quality of Rietveld refinement is measured by parameters of goodness factor (χ^2), weighted profile factor (R_{WP}) and R expected (R_{EXP}). For the interpretation, values of observed and computed XRD peak intensity at the position of $2\theta_i$ are assigned to $y_{i,O}$ and $y_{i,C}$, respectively. The Rietveld algorithm targets to minimize the weighted sum of squared differences between the observed and computed intensity values [i.e., $\sum w_i\left(y_{i,O} - y_{i,C}\right)^2$], where w_i is $1/\sigma^2[y_{i,O}]$. $\sigma[y_{i,O}]$ is uncertainty estimate for $y_{i,O}$. R_{WP} is the most meaningful of the weighted profile R-factors because of the minimized residuals. It can be expressed by,

$$R_{WP}{}^2 = \frac{\sum w_i(y_{i,O} - y_{i,C})^2}{\sum w_i(y_{i,O})^2} \quad (2\text{-}5)$$

The best possible value of R_{WP} expected for the number of data points (N) can be represented as the expected R-factor, R_{EXP} [62]. R_{EXP} is described below,

$$R_{EXP}{}^2 = \frac{N}{\sum w_i (y_{i,O})^2} \quad (2\text{-}6)$$

The statistical quality of the refinement is explained by Chi-squared (χ^2). They are calculated through equations as written below,

$$\chi^2 = R_{WP}/R_{Exp} \quad (2\text{-}7)$$

A goodness of fit can be defined by χ^2, and its value of 1.3 or less is usually considered reasonable [62]. Too small χ^2 value means that the counting statistical errors are greater than the model errors either because of poor counting statistics or because of high background by slowly varied angle [62].

2.4 Displacement damage and Energy loss

A displacement cascade is induced by an elastic collision between a high-energy particle and a target atom. The initially displaced atom directly from an incident radiation particle is called as a primary knock-on atom (PKA). If the PKA has sufficient energy, the knocked lattice atom results to rest in an interstice of lattice, which generates an interstitial atom. Complementary, the original lattice site remains vacant to form a vacancy. This simple pair of interstitial and vacancy remaining stable is called as a Frenkel pair.

To initiate displacement from the lattice site, the transferred kinetic energy to the lattice atom should be higher than the threshold displacement energy (E_d). E_d is a material dependent physical quantity. In general, experimental measurement of E_d is difficult for ceramics due to their complex structure [11,63]. The values of E_d are also dependent on the crystallographic direction [64], and temperature.

In a collision between a charged particle and a target atom nucleus, the mean free path between these two-body collisions should be greater than the interatomic spacing. We can apply the law of conservation of energy and momentum in the elastic collision satisfied with nonrelativistic mechanics.

$$T = \frac{4M_1M_2}{(M_1+M_2)^2} E\sin^2(\frac{\theta}{2}), \quad (2\text{-}8)$$

where T is the transferred energy to the PKA, E is the incident particle energy, θ is the angle of deflection of the incident particle as a result of the collision, M_1 is incident particle mass and M_2 is struck atomic mass. When the θ = 0, the T shows the maximum value, T_m, which is written as,

$$T_m = \frac{4M_1M_2}{(M_1+M_2)^2} E \quad (2\text{-}9)$$

For the case of high-energy electrons, relativistic quantum mechanics should be used for the calculation. As assuming that M_1 is an electron (m_e), the rest energy is written by Eq. (2-10) with an approximation of $M_1 \ll M_2$ as follows,

$$M_1c^2 = m_ec^2 = 0.511 \text{ (MeV)}, \quad (2\text{-}10)$$

where c is the light velocity (2.998×10^8 m/s). By adding the relativistic correction, T_m given by the incident electron to the target atom is expressed as,

$$T_m = \left(\frac{2m_e}{M}\right)\left(\frac{E+2m_ec^2}{m_ec^2}\right)E, \quad (2\text{-}11)$$

where E is incident electron energy (MeV), M is mass of PKA (u).

To understand displacement damage generation by electron irradiation, E_d should be higher than T_m. The relationship between T and E_d can be explained by,

i) $T_m < E_d$: No displacement occurs,

ii) $T_m \geq E_d$: Displacement occurs displaced atoms remain as the Frenkel pairs producing defects such as displacement loop or voids.

iii) $T_m \gg E_d$ (i.e., T > ~1 keV): PKA produce displacement chain reaction to surrounding atoms, which is called as cascade collision.

The displacement cross-section (σ_d) for electron-nuclear collision can be measured for the range of angle between θ_m and π for the quantity of greatest interest in the interpretation of radiation damage. σ_d was evaluated by McKinley-Feshbach formula [65],

$$\sigma_d = \frac{\pi}{4}(b')^2\left\{\frac{T_m}{E_d} - 1 - \beta^2 \ln\frac{T_m}{E_d} + \pi\alpha\beta\left[2\left(\frac{T_m}{E_d}\right)^{1/2} - \ln\frac{T_m}{E_d} - 2\right]\right\}, \qquad (2\text{-}12)$$

where $b' = \frac{2Ze^2}{mv^2}(1-\beta^2)^{1/2}$, $\alpha = Ze^2/\hbar c$, $\beta = v/c$, v is velocity of the electron incident on a nucleus of charge Ze. The σ_d calculation for O and Ce sublattice in ceria as a function of incident electron energy will be shown in Chapter 4.

When a charged particle incident to a target material, it loses the kinetic energy through interaction with the nuclei or electrons in the target matter. The energy loss in a targeted matter determines the final distribution of defects. The energy loss which is referred to as stopping power is noted as

$$S(E) = -\frac{dE}{dx} = \left(-\frac{dE}{dx}\right)_n + \left(-\frac{dE}{dx}\right)_e, \qquad (2\text{-}13)$$

where the total stopping power $S(E)$ is defined as the differential of its energy (E) by the penetration depth, or $-\frac{dE}{dx}$. The total stopping power is the sum of nuclear (n) and electronic (e) stopping power. The electronic and nuclear stopping power calculation results for oxygen ions in CeO_2 are shown in Figure 2-5. The threshold displacement energy of oxygen ion ($E_{d,O}$) value was used as 14 eV for this calculation. The left y-axis is electronic stopping power (S_e) and the right one is nuclear stopping power (S_n). The S_e showed higher values than the values of S_n, and the energy loss mostly occurred by S_e with the increase of the primary electron energy. For the thin TEM samples (thickness: ~100 nm), S_e is negligible for the E ranging of 200 keV < E < 1500 keV as 5 ~ 6 eV, while the think samples for CL measurement (thickness: ~150

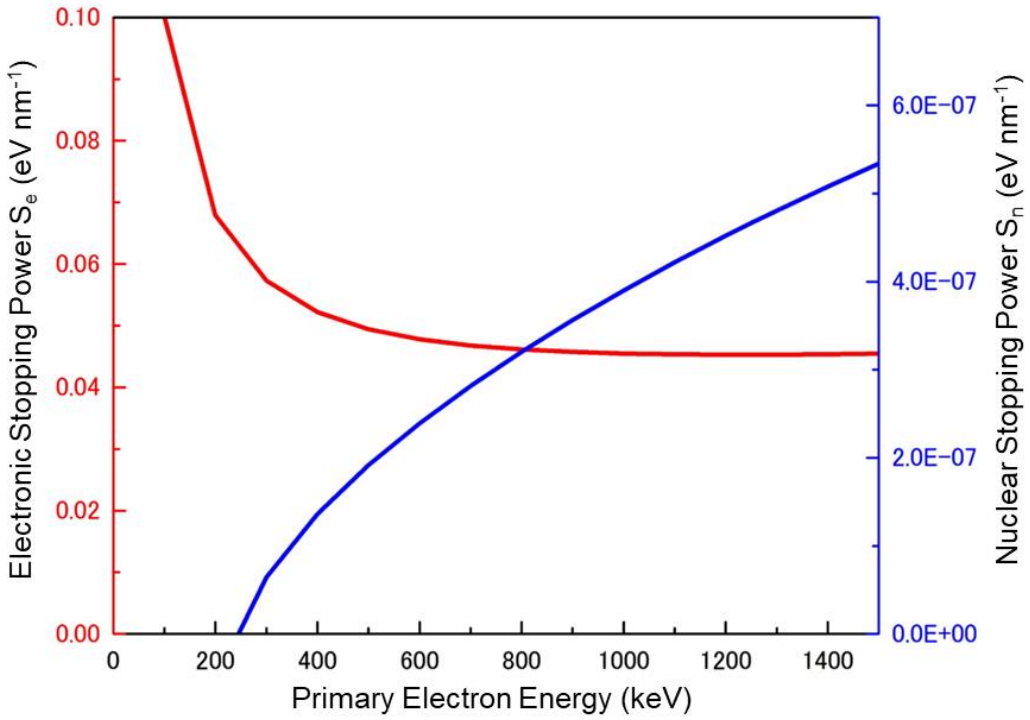

Figure 2-5. Oxygen ion electronic and nuclear stopping power in CeO_2 as a function of primary electron energy. The threshold displacement energy of oxygen ion ($E_{d,O}$) was 14 eV for this calculation.

μm) showed high S_e as 8 ~ 9 keV. Despite high S_e values for thick samples, the reduction of S_e is dominant only for E < 200 keV. Therefore, displacement is mainly depending on the increase of S_n versus primary electron energy.

2.5 F center and CL spectroscopy

Defect charge state and electronic structure is important properties of an ionic crystal. The defects located within band gap cause absorptions and emissions of visible light. This defect is called F center (Farbe center or color center). F centers are generated in laser-active metallic oxides. It is formed by as the anion is excited; one or more unpaired electrons are trapped by the anion vacancy site. F centers are designated according to its charge state, such as F^0, F^+ or F^{++} centers by the number of captured electrons of two, one, or zero, respectively.

Figure 2-6 illustrates F centers and Ce ions (Ce^{3+}, Ce^{4+}) in ceria. The distribution of oxidation number of Ce ion around the F center was involved in the charge state of the F center according to the number of electrons left behind at a vacancy or 4*f* level [66,67]. The conversion of F and F^+ centers is related to the excitation and ionization cross-section, the intensity of incident electrons, and the number of excited F^+ centers (F^{+*}) [68]. The energy level of F centers is ceria was interpreted by photoluminescence spectroscopy, electron paramagnetic resonance (EPR), and density functional theory (DFT) calculation [69].

Cathodoluminescence (CL) is an optical and electromagnetic phenomenon using pulses from high-energy electrons (cathode rays) as the means of excitation. The CL emission is generally collected for imaging or spectroscopy. CL image gives an important information on different phases, point defects or impurities localization. On the other hand, CL spectroscopy provides a specific wavelength emitted from impurities and defects in band gap materials giving its charge number.

The electron beam for CL measurement is generally produced from an electron microscope [e.g., SEM, scanning transmission electron microscope (STEM)], electron-prove microanalysis (EPMA), or cathodoluminescence microscope. These primary electron energies are generally too high to directly excite electrons. Therefore, the inelastic scattering of the primary electrons in the target leads to the emission of secondary electrons, and the secondary electrons excite the electrons with a kinetic energy higher than band gap of the target.

CL emission process can be explained by the electron and hole trapping and de-trapping in phosphor interaction. At first, the secondary electrons are produced by elastic and inelastic scattering process. They produce electron and hole pairs and give rise electron and hole trapping at defects or impurities levels in the band gap. The trapped electrons and holes are excited by primary and secondary electrons. Then, light emitted by radiative decay from excited states. Finally, the electrons and holes are recombined together, and CL light is emitted. The CL cross-section (σ_{CL}) can be shown schematically in Figure 2-7 and written as,

$$\sigma_{CL} = \sigma_i \sigma_t \sigma_e \sigma_r, \tag{2-14}$$

where σ_i is the ionization cross-section generating free electron hole pairs by elastic and inelastic collision, σ_t is the trapping cross-section for thermalized electrons or holes on electronic levels of defects or impurities, σ_e is the excitation cross-section of these levels by primary and secondary electrons, and σ_r is the radiative-decay cross-section from excites state [25]. Non-radiative recombination takes place from ground state to the valence band states [70].

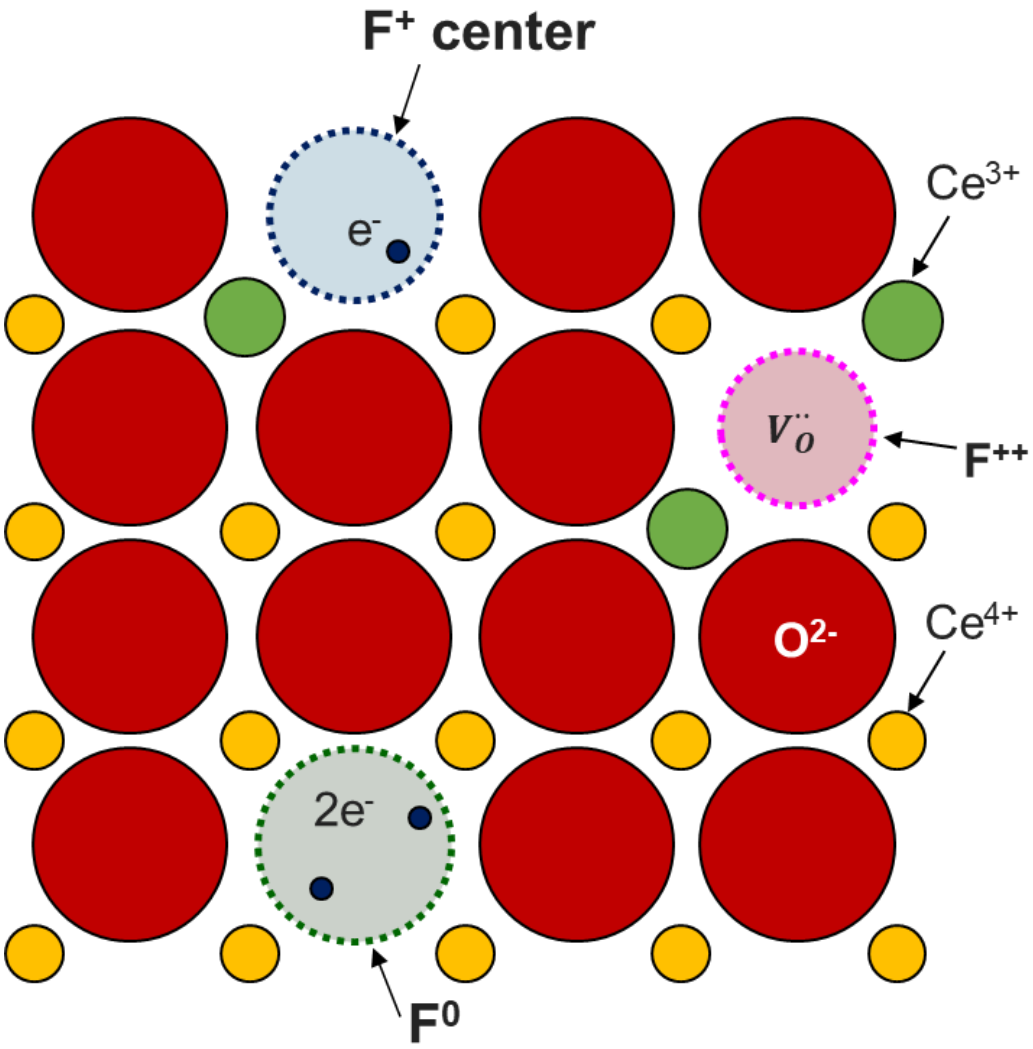

Figure 2-6. Scheme of F centers, cerium (Ce^{3+}, Ce^{4+}) and O^{2-} ions in ceria (100) plane.

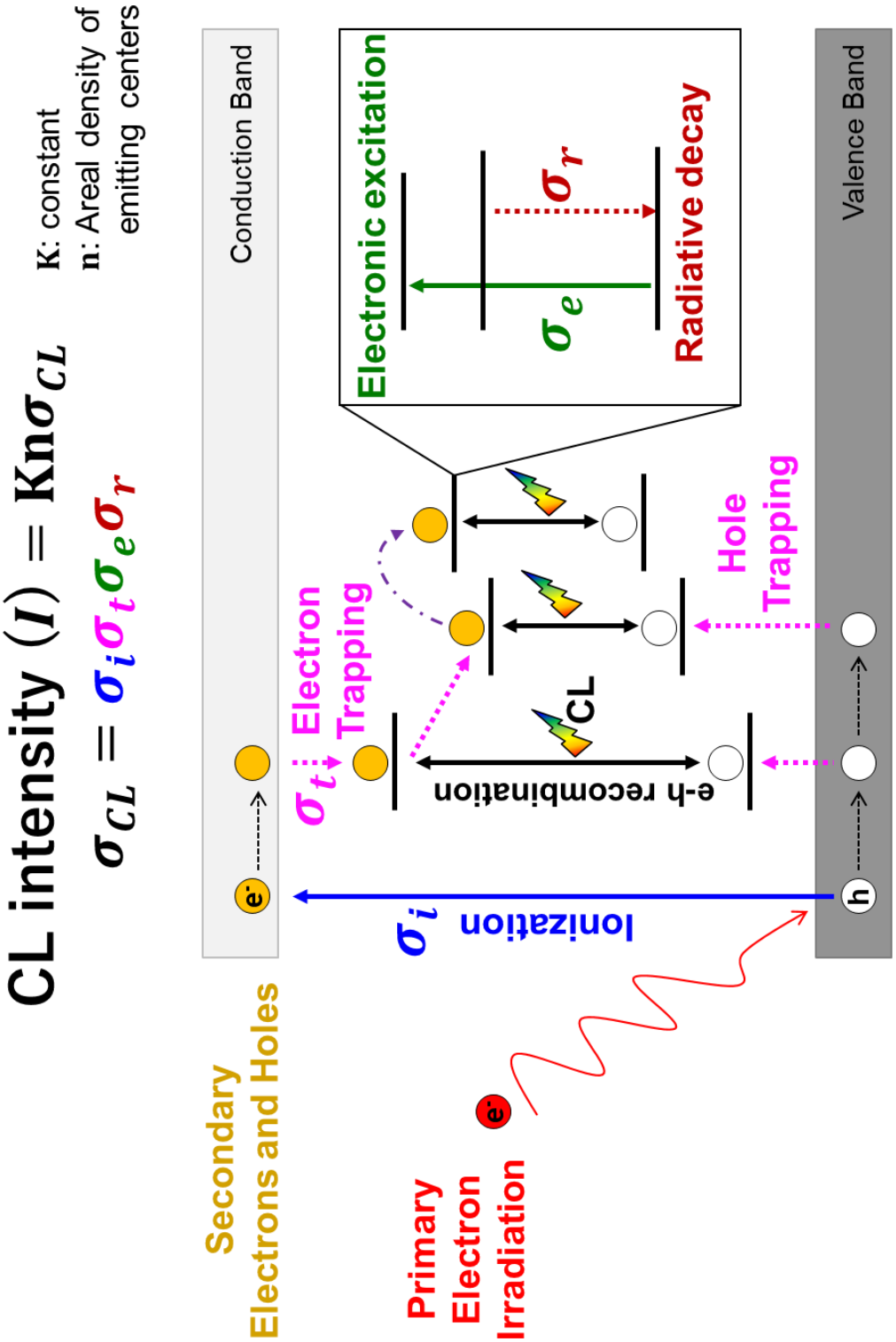

Figure 2-7. Scheme of cathodoluminescence (CL) emission process.

Chapter 3

Experimental detail

3.1 Introduction

In this dissertation, atomistic and electronic characteristics of radiation-induced displacements in ceramics and their crystal microstructure evaluation with heavy ion irradiation were elucidated in a wide range of scale analysis methods to understand the synergetic effect and kinetics of point defects under irradiation. In this chapter, the structural properties of virgin ceramics before the irradiation, and electron/ion irradiation experimental conditions were described in detail. Moreover, experimental techniques, for instance, XRD, Raman spectroscopy, TEM methods, *in-situ* CL spectroscopy under high-energy electron irradiation, and experiment conditions operated in this dissertation were described.

3.2 Specimens

Single crystal ceria, polycrystalline ceria and Gd_2O_3 doped ceria were used in this dissertation. The single crystal ceria was supplied from Dr. W. J. Weber in Oak Ridge National Laboratory in USA. The thickness of the specimen is around 1 mm. It was attached to half-disk shape of tungsten washer in diameter of 3 mm to adjust the specimen. The sample image is shown in Figure 3-1.

3.2.1 Synthesis

Polycrystalline ceria and Gd_2O_3 doped ceira ($Ce_{1-x}Gd_xO_{2-x/2}$) ($0.01 \leq x_{Gd} \leq 0.5$), were synthesized by solid state method. Ceria and Gd_2O_3 powders were supplied by Rare Metallic Co., Ltd., with 99.9% of purity. The impurities in ceria were shown in Table 3-1. Ceria and

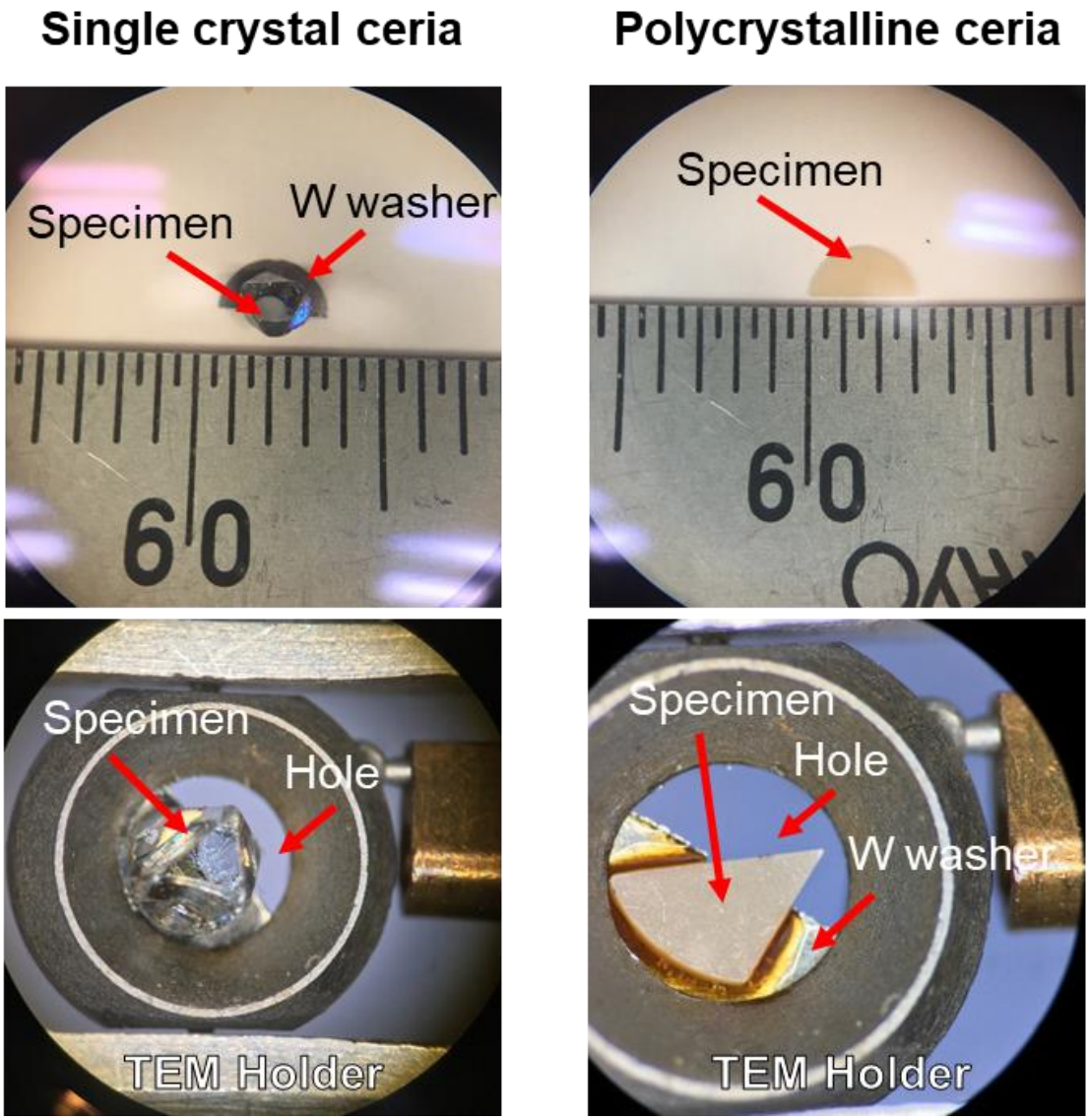

Figure 3-1. Single crystal and polycrystalline ceria specimen images.

Table 3-1. Impurities in ceria powder.

Element	Concentration (ppm)
Y_2O_3	< 5
La_2O_3	10
Pr_6O_{11}	< 5
Nd_2O_3	6
Sm_2O_3	< 5
Eu_2O_3	< 5
Gd_2O_3	< 5
Tb_4O_7	< 5
Dy_2O_3	< 5
Ho_2O_3	< 5
Er_2O_3	< 5
Tm_2O_3	< 5
Yb_2O_3	< 5
Lu_2O_3	< 5
CaO	< 5
Fe_2O_3	< 5
SiO_2	< 20

Gd_2O_3 powders were ball milled homogeneously with ethyl alcohol for 24 hours. The mixtures were compacted into a pellet by uniaxial pressure at 30 MPa for 15 minutes to make a condensed pellet type sample ($\varphi \approx 10$ mm, $t \approx 2$ mm). They were compressed again sealed in a plastic bag by hydraulic pressure at 150 MPa for 30 minutes. The compacted pellets were put in an alumina crucible within ceria powder and sintered in the air-atmosphere at a temperature of 1500 ℃ for 12 h followed by an additional annealing at 1000 ℃ for 3 h in the air. The sintered compact samples have ~95% of relative densities. The sintered samples were prepared as a disk type for ion irradiation in a diameter of 3 mm and a thickness of 150 μm. They were polished by diamond slurries in particles size of 9 μm, 3 μm and 0.5 μm (Masashino Denshi, inc., MP-1000(W)), and then removed distortion, deterioration layers and fine scratch marks using colloidal silica (Masashino Denshi, inc.).

3.2.2 Heavy ion irradiation

The thin disk-type samples in thickness of 150 μm were irradiated at ambient temperature with 200 MeV $^{131}Xe^{14+}$ ions using the Tandem accelerator at Tokai Research and Development Center, Japan Atomic Energy Agency (JAEA-Tokai) to fluence ranging from 3×10^{11} to 1×10^{13} cm^{-2}. The electronic (S_e) and nuclear (S_n) stopping power of the 200 MeV Xe^{14+} ion for CeO_2 and $Ce_{0.5}Gd_{0.5}O_{1.75}$ were calculated with the Stopping and Range of Ions in Matter (SRIM) code [71] with assumptions of displacement energies of 60 eV for Ce, 70 eV for Gd and 30 eV for O atoms, respectively [9,72]. Initial values of S_e at the surface were evaluated to be 27.3 and 26.5 keV nm^{-1} for CeO_2 and $Ce_{0.5}Gd_{0.5}O_{1.75}$, respectively, whereas values of S_n at the surface region were negligible, 0.07 and 0.05 keV nm^{-1} for CeO_2 and $Ce_{0.5}Gd_{0.5}O_{1.75}$, respectively, compared to S_e. The maximum of S_n for CeO_2 and $Ce_{0.5}Gd_{0.5}O_{1.75}$ is 0.96 and 0.89 keV nm^{-1} at a depth of 11.3 and 12.2 μm, respectively.

3.2.3 Ion thinning

For the thin-foil sample preparation suitable for TEM observation, the thin disk-type samples with a diameter of 3 mm were attached to a single-hole molybdenum TEM grid (Φ = 1.2 μm) to keep them from destruction during the dimpling process. The center of the sample was dimpled using diamond slurries from the opposite side of the irradiated surface, followed by an ion thinning using an ion-milling system (PIPSII M-695, Gatan Inc.) with 5 keV Ar ion beams at 8 deg. until a small hole was formed. A dual-beam mode for both side milling was followed to enlarge the hole size up to ~200 μm. Contamination and Ar-ion damaged layers were finally removed using 0.5 keV Ar ions for 30 min. A thin carbon film was coated on the irradiated samples to weaken the charge-up effect during TEM observations.

3.3 XRD measurement

XRD experiments were performed at room temperature by an XRD Rigaku. SmartLab® diffractometer with Cu-Kα ($K\alpha_1$ = 0.15406 nm, $K\alpha_2$ = 0.15444 nm) radiation x-ray source (30 mA, 40 kV) of monochromatic θ-2θ scans. The XRD facility is shown in Figure 3-2. XRD patterns were recorded under continuous rotation from 20 to 90 2θ deg. at a step size of 0.01 deg. A part of sintered virgin samples was ground to a powder and was mounted in a glass holder with a volume of 200 mm^3, and the pattern was obtained with a scan speed of 10 deg. min^{-1}.

On the other hand, XRD patterns of ion-irradiated samples were measured with a bulk type of samples. The Cu-Kα X-ray penetration depth in $Ce_{1-x}Gd_xO_{2-x/2}$ is 2.26 μm for 90 deg. [73], while the projected range of 200 MeV Xe^{14+} ions is 11 ~ 12 μm. Therefore, signals from ion-irradiated samples were generated from the irradiated surface region, including ion tracks caused by electronic stopping power [71], and the unirradiated layer beneath the ion-irradiated surface does not influence the XRD patterns. A non-reflective holder, made with single crystal

Figure 3-2. XRD measurement facility (SmartLab, Rigaku Co.) at the Center for Advanced Instrumental Analysis in Kyushu University

silicon in an orientation that does not satisfy the diffraction conditions, was used for holding ion-irradiated samples of a relatively small size of 3 mm in diameter with a scan speed of 3 deg. min^{-1} to enhance the intensity. The XRD patterns from thin disk-shaped samples were also obtained by the virgin samples in the same measurement conditions to compare the intensity with those of irradiated samples. The crystal structure of each sample was refined by the Rietveld method using FullProf suite software [56] based on the split Pseudo-Voigt function, and the XRD patterns from Cu-$K\alpha_1$ radiation were only used for the analysis.

3.4 Raman spectroscopy

Micro-Raman spectra were recorded at room temperature with 532 nm Nd-YAG laser excitation in the backscattering geometry using an Invia Reflex® Renishaw spectrometer coupled with an Olympus microscope containing a $x - y - z$ stage. The TO/LO peak of silicon wafer was used as a reference spectrum. Spectra were collected between 100 and 1100 cm^{-1} for virgin $Ce_{1-x}Gd_xO_{2-x/2}$ samples with a focal spot of 1×1 μm^2 inside a single grain and collected through a 100 times objective. The laser power was kept below 1-mW to avoid in-beam sample annealing. Raman spectra were obtained from virgin samples in CEA, France by Dr. Jean-Marc Costantini.

3.5 Transmission electron microscopy (TEM)

The SAED patterns and bright-field (BF) TEM images were taken by using a conventional TEM (JEM-2100HC, JEOL Ltd.) in the Ultramicroscopy Research Center (URC) of Kyushu University at an accelerating voltage of 200 kV. A photo of JEM-2100HC is shown in Figure 3-3. For the imaging, a parallel beam was used with the opened condenser lens aperture and spot size 2. A biaxial holder (JEOL EM-31630) was used to tilt the sample up to ± 38° and ± 30° to x and y-axis, respectively. JEM-2100HC performance is written below.

Figure 3-3. A conventional TEM (JEM-2100HC, JEOL Ltd.) in Kyushu University.

- Acceleration voltage: 100, 120, 200 kV
- Resolution: 0.31 nm for point, 0.14 nm for lattice
- Magnification: 1 k ~ 800 k
- Minimum probe diameter: 1~5 μm

3.6 High voltage electron microscope (HVEM)

The HVEM (JEM 1300NEF, JEOL Ltd.) of the URC was operated to detect *in-situ* CL under high-energy electron irradiation. A photo of JEM-1300NEF is shown in Figure 3-4. A scheme of it below the acceleration tube system is shown in Figure 3-5. The electrons are emitted from LaB_6 filament and accelerated by using the acceleration tube with certain energies. The intensity of the electron beam and parallel illumination is adjusted by the condenser lens and irradiated to the specimen. It is possible to observe and record a magnified image of the specimen on the fluorescent screen if the specimen is very thin where electrons transmit the specimen. High-resolution imaging by using an Omega-type energy filter, elemental mapping with SDD XEDS detector, or EELS system are available with the HVEM. The performance of the HVEM is written below.

- Acceleration voltage: 400 ~ 1250 kV
- Resolution: 0.12 nm for point, 0.10 nm for lattice
- Magnification: 0.2 k ~ 1200 k
- Minimum probe diameter: 1.6 nm

Figure 3-4. HVEM (JEM 1300NEF, JEOL Ltd.) – CL facility in Kyushu University.

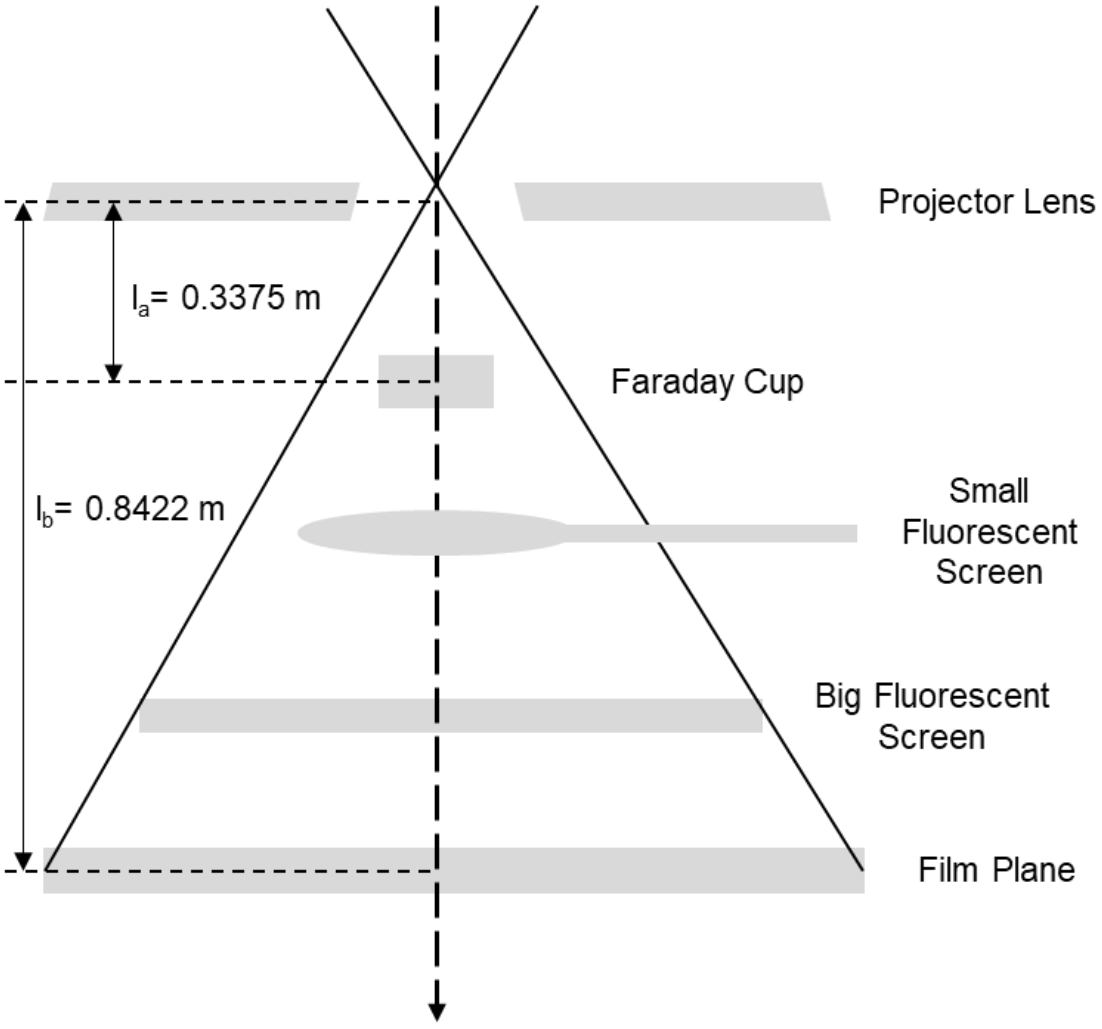

Figure 3-5. Scheme of JEM-1300NEF below projector lens.

3.7 Scanning electron microscope (SEM)

SEM produces images of a specimen by scanning a focused electron beam in a vacuum on a specimen. Secondary electrons, backscattered electrons, x-ray, lights, etc. are emitted from the specimen during the scanning of the electron beam. The SEM consists of an electron gun to emit electrons, the condenser lens and scanning coil to scan electrons, the specimen stage to put and arrange the specimen, detector to detect emitted from the specimen surface. The SEM (SU6600, Hitachi Ltd.) of the Center of Advanced Instrumental Analysis at Kyushu University was operated, and it is shown in Figure 3-6. The focused beams of electrons (0.5 ~ 30 keV) were used from the Schottky emission electron source. The SEM is interfaced with a CL system (Gatan Inc.) to collect CL spectra. The performance of the SEM is written below.

- Secondary electron resolution: 3.0 nm (1 kV), 1.2 nm (30 kV)
- Reflected electron resolution: 3.0 nm (30 kV)
- Vacuum level: 10 ~ 300 Pa (for low vacuum), ~10^{-4} Pa (for high vacuum)
- Magnification: 10 ~ 600 k
- Probe current: 1 ~ 200 nA

3.8 *In-situ* CL spectroscopy system and measurement conditions

3.8.1 High-energy electron irradiation

The CL emission was collected through an optical fiber probe system, which is installed near the specimen port in the HVEM as shown in Figure 3-7. An optical fiber probe was used to correct CL signals, which consist of an optical fiber probe with a 600 μm core diameter and copper coating, which is designed for high throughput in the 180 ~ 1200 nm wavelength range

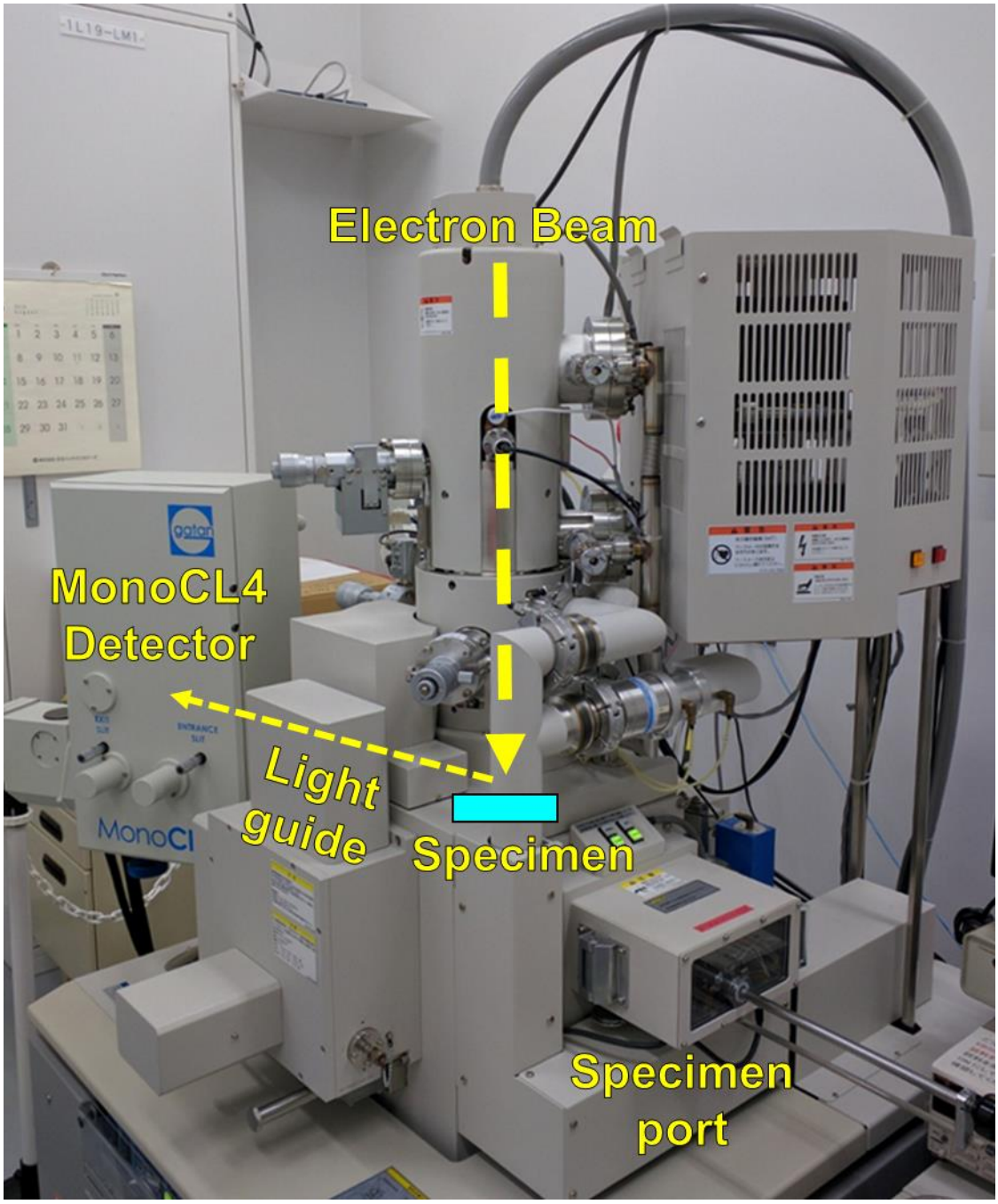

Figure 3-6. SEM-CL facility view of specimen port with CL detection guide lines and a detector.

(ref. 151-AC-AC-UV600, Chiyoda Electronics Co., Ltd). The fiber was inserted through a small hole in diameter of 2 mm and it was aligned at 44° from the electron beam direction without any disturbance for TEM observation. CL signals can be collected with the cooperation of various sample holders and other analyzing tools. CL spectra in the 200 ~ 950 nm wavelength were recorded with a Czerny-Tuner HAMAMATSU MCA spectrometer (PMA-12 C10027-1) equipped with a cooled CCD linear image sensor (1024 channels). The wavelength resolution of the spectrometer was 2 nm. Each spectrum can be taken under the electron beam.

The electron energy was changed during the CL measurement for 400, 600, 800, 1000, and 1250 keV. The electron beam-current density was also changed by changing the intensity of the condenser lens. The electron beam flux (φ) was adjusted in the range from 2.6×10^{21} to 7.7×10^{21} $m^{-2}s^{-1}$ with a beam diameter of 30 μm at the specimen position. The thickness of specimens is ~150 μm for CL measurement for the high number of counts from the electron irradiation. Therefore, the observation of microstructure using HVEM during CL measurement is not available. The half disk-shaped sample was used to adjust the shape, size, and current of the transmission electron beam at the hole in the specimen. The CL spectra were obtained in the magnification × 10k. The specimen holder was used for a biaxial cooling holder (GATAN636). The holder was equipped with a liquid-nitrogen cooling stage for temperature down to about 100 K and up to room temperature (300 K), preventing excessive in-beam heating of samples and temperature control and regulation. The CL spectra were detected for 30 seconds under electron beam in wavelength raging between 195 and 950 nm. The spectra were averaged out for 5 recordings and repeated 5 times for high reproducibility.

Table 3-2. Optical fiber probe performance used in HVEM (JEM-1300NEF).

Optical fiber	SiO_2, Cu coating, core φ = 600 μm, UV transmission
Wavelength range	180 ~ 1200 nm
Fiber protection	Stainless tube, φ = 1.8 mm
Connector	SMA905
Fiber optic application	Optical ball lens, φ = 1 mm
Loss in fiber	In the near the visible range (< 0.04 dBm^{-1} at 400 nm)
Remain in fiber	In the near UV range (< 0.3 dBm^{-1} at 300 nm)

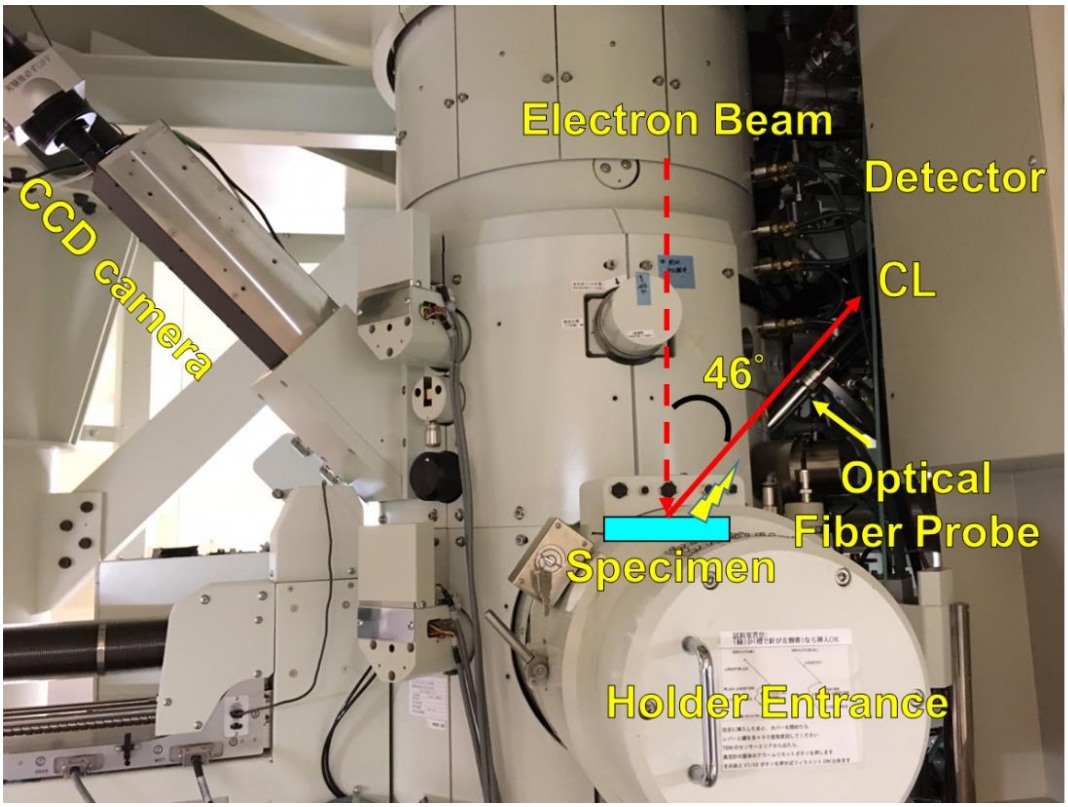

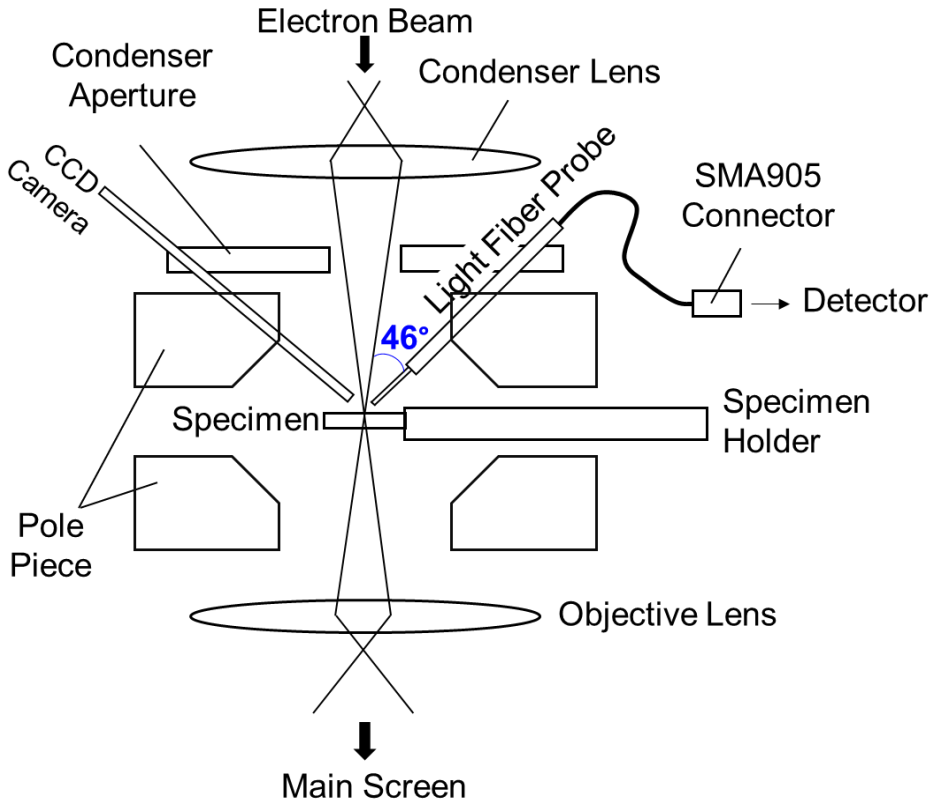

Figure 3-7. HVEM-CL facility view of specimen port, CL (optical fiber) probe and detector and its schematic image [24].

3.8.2 Evaluation of electron irradiation fluence

A Faraday cup, inserted between the specimen and fluorescent screen was used for HVEM to adjust electron irradiation fluence. Accurate electron beam current can be measured with correcting the loss of backscattered electrons and secondary electrons, with a cylindrical shape of a Faraday cup as shown in Figure 3-8. Figure 3-5 is a scheme of HVEM-CL (JEM-1300NEF) below projector lens. R_S was obtained by conversion of the diameter of the Faraday cup and factors below,

$$R_S = R_F \frac{l_b}{l_a} \frac{1}{M}, \tag{3-1}$$

where R_F, l_a, l_b, and M represent diameter of entrance aperture of Faraday up, distance between cross-over of projector lens and Faraday cup, distance between cross-over of projector lens and film plane, and magnification of image plane, respectively.

The total number of electrons incident on Faraday cup is equal to the number of electrons in the electron beam at specimen penetration position. The number of measured electrons per unit time was determined by dividing the current measured from Faraday cup by the elementary charge. The irradiation electron beam intensity (φ) can be calculated by dividing the number of electrons by the area of entrance aperture of Faraday cup as written below,

$$\varphi = \frac{I}{e\pi(R_S/2)^2}, \tag{3-2}$$

where I is current value measured by Faraday cup (A), e is elementary charge (1.602×10^{-19} C). For JEM-1300NEF, $R_F = 1.00 \times 10^{-3}$ m, $l_a = 0.3375$ m, $l_b = 0.8422$ m as shown in Figure 3-5.

3.8.3 Low-energy electron irradiation (MonoCL4 System)

The MonoCL4 system (Gatan Inc.) was used to lead and detect CL emission from the sample under 20 keV electron irradiation in the SEM. The MonoCL4 system consists of a parabolic mirror, light guide to use the emitted CL light, detector, and photomultiplier tube to count photons as shown in Figure 3-9. The parabolic mirror is located to cover the specimen stage. The CL photons are emitted from the specimen, which is generated by the electron beam illumination to the specimen after passing through an aperture with 1 mm in diameter. The CL photons were reflected by the mirror and collected at a detector. The CL photons are collected through light guide toward to the detector in every wavelength. Particular wavelength of CL light could be measured locating diffraction grating since dispersion of the light depends on an angle and variety of the grating.

Electrons with an energy of 20 keV were used in this dissertation. Electron beam current of I = ~1.67 nA was obtained in the magnification ×10k. *In-situ* CL spectra were measured at monochromatic mode in wavelength ranging from 200 nm to 950 nm in a step size 2 nm and dwell time 2 seconds.

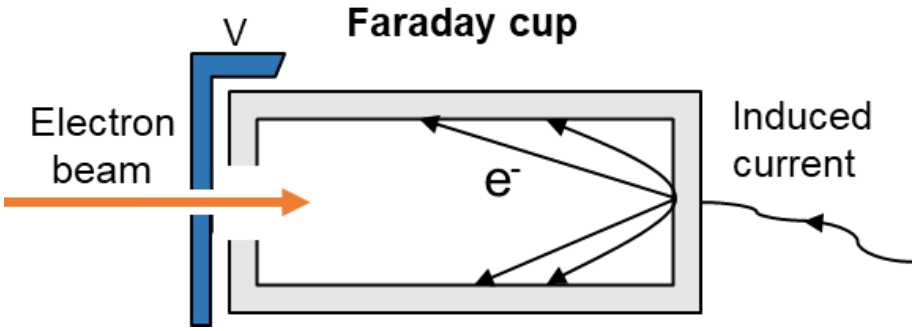

Figure 3-8. Faraday cup for measurement of electron irradiation dose installed in HVEM.

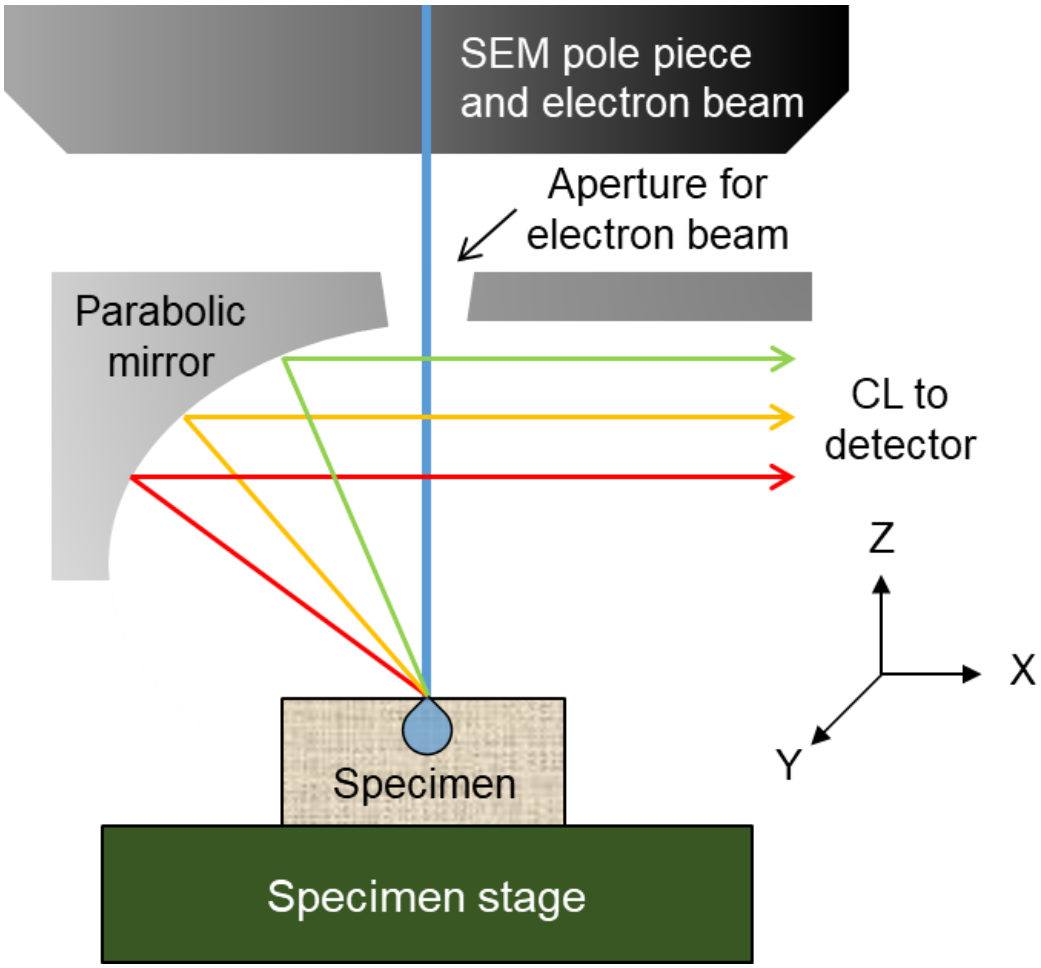

Figure 3-9. CL emission in MonoCL4 system through parabolic mirror.

Chapter 4

Development of *in-situ* CL technique in ceria under electron irradiation

4.1 Introduction

Ceria is a surrogate of fuels and transmutation targets for a nuclear reactor. Therefore, understanding the production and growth of radiation-induced defects during irradiation is of importance for the safe use of nuclear reactors. In this chapter, the point defects production and its charge states were investigated to understand the kinetics of displacement in-beam state. For this purpose, the *in-situ* CL spectroscopy technique was operated during high-energy electron irradiation using the HVEM. Complementary CL spectra were also obtained for low-energy electron irradiation by using the SEM. The electrical configurations of ceria under high-energy electron irradiation and CL emission from the point defects were evaluated depending on electron energy temperature.

4.2 Materials and Experimental Procedure

In-situ CL spectra were measured from pure single crystal and polycrystalline ceria samples under high- and low-energy electron irradiation. A single crystal ceria supplied by Dr. W. J. Weber of Oak Ridge National Laboratory and the polycrystalline sintered ceria samples were used in this study. The detail of sample information is described in Chapter 3.

For high-energy electron irradiation, the HVEM-CL facility (Figure 3-7) operated electron energies from 400 keV to 1250 keV at temperatures of 100, 200, and 300 K.

Meanwhile, the CL spectra under low-energy electron irradiation were obtained from the SEM-CL facility (Figure 3-6) at 300 K. The energy was 20 keV which is out of $E_{d,O}$ bound. All the obtained spectra were fitted with a Gaussian function and the intensity of bands were integrated to interpret energy and temperature dependence of CL emission. The details of equipment and experimental conditions are described in Chapter 3.

4.3 Results

4.3.1 Displacement cross-section calculation

The displacement cross-section (σ_d) in ceria induced by energetic electrons through elastic collisions was calculated by using SMOTT/POLY computer code [74] based on Eq. (2-12). The threshold displacement energies (E_d) were assumed based on the reported values of E_d for Ce ($E_{d,Ce}$: 44 ~ 58 eV) and O ($E_{d,O}$: < 33 eV) sublattices [9].

The calculated total σ_d is shown in Figure 4-1. The threshold electron energy to induce elastic displacement was evaluated where the cross-section exceed 1 barn: those were 150 ~ 200 keV for oxygen sublattice ($E_{0,O}$) and 1300 ~ 1600 keV for Ce sublattice ($E_{0,Ce}$), respectively. These results indicate that the electron irradiation by using a HVEM in the energies range of 400 ~ 1250 keV generates displacement damage only for oxygen sublattice. Therefore, the CL spectra obtained by using HVEM would include an additional band induced by F centers. On the other hand, atomic displacement will not be induced with 20 keV electrons. Therefore, one can hypothesize that the CL spectra obtained using SEM are induced by ionization or natural defects by energy transfer to electrons at Ce 4*f* level.

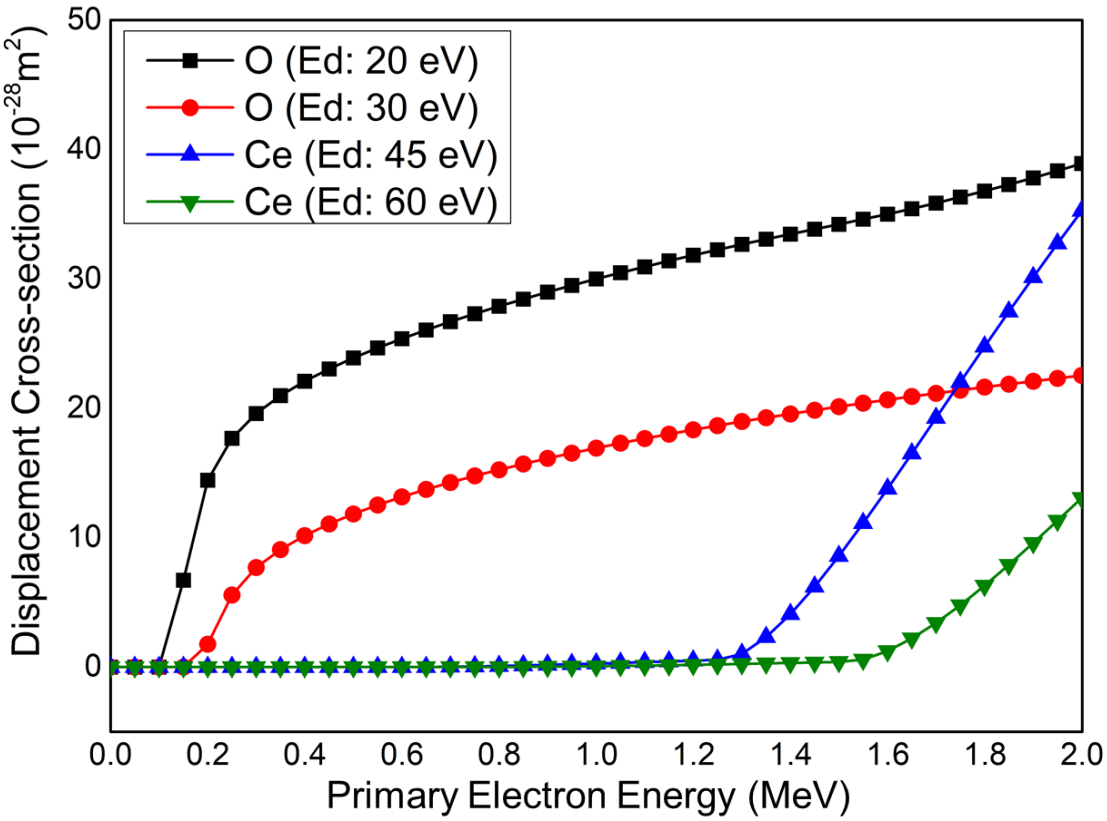

Figure 4-1. Oxygen and cerium atoms displacement cross section in ceria by electron-nucleus collisions calculated by SMOTT/POLY computer code [74].

4.3.2 CL spectra in single crystal ceria

CL spectra under high- and low-energy electron irradiation in single crystal ceria were obtained. For high-energy electron irradiation, one spectrum was taken under electron irradiation for 30 seconds at 300 K ~ 100 K, and the spectra were averaged out for 5 recordings for 400 keV ~ 1250 keV electrons. The spectra were fit with Gaussian profiles. Figure 4-2 shows an example of *in-situ* CL spectrum for 600 keV electron irradiation together with fitted curves by Gaussian function. 4 Gaussian bands were appeared at photon energies of 1.6 eV, 2.4 eV, 2.9 eV, and 4.2 eV with full-width at half-maximum (FWHM) of 0.4 eV, 0.8 eV, 0.5 eV, and 1.1 eV, respectively. A sharp and intense unresolved line was seen at 1.79 eV (probably R-lines of Cr^{3+} impurities). Cr^{3+} exhibits narrow-band emission at around 700 nm because of spin-forbidden $^2E \rightarrow {}^4A_2$ transition or broadband emission ranging from 650 nm to 1600 nm because of the spin-allowed $^4T_2 \rightarrow {}^4A_2$ transition [75] and a small doublet at 1.73 ~ 1.75 eV, and another broader impurity line at 1.85 eV were observed.

CL spectra were also measured for electrons with 20 keV at a constant beam current of 1.7 nA at room temperature, and they are shown in Figure 4-3. The CL band characteristics for 20 keV electrons are described in Table 4-1. Only one broad CL band at 2.4 eV was observed and this band was divided into two bands at 2.37 eV and 2.84 eV by Gaussian fitting.

For high-energy electron irradiation, CL spectra were measured at different electron energies of 400, 600, 800, 1000, and 1250 keV at constant beam-flux of 3.8×10^{21} $m^{-2}s^{-1}$. The CL spectra were obtained by averaging out the recordings after 0 ~ 150 seconds at 300, 200, and 100 K as shown in Figure 4-4. Further, the average CL band characteristics in single crystal ceria were summarized in Table 4-1 for electron irradiation with 400 keV ~ 1250 keV. The CL intensity for F^+ center band is dependent on electron energy, and it showed a maximum at 600 keV electrons.

4.3.3 CL spectra in polycrystalline ceria

CL spectra under high- and low-energy electron irradiation in polycrystalline ceria were obtained. For high-energy electron irradiation, one spectrum was taken under electron irradiation for 30 seconds at 300 ~ 100 K and the spectra were averaged out for 5 recordings for 400 keV ~ 1250 keV electrons. The spectra were fit with Gaussian profiles. Similar to the spectrum with 600 keV electrons [Figure (4-2)], spectra with 400 keV ~ 1250 keV electrons were fitted with 4 Gaussian bands, which were recorded at photon energies of 1.6 eV, 2.1 eV, 2.7 eV, and 4.2 eV with full-width at half-maximum (FWHM) of 0.4 eV, 0.8 eV, 0.6 eV, and 1.2 eV, respectively. A sharp and intense unresolved line was seen at 1.79 eV (probably R-lines of Cr^{3+} impurities [75]) and a small doublet at 1.73 ~ 1.75 eV and another broader impurity line was observed at 1.85 eV.

CL spectra were also measured for electrons with 20 keV at a constant beam current of 1.7 nA at room temperature, and they are shown in Figure 4-3. The CL bands characteristics for 20 keV electrons are described in Table 4-2. Only one broad CL band at 2.5 eV was observed and this band was divided into two bands at 2.35 eV and 2.80 eV by Gaussian fitting.

For high-energy electron irradiation, CL spectra were measured at different electron energies of 400, 600, 800, 1000, and 1250 keV at constant electron beam-flux of 3.8×10^{21} $m^{-2}s^{-1}$. The CL spectra were obtained by averaging out the recordings after 0 ~ 150 seconds as shown in Figure 4-5. Further, the average CL band characteristics in polycrystalline ceria were summarized in Table 4-2 for electron irradiation with 400 keV ~ 1250 keV. The CL intensity for F^+ center band is dependent on electron energy, and it showed a faint maximum for 600 keV electrons.

Table 4-1. CL band characteristics and defect assignments for the ceria single crystal samples.

	Band center (eV)	FWHM (eV)	Defect
HVEM (300 K)	4.2	1.1	F^+ center
	2.9	0.5	Ce^{3+}_{I}
	2.4	0.8	Ce^{3+}_{II}
	1.7	0.4	Impurity
HVEM (200 K)	4.2	1.2	F^+ center
	2.9	0.5	Ce^{3+}_{I}
	2.5	0.9	Ce^{3+}_{II}
	1.6	0.4	Impurity
HVEM (100 K)	4.2	1.1	F^+ center
	3.0	0.4	Ce^{3+}_{I}
	2.6	0.9	Ce^{3+}_{II}
	1.6	0.5	Impurity
SEM (300 K)	2.7	0.7	Ce^{3+}_{I}
	2.3	0.6	Ce^{3+}_{II}

Table 4-2. CL band characteristics and defect assignments for the ceria polycrystalline samples.

	Band center (eV)	FWHM (eV)	Defect
HVEM (300 K)	4.2	1.2	F^+ center
	2.7	0.6	Ce^{3+}_{I}
	2.1	0.8	Ce^{3+}_{II}
	1.5	0.4	Impurity
HVEM (200 K)	4.3	1.3	F^+ center
	2.9	0.5	Ce^{3+}_{I}
	2.2	0.9	Ce^{3+}_{II}
	1.7	0.6	Impurity
HVEM (100 K)	4.3	1.4	F^+ center
	2.8	0.7	Ce^{3+}_{I}
	2.1	0.7	Ce^{3+}_{II}
	1.6	0.6	Impurity
SEM (300 K)	2.8	0.7	Ce^{3+}_{I}
	2.4	0.6	Ce^{3+}_{II}

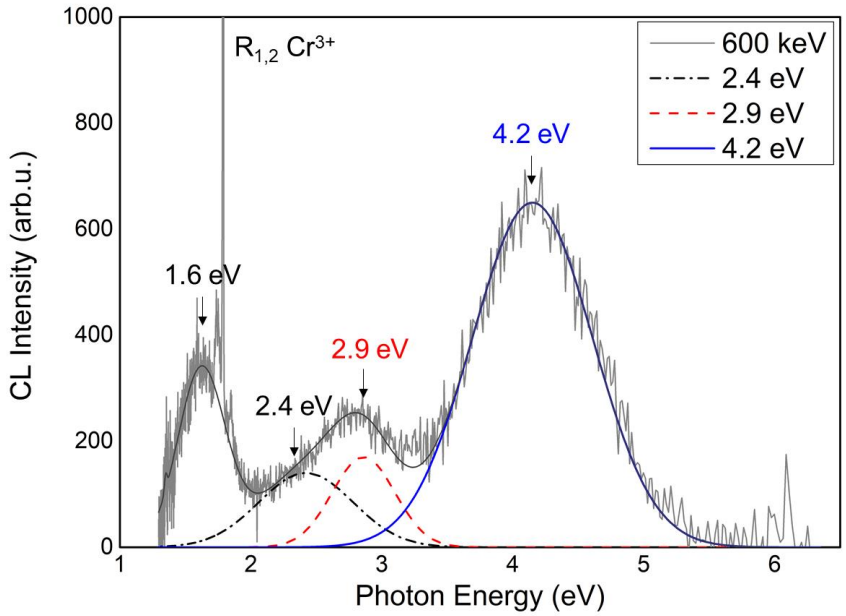

Figure 4-2. Assignment of CL bands at 300 K of the ceria single crystal for 600 keV electron excitation. Dotted, dashed, and dotted-dashed lines are fitted spectra and solid line is the Gaussian curve used for fits of spectrum.

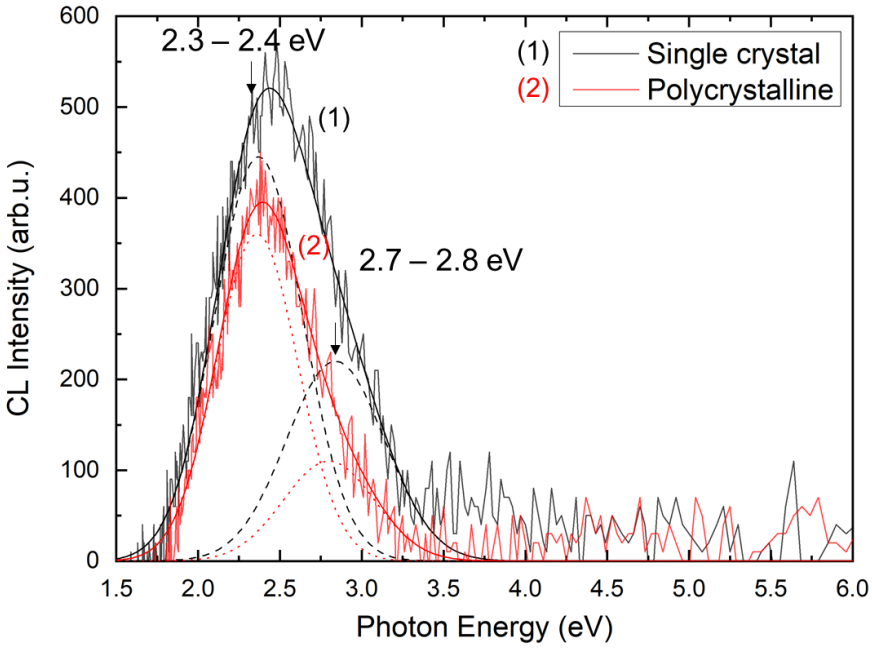

Figure 4-3. CL spectra at 300 K of the ceria single crystal and polycrystalline sample for 20 keV electron excitation. Dashed and dotted lines are the fitted spectra and solid lines are the Gaussian curves used for least-square fits.

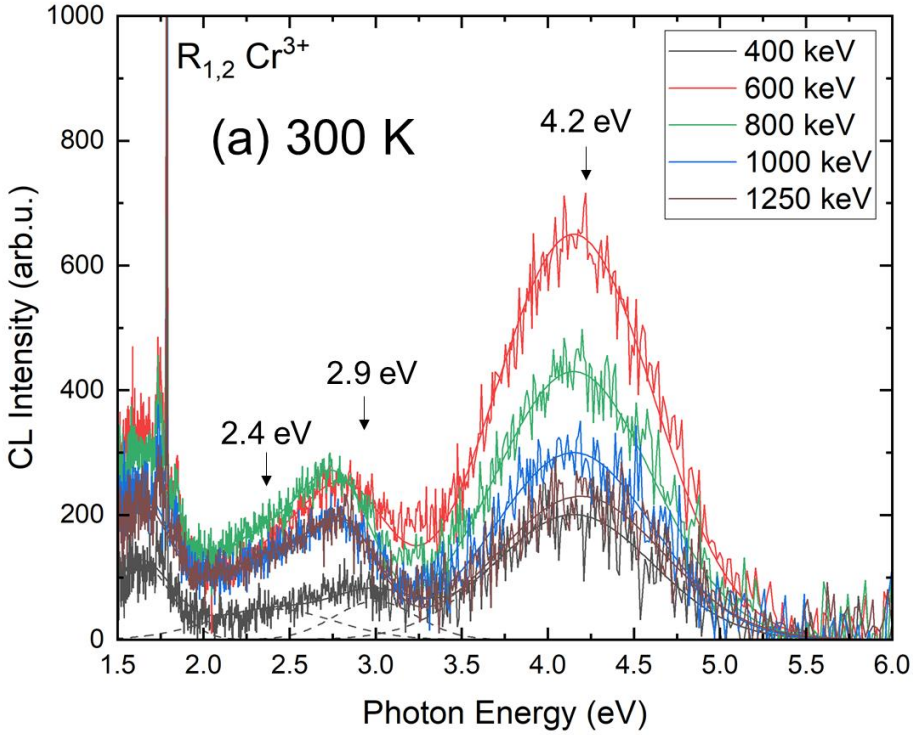
$R_{1,2}$ Cr^{3+}
(a) 300 K
400 keV
600 keV
800 keV
1000 keV
1250 keV
4.2 eV
2.9 eV
2.4 eV
CL Intensity (arb.u.)
Photon Energy (eV)

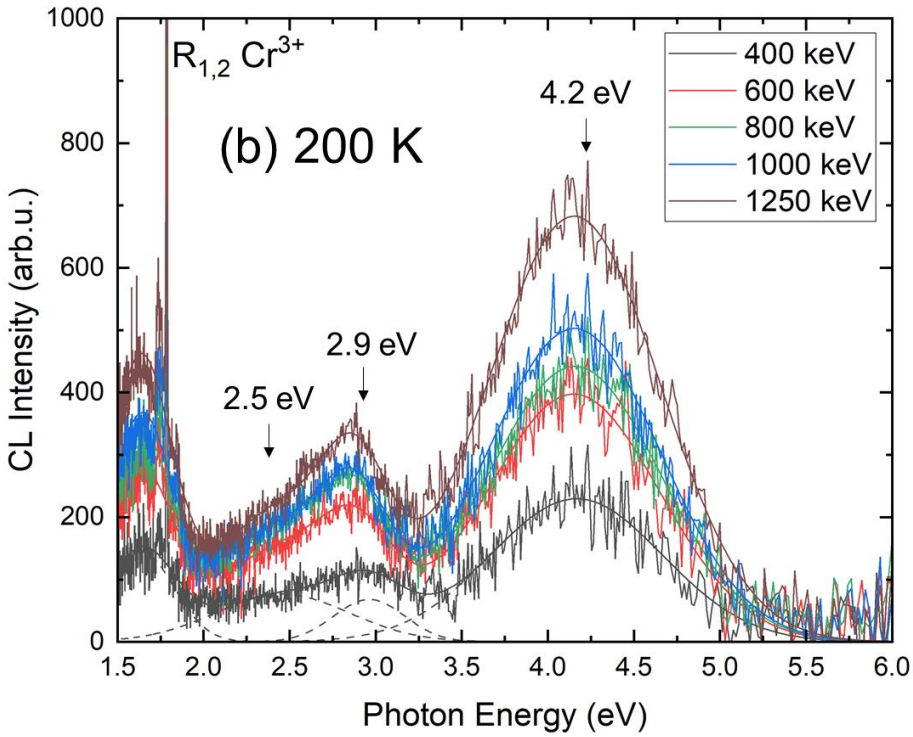
$R_{1,2}$ Cr^{3+}
(b) 200 K
400 keV
600 keV
800 keV
1000 keV
1250 keV
4.2 eV
2.9 eV
2.5 eV
CL Intensity (arb.u.)
Photon Energy (eV)

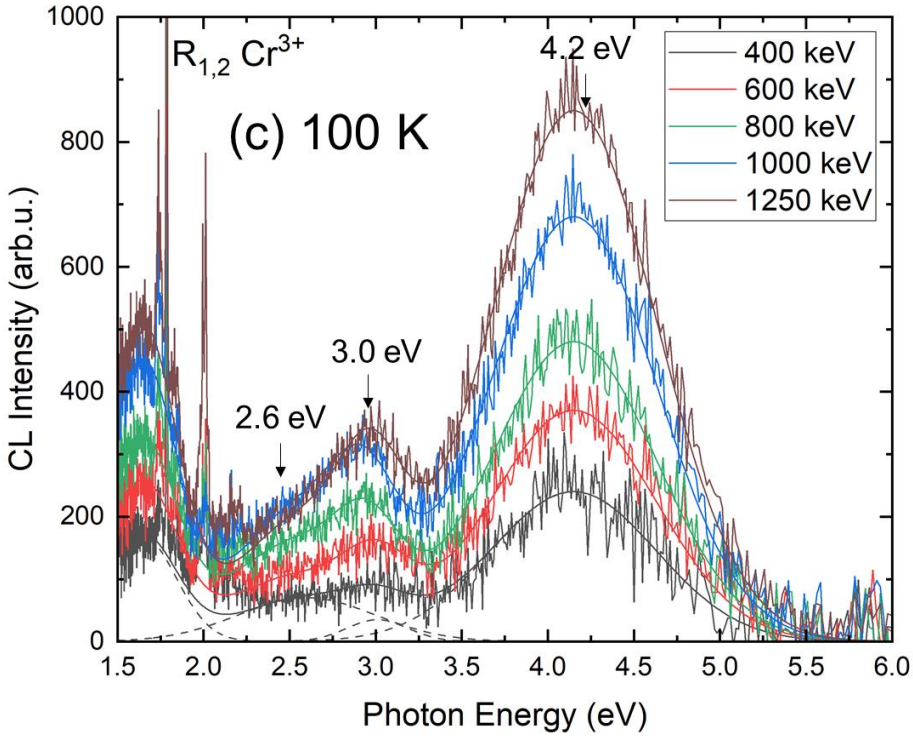

Figure 4-4. CL spectra at (a) 300 K, (b) 200 K, and (c) 100 K of the ceria single crystal sample for electrons of variable energy at fluences of 5.74 x 10^{23} m^{-2}. Dashed lines are the fitted spectra and solid lines are the Gaussian curves used for least-square fits.

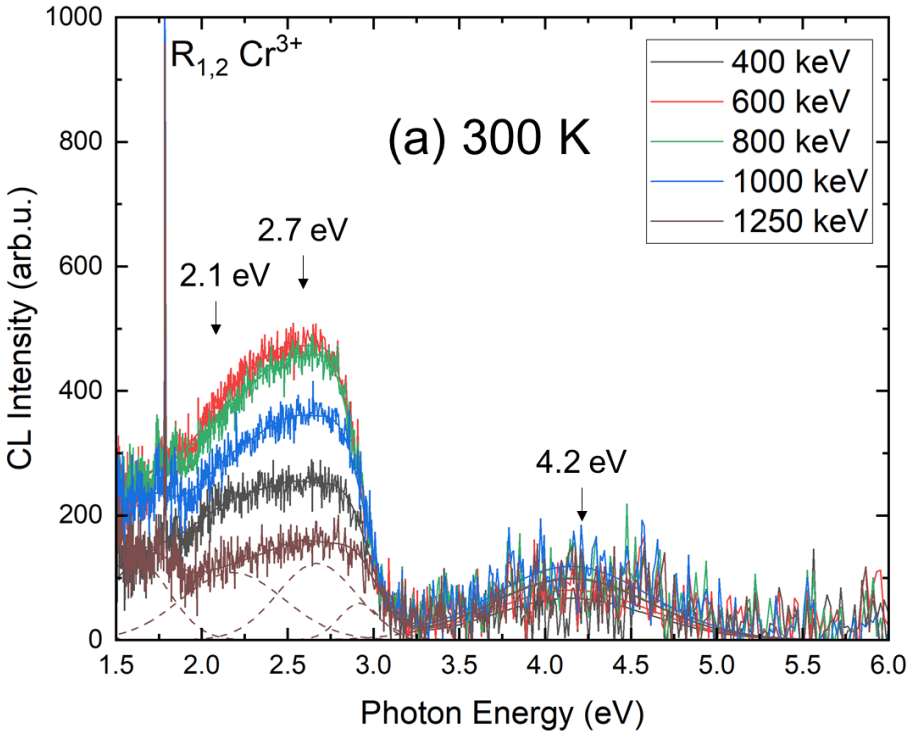
R1,2 Cr3+
(a) 300 K
400 keV
600 keV
800 keV
1000 keV
1250 keV
2.7 eV
2.1 eV
4.2 eV
CL Intensity (arb.u.)
Photon Energy (eV)

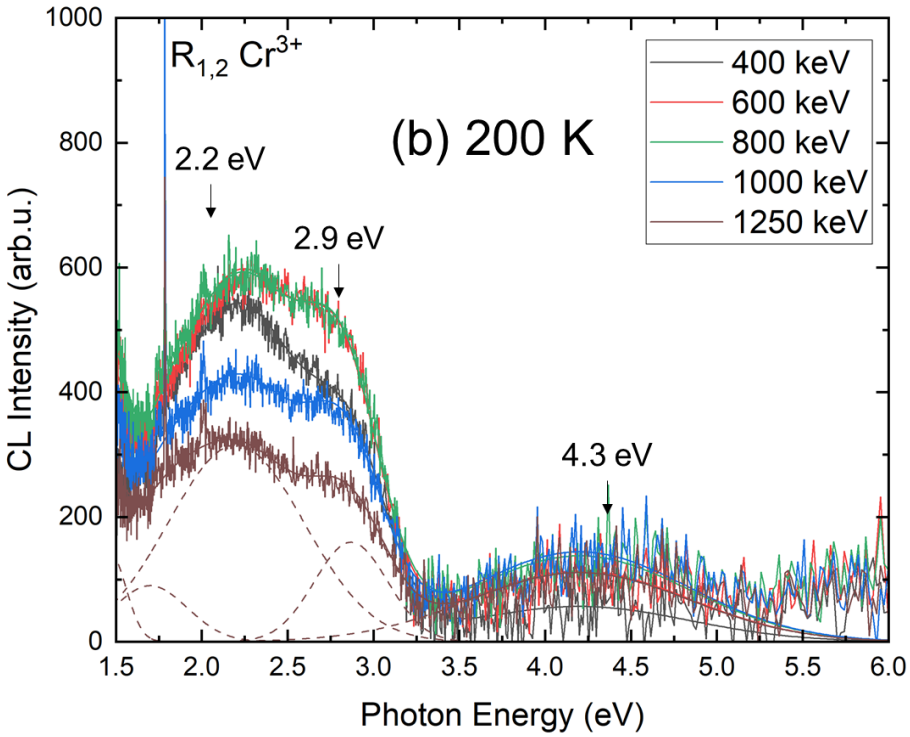
R1,2 Cr3+
(b) 200 K
400 keV
600 keV
800 keV
1000 keV
1250 keV
2.2 eV
2.9 eV
4.3 eV
CL Intensity (arb.u.)
Photon Energy (eV)

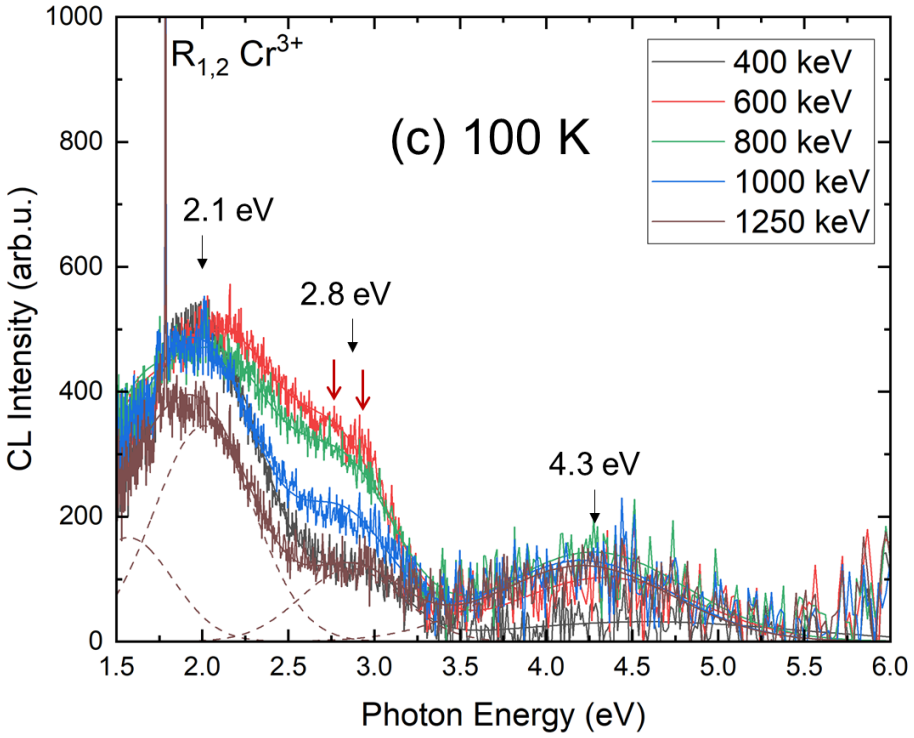

Figure 4-5. CL spectra at (a) 300 K, (b) 200 K, and (c) 100 K of the ceria polycrystalline sample for electrons of variable energy at fluences of 5.74 x 10^{23} m^{-2}. Dashed lines are the fitted spectra and solid lines are the Gaussian curves used for least-square fits.

4.4 Discussion

CL in oxides is emitted by thermalized secondary electrons (SEs) and holes generated by elastic and inelastic collisions with energetic electrons [70]. The CL signal is usually proportional to the volume density of the carriers, and it is produced during the trapping of these thermalized SEs by defect and impurity levels in the band gap [68,76]. It indicates that CL emission in thin samples is not proportional to the energy of primary electrons since they are mostly transmitted through the targets as indicated by simulations by the ESTAR code [77] (Table 4-3).

The extrinsic CL is assumed that it results from electronic excitation and radiative decay from the defect and impurity levels by thermalized SEs [70]. At 300 K, most shallow levels created by impurities and defects are fully ionized while deep levels created by charged point defects are partially filled. The CL cross-section consists of four independent steps as described in Eq. (2-14) i.e. ($\sigma_{CL} = \sigma_i \sigma_t \sigma_e \sigma_r$) [70]. Trapping of thermalized carriers may also occur directly on excited states rather than on the ground state of the defect levels. In that case, the CL process is reduced to three steps only. Thermal quenching by phonon-assisted non-radiative channels reduces the CL yield at a high temperature [78,79]. For the temperature effect in CL intensity, σ_t increases with temperature, whereas σ_r decreases with temperature [70]. However, the quenching effect by other non-radiative decay to the defect and impurity levels is still puzzling and difficult to explain in detail [79]. The radiative decay of exciton across the band gap is quenched at a high temperature (< 55 K) which can be assumed as intrinsic CL emission [78]. The CL spectra at 5.5 ~ 6 eV were not observed in ceria which was deduced by EELS [80,81].

Table 4-3. Characteristics of electron irradiations of CeO_2 (mass density = 7.215 g cm^{-3}), computed with the ESTAR code [77] for different primary electron energies (E) and mean ionization energy I = 407.6 eV: CSDA range, and total inelastic stopping power ($(-dE/dx)_{inel}$)

E (keV)	20	400	600	800	1000	1250
Range (µm)	2.3	289	500	720	943	1221
(-dE/dx)inel. (MeV μm^{-1})	52×10^{-4}	9.9×10^{-4}	9.2×10^{-4}	9.0×10^{-4}	9.0×10^{-4}	9.1×10^{-4}

4.4.1 Analysis of CL spectra

The CL spectra observed in this study showed three broad bands. These bands were centered at photon energies of around 1.6 eV, 2.1 ~ 2.5 eV, 2.8 ~ 3.0 eV, and 4.2 eV. Interpretation of the CL bands was referred to the literature of PL data in ceria, although they suggested various energy levels for each defect. For example, Aškrabič et al. assigned the PL band centered at 1.7 eV results from the charge transfer transitions from F^+ centers ($V_O^{\cdot}$) to the oxygen 2*p* states, and the band at 2 ~ 2.5 eV is F^0/F^+ centers [69]. Alternatively, the same bands at 2 ~ 2.5 eV were associated to $5d^1 \rightarrow 4f^1$ transitions of Ce^{3+} ions in non-stoichiometric nano-crystalline ceria (nc-CeO_2) by Maksimchuk et al. [82]. Generally, PL bands at ~2 eV are considered to attribute to Ce^{3+} luminescence, for example in the case of YAG: Ce^{3+} [83] and ZrO_2: Ce^{3+} [84]. Finally, the bands at 3.1 ~ 3.15 eV were ascribed by Morshed et al. to $4f \rightarrow 2p$ charge transfer transitions for CeO_2 films on a silicon substrate [85] and nc-CeO_2 [82]. Also, the band at 2.9-3.0 eV was also assigned by Aškrabič et al. to charge transfer transitions from the F^{2+} center ($V_O^{\cdot\cdot}$) level to Ce^{3+} ($4f^1$) for nc-CeO_2 [69]. The emission band at 3.18 eV in Lu_2SiO_5:Ce^{3+} (LSO: Ce^{3+}) was attributed to Ce^{3+} in Lu site by Suzuki et al. [86]. However, Jia et al. suggested two PL bands for each Ce^{3+} level for LSO: Ce^{3+} by *ab initio* calculations; Ce^{3+} in a crystallographic site occurs at higher photon energy (~ 3.2 eV) than that of a Ce^{3+} adjacent to an oxygen vacancy (~ 2.6 eV) [87].

It seems confusing with the variety of interpretations, but it was overlooked that two Ce^{4+} ions are connected with two O^{2-} ions as shown in Figure 4-6. Let us consider a cluster of neutral oxygen vacancy ($V_O^{\times}$) at one oxygen site connecting the two Ce^{4+} ions (Ce^{4+}-$V_O^{\times}$-Ce^{4+}) where the other connecting O^{2-} ion is not shown in the cluster for clarity. According to first principle calculations, the two electrons of $V_O^{\times}$ are primarily localized on the two Ce^{4+} ions that are next to each other, generating a Ce^{3+}-$V_O^{\cdot\cdot}$-Ce^{3+} cluster with more than 0.9 electrons localized on each

Ce and just around 0.1 electron remaining on the vacancy site [88]. The high electron density at cerium sites promotes the interpretation of CL data in terms of Ce^{3+} optical transitions rather than V_O-type (or F-type in spectroscopic notation) transitions, notwithstanding the partial electron delocalization. As a result, it can be taken into consideration that the various electronic configurations of the neutral oxygen vacancy $V_O^{\times}$, described in terms of a Ce^{4+}-$V_O^{\times}$-Ce^{4+} cluster rather of adopting the description of oxygen vacancies in terms of F, F^+ and F^{2+} centers.

Thereby, three different electronic configurations for this cluster can be assumed considering the electro-neutrality, leading to two or three types of Ce^{3+} ions (Figure 4-6): (i) Neutral configuration (Ce^{3+}-$V_O^{\cdot\cdot}$-Ce^{3+}) with two neighboring Ce^{3+} ions, (ii) One positive configuration (Ce^{3+}-$V_O^{\cdot\cdot}$-Ce^{4+}) with the other electron trapped in the form of a Ce^{3+} at undistorted substitution location further from the vacancy, and (iii) Two positive configuration (Ce^{4+}-$V_O^{\cdot\cdot}$-Ce^{4+}) with the two electrons trapped at two undistorted Ce^{3+} sites farther away from the vacancy. Configurations (i), (ii) and (iii) correspond to the F center ($V_O^{\times}$), F^+ center ($V_O^{\cdot}$) and F^{2+} center ($V_O^{\cdot\cdot}$), respectively. In configurations (i) and (ii), CL detects only the Ce^{3+} ions where the compensating electrons are trapped. Only the Ce^{3+} ions in configurations (i) and (ii) where the compensating electrons are confined are detected by CL. As will be explained later, in the case of configuration (iii), CL comprises both the emission of Ce^{3+} and of a traditional F^+ center.

In the present results, two broad CL bands were fitted regardless of primary electron energies centered at 2.1-2.5 eV and 2.7-3.0 eV with FWHM of ~0.5 eV at 300 K (Figures 4-3 ~ 4-5). For the polycrystalline sample, they have more intense emission for Ce^{3+} ions in than in the single crystal. Those two CL bands arise from spin and parity-allowed $5d^1 \rightarrow 4f^1$ electric-dipole transitions with large oscillator strengths. The $4f^1$ (^2F) level of Ce^{3+} is split into $^2F_{5/2}$ and $^2F_{7/2}$ sub-levels by the spin-orbit coupling interaction, with an energy difference of ~0.25 eV (~2,000 cm^{-1}) [89–93]. The spin-orbit coupling is shown in Figure 4-5 (c) with the red arrows.

It might be tempting to attribute the two prominent CL bands to the two $5d^1 \rightarrow 4f^1$ ($^2F_{7/2}$, $^2F_{5/2}$) transitions. However, there are several arguments against this interpretation. In the case of the polycrystalline sample: a) the splitting of 0.5 eV at 300 K to 0.9 eV at 100 K between these bands is larger than the theoretical value 0.25 eV for the spin-orbit splitting of Ce^{3+}; b) the observed splitting increases from 0.5 to 0.9 eV, whereas the spin-orbit coupling should be independent of temperature; c) the low energy CL band shifts to lower temperature (2.3 to 2.0 eV) upon decreasing the temperature from 300 K to 100 K; d) the intensities of the two transitions differ by a factor ~5 (~1.5 for the single crystal).

Ce_I (2.8 – 3.0 eV) and Ce_{II} (2.1 – 2.5 eV) are assigned to the two types of CL bands from Ce^{3+} emitting centers compared to the empirical and theoretical analysis in LSO: Ce^{3+} [87]. The CL band Ce_I can be attributed to a Ce^{3+} at an unperturbed crystallographic site of CeO_2, and the CL band Ce_{II} to a Ce^{3+} adjacent to an oxygen vacancy. These CL bands have two characteristics that support this interpretation: a) the low energy CL band (~2 eV) exhibits a temperature quenching effect as it is weaker at 300 K than at 100 K (Figure 4-5 (c), marked with arrows in red color), suggesting that the band ~3 eV may be composed of two components separated by about 0.25 eV, corresponding to the spin-orbit splitting of Ce^{3+}. These two characteristics were also seen in LSO:Ce^{3+} [87] for Ce^{3+} at an undistorted crystallographic position and for a Ce^{3+} next to an oxygen vacancy, respectively. Assuming a 5.5 ~ 6 eV energy gap between the conduction band (Ce-5*d*) and the valence band (O-2*p*), the schematic energy levels of Ce_I and Ce_{II} centers are shown in Figure 4-8 [80,81,93,94]. In Figure 4-6, configurations (ii) and (iii) of the oxygen vacancy correspond to the Ce_I center (2.8 ~ 3.0 eV), attributed to a Ce^{3+} at an undistorted crystallographic site, while configurations (i) and (ii) of the oxygen vacancy correspond to the Ce_{II} center (2.1 ~ 2.5 eV), attributed to a Ce^{3+} adjacent to an oxygen vacancy.

The broad CL emission band around ~4 eV was observed for 400 keV ~ 1250 keV electron irradiation (Figures 4-4 and 4-5) unlike 20 keV (Figure 4-3). The broad 4.2 eV band is more intense in the single crystal (Figures 4-4) than in the polycrystalline sample (Figures 4-5). It is also represented in Figure 4-2 for the CL spectrum of the single crystal irradiated at the electron energy of 600 keV. Previously, the F^+ center for sapphire (α-Al_2O_3) and YSZ were assigned to similar CL bands with centers at 3.8 eV and 4.1 eV, respectively [25,70]. The schematic model of oxygen vacancy (Figure 4-6) suggests that the 4.2 eV band could be related to configuration (iii), in which the vacancy is represented by an F^{2+} center ($V_O^{\cdot\cdot}$) and two nearby Ce^{4+} ions. As a result, this center loses the Ce^{3+} feature. The 4.2 eV band may be the result of an electron being captured by the vacancy (the Ce^{4+}-$V_O^{\cdot\cdot}$-Ce^{4+} cluster) and emitting from the F^+ center. The caught electron is concentrated just before emission on the oxygen vacancy site, which corresponds to an excited F^+ core, at the center of this symmetric cluster. The Frank-Condon principle states that during the emission, the electron is still localized at the V_O site. This final state corresponds to an unrelaxed (transient) state of the F^+ ground state. Immediately after the emission, the electron is then shifted to one of the two Ce^{4+}, giving a Ce^{3+}-$V_O^{\cdot\cdot}$-Ce^{4+} cluster. This center corresponds to the relaxed state of the F^+ center. The F^+ center CL emission is described in a schematic configuration as shown in Figure 4-7. Almost all of CL bands have a FWHM of about 0.5 eV, except for the 4.2-eV band having a width of ~1 eV as the other F^+ centers in sapphire and YSZ [25,36,70,95]. The assignment of the CL bands is summarized in Figure 4-8 and Tables 4-1 ~ 4-2.

For the previous EPR results, information only for the Ce^{3+} were observed after electron irradiation without detection of F^+ center [96]. However, CL showed F^+ center emission at 4.2 eV during irradiation which indicates relaxed state of F^+ center has a short lifetime and the electron is immediately transferred to ground state of Ce_{II} forming the Ce^{3+}-$V_O^{\cdot\cdot}$-Ce^{4+} cluster.

Moreover, it suggests that relaxed state of F^+ center located a higher energy level from the valence band (~1.8 eV) than that of Ce_{II}, which is corresponding to the first principle calculations results suggested by Han et al., that Ce 4*f* sate is located at ~1.4 eV from the valence band [88]. A schematic diagram of energy level in ceria is proposed in Figure 4-8.

In addition, the CL band at 4.2 eV was not observed in both single and poly crystal samples for 20 keV electron irradiation (Figure 4-3). The oxygen atom displacement cross-section [97] was calculated by using SMOTT/POLY code [74,98] devised for polyatomic targets (Figure 4-1). These calculations take into account the primary electron-nucleus collisions and small atomic displacement cascade contribution, and the admitted value of threshold displacement energy of $E_{d,O}$ = 35 eV based on the upper boundary value (33 eV) deduced from experiments at the HVEM [74]. Note that molecular dynamics simulations gave smaller values of 27 eV [9], and 20 to 35 eV [99]. A larger value of $E_{d,Ce}$ = 58 eV is admitted for cerium [74]. Our data show that oxygen displacement by elastic electron-nucleus collisions can only occur for electron energies higher than ~200 keV [97]. This explains the lack of 4.2 eV CL band in CeO_2 irradiated by 20 keV electrons (Figure 4-3). However, it must be noticed that the Ce_I (~2.7 eV) and Ce_{II} (~2.3 eV) CL bands are present even after 20 keV electron irradiation and may originate from two possible processes: (a) excitation of Ce^{3+} at lattice position (Ce_I) and Ce^{3+} adjacent to preexisting oxygen vacancies (Ce_{II}), and (b) the production of oxygen vacancies in configurations (i) and (ii) by electronic excitations. Hypothesis (b) is not totally unlikely as the inelastic stopping power $(-dE/dx)_{inel}$ is 4 to 6 times larger for 20 keV electrons than for 400 keV to 1250 keV, where it is nearly constant (Table 4-3).

The 4.2 eV band is substantially smaller in the sintered sample than in the single crystal (Figures 4-4 ~ 4-5) when their CL spectra are compared, regardless of temperature, whereas the Ce^{3+} ion signal is stronger even though the sintered sample is thinner. Due to the short

lifetime of the excited state and low temperatures, this effect cannot result from defect diffusion to the grain boundaries of the sintered sample, as could be expected. The contaminants [79,100] separated at grain boundaries may be more closely related to athermal non-radiative channels. Because of thermal quenching at temperatures of 100 K and above, the emission lines of these contaminants could not be seen. Such a reduction could potentially be caused by the prompt recombination/annihilation of oxygen Frenkel pairs at grain boundaries.

Finally, a 3d-transition element impurity, such as Ti^{3+} in sapphire [68,76], is likely the cause for the rather broad CL band at 1.7 eV (FWHM = 0.4 eV) observed for high energy electron irradiation (Figures 4-4 ~ 4-5). This band has previously been observed for oxide systems with different band gap energies [25,70]. The extremely narrow peaks in this 1.7 eV band are caused by Cr^{3+} impurities in oxide hosts and their ^2E - $^4A_2$ emission bands ($R_{1,2}$ lines) [63].

4.4.2 Effect of electron energy

Diffusion and recombination processes at the surface of excess free minority carriers were taken into account to model the electron-energy dependence of the CL signal in the case of semiconductors, where the effect of electron energy was previously addressed for low-energy electron excitations ($E \leq 40$ keV) of n-doped GaAs in a SEM [101,102]. The depth dependence of the light emission yield brought on by self-absorption results in a maximum. In the presence of a dominant surface recombination, the maximum changes to a higher voltage [102]. The primary electrons are shot through the targets in the current work on CeO_2, however, and the secondary electron distribution can be thought of as homogeneous across the sample thickness regardless of the source electron energy [70]. Unlike to low-energy electron irradiation of semiconductors [101], the maximum in CL intensity (Figure 4-9) cannot result

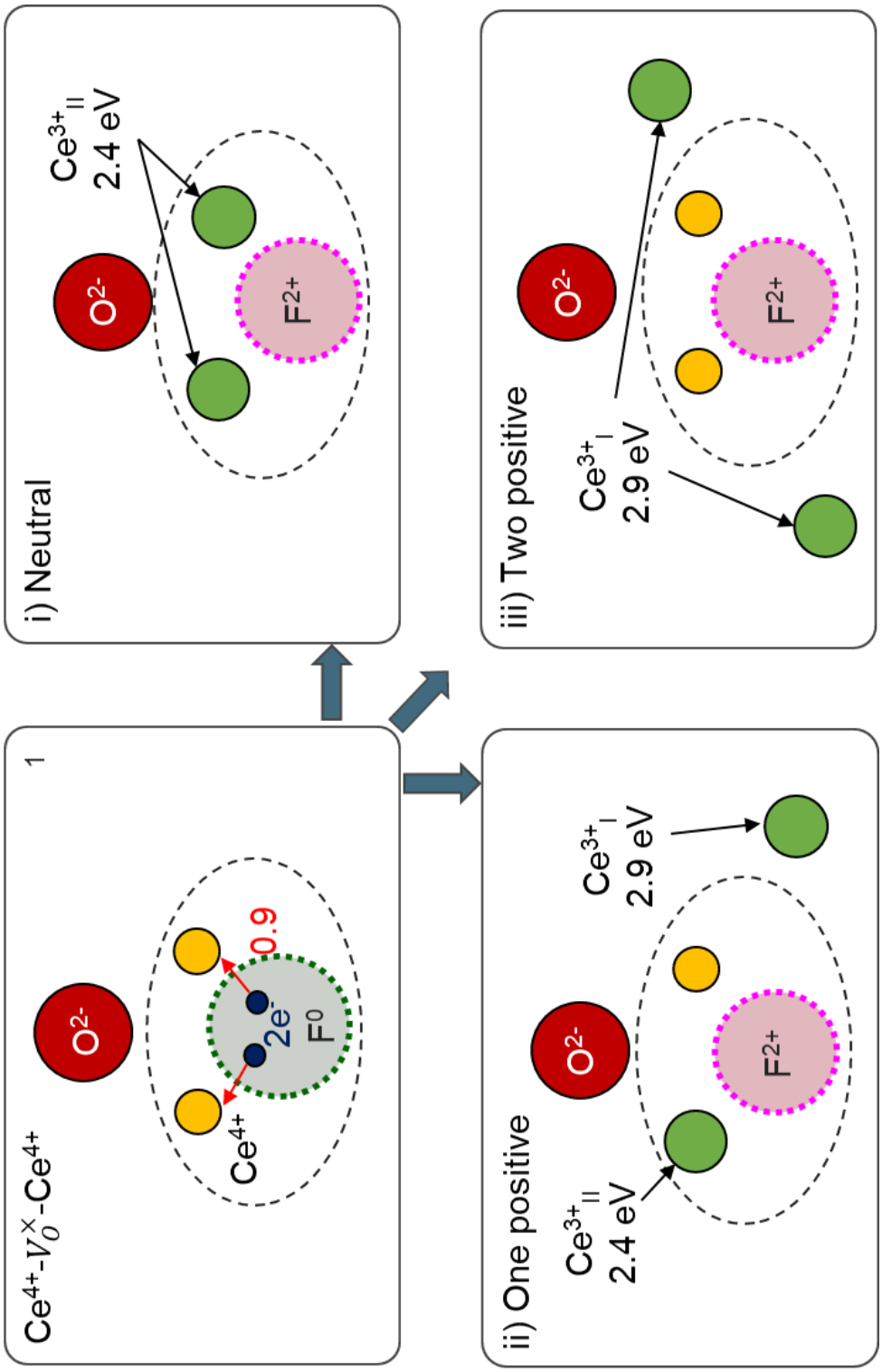

Figure 4-6. Schematic representation of different electronic configuration of a neutral oxygen vacancy in ceria.

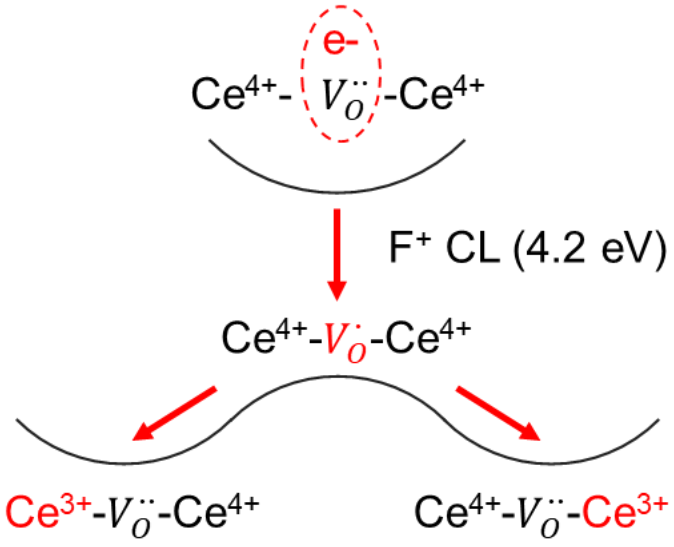

Figure 4-7. Schematic configuration coordinate representation of the F^+ center emission. The site of the unpaired electron is represented in red.

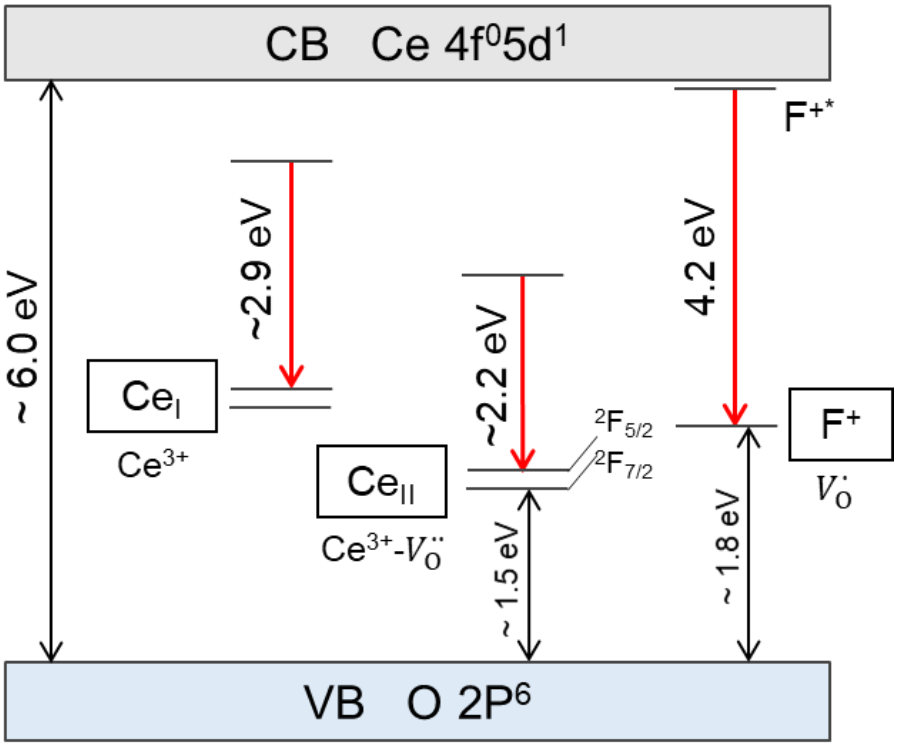

Figure 4-8. Sketch of electronic levels in the band gap of ceria possessing oxygen vacancies.

from inhomogeneity of the depth profile of secondary electrons and drift of excess carriers to the insulator surface.

For the various primary electron energies, little variation in cross-sections was seen at low cut-off energies ($E_s = E_{cut}$) values [70]. This translates into minor variations in $(dE/dx)_{inel}$ (Table 4-3), which are mostly driven by the input of low-energy secondary electrons [103]. Noting that $(dE/dx)_{inel}$ has its minimal value in this energy range (400 keV ~ 1250 keV), the highest CL intensity as a function of primary electron energy (Figure 4-9) cannot be explained by the minor fluctuations in $(dE/dx)_{inel}$ by just 10 % (Table 4-3). As a result, between 400 keV and 1250 keV, the sample produces almost the same amount of electron-hole pairs [104].

E_{cut}, which is the energy corresponding to an electron range equal to the sample thickness as calculated by the ESTAR computer code [77], was utilized as previously to choose the range of efficient secondary electrons yielding the maximum light emission yield. This number is obviously higher for the single crystal that is 0.5 mm thick (E_{cut} = 600 keV) than it is for the sintered sample that is 150 µm thick (E_{cut} = 250 keV). According to calculations of the survival probability of secondary electrons inside a 150 µm thick YSZ target vs E_s for E = 400 keV and E = 1250 keV, secondary electrons' spatial distributions were used to support this rough approximation [70].

However, we anticipate that the excitation cross-section (σ_e) will decline more quickly than the main electron energy. Upon electron irradiation up to 1 GeV above a maximum at low energy (< 100 eV), this type of decline was in fact seen for the apparent cross section for fluorescence of molecular levels of nitrogen N_2 [105]. Such phenomenon is also possible when a secondary electron is trapped on an excited state rather than the defect level's ground state.

Moreover, the displacement cross-section (σ_d) should increase with the CL integrated intensity (I_{CL}) for point defects caused by elastic collisions. We therefore suppose that I_{CL} can written as follows

$$I_{CL} = \mathrm{K}\sigma_{CL}\sigma_d, \quad (4\text{-}1)$$

where K is a constant that includes all elements of the experimental setup and conditions. According to the presumption, the cross-section for electron/hole trapping can be roughly calculated as $(E - E_0)^{\beta}$, for $E \geq E_0$, where E_0 is the electron energy threshold for atomic displacement. However, it is possible to believe that σ_t just depends on temperature and not directly on E as a characteristic of the defective electronic levels [70]. On the other hand, the radiative decay cross-section (σ_r) decreases with E, since the luminescence can be quenched by increasing the point defect concentration [79,100]. Therefore, a dependence of $E^{-\alpha}$stands for the product of σ_r and σ_e. Thus, the primary electron energy dependence of I_{CL} can be surmised as

$$I_{CL} = \mathrm{K}'E^{-\alpha}(E - E_0)^{\beta}, \quad (4\text{-}2)$$

where K' is another constant. A strong decay of I_{CL} versus E due to a large α exponent is required to counteract the steep increase of the total displacement per atom (dpa) induced inside a 150 µm thick sample by the primary electrons and the secondary electron cascade versus E. Due to the lesser E_d value of oxygen atoms (35 eV) compared to cerium atoms (58 eV), those dpa values solely result from oxygen displacement [74].

Such kind of function yields a maximum of I_{CL} versus E for both samples at 300 K (Figure 4-9) whereas I_{CL} is expected to increase steadily if σ_d is only considered. A limiting factor must be included to account for this maximum. Least-square fits with Eq. (4-2) give values of E_0 and α and β exponents for the various bands (Table 4-4). The value of E_0 ~400 keV for the F^+ center 4.2 eV band of the single crystal and polycrystalline sample at 300 K is

rather consistent with the data of oxygen displacement by elastic electron-nucleus collisions. The threshold E_0 value is comprised of between 200 keV and 400 keV in agreement with the CL data. The α exponent (~2) agrees with previous results for F^+ center bands in sapphire and YSZ single crystals with values of ~3 [70]. A smaller exponent (~0.6) is deduced for the 4.2 eV band of the polycrystalline sample at 300 K (Table 4-4). The behavior of CL bands assigned to the luminescence of Ce^{3+} at 300 K is quite similar for both kinds of samples with α exponents of ~1.5 (Table 4-4). Fitted parameters for the polycrystalline sample at 100 K and 200 K show similar consistent data versus electron energy. The behavior of CL bands related to Ce^{3+} luminescence at 300 K show that these ions are definitely produced with a similar threshold electron energy as the F^+ centers by charge compensation of the 2+ oxygen vacancies for the high-energy electrons. In contrast, the same CL bands for the 20 keV electron excitation likely derive from ionization effects [106].

Such an analysis, however, is not applicable to the F^+ center data of the single crystal at 100 K and 200 K, which indicate a constant increase against electron energy above the E_0 400 keV threshold energy rather than a maximum [Figures 4-9 (b-c)]. The 100 K values are extrapolated linearly to get an E_0 value of about 100 keV [Figure 4-9(c)]. It appears that Eq. (4-2) is solely left with the $(E - E_0)^\beta$ a term for σ_d. According to Draeger et al., the increase in I_{CL} is roughly in line with the rise in d from 400 keV to 1250 keV [97]. Table 4-4 contains the three bands' fitted values.

The relationship between an increase in electron energy and a drop in temperature depends on the corresponding evolutions of σ_{CL} and σ_d: reducing the sample temperature can result in either a maximum or an ongoing increase in I_{CL}. This is comparable to the temperature effect, which produces either a maximum or a continuous increase for a given electron energy [70]. Remember that σ_r decays with temperature owing to thermal quenching, as was

Table 4-4. Fitting parameters for the electron-energy dependence of CL bands of ceria

Temp.	Crystal		Band	E_0 (MeV)	α	β
300 K	Single	4.2 eV	F^+ center	399	2.20	0.37
		2.9 eV	Ce^{3+}_{I}	396	1.39	0.39
		2.4 eV	Ce^{3+}_{II}	396	1.11	0.39
	Poly	4.2 eV	F^+ center	388	0.61	0.37
		2.7 eV	Ce^{3+}_{I}	398	1.41	0.25
		2.1 eV	Ce^{3+}_{II}	398	1.57	0.25
200 K	Single	4.2 eV	F^+ center	287	0	0.36
		2.9 eV	Ce^{3+}_{I}	250	0	0.34
		2.5 eV	Ce^{3+}_{II}	250	0	0.34
	Poly	4.3 eV	F^+ center	385	0.67	0.38
		2.9 eV	Ce^{3+}_{I}	375	0.96	0.27
		2.2 eV	Ce^{3+}_{II}	375	1.23	0.27
100 K	Single	4.2 eV	F^+ center	355	0	0.36
		3.0 eV	Ce^{3+}_{I}	371	0	0.45
		2.6 eV	Ce^{3+}_{II}	340	0.03	0.43
	Poly	4.3 eV	F^+ center	396	1.22	0.32
		2.8 eV	Ce^{3+}_{I}	397	1.10	0.28
		2.1 eV	Ce^{3+}_{II}	387	0.41	0.28

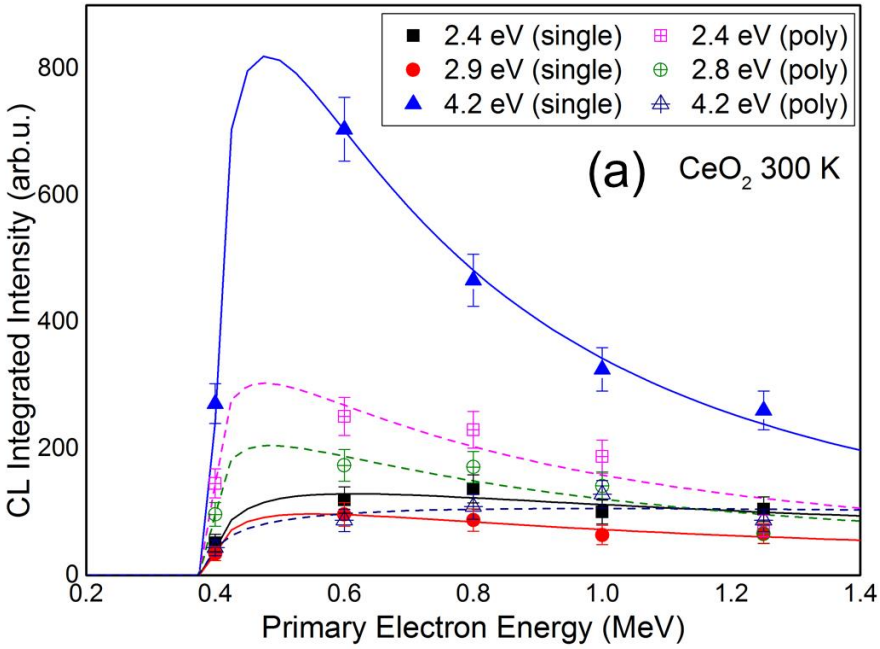
2.4 eV (single)
2.9 eV (single)
4.2 eV (single)
2.4 eV (poly)
2.8 eV (poly)
4.2 eV (poly)
(a) CeO2 300 K
CL Integrated Intensity (arb.u.)
Primary Electron Energy (MeV)
0
200
400
600
800
0.2
0.4
0.6
0.8
1.0
1.2
1.4

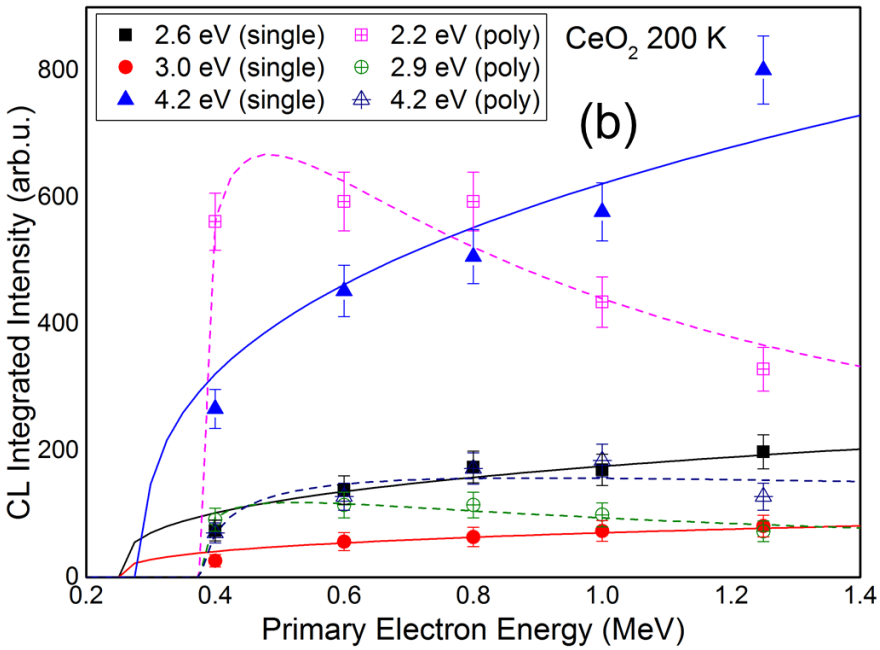
2.6 eV (single)
3.0 eV (single)
4.2 eV (single)
2.2 eV (poly)
2.9 eV (poly)
4.2 eV (poly)
CeO2 200 K
(b)
CL Integrated Intensity (arb.u.)
Primary Electron Energy (MeV)
0
200
400
600
800
0.2
0.4
0.6
0.8
1.0
1.2
1.4

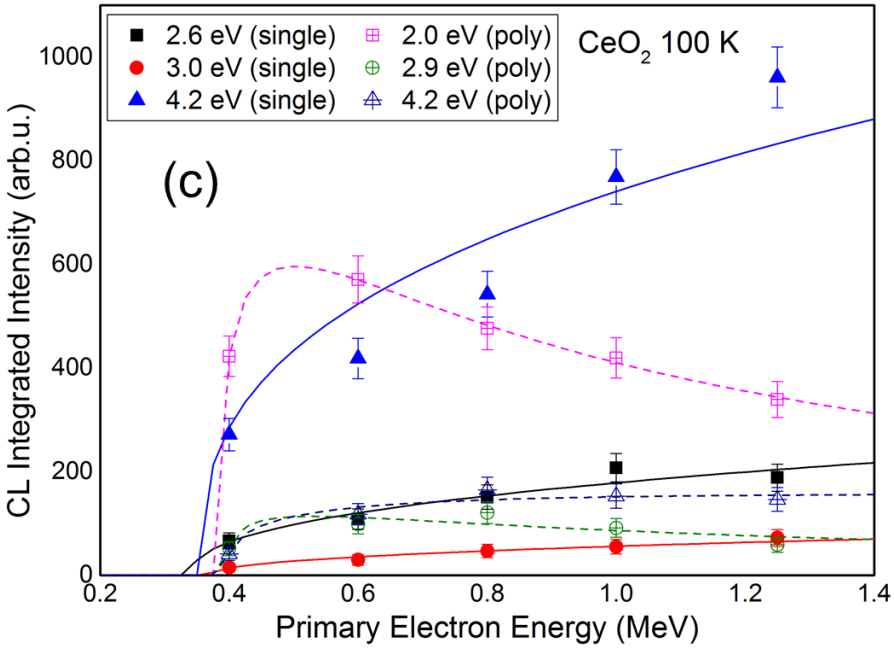

Figure 4-9. CL integrated intensities of the CL bands at (a) 300 K, (b), 200 K, and (c) 100 K versus electron energy for the ceria single crystal (full symbols) and polycrystalline sample (open symbols). Each set of data was recorded for a similar flux and fluence. Solid and dashed lines are least-square fits with Eq. (4-2) for the single crystal and polycrystalline sample, respectively.

previously mentioned [70,78,79,100]. According to the fits, this implies that the exponent should be temperature dependent (Table 4-4). This could explain why a maximum is observed in the sintered sample for a distinct thermal quenching behavior of the luminescence, whereas an almost linear increase of I_{CL} for F^+ centers is observed in the single crystal at 100 K and 200 K.

4.5 Conclusions

In an HVEM, the CL of cerium dioxide was investigated for electron energies ranging from 400 keV to 1250 keV at 100 K, 200 K, and 300 K, as well as for 20 keV electrons at 300 K in a SEM. Only the high-energy electrons (> 200 keV) show a broad, noticeable CL band that is centered at photon energy of 4.2 eV, whereas all electron energies show smaller bands at 2.3 ~ 2.6 eV and 2.8 ~ 3.0 eV. The emission of F^+ centers due to elastic electron-nucleus collisions over a threshold electron energy equivalent to the oxygen displacement energy is attributed to the 4.2 eV band. The charge compensation of oxygen vacancies for the high-energy (400 ~ 1250 keV) electrons and ionization effects for the low-energy (20 keV) electron excitation with a larger inelastic stopping power are attributed to the lower energy CL bands, respectively. At 100 K and 200 K, similar spectra are obtained, but with larger and slightly shifted emission bands. Regardless of temperature, the effects of grain boundaries cause the F^+ center CL signal for the polycrystalline sample to be weaker than the single crystal under the identical circumstances. The interaction between the oxygen displacement cross-section and the luminescence cross-section is used to explain the dependency of CL integrated intensities as a function of primary electron energy for both types of targets.

Chapter 5

Microstructure and radiation response of ceria and Gd_2O_3 doped ceria

5.1 Introduction

The point defects are important for lattice stability and subsequent damage accumulation/annihilation [107]. The trivalent doped ceria, such as Gd_2O_3 doped ceria, generates oxygen vacancies for the compensation of charge neutrality, and the oxygen deficiency of Gd_2O_3 doped ceria is generally higher than pure ceria. In the nuclear reactor, Gd_2O_3 dopant concentration in Gd_2O_3-UO_2 fuel is not high (i.e., < 6 Gd at% for BWR and < 14 Gd at% for PWR). However, the concentration of natural oxygen vacancies is mainly controlled by dopant concentration, and knowledge of the radiation response in high- and wide-concentration of Gd_2O_3 doped ceria is rather limited. In this chapter, the microstructure of virgin and heavy-ion irradiated Gd_2O_3 doped ceria ($Ce_{1-x}Gd_xO_{2-x/2}$) was evaluated in a wide range of Gd dopant concentrations ($0 \leq x_{Gd} \leq 0.5$) to gain insight into the fundamental understanding of radiation response in oxygen-deficient ceramics. For this purpose, a variety of analytical techniques with a wide-scale range was operated, such as XRD, micro-Raman spectroscopy, and TEM.

5.2 Materials and Experimental procedure

Sintered CeO_2 and $Ce_{1-x}Gd_xO_{2-x/2}$ ($0.01 \leq x_{Gd} \leq 0.5$) were used in this chapter and the details of sample preparation methods were described in Chapter 3. The virgin samples were analyzed by XRD measurements in powder type and thin bulk samples prepared from the same

bulk sinters. Raman spectroscopy and TEM observation were also utilized with bulk samples. The thin bulk samples were irradiated at ambient temperature with 200 MeV $^{131}Xe^{14+}$ ions from the JAEA-Tokai to fluence ranging from 3×10^{11} to 1×10^{13} cm^{-2}. They were also analyzed by XRD and TEM observation. The details of experimental conditions are also described in Chapter 3.

5.3 Results

5.3.1 Virgin samples

Figure 5-1 shows the powder XRD patterns of sintered virgin $Ce_{1-x}Gd_xO_{2-x/2}$ (x_{Gd} = 0, 0.01, 0.05, 0.1, 0.2, 0.3, 0.4, and 0.5) samples and unsintered as-received Gd_2O_3 powder. For low Gd concentrations ($x_{Gd} \leq 0.3$), the samples exhibit a single F-type structure, as same as CeO_2. As the Gd_2O_3 doping concentration increases, the C-type characteristic peaks start to be detected from $x_{Gd} = 0.4$, and the intensity of the C-type peaks is increased at $x_{Gd} = 0.5$, as shown in the inset magnified figure in Figure 5-1.

Examples of Rietveld refinement results are shown in Figures 5-2(a) and 5-2(b) for CeO_2 and $Ce_{0.5}Gd_{0.5}O_{1.75}$, respectively. The analysis revealed that a sintered CeO_2 sample has the F-type structure and $Ce_{0.5}Gd_{0.5}O_{1.75}$ has both the F-type and C-type structures by Gd_2O_3 doping. The Rietveld refinement's goodness of fit (χ^2) was defined as the ratio of the expected (R_{EXP}) to weighted (R_{WP}) R-factors as $\chi^2 = (R_{WP}/R_{EXP})^2$. The R_{WP}, R_{EXP}, and χ^2 results for all virgin powder samples are summarized in Table 5-1. CeO_2 and $Ce_{1-x}Gd_xO_{2-x/2}$ samples with values of x_{Gd} in the range of $0.01 \leq x_{Gd} \leq 0.3$ were refined only using the Fm-3m phase since the C-type characteristics peaks did not appear in the patterns, while $Ce_{0.6}Gd_{0.4}O_{1.80}$ and $Ce_{0.5}Gd_{0.5}O_{1.75}$ samples were refined using two phases of fluorite (Fm-3m) and bixbyite (Ia-3) structure. The phase fractions obtained by Rietveld refinement was 71% (fluorite) and 29% (bixbyite) for

$Ce_{0.6}Gd_{0.4}O_{1.80}$ sample, 59% (fluorite) and 41% (bixbyite) for $Ce_{0.5}Gd_{0.5}O_{1.75}$ sample. The value of χ^2 is usually considered reasonable if the value of χ^2 is less than 1.3 [62]. In the present analyses, χ^2 is close to 1.3 for samples of $0.1 \leq x_{Gd} \leq 0.5$. However, the values of χ^2 for $0 \leq x_{Gd} \leq 0.05$ show slightly higher values than the criterion. This is due to the large number of XRD counts that may attribute to the increase in the differences between R_{EXP} and R_{WP}, even with minor imperfections of fitting in the peak shapes and positions [108].

The lattice parameter (a) and microstrain (ε) were evaluated using the Braggs' angles and full-width half-maximum (FWHM) results derived from the Rietveld refinement [109]. The lattice parameter for each sample was determined by the Nelson-Riley plot [110]. The lattice parameter for each Bragg reflection plane of a cubic cell is given by the equation:

$$a_{hkl} = d\sqrt{h^2 + k^2 + l^2}, \quad (5\text{-}1)$$

where d is the d-spacing obtained from the Braggs' equation, hkl the Miller indices of the crystal. The Nelson-Riley function $f(\theta)$ is given by:

$$f(\theta) = (\cos^2\theta/\sin\theta) + (\cos^2\theta/\theta), \quad (5\text{-}2)$$

where θ is the Braggs' angle. The lattice parameter for each sample was calculated from the y-intercept of linear regression on a plot of a_{hkl} versus $f(\theta)$, as an example shown in Figure 5-3(a). The evaluated lattice parameter is plotted in Figure 5-4 as a function of Gd concentration with error bars representing the standard deviation of the linear regression fitting results. The results show that the lattice parameter based on the F-type structure Miller indices ($a_{F\text{-type}}$) increases from 0.5411 to 0.5430 nm for $0 \leq x_{Gd} \leq 0.3$, and saturates to 0.5432 nm for $x_{Gd} > 0.3$. In addition, the lattice parameters for x_{Gd} = 0.4 and 0.5 samples were calculated using the Nelson-Riley plot based on the C-type structure Miller indices ($a_{C\text{-type}}$). The lattice parameter for the C-type structure is double of the F-type structure. Hence, the $a_{F\text{-type}}$ for x_{Gd} = 0.4 and 0.5 is almost similar to half of the values of $a_{C\text{-type}}$ (i.e. $a_{F\text{-type}} \approx 1/2a_{C\text{-type}}$).

The theoretical lattice parameter (a_{Vegard}) was deduced from Vegard's law based on a model of rare-earth (RE) doped CeO_2 [111], which is given by:

$$a_{\mathrm{Vegard}} = 4/\sqrt{3}\left[x_{\mathrm{Gd}}r_{\mathrm{Gd}} + (1 - x_{\mathrm{Gd}})r_{\mathrm{Ce}} + (1 - 0.25x_{\mathrm{Gd}})r_{\mathrm{O}} + 0.25x_{\mathrm{Gd}}r_{\mathrm{V_O}}\right] \times 0.9971, \quad (5\text{-}3)$$

where the ideal ionic radius of Gd^{3+} (r_{Gd}), Ce^{4+} (r_{Ce}), O^{2-} (r_{O}), and V_O ($r_{\mathrm{V_O}}$) are assigned to r_{Gd}= 0.1053 nm, r_{Ce} = 0.0970 nm, r_{O} = 0.1380 nm, and $r_{\mathrm{V_O}}$ = 0.1164 nm, respectively. The constant 0.9971 is a ratio of the actual lattice parameter of CeO_2 from the JCPDS card (0.5411 nm) to the calculated lattice parameter derived from the ionic radii of Ce^{3+} and O^{2-} (0.5427 nm). The $r_{\mathrm{V_O}}$ for RE doped CeO_2 is 0.1164 nm regardless of dopant cation concentration and radius [111]. The calculated a_{Vegard} is shown as a solid line in Figure 5-4, which fairly coincides with small discrepancies ($\Delta a \leq 0.0001$ nm) for $0 \leq x_{Gd} \leq 0.3$, and deviates from the data due to the saturation.

The microstrain can be derived from Braggs' angle and FWHM of the diffraction peaks from XRD refinement results [109]. The microstrain is estimated by the y-intercept extrapolation and the slope of the Williamson-Hall [$\beta\cos\theta = K\lambda/D + 4\varepsilon\sin\theta$] and Halder-Wagner [$(\beta/\tan\theta)^2 = (K\lambda/D)\cdot(\beta/\tan\theta\sin\theta) + 16\varepsilon^2$] plots, where θ is Braggs' angle, β is FWHM, K is a shape constant which is taken into 0.94, and λ is the wavelength of Cu-Kα_1 radiation (0.15406 nm) [112,113]. The corresponding example plots are shown in Figures. 5-3(b) and 5-3(c) for a sample of $Ce_{0.8}Gd_{0.2}O_{1.90}$. The mean values of the microstrain are plotted against Gd dopant concentrations in Figure 5-4. The values of the microstrain increase with Gd concentration and show significant relaxation around x_{Gd} = 0.2, followed by a constant value within the experimental errors beyond x_{Gd} > 0.3.

Micro-Raman spectra between 220 and 700 cm^{-1} with fluorescence background corrections were shown in Figure 5-5. For pure CeO_2, a prominent peak at around 465 cm^{-1},

Table 5-1. XRD and TEM analysis results of $Ce_{1-x}Gd_xO_{2-x/2}$ samples for each Gd concentration (x_{Gd}). The Rietveld refinement performed using FullProf Suite software [67] and its results; weighted profile factor (R_{WP}), expected factor (R_{EXP}), goodness of fit (χ^2). Empirical lattice parameters (a) calculated by the Nelson-Riley plot [105] for virgin and irradiated samples (fluence = 3×10^{12} and 1×10^{13} cm^{-2}), damage cross-section (σ) and track radius (R) deduced from XRD profiles, and track-core radius (R_0) and cross sections (σ_0) deduced from BF-TEM images.

x_{Gd}	R_{WP} (%)	R_{EXP} (%)	χ^2	a (nm)			σ (cm^2)	R (nm)	σ_0 (cm^2)	R_0 (nm)
				Virgin	$3x10^{12}$ cm^{-2}	$1x10^{13}$ cm^{-2}				
0	16.9	9.1	3.4	0.5411	0.5412	0.5413	$23.7x10^{-13}$	8.7	$0.4x10^{-13}$	1.1
0.01	16.8	9.6	3.0	0.5412						
0.05	14.6	9.7	2.3	0.5415						
0.1	16.8	13.0	1.7	0.5419	0.5420	0.5420	$19.9\ x10^{-13}$	8.0		
0.2	17.1	14.1	1.5	0.5426	0.5425	0.5426	$1.4\ x10^{-13}$	6.6	$0.2x10^{-13}$	0.7
0.3	17.2	14.7	1.4	0.5430	0.5430	0.5430	$8.9\ x10^{-13}$	5.3		
0.4	16.3	15.6	1.1	0.5432	0.5432	0.5432	$8.9\ x10^{-13}$	5.3		
0.5	8.6	6.5	1.0	0.5432	0.5433	0.5432	$7.5\ x10^{-13}$	4.9	$0.09x10^{-13}$	0.5

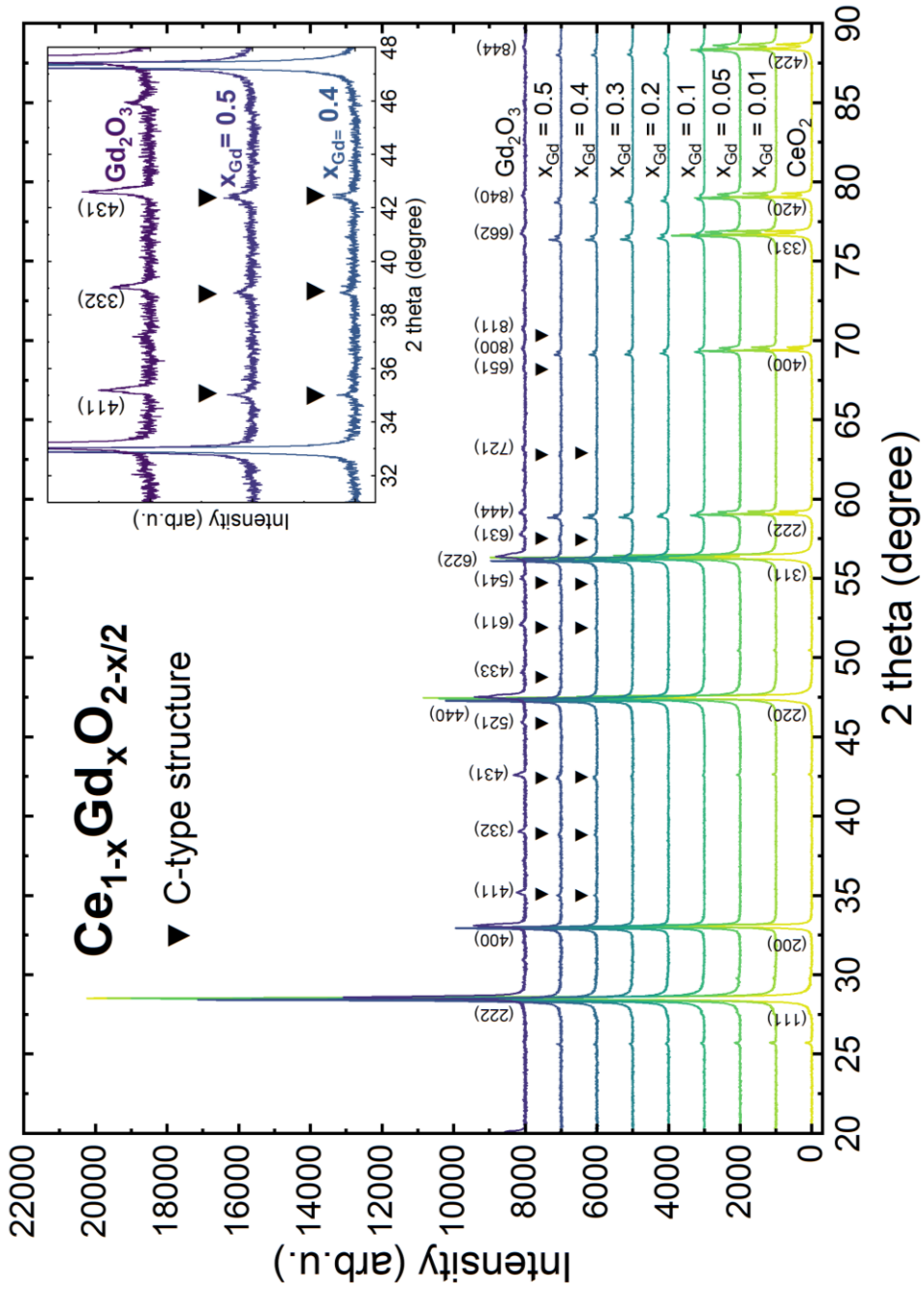

Figure 5-1. Powder XRD patterns of virgin $Ce_{1-x}Gd_xO_{2-x/2}$ and as-received Gd_2O_3 (x_{Gd} = 1). The (*hkl*) planes of the F-type and C-type structures are noticed on the CeO_2 and Gd_2O_3 profiles, respectively. The characteristics of the C-type structure are indicated on the peaks (▼). Inset shows magnified XRD patterns for $Ce_{0.6}Gd_{0.4}O_{1.80}$, $Ce_{0.5}Gd_{0.5}O_{1.75}$ and Gd_2O_3 samples.

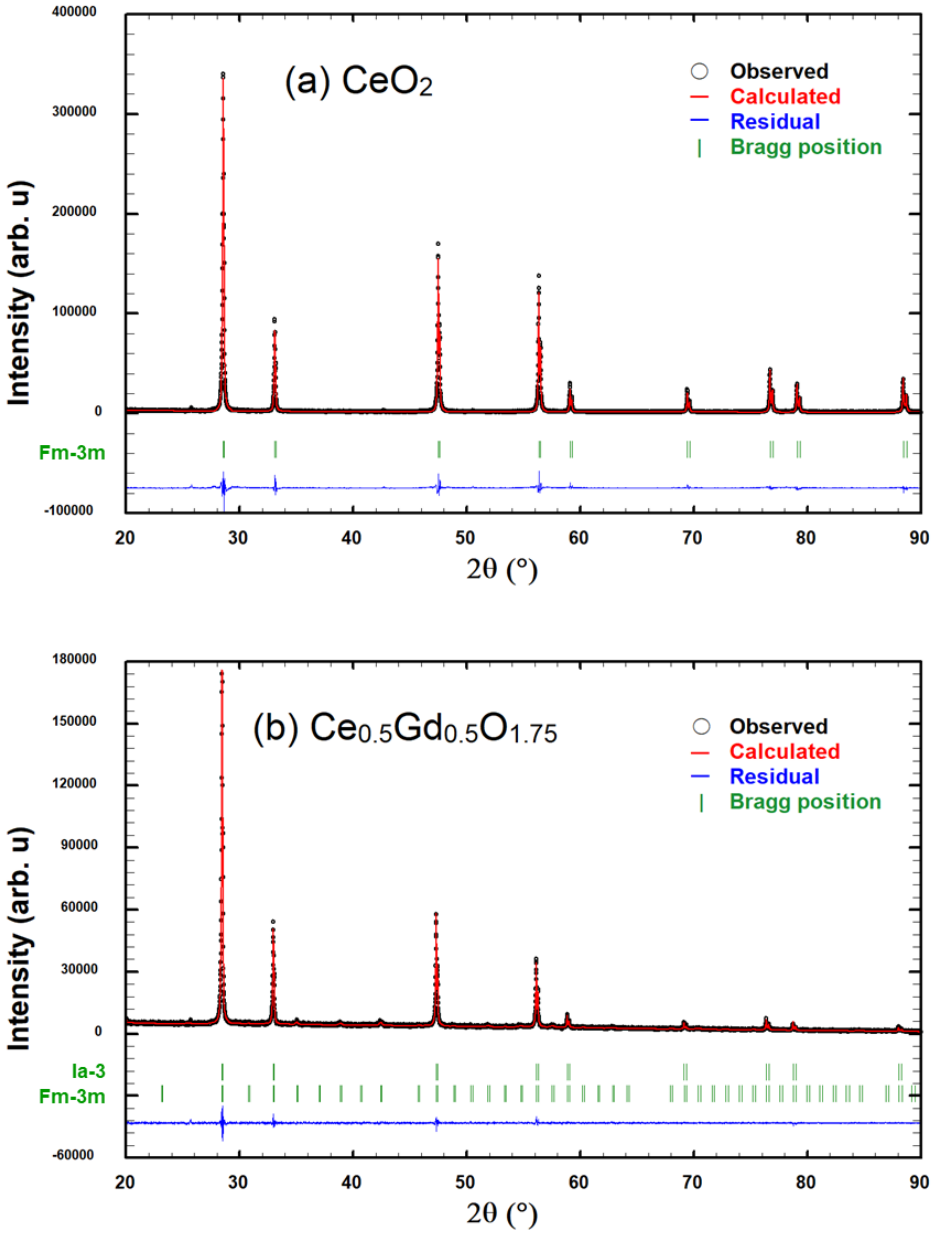

Figure 5-2. Observed (open circles) and Rietveld refinement calculated (red) XRD patterns of (a) CeO_2 and (b) $Ce_{0.5}Gd_{0.5}O_{1.75}$ with the residuals below (blue). The characteristics (*hkl*) of fluorite and cubic plane indices are noticed with Bragg reflection position (green).

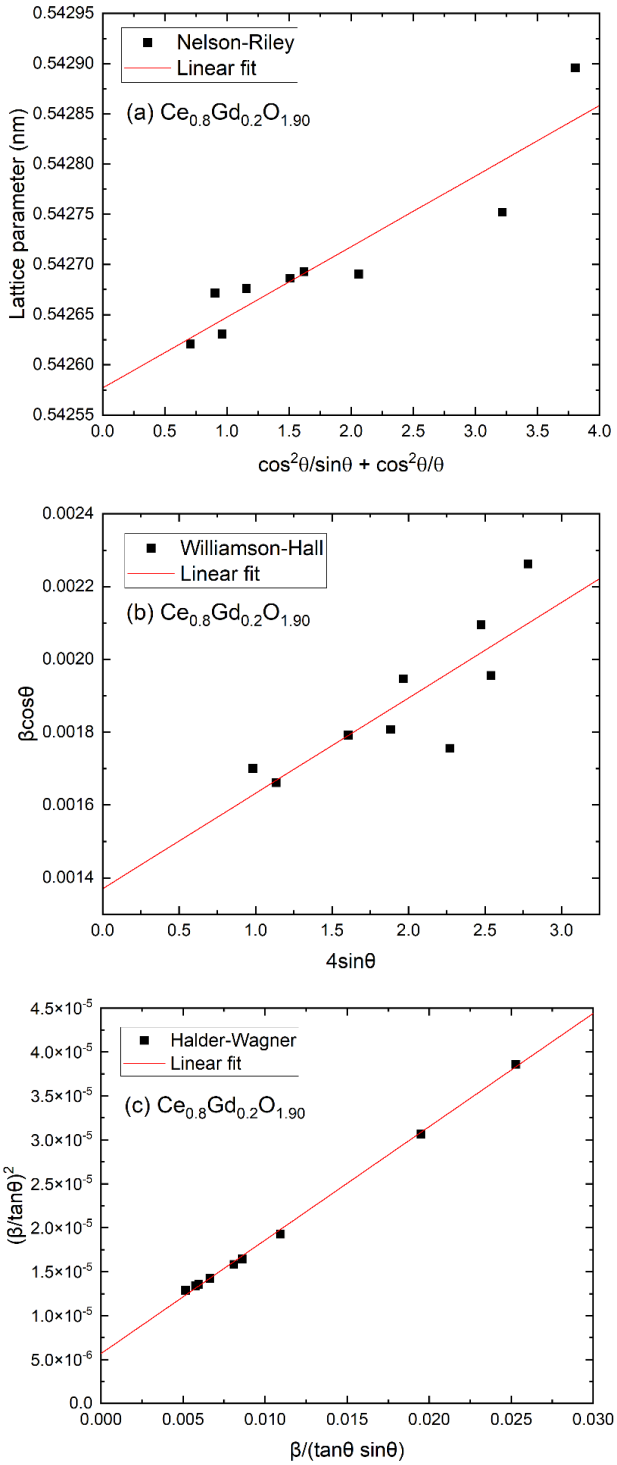

Figure 5-3. Examples of plots of (a) Nelson-Riley, (b) Willamson-Hall, and (c) Halder-Wagner for $Ce_{0.8}Gd_{0.2}O_{1.90}$ and the linear regression fits (red line).

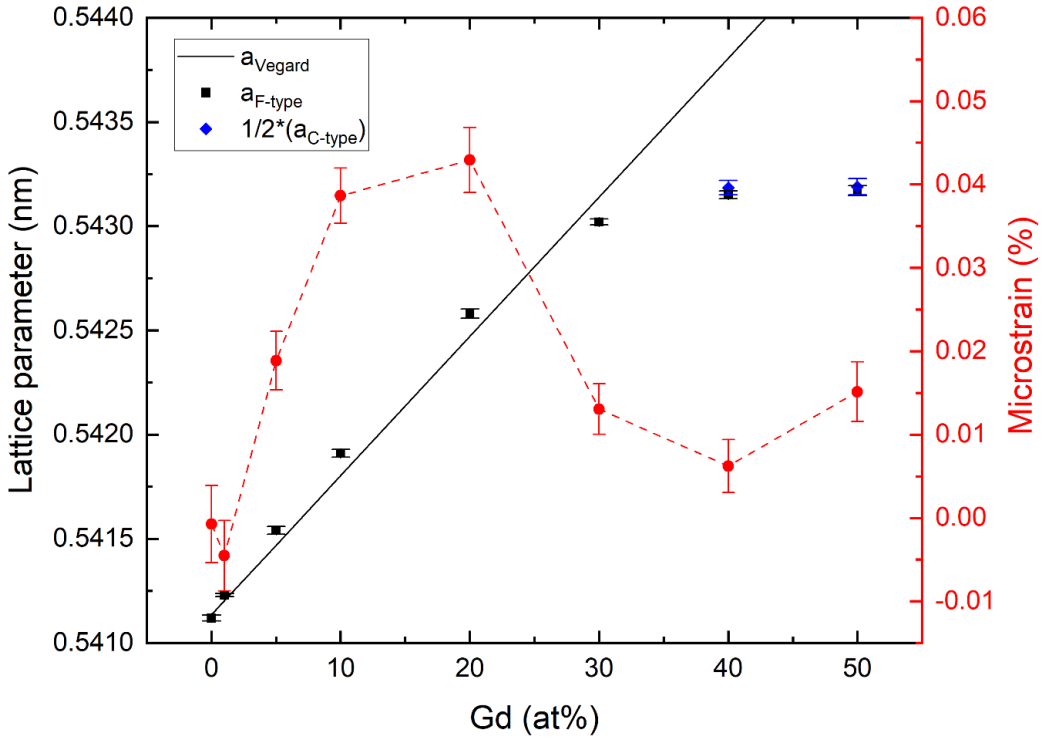

Figure 5-4. The lattice parameter (black, blue, left) and microstrain (red, right) in virgin $Ce_{1-x}Gd_xO_{2-x/2}$ samples as a function of Gd atomic concentration. Dashed and dotted lines are guides to the eyes. A solid line is the theoretical lattice parameter based on Vegard's law (a_{Vegard}), or Eq. (5-3).

five narrow satellites (490 ~ 555 cm^{-1}), and broad bands at around 250, 330, 365, 410 and 670 cm^{-1} were observed. Those peaks were fitted by Lorentzian function at 467 cm^{-1}, and Gaussian function at 251, 334, 365, 410, 493, 513, 523, 537, 555 and 670 cm^{-1}. The signal at 467 cm^{-1} is attributed to the F_{2g} symmetric vibration mode of Ce-O bond in 8-coordination ($Ce^{4+}O_8$) in the F-type structure [114,115]. The five satellites were discussed to native oxygen deficiency with 8-coordination cubes around Ce^{4+} and Ce^{3+} ions in CeO_{2-x} [116–119]. The bands centered at 251 cm^{-1} are assigned to the folded $E_g(X)$ (in directions of [00ζ]) [117,120,121]. The weak and broad bands at 334, 365, and 410 cm^{-1} are assigned to the folded $E_g(L)$, $E_u(L)$ and $A_{1g}(L)$ modes, respectively, in the [ζζζ] directions [121]. The sharp peak at 670 cm^{-1} could be attributed to the combination mode of the F_{2g} mode (467 cm^{-1}) with the A_{1u} mode (227 cm^{-1}) [121].

As a consequence of Gd_2O_3 doping, the F_{2g} mode was broadened, and it merged with the shifted first satellite (487 cm^{-1}) that appeared in the Gd_2O_3 doped samples. The last four satellites (513 ~ 555 cm^{-1}) were broadened and decayed by Gd_2O_3 doping, as well as the bands at 250 ~ 410, and 670 cm^{-1}. Meanwhile, new broadband has appeared at 600 cm^{-1} growing with Gd concentration, which was induced by intrinsic oxygen vacancy formation due to partial reduction of Ce^{4+} ions to Ce^{3+} ions [122].

For samples with high concentration Gd in the range of $0.3 \leq x_{Gd} \leq 0.5$, the latter four satellites disappeared, while broad bands were newly observed at 265, 375, and 565 cm^{-1}, and they are growing with Gd concentration. The bands at 265 and 565 cm^{-1} were ascribed to the interaction between the oxygen vacancies and the six next-nearest neighbor O^{2-} ions [123]. The band at 375 cm^{-1} originated from C-type Gd^{3+} in 6-coordination [124]. The two bands at 565 and 600 cm^{-1} were merged at $x_{Gd} = 0.5$.

The microstructure of $Ce_{1-x}Gd_xO_{2-x/2}$ samples was evaluated by conventional TEM. Figure 5-6 represents SAED patterns from virgin samples of CeO_2, $Ce_{0.8}Gd_{0.2}O_{1.90}$, and

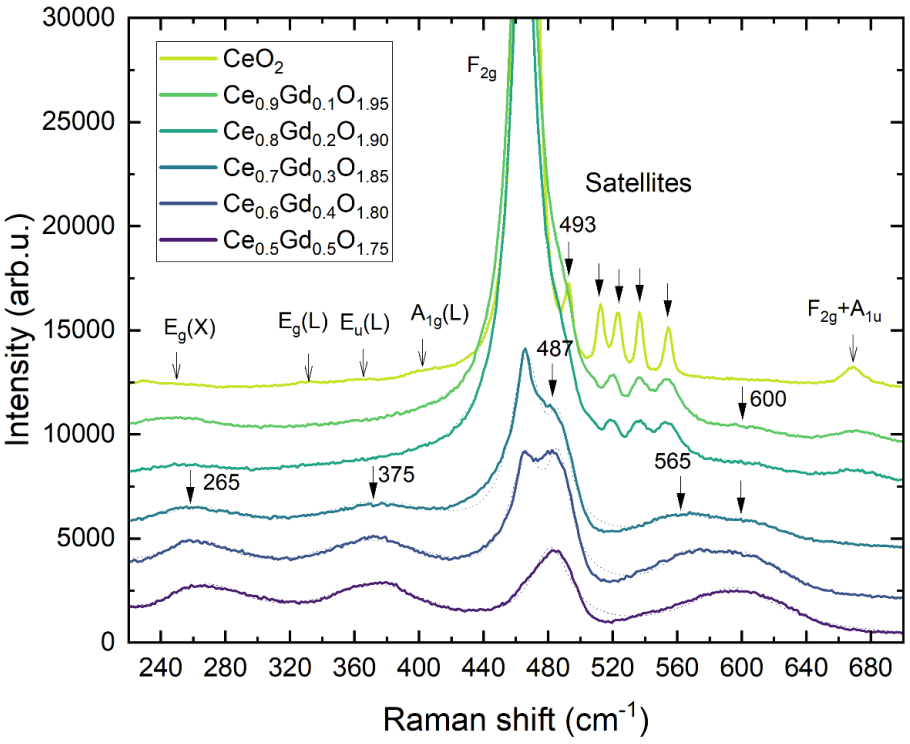

Figure 5-5. Micro-Raman spectra of virgin $Ce_{1-x}Gd_xO_{2-x/2}$ samples. Dotted lines are the sum of Lorentzian or Gaussian fitted curves.

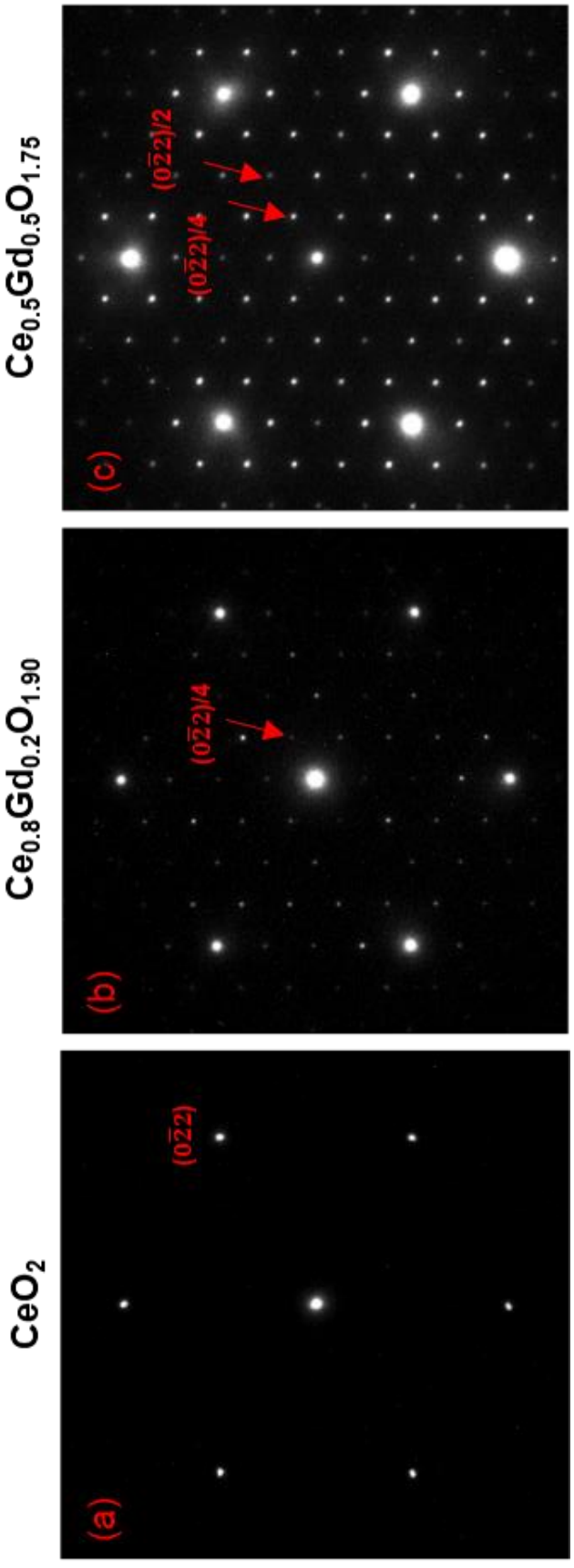

Figure 5-6. SAED patterns of virgin (a) CeO_2, (b) $Ce_{0.8}Gd_{0.2}O_{1.90}$, and (c) $Ce_{0.5}Gd_{0.5}O_{1.75}$ samples along the [111] zone axis.

$Ce_{0.5}Gd_{0.5}O_{1.75}$ taken along the [111] direction. The pure F-type structure reflections (reciprocal vector: $\boldsymbol{G_F}$) are seen in the virgin CeO_2 sample [Figure 5-6(a)]. For the Gd_2O_3 doped CeO_2 samples, extra spots have appeared at $\boldsymbol{G_F \pm \{220\}^*/4}$ and $\boldsymbol{G_F \pm \{220\}^*/2}$, and their intensity increases with increasing Gd concentration. The extra spots are induced by the formation of the domain and/or phase of C-type structure in the F-type phase [125], which will be discussed in section 5.4.1.

In this section, the microstructure in virgin $Ce_{1-x}Gd_xO_{2-x/2}$ samples was observed against to Gd_2O_3 dopant concentration on a wide range of scales. The XRD patterns showed the C-type structure creation in a high concentration of dopant. The XRD refinement results showed the saturation of lattice parameters and the relaxation of the microstrain at dopant concentrations higher than $x_{Gd} = 0.3$. Furthermore, the C-type characteristic Raman band at 375 cm^{-1} appeared for $x_{Gd} \geq 0.3$ with the decay and broadening of F_{2g} mode and satellites. According to TEM-SAED analysis, extra spots at $\boldsymbol{G_F \pm \{220\}^*/4}$ and $\boldsymbol{G_F \pm \{220\}^*/2}$ were observed for $x_{Gd} \geq 0.2$. These comprehensive experimental results provide the information on nucleation-and-growth of the C-type structure in the F-type matrix and a threshold of gadolinium dopant concentration in CeO_2 for the microstructure evaluation.

5.3.2 Irradiated samples with 200 MeV Xe^{14+} ions

The microstructure of $Ce_{1-x}Gd_xO_{2-x/2}$ samples evaluated after ion irradiation at room temperature. XRD patterns of thin bulk type virgin and irradiated $Ce_{1-x}Gd_xO_{2-x/2}$ (x_{Gd} = 0, 0.2, 0.5) samples are shown in Figure 5-7 for the 2θ angle range corresponding to (331) and (420) peaks to ion fluence of 3×10^{12} and 1×10^{13} cm^{-2}. The XRD profiles were fitted by the Pseudo-Voigt function based on the fluorite structure. All samples clearly show the F-type structure peaks, showing that no amorphization was induced by 200 MeV Xe ion irradiation as observed

in references [126,127]. For the irradiated samples, the C-type XRD peaks were diminished by irradiation (see the inset in Figure 5-7). Phase transition to the monoclinic structure was not observed, as reported in an ion-irradiated C-type structure of sesquioxide [128]. In addition, new asymmetric peaks appeared at approximately 0.1 deg. lower than the F-type structure peaks of $K\alpha_1$. The asymmetric peaks were grown and broadened with increasing ion fluence without any splitting of peaks. A new phase reported in reduced CeO_{2-x} samples ($CeO_{1.71} - CeO_2$) [129], which is featured by splitting of F-type structure peaks, was not recognized. The peaks are, therefore, considered to be induced by lattice distortion of the F-type structure by ion irradiation, and they were assigned to the peak of Damage-$K\alpha_1$ hereafter. The Damage-$K\alpha_1$ decays with increasing Gd concentration, and it almost completely disappeared for $x_{Gd} > 0.3$.

The lattice parameters of irradiated samples were deduced from the $K\alpha_1$ and Damage-$K\alpha_1$ peaks using the Nelson-Riley analysis based on the F-type structure. Results are shown in Figure 5-8 for ion fluence of 3×10^{12} and 1×10^{13} cm^{-2}, together with the lattice parameter of virgin samples ($a_{F\text{-type}}$) and the theoretical one (a_{Vegard}). Both $a_{K\alpha1}$ and $a_{Damage\text{-}K\alpha1}$ are seen to increase with x_{Gd} to reach saturation for $x_{Gd} > 0.3$, as observed in virgin samples ($a_{F\text{-type}}$). Further, the values of $a_{K\alpha1}$ show slight change after irradiation regardless of ion fluence. On the other hand, the values of $a_{Damage\text{-}K\alpha1}$ revealed higher values than $a_{F\text{-type}}$. The difference between $a_{K\alpha1}$ and $a_{Damage\text{-}K\alpha1}$ was greater for high fluence (1×10^{13} cm^{-2}) than low fluence (3×10^{12} cm^{-2}). The estimated lattice expansion of $\Delta a_{K\alpha1}/a_{F\text{-type}}$ in CeO_2 at a fluence of 1×10^{13} cm^{-2} was 0.04%. This is consistent with reported values of 0.06 ~ 0.07% by Ohno et. al. and Tracy et. al. obtained in CeO_2 with 200 MeV and 167 MeV Xe, and 950 MeV Au irradiation [130,131]. A slightly smaller value than the previous reports might be due to the lower ion fluence (1×10^{13} cm^{-2}) than references (1×10^{14} cm^{-2}). On the other hand, the change in the lattice parameter of the new shoulder peak, $\Delta a_{Damage\text{-}K\alpha1}/a_{F\text{-type}}$ showed rather large values of

0.12 ~ 0.14 % for CeO_2 and $Ce_{0.9}Gd_{0.1}O_{1.95}$. It is also noted that the value of $\Delta a_{\text{Damage-K}\alpha 1}/a_{\text{F-type}}$ was remarkably observed for low Gd concentration, and the lattice expansion became small for high Gd concentration samples above $x_{Gd} = 0.2$.

Figure 5-9 shows plane-view BF-TEM images of $Ce_{1-x}Gd_xO_{2-x/2}$ (x_{Gd} = 0, 0.2, 0.5) samples irradiated to a fluence of 1×10^{13} cm^{-2}, which were taken in a kinematical over-focus condition with a defocus value of $\Delta f = +1.0$ μm. As examples are noted with arrows in Figures 5-9(a) ~ 5-9(c), black dot contrast is observed as Fresnel contrast. The contrast represents the cylindrical defects of ion tracks observed at an end-on condition [126]. The ion-track radius (R_0) was evaluated to be 1.1 nm for CeO_2 and it gradually decreases to 0.7 and 0.5 nm for $Ce_{0.8}Gd_{0.2}O_{1.90}$ and $Ce_{0.5}Gd_{0.5}O_{1.75}$, respectively. They are reported in Table 5-1 with the cross-section values (σ_0) deduced by $\sigma_0 = \pi R_0^2$. These sizes are significantly smaller than the reported values obtained by XRD and TEM [117,132,133]. Since ion tracks in this study were observed as Fresnel contrast, the contrast represents the core region of ion tracks including a high concentration of vacancies [10,134], but not the strained regions around ion tracks. It is also noted that the size of Fresnel contrast varies with the defocus condition, or Δf [116], and the value of Δf = +1 gives a small and sharp contrast of ion tracks. The areal density of ion tracks for CeO_2, $Ce_{0.8}Gd_{0.2}O_{1.90}$, and $Ce_{0.5}Gd_{0.5}O_{1.75}$ was evaluated to be 5.9×10^{11}, 5.9×10^{11}, and 2.8×10^{11} cm^{-2}, respectively, and the density decreased at the high Gd content sample. It is reported that the density of ion tracks induced by 200 MeV Xe ions in CeO_2 increases linearly with ion fluence and saturates at high fluence higher than around 1×10^{12} cm^{-2}, which was discussed due to the balance between the formation and recovery of the core damage region of ion tracks [126,135]. The ion track density of the CeO_2 sample, which was obtained at a fluence of 1×10^{13} cm^{-2} in this study, seems to be saturated since the ion fluence is sufficiently higher than the reported fluence. Although there have been no data for the accumulation of ion tracks

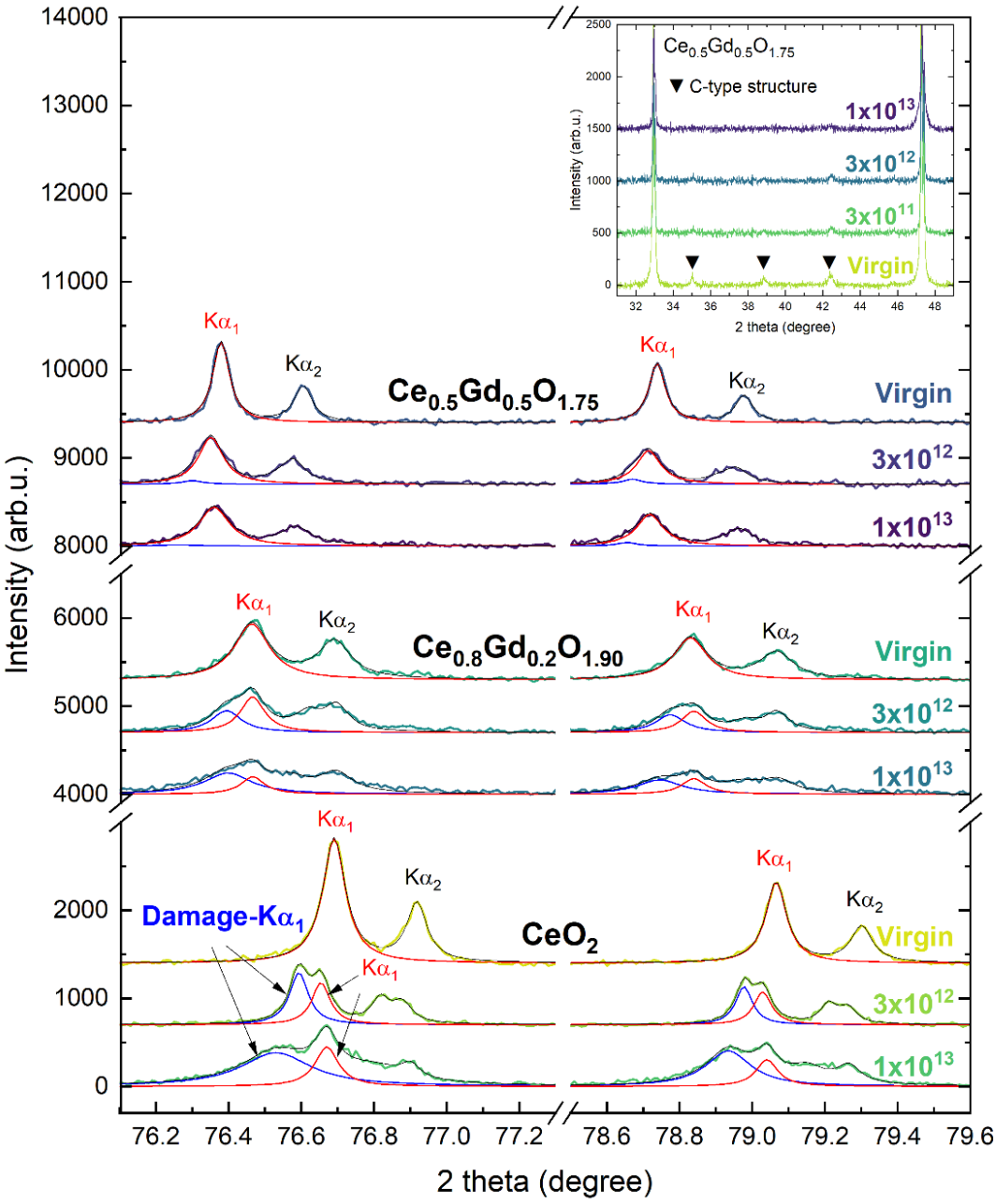

Figure 5-7. XRD patterns of (331) and (420) planes from virgin and irradiated $Ce_{1-x}Gd_xO_{2-x/2}$ samples (x_{Gd} = 0, 0.2, 0.5) with 200 MeV Xe^{14+} ions to fluence of 3×10^{12} cm^{-2} and 1×10^{13} cm^{-2}. $K\alpha_1$ (red) and Damage-$K\alpha_1$ (blue) peaks were fitted by the Pseudo-Voigt function. Inset shows the C-type characteristic peaks (▼) for virgin and irradiated $Ce_{0.5}Gd_{0.5}O_{1.75}$ samples at fluences ranging from 3×10^{11} to 1×10^{13} cm^{-2}.

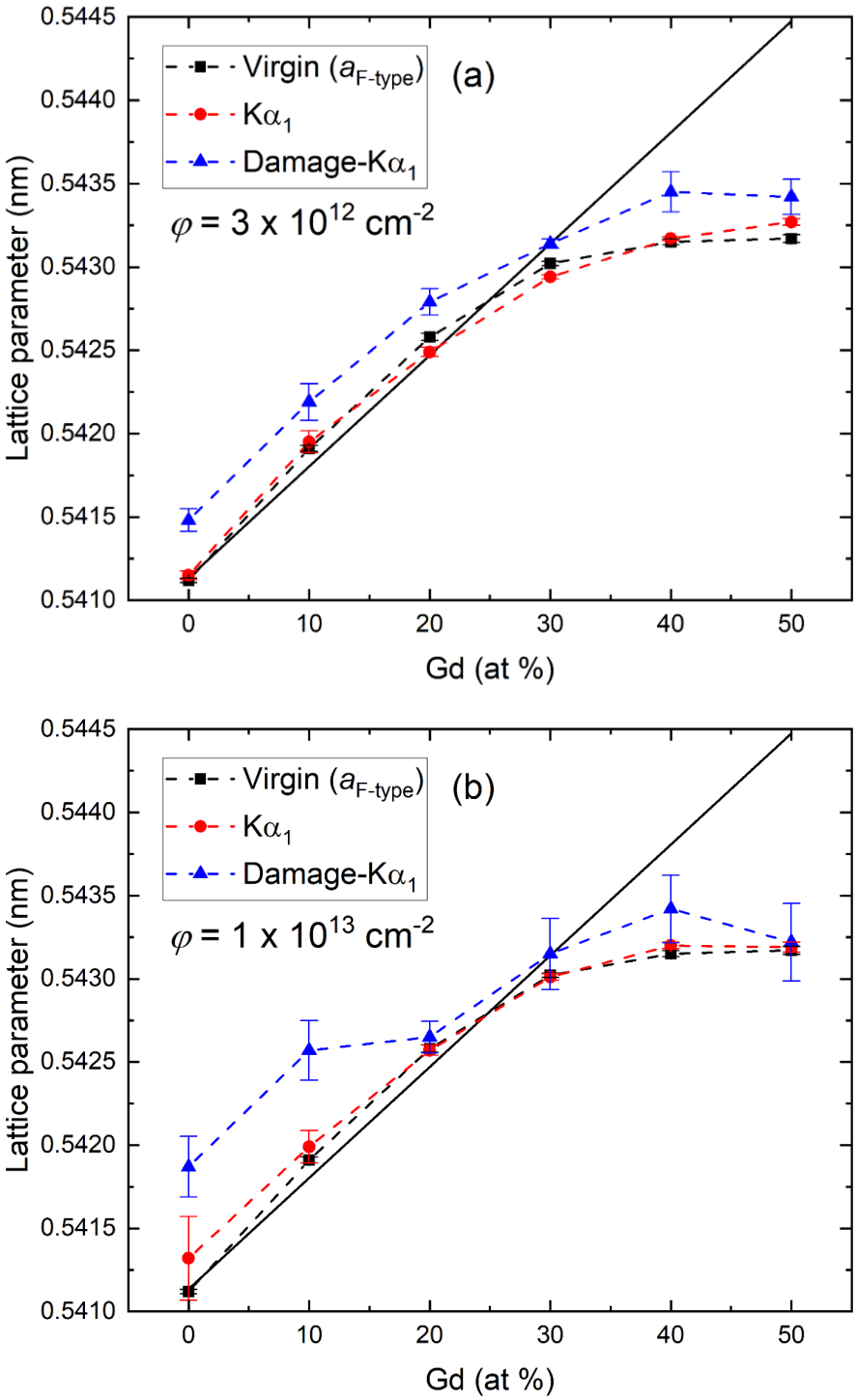

Figure 5-8. The lattice parameters of $Ce_{1-x}Gd_xO_{2-x/2}$ after ion irradiation to fluences of (a) 3×10^{12} cm^{-2} and (b) 1×10^{13} cm^{-2} comparing to virgin samples ($a_{F\text{-}type}$). Dashed lines are guides to the eyes. A solid line is the theoretical lattice parameter of virgin samples (a_{Vegard}) obtained from Eq. (5-3).

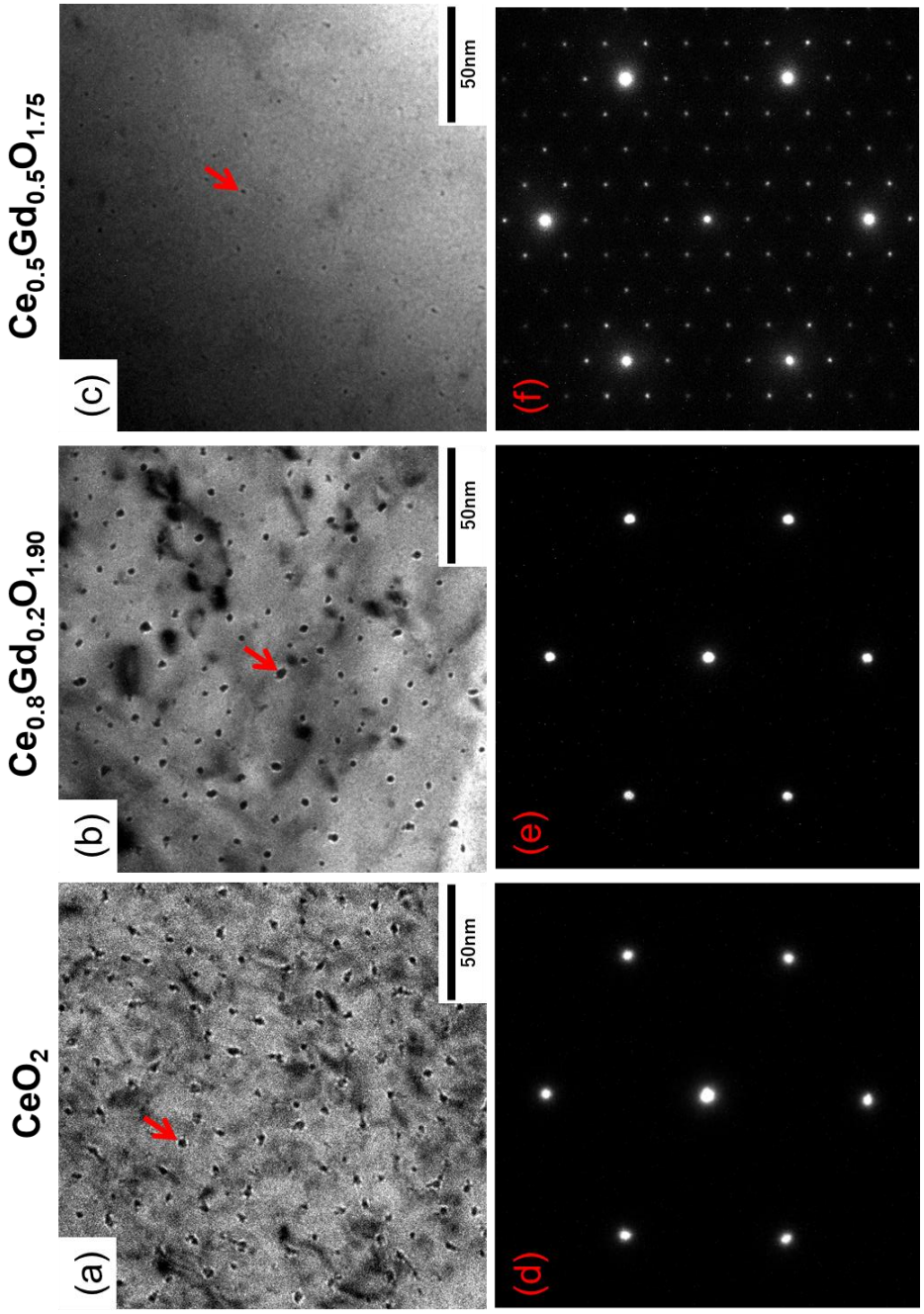

Figure 5-9. BF-TEM images showing Fresnel contrast taken from the direction along the incident ions in (a) CeO_2, (b) $Ce_{0.8}Gd_{0.2}O_{1.90}$, and (c) $Ce_{0.5}Gd_{0.5}O_{1.75}$ with 200 MeV Xe^{14+} ions to a fluence of 1×10^{13} cm^{-2}. BF images were taken in a kinematical over-focus condition with a defocus value of $\Delta f = +1.0$ µm. The corresponding SAED patterns along the [111] zone axis are shown in (d) – (f).

in Gd_2O_3 doped CeO_2, the density of ion tracks for high concentration $Ce_{1-x}Gd_xO_{2-x/2}$ samples might be depressed under an assumption that a fluence of 1×10^{13} cm^{-2} is in the saturation range as same as CeO_2. Figures 5-9(d) ~ 5-9(f) show the corresponding SAED patterns taken along the [111] zone axis. The F-type reflections are clearly visible in all samples, whereas the extra spots were eliminated for $Ce_{0.8}Gd_{0.2}O_{1.90}$ [Figure 5-9(e)]. The intensity of the $\boldsymbol{G_F}$ **± {220}*/2** reflections for the $Ce_{0.5}Gd_{0.5}O_{1.75}$ sample is reduced significantly due to the ion irradiation [Figure 5-9(f)], and the SAED pattern of $Ce_{0.8}Gd_{0.2}O_{1.90}$ is similar to the $Ce_{0.5}Gd_{0.2}O_{1.90}$ sample without ion-irradiation [Figure 5-6(b)].

5.4 Discussion

5.4.1 C-type structure formation in $Ce_{1-x}Gd_xO_{2-x/2}$

The phase transition in the miscibility gap has been discussed in trivalent Ln doped ceria-based oxides solutions in literature, such as $Ce_{1-x}Yb_xO_{2-x/2}$ [136], $Ce_{1-x}Y_xO_{2-x/2}$ [137], and $Ce_{1-x}La_xO_{2-x/2}$ [138]. The amount of Ln dopant for the phase transition depends especially on its ionic radii [42]. The phase transition in $Ce_{1-x}Gd_xO_{2-x/2}$ was observed in a wide range scale by Raman spectroscopy [123,124], EXAFS [47,139], XRD [137,140–142], and oxidative drop solution calorimetry [143]. However, the reported value of x_{Gd} for the phase transition was different in literature in the range from x_{Gd} = 0.13 to 0.54. Such a wide range of x_{Gd} values is related to the similarity of the F-type and C-type structures, and different synthesis methods of materials. The average value of x_{Gd} from the above literature is 0.34. In the present study, the C-type structure was observed by XRD patterns without peak splitting for $x_{Gd} > 0.3$, which coincides with the average value deduced from the literature.

As shown in Figure 5-4, the lattice parameter of the virgin sample ($a_{F\text{-type}}$) increased following Vegard's law to saturate at $x_{Gd} > 0.3$, where the formation of the C-type structure

was observed. High resolution TEM observation of $Ce_{1-x}Gd_xO_{2-x/2}$ samples has found the formation of nano-scale domains of the C-type structure at $x_{Gd} = 0.2$ in the F-type matrix, and the size of the C-type nanodomain increased with Gd concentration [51]. Ou et al. suggested from the analysis and simulation of SAED patterns that the ordering of oxygen vacancies was initiated in the C-type nanodomains [125]. The SAED patterns of the virgin $Ce_{0.8}Gd_{0.2}O_{1.90}$ sample shown in Figure 5-6(b) clearly demonstrated extra spots at $\boldsymbol{G_F \pm \{220\}^*/4}$ and $\boldsymbol{G_F \pm \{220\}^*/2}$, despite the XRD pattern revealing single F-type structure (Figure 5-1). This implies that the ordering of oxygen vacancies occurred in the stable F-type structure at $x_{Gd} = 0.2$, and it grows to the C-type precipitates in the F-type matrix at the concentration of $x_{Gd} > 0.2$.

The above interpretation of the formation of the C-type structure at $x_{Gd} > 0.2$ coincides with the Raman spectroscopy result. For pure CeO_2, Raman shifts related to Ce^{4+}-O and Ce^{3+}-O bonds in the F-type structure were observed at the F_{2g} mode and at the first satellite (493 cm^{-1}), respectively, due to the reversible redox in CeO_{2-x} [118]. For Gd_2O_3 doped CeO_2, the F_{2g} mode sharply decayed with the increase of Gd concentration especially for higher values of $x_{Gd} > 0.2$ (Figure 5-5), due to the loss of symmetry of Ce^{4+}-O. Furthermore, a shift of the first satellite to 487 cm^{-1} was observed by Gd_2O_3 doping from $x_{Gd} = 0.1$. The shifted peak, which is assigned to Gd^{3+}-O bond in the F-type structure with 8-fold coordination [124], was growing gradually with Gd concentration compared to the change in the F_{2g} mode. On the other hand, for $x_{Gd} = 0.3$, a new broad Raman band appeared at 375 cm^{-1} and grew with Gd concentration, which was assigned to the 6-coordinated Gd^{3+}-O bond in the C-type structure [124]. Those results and interpretation imply that the growth of the C-type structure with Gd^{3+}-O bonds in the F-type structure started to grow at $x_{Gd} = 0.1$ and those in the C-type structure generated at $x_{Gd} = 0.3$.

The formation of the C-type structure is also linked to the microstrain relaxation. The microstrain was observed to increase with x_{Gd} while it was relaxed at around $x_{Gd} = 0.2 – 0.3$ (Figure 5-4). The microstrain was induced by the substitution of Gd^{3+} ions with a large ionic radius into the Ce^{4+} sites and the associated creation of oxygen vacancies [141,144]. Kossoy et al. observed a sharp decrease in the distance of Ce-O bond at $x_{Gd} = 0.2 – 0.25$ by EXAFS and XRD analysis. The structural distortion is influenced strongly by the change in the distance of the first shell (Ce-O and Gd-O) rather than that of the second shell (Ce-Ce and Gd-Ce) [139]. Therefore, the sharp relaxation of the microstrain observed at around $x_{Gd} = 0.2 – 0.3$ is attributed to the reduction of the coordination number of Ce ions, together with the development of oxygen vacancy ordering in the formation of the C-type precipitates in the F-type matrix.

5.4.2 Disappearance of C-type structure and damage recovery induced by heavy ion irradiation in $Ce_{1-x}Gd_xO_{2-x/2}$

The microstructure change of $Ce_{1-x}Gd_xO_{2-x/2}$ was evaluated after heavy ion irradiation by XRD and TEM analysis. The XRD patterns revealed a non-amorphized F-type structure after 200 MeV Xe ion irradiation. Slight changes in the lattice parameters of $a_{K\alpha1}$ (Table 5-1) indicate the F-type matrix is not largely expanded by irradiation. Xe ion irradiation, however, induced Damage-$K\alpha_1$ peaks at the shoulder of each $K\alpha_1$ peak, and those peaks were broadened with the increase of ion fluence whereas $K\alpha_1$ peaks decrease their intensities. The larger value of the lattice parameter of $a_{Damage\text{-}K\alpha1}$ than $a_{K\alpha1}$ indicates that the lattice of the damaged region was expanded by ion irradiation. The peaks of damage-$K\alpha_1$ were, therefore, understood caused by the lattice distortion of the F-type structure around the core region of ion tracks. The difference in the $a_{K\alpha1}$ and $a_{Damage\text{-}K\alpha1}$ values for the samples irradiated to low fluence (3×10^{12} cm^{-2}) is

almost constant regardless of x_{Gd} values [Figure 5-8(a)]. On the other hand, the discrepancy of the high fluence sample (1×10^{13} cm^{-2}) depends on Gd concentration. A larger discrepancy appeared for $x_{Gd} < 0.2$, while the discrepancy showed a low constant value above $x_{Gd} = 0.2$ within the experimental errors. This indicates that the lattice distortion is remarkable for $x_{Gd} < 0.2$ where the concentration of oxygen vacancies is relatively low without a fully ordered condition in the C-type structure.

To analyze the damage cross-section of 200 MeV Xe ions against the Gd concentration, the XRD peaks shown in Figure 5-1 were fitted by the Pseudo-Voigt function and the intensities were integrated. For the damage kinetics analysis, using the peak area parameter is much more accurate than the peak intensity since it contains strain and size information of the crystal induced by ion irradiation. In the following analysis, the damaged region was assumed to have no contributions to the original XRD peaks [145]. The area of $K\alpha_1$ peaks (A) at the (331) plane of an ion-irradiated sample was normalized to that of the corresponding virgin sample (A_0), and it was plotted in Figure 5-10 as a function of ion fluence (φ). As expected, the normalized value of A/A_0 decreases as a function of fluence to saturation at high fluence. The fraction of damaged regions (δ) can be estimated as

$$\delta = (S/\sigma)[1 - \exp(-\sigma\varphi)], \quad (5\text{-}4)$$

where S is the cross-section for recovery induced by ion-track over-lapping, σ is the damage cross-section. Assuming a linear dependence of A on δ, A is given by a decay function of

$$A = A_0 + (A_\infty - A_0)[1 - \exp(-\sigma\varphi)], \quad (5\text{-}5)$$

where A_∞ is the saturated area value. Fitting results are shown in Figure 5-10 as dashed lines for each sample. The values of A_∞/A_0 were found to increase with x_{Gd}: those were evaluated to be 0.26 for CeO_2 and 0.71 for $Ce_{0.5}Gd_{0.5}O_{1.75}$. The ratio of A_∞/A_0 for CeO_2 was saturated at $\varphi = 1 \times 10^{12}$ cm^{-2}, which shows a good agreement with the areal density saturation trends

versus φ determined by TEM and STEM observations [126,127]. For Gd_2O_3 doped CeO_2 samples at x_{Gd} = 0.4 and 0.5, the values of A_∞/A_0 were saturated at a rather higher fluence of ~5×10^{12} cm^{-2}. The values of σ were deduced by Eq. (5-5), and they showed to decrease with x_{Gd}. Particularly for $x_{Gd} > 0.2$, the values of σ show rapid reduction versus Gd concentration. The values of σ and track radii (R) deduced by $R = (\sigma/\pi)^{1/2}$ are reported in Table 5-1, together with the cross-section (σ_0) and the track radii (R_0) evaluated by Fresnel contrast of BF-TEM images.

The track radius deduced from XRD and TEM is plotted in Figure 5-11. The evaluated value of the ion track radius of the CeO_2 sample was 8.7 nm and it is significantly larger than the size obtained by Fresnel contrast of BF-TEM, or 1.1 nm. The evaluated size by XRD analysis reveals a good agreement with the recovery size (8.4 nm) evaluated based on the modeling of the accumulation process of ion tracks, where a saturation regime is interpreted on a balanced condition between the formation of a new ion track and the elimination of preexisting tracks within the recovery region [126,127]. It suggests that the obtained size by the present XRD study possesses the same physical meaning of recovery from the thermal spike regime. Figure 5-11 also shows that the radius of the ion track decreases with the increase of Gd concentration, showing a saturation at values of $x_{Gd} > 0.3$. This is a clear indication that the recovery cross-section of the ion track damage is influenced by the concentration of the oxygen vacancies and their ordering.

At the same time, the C-type XRD peaks (see the inset in Figure 5-7) and the extra spots in the SAED patterns (Figure 5-9) disappeared with 200 MeV Xe ion irradiation, indicating the destruction of the ordering structure of oxygen vacancies and the C-type structure. The ordered structure of oxygen vacancies is considered to be disappeared through the recombination with interstitial oxygens induced by ion irradiation. Patel et al. [146] also observed the reduction of

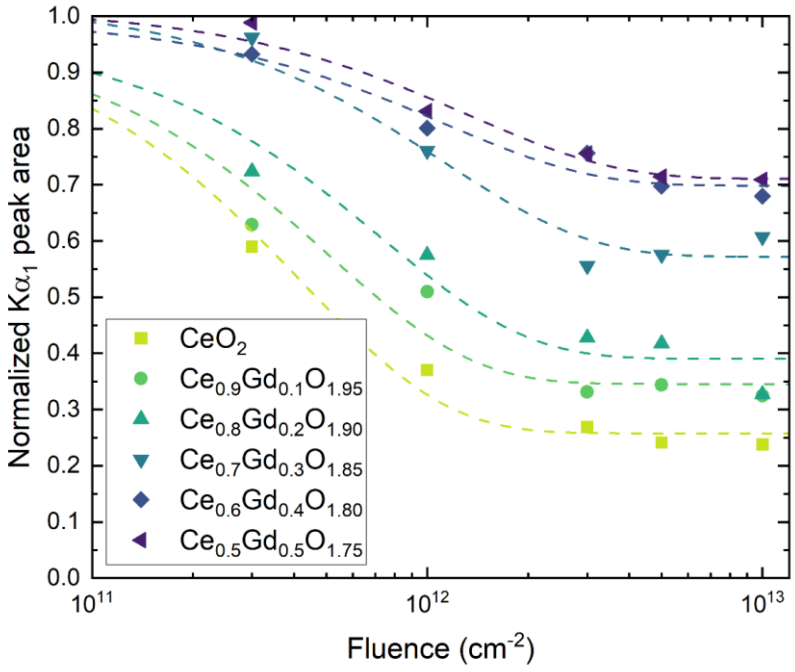

Figure 5-10. Area of normalized $K\alpha_1$ peaks fitted by the Pseudo-Voigt function as a function of fluence. Dashed lines are fits of area data with Eq. (5-5).

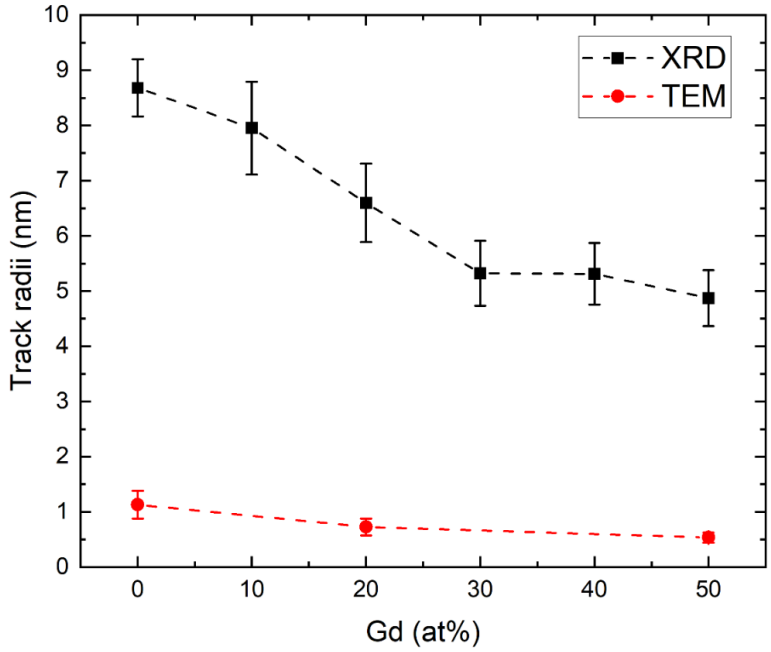

Figure 5-11. Track radius in $Ce_{1-x}Gd_xO_{2-x/2}$ against Gd atomic concentration deduced by from XRD analysis using Eq. (5-5), and Fresnel contrast BF-TEM images. Dashed lines are guides to the eyes.

lattice strain by XRD analysis in $Ce_2Gd_2O_7$ or $Ce_{0.5}Gd_{0.5}O_{1.75}$ irradiated with 92 MeV Xe^{26+} ions, and they suggested the radiation damage recovery occurred through the ordered oxygen vacancies in the C-type domain walls. The SAED pattern of $Ce_{0.5}Gd_{0.5}O_{1.75}$ irradiated to a fluence of 1×10^{13} cm^{-2} showed a partial elimination of extra spots [Figure 5-9(f)] compared to the unirradiated condition [Figure 5-6(c)], and the pattern and intensity of extra spots in the SAED pattern in Figure 5-9(f) resemble that of the virgin $Ce_{0.8}Gd_{0.2}O_{1.90}$ sample [Figure 5-6(b)]. Since the microstructure of $Ce_{0.8}Gd_{0.2}O_{1.90}$ is considered to contain nano-sized domains of the C-type structure in the F-type matrix [125], the SAED result suggests that the elimination of the C-type structure under ion irradiation might be proceeded gradually passing through the ordering condition of oxygen vacancies with nano-sized domains, but not directly from the C-type precipitates to the F-type matrix. This is consistent with the remarkable change in the recovery process observed in Figures 5-10 and 5-11 at $x_{Gd} = 0.2 \sim 0.3$, and this implies an important role in the ordering of oxygen vacancies for the recovery process during ion irradiation with 200 MeV Xe ions.

5.5 Conclusions

We have studied the microstructure evolution of virgin and 200 MeV Xe^{14+} ion irradiated $Ce_{1-x}Gd_xO_{2-x/2}$ samples for a wide range of Gd concentrations ($0 \leq x_{Gd} \leq 0.5$) at room temperature through comprehensive structural analysis of XRD, micro-Raman spectroscopy and TEM. The lattice parameter increased with the increase of Gd concentration and simultaneous creation of charge-compensation oxygen vacancies. The lattice parameter was saturated at $x_{Gd} > 0.3$ due to the formation of the C-type structure in the F-type matrix. The reduction in the F-type symmetry with the formation of the C-type structure associated with

ordered oxygen vacancies was observed at $x_{Gd} \geq 0.2$ consistently from the experimental techniques used in the present study.

The XRD and TEM results showed that all the compositions of $Ce_{1-x}Gd_xO_{2-x/2}$ samples were resistant to amorphization and sustained the F-type structure with 200 MeV Xe ion irradiation. In the XRD patterns, asymmetrical peaks (Damage-$K\alpha_1$) were observed on the shoulders of F-type peaks ($K\alpha_1$), and the asymmetry was decreased with the increase of Gd concentration. The asymmetric peaks are caused by the lattice distortion in the F-type structure due to the formation of damaged regions induced by ion tracks. On the other hand, the C-type structure has disappeared with ion irradiation because of the loss of the ordered oxygen vacancy structure in the C-type domain. Analysis of the radiation-induced recovery by XRD patterns with ion irradiation showed track radii, or recovery radii, decreases with the Gd concentration. Besides, the XRD analysis showed rapid recovery of radiation damage for values of $x_{Gd} = 0.2 \sim 0.3$, suggesting an important role of oxygen vacancy ordering in the C-type structure for the recovery process in Gd_2O_3 doped CeO_2.

Chapter 6

Application of *in-situ* HVEM - CL technique to CeO_2 doped with Gd_2O_3

6.1 Introduction

Ceria is an oxygen-deficient material since Ce^{4+} reversibly reduces to Ce^{3+} ion generating intrinsic oxygen vacancies for charge neutrality. As mentioned in Chapter 1, ceria has been used as a surrogate of nuclear fuel and it is doped with Gd_2O_3 for a burnable poison. Doping of Gd_2O_3 also produces oxygen vacancies as described $Ce_{1-x}Gd_xO_{2-x/2}$ by the substitution of Gd^{3+} into Ce^{4+} ion sites due to their similar ionic radii (i.e. r_{Gd}= 0.1053 nm, r_{Ce} = 0.0970 nm). The oxygen deficiency in $Ce_{1-x}Gd_xO_{2-x/2}$ is mostly controlled with the concentration of Gd dopant.

Oxygen point defects are also produced by high-energy electron irradiation. Frenkel defects are created by elastic collisions transferring energies over threshold displacement energy (E_d) of oxygen atoms. In Chapter 4, it was found that F^+ centers (1+ charged oxygen vacancies) were generated in pure CeO_2 in a short time under high-energy electron irradiation (400 ~ 1250 keV) by using the HVEM-CL facility. The in-beam charge states of defects and their electronic configurations were modeled through *in-situ* CL spectroscopy.

As described in Chapter 5, oxygen vacancies were shown to have an important role for the radiation recovery in $Ce_{1-x}Gd_xO_{2-x/2}$. Ordered oxygen vacancies were observed in the C-type structure in $Ce_{1-x}Gd_xO_{2-x/2}$ for the composition of $x_{Gd} > 0.2$, and this attributed for the reduction of the density and size of ion tracks induced by 200 MeV Xe ion irradiation. Those results suggest that oxygen vacancies act as a sink of irradiation-induced interstitials.

The displacement damage of O ions was found to influence the charge states of cation and F^+ center, and those strongly depend on the localized position in their lattice site. It is, therefore, interesting and indispensable to investigate the electronic states of ions and F^+ centers under electron irradiation during the production of oxygen vacancies. In this chapter, the oxygen point defects creation in $Ce_{1-x}Gd_xO_{2-x/2}$ under high-energy electron irradiation was evaluated by *in-situ* CL spectroscopy for a wide range of Gd dopant concentrations in the samples. Energy levels and energy dependence of F center and impurities were investigated regarding of dopant concentration.

6.2 Materials and experimental procedure

Sintered thin (~150 μm) half disk-shaped polycrystalline $Ce_{1-x}Gd_xO_{2-x/2}$ samples ($0.01 \leq x_{Gd} \leq 0.5$) were used to obtain *in-situ* CL spectra using the HVEM-CL facility (Figures 3-4 and 3-7) at electron energies from 400 keV to 1250 keV at the temperature of 300 K. Also, the CL spectra under low-energy (20 keV) electron irradiation were corrected by using the SEM-CL facility (Figure 3-6) at the temperature of 300 K. All obtained spectra were fitted by a Gaussian function and the intensity of CL bands were integrated to interpret CL emission dependence with electron energy and Gd dopant concentration. The detailed information for sample preparation, the HVEM-CL facility together with the *in-situ* measurement conditions were described in Chapter 3.

6.3 Results

6.3.1 Displacement cross-section calculation

The displacement cross-sections (σ_d) of oxygen, cerium, and gadolinium atoms in $Ce_{1-x}Gd_xO_{2-x/2}$ induced by electron-nuclear elastic collisions were calculated by using SMOTT/

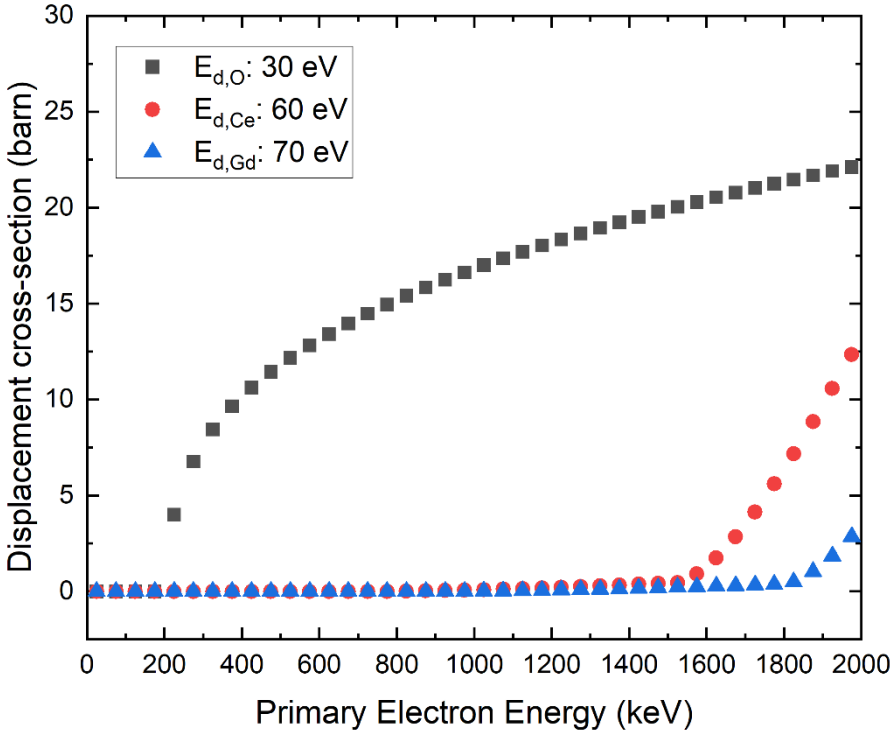

Figure 6-1. Oxygen, cerium, gadolinium atoms displacement cross section in Gd_2O_3 doped ceria by electron-nucleus collisions calculated by SMOTT/POLY computer code [74]. The values of E_d for each atom were referred to literature proposed by Yasunaga et al. [9] and Konobeyev et al. [72]

POLY computer code [74] based on Eq. (2-12). The threshold displacement energies (E_d) for each atom were assumed based on the reported values of Ce ($E_{d,Ce}$: 44 ~ 58 eV), O ($E_{d,O}$: < 33 eV) [9], and Gd ($E_{d,Gd}$: 71 ± 16 eV) [72] sublattices. The calculated total σ_d is shown in Figure 6-1 as a function of electron energy. The threshold electron energies in ceria where the cross-sections exceed 1 barn were evaluated in Chapter 4 for oxygen ($E_{0,O}$: 150 ~ 200 keV) and cerium ($E_{0,Ce}$: 1300 ~ 1600 keV) sublattices. The value of $E_{0,Gd}$ was evaluated in Fig.6-1 to be 1700 ~ 1900 keV. The selective oxygen displacement using HVEM in its energy range (400 ~ 1250 keV) was deduced for $Ce_{1-x}Gd_xO_{2-x/2}$ the total σ_d calculation results, while 20 keV electron irradiation hardly induces displacements of lattice atoms as same as the case of ceria described in Chapter 4.

6.3.2 CL spectra in polycrystalline Gd_2O_3 doped CeO_2

CL spectra in sintered polycrystalline $Ce_{1-x}Gd_xO_{2-x/2}$ (x_{Gd} = 0, 0.01, 0.05, 0.1, 0.2, 0.3, 0.4, 0.5) were obtained under high- and low-energy electron irradiation. For high-energy electron irradiation, one spectrum was taken under electron irradiation for 30 seconds at 300 K, and the spectra were averaged out for 5 recordings for 400 keV ~ 1250 keV electrons. The spectra were fitted using the Gaussian function. Figure 6-2 shows an example of *in-situ* CL spectrum for 1250 keV electron irradiation in ceria and $Ce_{0.5}Gd_{0.5}O_{1.75}$ together with fitted Gaussian profiles. 4 Gaussian bands were recorded at photon energies of ~1.7 eV, 2.2 ~ 2.4 eV, 2.4 ~ 2.8 eV, and ~4.3 eV with full-width at half-maximum (FWHM) of 0.6 ~ 0.9 eV, 0.5 ~ 0.7 eV, 0.3 ~ 0.6 eV, and 1.6 eV, respectively. A sharp and intense unresolved line was observed at 1.79 eV (probably R-lines of Cr^{3+} impurities [75]) for all samples, and a small doublet at 1.73 ~ 1.75 eV and another broader impurity line was observed at 1.85 eV.

CL spectra were measured at different electron energies of 400, 600, 800, 1000, and 1250 keV for all Gd_2O_3 doped samples at a constant electron beam-flux of 3.8×10^{21} $m^{-2}s^{-1}$. The CL spectra were obtained by averaging out the recordings after 0 ~ 150 seconds, and they are shown in Figure 6-3 with the Gaussian fitted profiles (dashed lines). Further, the average CL band characteristics, such as the band center (eV), FWHM (eV), and the types of defects in all samples of $Ce_{1-x}Gd_xO_{2-x/2}$ (x_{Gd} = 0, 0.1, 0.2, 0.3, 0.4, 0.5) were summarized in Table 6-1.

CL spectra were also measured for electrons with 20 keV at a constant beam current of 1.7 nA at the temperature of 300 K. The measured CL spectra are shown in Figure 6-4 with the Gaussian fitted profiles (dashed and dotted lines) for x_{Gd} = 0, 0.2, 0.3, 0.5 samples. The CL band characteristics for 20 keV electron irradiation are described in Table 6-2. Only one broad CL band centered at ~2.5 eV was observed in the samples for $x_{Gd} \leq 0.2$, and this band was divided into two bands centered at 2.3 eV and 2.6 ~ 2.7 eV by Gaussian fitting. It is noted here that the CL band was reduced for the samples with high Gd dopant concentration for $x_{Gd} > 0.2$, which is caused by the quenching of CL emission and will be discussed later.

6.4 Discussion

6.4.1 Cation CL emission with point defects production

CL from oxides under high energy electron irradiation is emitted by recombination of thermalized secondary electrons and holes while most of primary electrons are transmitted [70]. It is shown in Table 6.3 by the values of range and electronic stopping power of ceria and Gd_2O_3 doped ceria (x_{Gd} = 0.5) samples simulated by using the ESTAR code [77].

For sufficient CL intensity detection, a large volume of sample was used in the HVEM-CL measurements to increase the electron and hole carriers. To this end, CL spectra were obtained from thick (~150 μm) $Ce_{1-x}Gd_xO_{2-x/2}$ samples under 400 keV ~ 1250 keV electron

Table 6-1. CL band characteristics and defect assignments for $Ce_{1-x}Gd_xO_{2-x/2}$ (x_{Gd} = 0, 0.1, 0.2, 0.3, 0.4, 0.5) under high-energy (400 keV ~ 1250 keV) electron irradiation.

x_{Gd}	Band center (eV)	FWHM (eV)	Type of defect	x_{Gd}	Band center (eV)	FWHM (eV)	Type of defect
0	4.3	1.6	F^+ center	0.3	4.3	1.6	F^+ center
	2.8	0.4	Ce^{3+}_{I}		2.6	0.3	Ce^{3+}_{I}
	2.4	0.5	Ce^{3+}_{II}		2.3	0.7	Ce^{3+}_{II}
	1.8	0.6	Impurity		1.8	0.7	Impurity
0.1	4.3	1.6	F+ center	0.4	4.3	1.6	F+ center
	2.8	0.6	Ce3+I		2.6	0.3	Ce3+I
	2.4	0.6	Ce3+II		2.3	0.7	Ce3+II
	1.7	1.0	Impurity		1.7	0.8	Impurity
0.2	4.3	1.6	F+ center	0.5	4.2	1.6	F+ center
	2.6	0.3	Ce^{3+}_{I}		2.4	0.3	Ce^{3+}_{I}
	2.4	0.7	Ce^{3+}_{II}		2.2	0.7	Ce^{3+}_{II}
	1.7	0.8	Impurity		1.7	0.9	Impurity

Table 6-2. CL band characteristics and defect assignments for $Ce_{1-x}Gd_xO_{2-x/2}$ (x_{Gd} = 0, 0.1, 0.2) under low-energy (20 keV) electron irradiation.

x_{Gd}	Band center (eV)	FWHM (eV)	Type of defect
0	2.6	0.6	Ce^{3+}_{I}
	2.3	0.7	Ce^{3+}_{II}
0.1	2.8	0.8	Ce^{3+}_{I}
	2.2	0.7	Ce^{3+}_{II}
0.2	2.7	0.8	Ce^{3+}_{I}
	2.3	0.7	Ce^{3+}_{II}

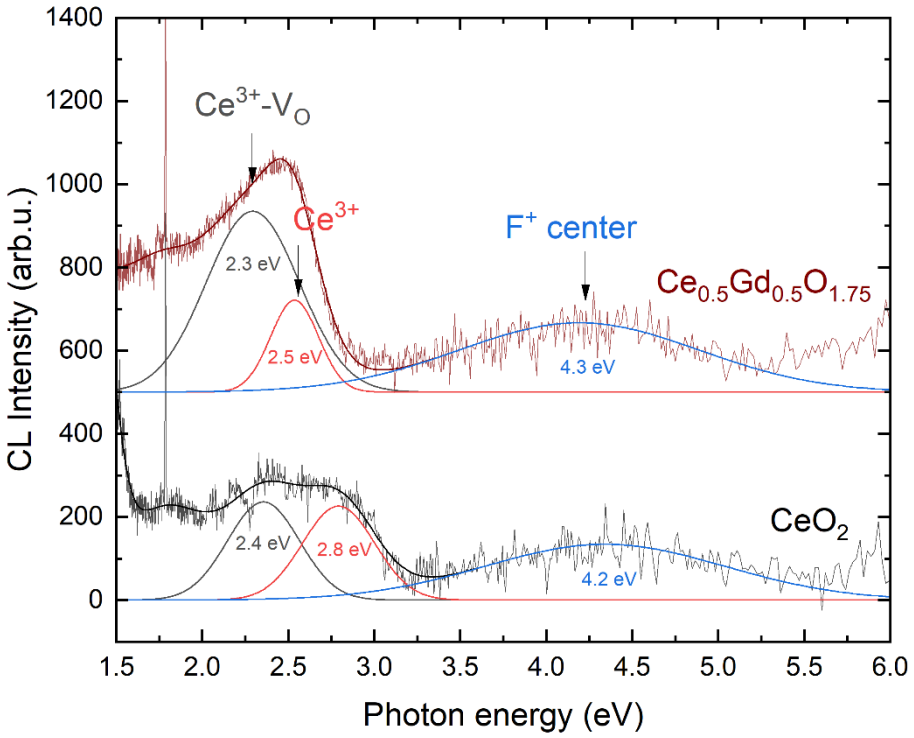

Figure 6-2. *In-situ* CL spectra for 1250 keV electron irradiation in ceria and Gd_2O_3 doped ceria at 300 K.

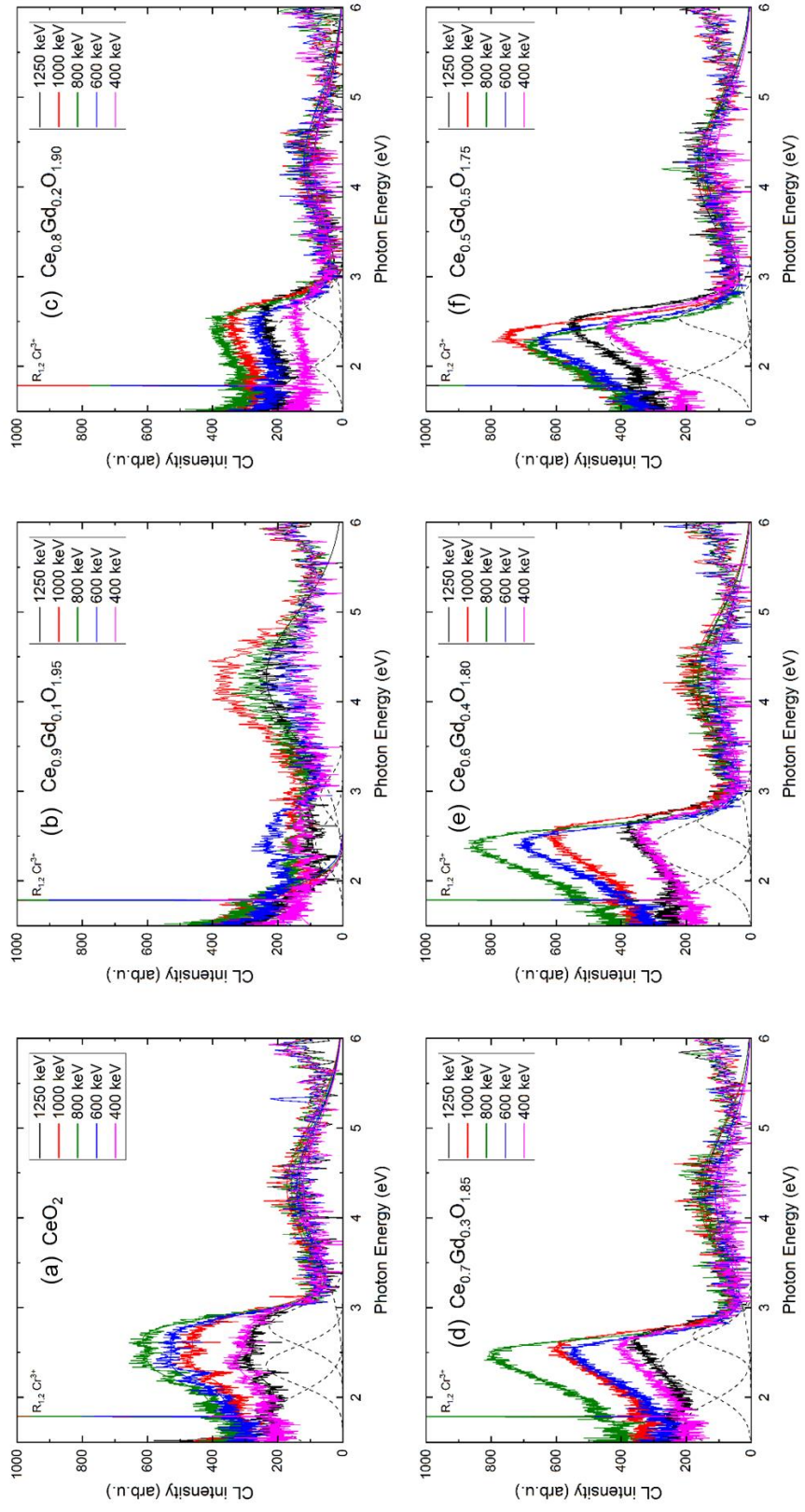

Figure 6-3. CL spectra at 300 K of polycrystalline ceria and Gd_2O_3 doped ceria ($Ce_{1-x}Gd_xO_{2-x/2}$) for $0.1 \leq x_{Gd} \leq 0.5$ at fluences of 5.7 x 10^{23} m^{-2}. Dashed lines are the fitted spectra and dotted lines are the Gaussian curves used for least-square fits.

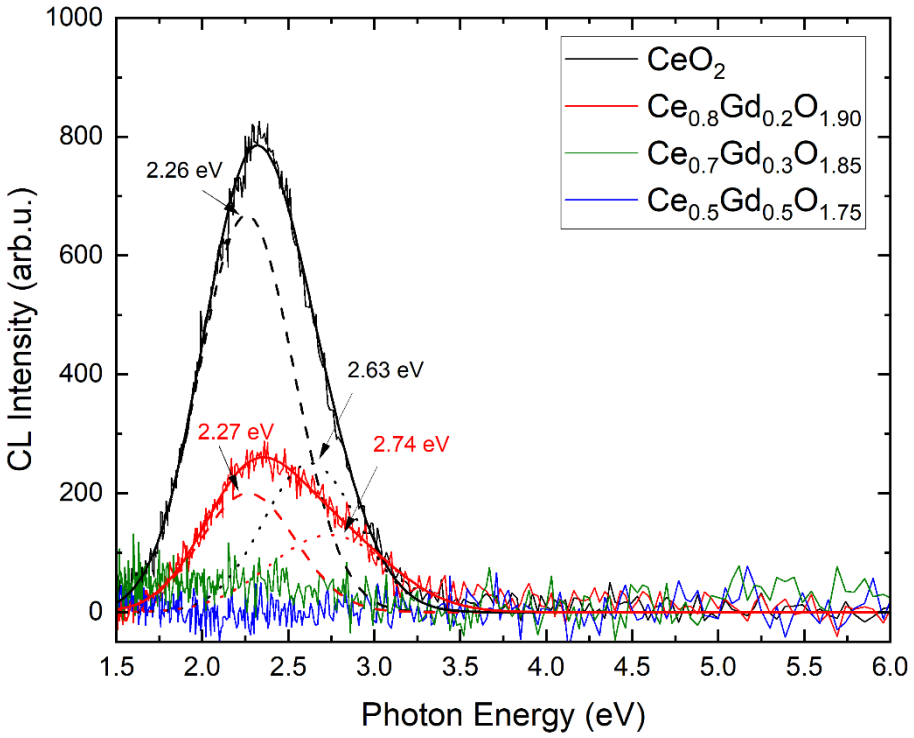

Figure 6-4. *In-situ* CL spectra for 20 keV electron irradiation in ceria and Gd_2O_3 doped ceria at 300 K. Dashed and dotted lines are fitted spectra and solid lines are Gaussian curves for least-square fits.

irradiation as same as pure CeO_2 samples, and the CL spectra showed enough intensity (Figure 6-3) as observed in pure polycrystalline ceria samples (Figure 4-5). The spectra were fitted by the Gaussian function, and the CL bands appeared at 2.2 ~ 2.4 eV, 2.4 ~ 2.8 eV, and 4.3 eV. These CL band positions are mostly similar to pure ceria results, which were measured at the temperature of 300 K [Figure 4-5(a) or Figure 6-3(a)].

In Chapter 4, CL bands for pure ceria were interpreted by experimental and theoretical methods. The CL emission was found to strongly link with oxygen vacancies, which form localized cation-V_O clusters. Namely, for pure ceria, CL bands centered at 2.1 eV, 2.7 eV, and 4.2 eV were assigned to i) Ce_I: Ce^{3+}, ii) Ce_{II}: Ce^{3+}-V_O, and iii) F^+ center, respectively. CL emission from Ce_I (2.7 eV) is induced by Ce^{3+} ions located in a site of cation sublattice far from V_O, while Ce_{II} is Ce^{3+} ions localized in a caton site near oxygen vacancy (V_O) that emits low energy (2.1 eV). On the other hand, CL emission from F^+ center at 4.2 eV was induced by a $(Ce_{Ce}^{\times} - V_O^{\cdot\cdot} - Ce_{Ce}^{\times})^{\cdot\cdot}$ trimer capturing an electron in ane oxygen vacancy $(Ce_{Ce}^{\times} - V_O^{\cdot} - Ce_{Ce}^{\times})^{\cdot\cdot}$, and immediately shifting the electron to one of the two Ce^{4+} (i.e. $Ce_{Ce}^{\times}$), resulting a $(Ce_{Ce}^{\times} - V_O^{\cdot\cdot} - Ce_{Ce}^{\prime})^{\cdot}$ trimer.

In the Gd_2O_3 doped ceria sample, the creation of extrinsic oxygen vacancies (denoted as $V_{O,ext}^{\cdot\cdot}$ hereafter) induced by charge compensation with Gd_2O_3 doping should be discussed before electronic excitation-induced point defects production. $V_{O,ext}^{\cdot\cdot}$ is generated in a dimer equilibrium process associating with the Gd dopant as expressed by $[Gd_{Ce}^{\prime} + V_{O,ext}^{\cdot\cdot} \leftrightarrow (Gd_{Ce}^{\prime} - V_{O,ext}^{\cdot\cdot})^{\cdot}]$. Trimer equilibrium equation $[2Gd_{Ce}^{\prime} + V_{O,ext}^{\cdot\cdot} \leftrightarrow (Gd_{Ce}^{\prime} - V_{O,ext}^{\cdot\cdot} - Gd_{Ce}^{\prime})^{\times}]$ can be also proposed. However, the low cation mobility rarely drives this reaction at low temperatures [43]. This trimer equilibrium equation in Gd_2O_3 doped ceria is similar to the defects creation in pure ceria induced by electronic excitation. It can be assumed that the Gd^{3+} dopants change not only the Ce^{3+}/Ce^{4+} redox equilibrium but also the excitation-induced defects equilibrium

by fixing the oxygen deficiency and reducing the number of Ce^{3+} ions. Therefore, (Gd'_{Ce}-V_O) cluster can be expressed as Ce_{II} or Ce^{3+}-V_O instead.

The photon energies of three CL bands (Ce^{3+}, Ce^{3+}-V_O, and F^+ center) observed in Gd_2O_3 doped ceria are plotted in Figure 6-5 as a function of Gd dopant concentration. Energies of Ce^{3+}-V_O and F^+ center showed constant regardless of the dopant concentration, while the peak of Ce^{3+} ion is seen to shift to lower energy (2.8 eV → 2.4 eV) with the increase of the Gd dopant concentration. The Ce^{3+} ion is localized far from oxygen vacancy, theirby this enegry shift is attributed to the increase of the direct band gap energy (E_G) between O 2*p* and Ce 4*f* bands. UV-visible absorption spectroscopy showed an increase of E_G in thin film samples from 3.6 eV for CeO_2 to 3.72 eV $Ce_{0.7}Gd_{0.3}O_{1.85}$ at 0 K since the lower overlapping capacity of 4*f* orbitals in the doped sample makes narrow 4*f* band [147]. On the other hand, for the low Gd dopant concentration ($x_{Gd} \leq 0.1$), no clear changes in E_G were observed [117]. For Gd_2O_3 doped ceria, Gd^{3+} has half-filed $4f^7$ orbital. Exciting an electron breaks the stabilization, and the excited electrons are more likely to be accommodated in the empty Ce $4f^0$ orbitals [147]. Therefore, the high Gd_2O_3 dopant concentration is considered to induce a narrow $4f^1$ band and decrease the value of E_G.

6.4.2 Auto-ionization thermal quenching model for CL emission

The CL bands were integrated versus Gd concentrations and primary electron energies, and they are shown in Figure 6-6 and Figure 6-8, respectively. The energy dependence will be discussed later. For the high energy electron irradiation, the CL emission dependence becomes clearer that shows a minimum for Ce^{3+} ion CL bands at x_{Gd} = 0.05, while F^+ center shows a maximum at x_{Gd} = 0.1. Beyond the x value, the CL emissions are observed to increase with the increase of the Gd dopant concentration for all electron energies. The quenching of CL bands

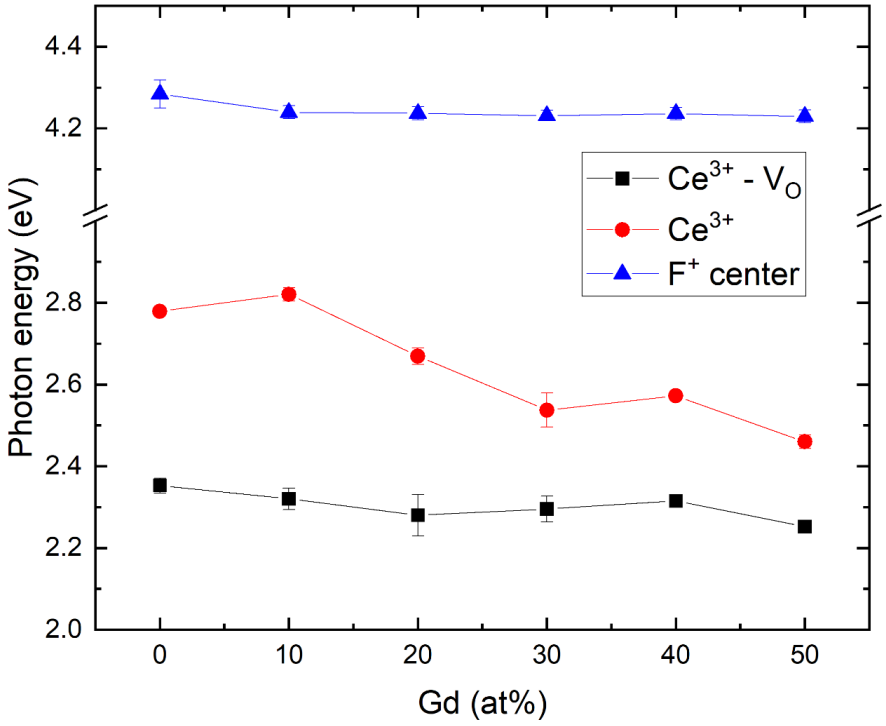

Figure 6-5. Photon energy for Ce^{3+} ions and F^{+} center in Gd_2O_3 doped ceria under high-energy electron irradiation versus Gd dopant atomic concentrations.

for Ce^{3+} ion at low Gd concentrations can be induced by the auto-ionization theory proposed by Dorenbos [148]. As an alternate explanation, a cross-over thermal quenching model has been suggested for 4*f*-5*d* system that induces non-radiative decay from the crossing point (X) between 4*f*-5*f* bands when the excited electron of 5*d* band overcomes the activation energy barrier (E_X) [149]. The CL emission and quenching model is described schematically in Figure 6-7. Figure 6-7(a) describes the luminescence emission for the case $E_X < E_R$, where E_R is an energy difference between the excited 5*d* level and the minimum 5*d* level. For the cross-over thermal quenching model, E_X should be smaller than 0.2 eV. However, it has been reported that ceria has a high value of $E_X > 1{,}5$ eV for Ce_{II} (i.e. Ce^{3+}-V_O) CL emission, which cannot induce CL emission due to the strong thermal quenching [87]. Thereby, auto-ionization theory has been suggested by Dorenbos for the thermal quenching of 4*f*-5*d* CL emission, whose schematic image is illustrated in Figure 6-7(c). 5*d* electron is transferred to the conduction band and becomes delocalized and mobile. Auto-ionization dissipates energy through other non-radiative mechanisms such as trapping or killer centers such as defects [150]. The increase of V_O concentration by Gd_2O_3 doping induces the 4*f*-5d thermal quenching by transferring electrons from V_O to Ce_{II} level, which results in the decrease in the recombination of e-h pairs.

In Figure 6-6, CL integrated intensities were growing versus Gd dopant concentration for $x_{Gd} > 0.05$. Let us consider the redox equilibrium equation. For electronic charge neutrality, the total oxygen vacancies concentration ($[V_O^{\cdot\cdot}]$) follows the equation below,

$$[V_O^{\cdot\cdot}] = \left[V_{O,int}^{\cdot\cdot}\right] + \left[V_{O,ext}^{\cdot\cdot}\right] = 1/4[Ce'_{Ce}] + 1/4[Gd'_{Ce}] \qquad (6\text{-}1)$$

However, $[V_O^{\cdot\cdot}]$ is mainly controlled by the Gd concentration for high dopant concentration [43]. The equation of (6-2) can be, therefore, rewritten as

$$[V_O^{\cdot\cdot}] = 1/2[Gd'_{Ce}]. \qquad (6\text{-}2)$$

Therefore, 4*f*-5*d* thermal quenching is reduced due to the rather low $V_O^{\cdot\cdot}$ creation comparing to Gd'_{Ce} creation for the high Gd_2O_3 concentration.

F^+ center CL emission in Gd_2O_3 doped ceria is indued by capturing electrons in a trimer as same as pure ceria. F^+ center CL emission is more likely to occur in a neutral cluster of $(Ce_{Ce}^{\times} - V_O^{\cdot\cdot} - Ce_{Ce}^{\times})^{\cdot\cdot}$ that includes no 3+ charged cations. However, for the high Gd_2O_3 concentration, $(Gd'_{Ce} - V_O^{\cdot\cdot} - Gd'_{Ce})^{\cdot\cdot}$ and $(Ce_{Ce}^{\times} - V_O^{\cdot\cdot} - Gd'_{Ce})^{\cdot\cdot}$ trimers are also growing together with $(Ce_{Ce}^{\times} - V_O^{\cdot\cdot} - Ce_{Ce}^{\times})^{\cdot\cdot}$. Despite of the increase of $[V_O]$ by Gd_2O_3 doping, F^+ center emission could have non-radiative decay or auto-ionization of the excited electron to 4*f* level.

6.4.3 Energy dependence of CL emission

The energy dependence of CL emission from the defects in pure ceria was discussed in Chapter 4. Electron energy dependence of I_{CL} results in a competitive process between the displacement cross-section (σ_d) with positive dependence against energy and the CL emission cross-section (σ_{CL}) with negative dependence [Eq. (4-1)]. For the Gd_2O_3 doped ceria samples, the I_{CL} for Ce^{3+} ions (i.e., $I_{CL,Ce-V_O}$ and $I_{CL.Ce}$) showed a maximum at ~800 keV. I_{CL} for F^+ center (i.e., $I_{CL,Fcenter}$) showed a maximum for $x_{Gd} \leq 0.1$, however, $I_{CL,Fcenter}$ gradually increased versus the energy for $x_{Gd} > 0.1$ (Figure 6-8). The competitive effect appeared strongly for the low Gd_2O_3 concentration samples, while the negative effects on the σ_{CL} was negligible for $I_{CL,Fcenter}$. The reduction of effect on σ_{CL} for low Gd_2O_3 concentration samples can be related to the thermal quenching due to the auto-ionization. Moreover, the CL spectra for the 20 keV electron irradiation (Figure 6-4) also showed a strong thermal quenching for the Ce^{3+} ion band since intrinsic oxygen vacancies are induced by the auto-ionization. However, the energy dependence in the doped samples is complex due to other parameters, such as strain

effect, and lattice size contraction, and it needs a more comprehensive theoretical or computational study to conclude the energy dependence equation.

For the summary, the schematic illustration of the energy band gap in Gd_2O_3 doped ceria can be suggested in Figure 6-9. The charge states of the defects in Gd_2O_3 doped ceria under electron irradiation were evaluated by using the *in-situ* HVEM-CL method compared to pure ceria. The charge states of cation defects and F^+ centers are highly close to that of pure ceria due to the similar point defect production mechanism with doped and non-doped samples. However, the rare-earth content Gd^{3+} was found to induce an energy shift in the CL spectrum due to the overlapping 4*f* orbitals in Gd^{3+} level. Also, high-dopant concentration samples showed strong 4*f*-5*d* CL thermal quenching by the auto-ionization due to the existence of oxygen vacancies.

6.5 Conclusions

In-situ HVEM-CL measurement technique was applied to yield charge state of point defects in polycrystalline Gd_2O_3 doped ceria ($Ce_{1-x}Gd_xO_{2-x/2}$) for a wide range of Gd dopant concentrations ($x_{Gd} = 0 \sim 0.5$). The CL spectra were obtained by 400 keV ~ 1250 keV electron irradiation in the HVEM, and 20 keV irradiation in the SEM. The CL bands appeared at 2.2 ~ 2.4 eV, 2.4 ~ 2.8 eV, and 4.3 eV were assigned to Ce^{3+}-V_O, Ce^{3+}, and F^+ center, respectively, which were qualitatively the same with pure ceria. The photon energy shift of Ce^{3+} ion band was induced by narrow $4f^1$ orbitals in the Gd^{3+} doped samples. Also, the high natural oxygen vacancy concentration in the doped samples derived thermal quenching of 4*f*-5*d* CL emission. The CL integrated intensities as function of primary electron energy is interpreted by the competitive interplay of displacement and CL emission cross-sections, but the energy

dependence for Ce^{3+} ions CL emission is much more affected by CL quenching effect than that of F^{+} center.

Table 6-3. Characteristics of electron irradiations of CeO_2 (mass density = 7.215 g cm^{-3}) and $Ce_{0.5}Gd_{0.5}O_{1.75}$ (mass density = 7.35 g cm^{-3}) computed with the ESTAR code [77] for different primary electron energies (E) and mean ionization energy I = 407.6 eV: CSDA range, and total inelastic stopping power ($(-dE/dx)_{inel}$).

E (keV)	20	400	600	800	1000	1250
CeO_2						
Range (μm)	2.1	265	460	663	869	1126
$(-dE/dx)_{inel}$ (MeV μm^{-1})	57×10^{-4}	11×10^{-4}	10×10^{-4}	9.8×10^{-4}	9.7×10^{-4}	9.7×10^{-4}
$Ce_{0.5}Gd_{0.5}O_{1.75}$						
Range (μm)	2.1	262	454	655	859	1113
$(-dE/dx)_{inel}$ (MeV μm^{-1})	57×10^{-4}	11×10^{-4}	10×10^{-4}	9.9×10^{-4}	9.8×10^{-4}	9.8×10^{-4}

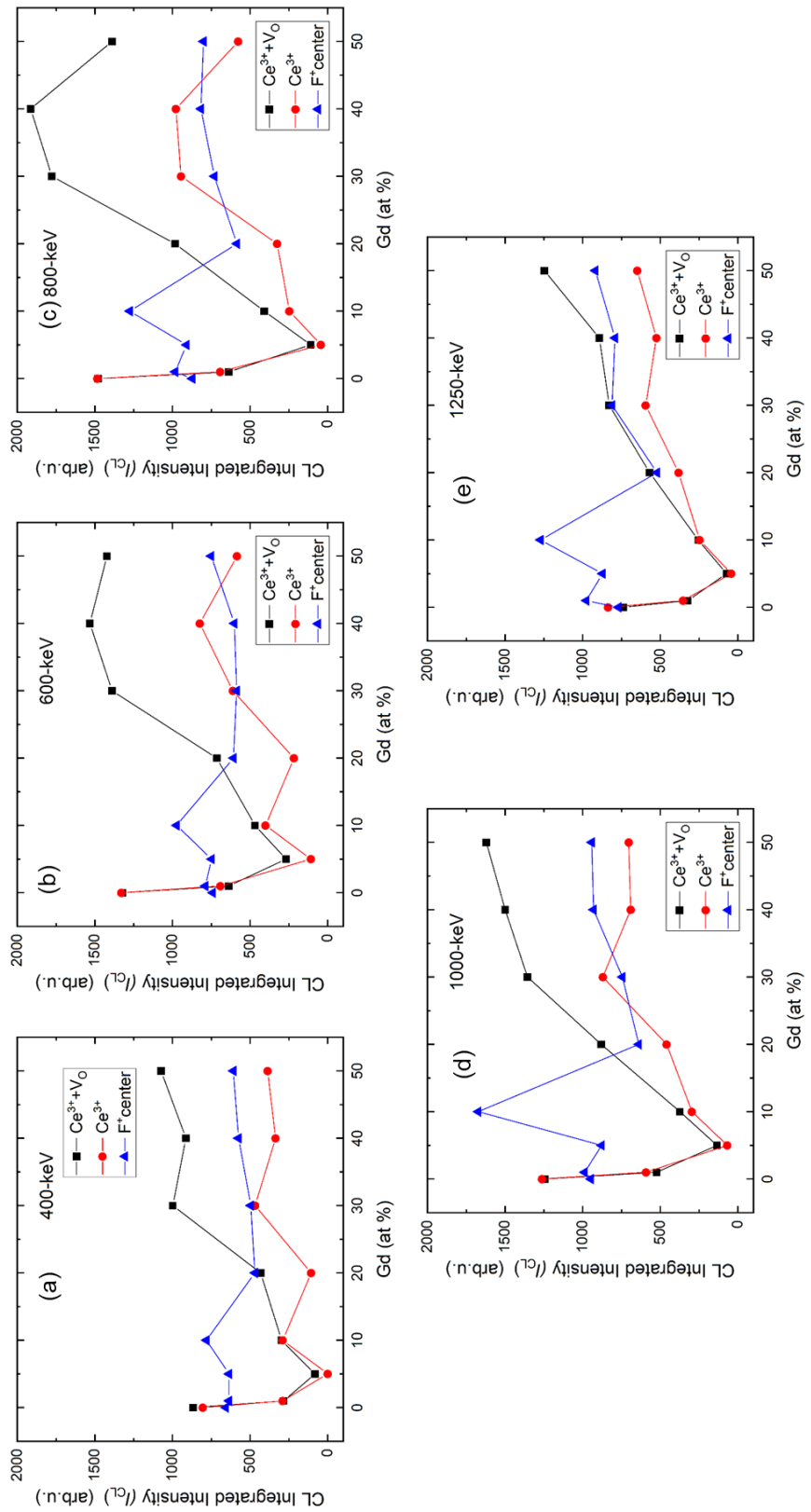

Figure 6-6. Gd dopant dependence versus integrated CL intensity in polycrystalline ceria and Gd_2O_3 doped ceria ($Ce_{1-x}Gd_xO_{2-x/2}$) for 400 keV ~ 1250 keV electron irradiation at 300 K.

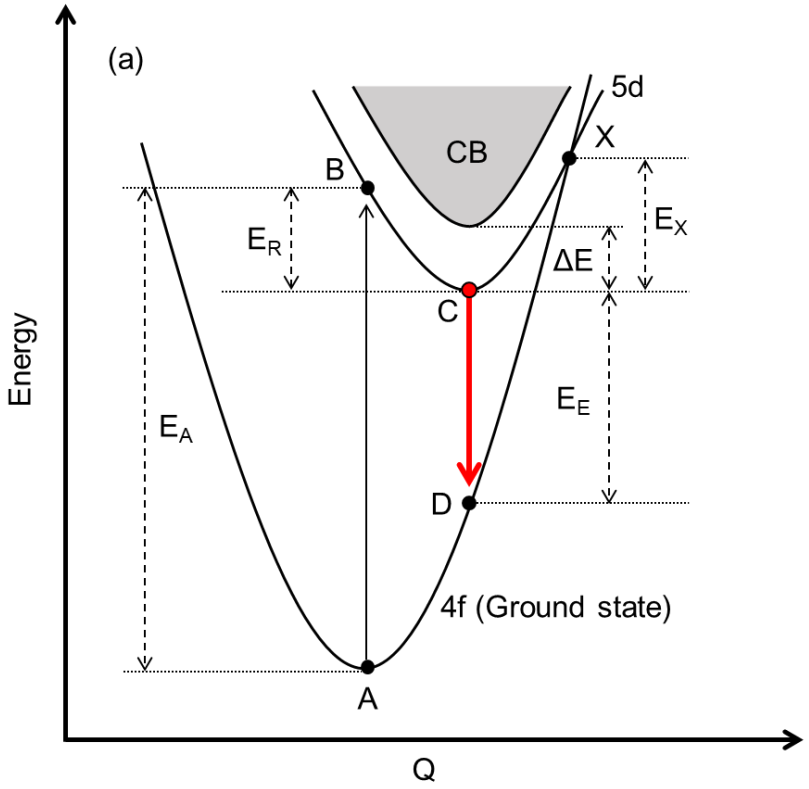
(a)
5d
CB
X
B
E_X
E_R
ΔE
C
Energy
E_E
E_A
D
4f (Ground state)
A
Q

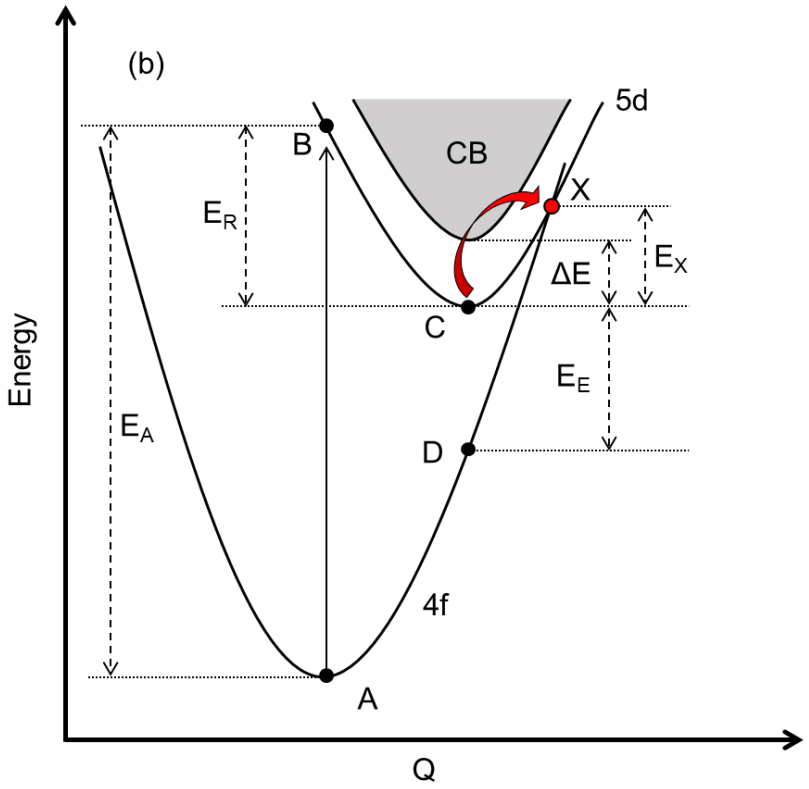
(b)
5d
B
CB
X
E_R
E_X
ΔE
C
Energy
E_E
E_A
D
4f
A
Q

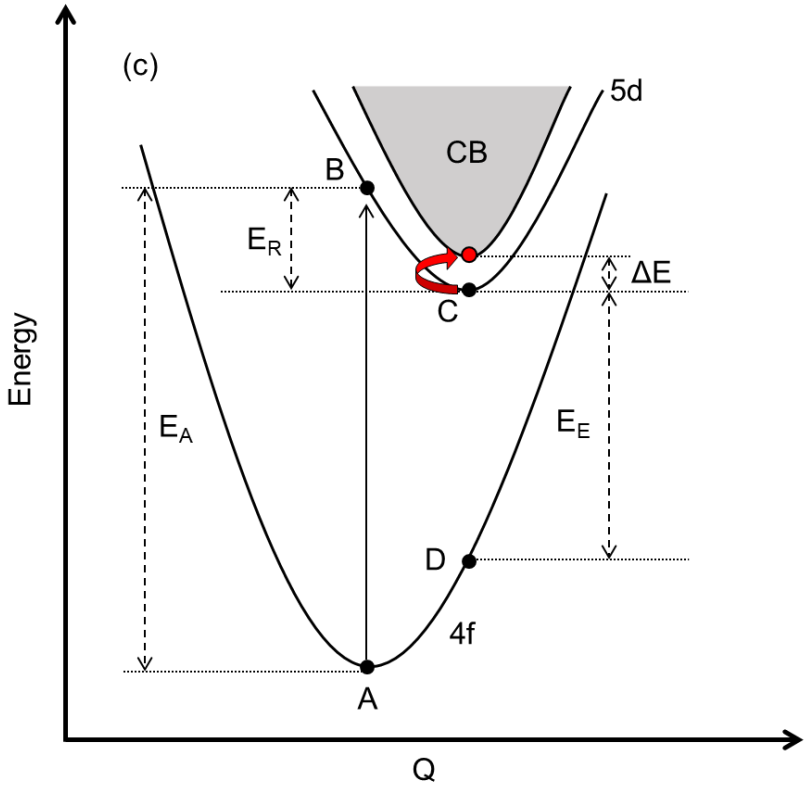

Figure 6-7. (a) The 4*f*-5*d* luminescence emission process for $E_x > E_R$ and comparison of thermal quenching models; (b) cross-over model ($E_x < E_R$) [149], (c) Dorenbos auto-ionization model [148].

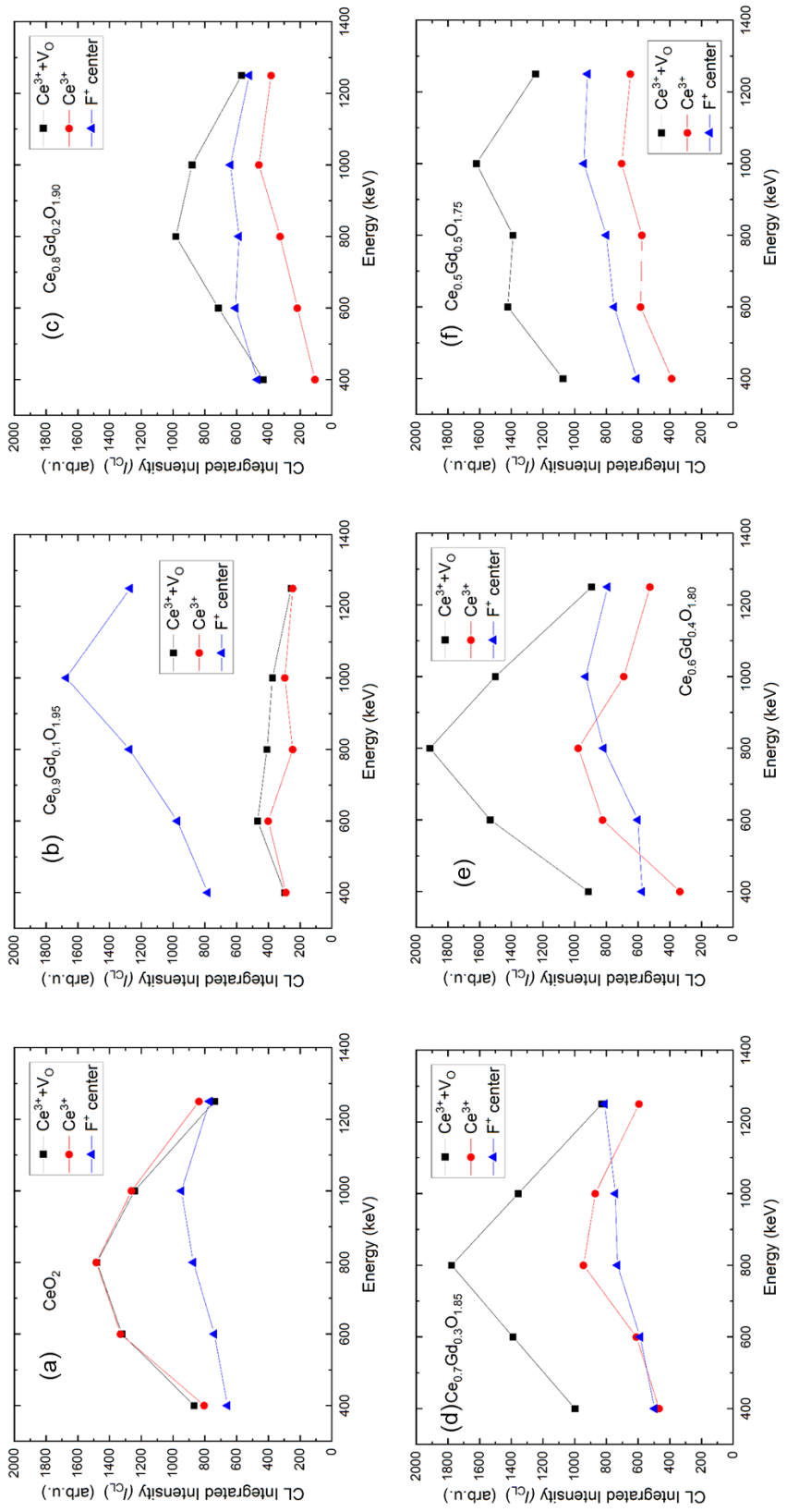

Figure 6-8. Energy dependence versus integrated CL intensity in polycrystalline ceria and Gd_2O_3 doped ceria ($Ce_{1-x}Gd_xO_{2-x/2}$) for $0.1 \leq x_{Gd} \leq 0.5$ at 300 K.

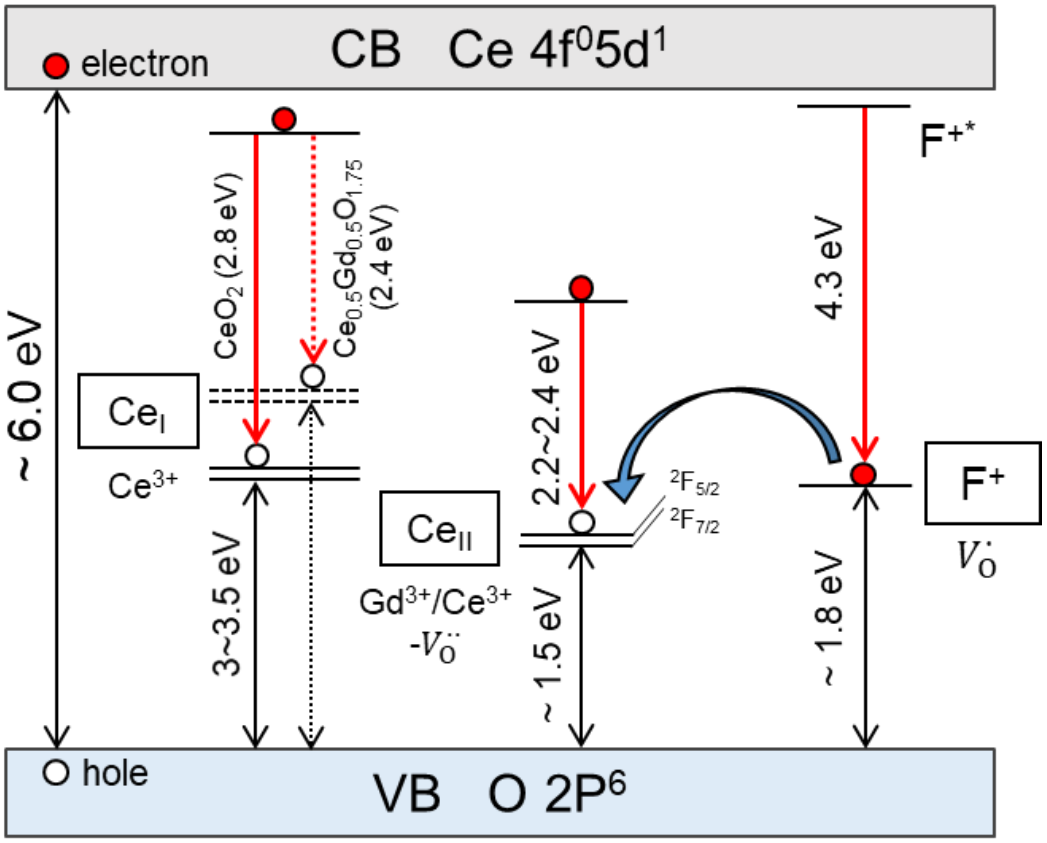

Figure 6-9. Sketch of electronic levels in the band gap of Gd_2O_3 doped ceria possessing oxygen vacancies.

Chapter 7

Concluding Remarks

7.1 General conclusions

CeO_2 or ceria is a considerable ceramic oxide as a surrogate and transmutation target for a nuclear reactor that has a radiation-resistant fluorite structure. Nuclear fuels, such as UO_2 are used to dope with Gd_2O_3, which is a burnable poison with a high thermal neutron absorption cross-section. Ceramic oxides have radiation damage by exposure to not only heavy ions but also electrons in the reactors. Therefore, understanding radiation response and damage production by ion/electron irradiation in the fuel materials is important for the safe use of the nuclear reactor. Information on the in-beam damage production is of importance since the defects are mobile during irradiation and the charge states of the defects are remarkable for the damage recovery kinetics. Moreover, the structural stability of the oxides as fuel materials is influenced by rare-earth doping and irradiation.

In this dissertation, the radiation-induced point defects and structural evaluation were investigated in ceria and Gd_2O_3 doped ceria. Point defects were produced by electronic excitation using the HVEM, and their charge state was interpreted by using *in-situ* CL spectroscopy. CL spectroscopy is a powerful technique to detect point scale defects, and the HVEM can produce oxygen point defects by accelerating voltages over the threshold displacement energy of oxygen atoms. In Chapter 4, the total displacement cross-section in ceria was calculated by using the SMOTT/POLY computer code [74] and CSDA range, and total inelastic stopping power ($(-dE/dx)_{inel}$) was computed with the ESTAR code [77] for different primary electron energies (E). CL spectra were obtained from pure ceria by electrons irradiation energy ranging from 400 keV to 1250 keV at the temperatures of 100 K, 200 K, and

300 K. Complementary CL spectra were measured as well as for 20 keV electrons at 300 K in the SEM. This chapter gave information on the charge state and electronic configurations of ceria under high-energy electron irradiation, and the CL emission from defects was evaluated depending on energy and temperatures.

In Chapter 5, ceria and Gd_2O_3 doped ceria ($Ce_{1-x}Gd_xO_{2-x/2}$) samples were studied to evaluate the microstructure evolution by Gd_2O_3 doping and heavy ion irradiation. The microstructure of virgin $Ce_{1-x}Gd_xO_{2-x/2}$ samples was investigated for a wide range of Gd concentrations ($0 \leq x_{Gd} \leq 0.5$) through comprehensive structural analysis of XRD, micro-Raman spectroscopy, and TEM. Thereafter, the samples were irradiated by 200 MeV Xe^{14+} ion at room temperature. The radiation damage and response, such as lattice parameter and phase changes in the samples were examined regarding the dopant concentration and irradiation conditions.

Finally, the *in-situ* HVEM-CL measurement technique was applied to yield information from point defects in $Ce_{1-x}Gd_xO_{2-x/2}$ under electron irradiation for a wide range of Gd dopant concentrations ($x_{Gd} = 0 \sim 0.5$). The CL spectra were obtained by 400 keV ~ 1250 keV electron irradiation in the HVEM, and 20 keV irradiation in the SEM. The CL spectra and charge states of point defects in $Ce_{1-x}Gd_xO_{2-x/2}$ were compared with pure ceria as interpreted in Chapter 4.

Based on the *in-situ* HVEM-CL analysis and microstructure evaluation experiment in virgin and swift heavy-ion (200 MeV Xe) irradiated Gd_2O_3 doped ceria, the contributions of this dissertation are summarized below the followings:

- The prominent CL emission centered at 4.2 eV was assigned to F^+ centers which were induced by elastic electron-nucleus collisions over a threshold electron energy (> 200 keV) equivalent to the oxygen displacement energy.
- CL bands centered at 2.3 ~ 2.6 eV and 2.8 ~ 3.0 eV were measured for all electron energies

(> 20 keV) which were induced by the charge compensation of oxygen vacancies for the high-energy (400 keV ~ 1250 keV) electrons and ionization effects for the low-energy (20 keV) electron excitation with a larger inelastic stopping power are attributed to the lower energy CL bands, respectively.

- At low temperatures (100 K and 200 K), similar CL spectra were obtained, but with larger and slightly shifted emission bands. Regardless of temperature, the effects of grain boundaries cause the F^+ center CL signal for the polycrystalline sample to be weaker than the single crystal under identical circumstances.

- The interaction between the oxygen displacement cross-section and the luminescence cross-section is used to explain the dependency of CL integrated intensities as a function of primary electron energy for both types of targets.

- The lattice parameter increased with the increase of Gd concentration and the simultaneous creation of charge-compensation oxygen vacancies. The lattice parameter was saturated at $x_{Gd} > 0.3$ due to the formation of the C-type structure in the F-type matrix.

- The reduction in the F-type symmetry with the formation of the C-type structure associated with ordered oxygen vacancies was observed at $x_{Gd} \geq 0.2$ consistently from the experimental techniques used in the present study.

- The XRD and TEM results showed that all the compositions of $Ce_{1-x}Gd_xO_{2-x/2}$ samples were resistant to amorphization and sustained the F-type structure with 200 MeV Xe ion irradiation. In the XRD patterns, asymmetrical peaks (Damage-$K\alpha_1$) were observed on the shoulders of F-type peaks ($K\alpha_1$), and the asymmetry was decreased with the increase of Gd concentration. The asymmetric peaks are caused by the lattice distortion in the F-type structure due to the formation of damaged regions induced by ion tracks.

- The C-type structure has disappeared with ion irradiation because of the loss of the ordered oxygen vacancy structure in the C-type domain.
- Analysis of the radiation-induced recovery by XRD patterns with ion irradiation showed track radii, or recovery radii decreases with the Gd concentration. Besides, the XRD analysis showed rapid recovery of radiation damage for values of x_{Gd} = 0.2 ~ 0.3, suggesting an important role of oxygen vacancy ordering in the C-type structure for the recovery process in Gd_2O_3 doped CeO_2.
- The CL bands appeared at 2.2 ~ 2.4 eV, 2.4 ~ 2.8 eV, and 4.3 eV, and they were assigned to Ce^{3+}-V_O, Ce^{3+}, and F^+ center, respectively, as well as pure ceria.
- The photon energy shift of the Ce^{3+} ion was induced by narrow $4f^1$ orbitals in the Gd^{3+} doped samples. Also, the high natural oxygen vacancy concentration in the doped samples derived thermal quenching of 4*f*-5*d* CL emission.
- The CL integrated intensities as function of primary electron energy were interpreted by the competitive interplay of displacement and CL emission cross-sections, but the energy dependence for Ce^{3+} ions CL emission is much more affected by CL quenching effect than that of F^+ center.

7.2 Directions for future research

Fluorite structure ceramics such as ceria and YSZ is remarkable materials for radiation-resistant materials, and study on their stability under irradiation is of importance for the long-term use of nuclear reactor. According to this dissertation, the *in-situ* HVEM-CL methods were developed to investigate the charge state of point defects. However, the reactor condition is not only exposure to electrons but also heavy ions at the same time. Recently, a synergetic effect of electron (S_e) and nuclear (S_n) stopping power is attracted for radiation recovery system in

the fluorite oxides. To understand the kinetics of the recovery system, the *in-situ* HVEM-CL technique was conducted with the ion irradiated oxides.

The CL emission obtained from the specimen is strongly dependent on parameters such as energy, temperature, beam flux, and quenching effects. Understanding the relationship between the CL intensity and these parameters, computational investigation and the other optical experimental system, such as photoluminescence should be followed together. In particular, the quenching effect on luminescence is much more complex due to a lot of ways to lose energy through transferring carriers, luminescence killer centers, or non-radiative decays. Thereby, more systematic experimental and theoretical calculations should be followed to understand CL emission from the defects.

Also, the RE-doped oxides showed structure evolution by RE doping and radiation. However, there are several methods to synthesize the RE-dopes oxides and characterization techniques of microstructure, which show different results despite of same composition samples. Therefore, more wide characterization techniques and dopant concentrations should be conducted for the structure evaluation experimental.

Moreover, radiation damage recoveries were confirmed at the high concentration of RE-doped oxides with the changes in phase and structure. The nano-domains and ordered oxygen vacancies induced by RE doping act as key properties for the recovery. These properties are on the nanoscale and their production and annihilation should be followed by high-resolution TEM methods such as STEM analysis to understand accurate radiation recovery phenomena. The strain/stress changes by RE-doping or irradiation in the domain boundaries are also noticeable properties to understand radiation response.

References

[1] S.F. Mughabghab, THERMAL NEUTRON CAPTURE CROSS SECTIONS RESONANCE INTEGRALS AND G-FACTORS I N D C INTERNATIONAL NUCLEAR DATA COMMITTEE, Vienna, 2003.

[2] S.J. Zinkle, Radiation-induced effects on microstructure, 1st ed., Elsevier Inc., 2012. https://doi.org/10.1016/B978-0-08-056033-5.00003-3.

[3] S.J. Zinkle, Microstructure of ion irradiated ceramic insulators, Nucl. Instrum. Methods B. 91 (1994) 234–246. https://doi.org/10.1016/0168-583X(94)96224-3.

[4] K. Yasuda, C. Kinoshita, R. Morisaki, H. Abe, Role of irradiation spectrum in the microstructural evolution of magnesium aluminate spinel, Philos. Mag. A Phys. Condens. Matter, Struct. Defects Mech. Prop. 78 (1998) 583–598. https://doi.org/10.1080/01418619808241924.

[5] K. Yasuda, C. Kinoshita, M. Ohmura, H. Abe, Production and stability of dislocation loops in an MgO-Al2O3 system under concurrent irradiation with ions and electrons, Nucl. Instrum. Methods Phys. Res. Sect. B. 166 (2000) 107–114. https://doi.org/10.1016/S0168-583X(99)00738-7.

[6] T. Sonoda, M. Kinoshita, Y. Chimi, N. Ishikawa, M. Sataka, A. Iwase, Electronic excitation effects in CeO2 under irradiations with high-energy ions of typical fission products, Nucl. Instrum. Methods Phys. Res. Sect. B. 250 (2006) 254–258. https://doi.org/10.1016/J.NIMB.2006.04.120.

[7] J.M. Costantini, F. Beuneu, Threshold displacement energy in yttria-stabilized zirconia, Phys. Status Solidi Curr. Top. Solid State Phys. 4 (2007) 1258–1263. https://doi.org/10.1002/pssc.200673752.

[8] K. Yasunaga, K. Yasuda, S. Matsumura, T. Sonoda, Nucleation and growth of defect clusters in CeO2 irradiated with electrons, Nucl. Instrum. Methods Phys. Res. Sect. B. 250 (2006) 114–118. https://doi.org/10.1016/J.NIMB.2006.04.091.

[9] K. Yasunaga, K. Yasuda, S. Matsumura, T. Sonoda, Electron energy-dependent formation of dislocation loops in CeO2, Nucl. Instrum. Methods Phys. Res. Sect. B. 266 (2008) 2877–2881. https://doi.org/10.1016/j.nimb.2008.03.204.

[10] K. Yasuda, J.-M. Costantini, G. Baldinozzi, Radiation-Induced Effects on Materials Properties of Ceramics: Mechanical and Dimensional Properties, in: Compr. Nucl.

Mater. Second Ed., 2nd ed., 2020: pp. 153–185. https://doi.org/10.1016/B978-0-12-803581-8.12052-1.

[11] S.J. Zinkle, C. Kinoshita, Defect production in ceramics, J. Nucl. Mater. 251 (1997) 200–217. https://doi.org/10.1016/S0022-3115(97)00224-9.

[12] D. Simeone, J.M. Costantini, L. Luneville, L. Desgranges, P. Trocellier, P. Garcia, Characterization of radiation damage in ceramics: Old challenge new issues?, J. Mater. Res. 30 (2015) 1495–1515. https://doi.org/10.1557/jmr.2015.77.

[13] E.A. Kotomin, A.I. Popov, Radiation-induced point defects in simple oxides, Nucl. Instrum. Methods Phys. Res. Sect. B. 141 (1998) 1–15. https://doi.org/10.1016/S0168-583X(98)00079-2.

[14] W. Hayes, A.M. Stoneham, Defects and Defect Processes in Nonmetallic Solids, Courier Corporation, 2012.

[15] F. Agulló-López, C.R.A. Catlow, P.D. Townsend, Point defects in materials, Academic press, 1988.

[16] J.M. Costantini, F. Beuneu, M. Fasoli, A. Galli, A. Vedda, M. Martini, Thermo-stimulated luminescence of ion-irradiated yttria-stabilized zirconia, J. Phys. Condens. Matter. 23 (2011). https://doi.org/10.1088/0953-8984/23/11/115901.

[17] V. Pagonis, M.L. Chithambo, R. Chen, A. Chruścińska, M. Fasoli, S.H. Li, M. Martini, K. Ramseyer, Thermal dependence of luminescence lifetimes and radioluminescence in quartz, J. Lumin. 145 (2014) 38–48. https://doi.org/10.1016/j.jlumin.2013.07.022.

[18] T. Yanagida, K. Kamada, Y. Fujimoto, H. Yagi, T. Yanagitani, Comparative study of ceramic and single crystal Ce:GAGG scintillator, Opt. Mater. (Amst). 35 (2013) 2480–2485. https://doi.org/10.1016/J.OPTMAT.2013.07.002.

[19] E. Goldstein, Arbeiten der wissenschaftlichen Gäste der Abtheilung I. Professor Goldstein's Untersuchungen über Kathodenstrahlen, Zeits. f. Instrumentenk. 16 (1896).

[20] L.A. Kappers, R.L. Kroes, E.B. Hensley, F+ and F′ centers in magnesium oxide, Phys. Rev. B. 1 (1970) 4151–4157. https://doi.org/10.1103/PhysRevB.1.4151.

[21] K. H. Lee, J. J. H. Crawford, Electron centers in single-crystal Al2O3, Phys. Rev. B. 15 (1977) 4065–4070. http://prb.aps.org/abstract/PRB/v15/i8/p4065_1.

[22] D.M. Hofmann, D. Pfisterer, J. Sann, B.K. Meyer, R. Tena-Zaera, V. Munoz-Sanjose, T. Frank, G. Pensl, Properties of the oxygen vacancy in ZnO, Appl. Phys. A Mater. Sci. Process. 88 (2007) 147–151. https://doi.org/10.1007/s00339-007-3956-2.

[23] N. Serpone, Is the band gap of pristine TiO2 narrowed by anion- and cation-doping of titanium dioxide in second-generation photocatalysts?, J. Phys. Chem. B. 110 (2006) 24287–24293. https://doi.org/10.1021/jp065659r.

[24] K. Furumoto, T. Tanabe, N. Yamamoto, T. Daio, S. Matsumura, K. Yasuda, Development of Novel Optical Fiber System for Cathodoluminescence Detection in High Voltage Transmission Electron Microscope, Mater. Trans. 54 (2013) 854–856.

[25] J.M. Costantini, Y. Watanabe, K. Yasuda, M. Fasoli, Cathodo-luminescence of color centers induced in sapphire and yttria-stabilized zirconia by high-energy electrons, J. Appl. Phys. 121 (2017) 153101. https://doi.org/10.1063/1.4980111.

[26] K. Yasuda, C. Kinoshita, S. Matsumura, Effects of Simultaneous Displacive and Ionizing Radiation in Ionic and Covalent Crystals, Defect Diffus. Forum. 206–207 (2002) 53–74. https://doi.org/10.4028/www.scientific.net/DDF.206-207.53.

[27] W.J. Weber, E. Zarkadoula, O.H. Pakarinen, R. Sachan, M.F. Chisholm, P. Liu, H. Xue, K. Jin, Y. Zhang, Synergy of elastic and inelastic energy loss on ion track formation in SrTiO3, Sci. Rep. 5 (2015) 1–6. https://doi.org/10.1038/srep07726.

[28] P.G. Klemens, Phonon scattering by oxygen vacancies in ceramics, Phys. B Condens. Matter. 263–264 (1999) 102–104. https://doi.org/10.1016/S0921-4526(98)01202-2.

[29] R.J. Tilley, Crystal Structure, 2006.

[30] C.R. Barrett, W.D. Nix, W.D. Nix, A.S. Tetelman, The principles of engineering materials, Prentice hall, 1973.

[31] R.W. Grimshaw, A.B. Searle, The chemistry and physics of clays and allied ceramic materials, 1971.

[32] C.B. Carter, M.G. Norton, Ceramic materials: science and engineering, Springer, 2007.

[33] N. Nitani, K. Kuramoto, T. Yamashita, Y. Nihei, Y. Kimura, In-pile irradiation of rock-like oxide fuels, J. Nucl. Mater. 319 (2003) 102–107. https://doi.org/10.1016/S0022-3115(03)00140-5.

[34] Z. Crnjak, B. Orel, Optical Properties of Pure CeO2 and Mixed CeO2/SnO2 Thin Film Coatings, Phys. Stat. Sol. 186 (1994) 33–36. https://doi.org/10.1002/pssb.2221860135.

[35] F. Marabelli, P. Wachter, Covalent insulator CeO2: Optical reflectivity measurements, Phys. Rev. B. 36 (1987) 1238–1243. https://doi.org/10.1103/PhysRevB.36.1238.

[36] P.J. Hay, R.L. Martin, J. Uddin, G.E. Scuseria, Theoretical study of CeO2 and Ce 2O3 using a screened hybrid density functional, J. Chem. Phys. 125 (2006). https://doi.org/10.1063/1.2206184.

[37] L. Eyring, The Binary Lanthanide Oxides: Synthesis and Identification, in: G. Meyer, L.R. Morss (Eds.), Synth. Lanthan. Actin. Compd. Top. f-Element Chem. Vol 2., Springer, Dordrecht, 1991: pp. 187–224. https://doi.org/10.1007/978-94-011-3758-4_8.

[38] P.N. Hazin, J.W. Bruno, H.G. Brittain, Luminescence Spectra of a Series of Cerium(III) Halides and Organometallics: Probes of Bonding Properties Using 4f-5d Excited States, Organometallics. 6 (1987) 913–918. https://doi.org/10.1021/om00148a002.

[39] R.D. Shannon, Application of the Periodic Bond Chain (PBC) Theory and Attachment Energy Consideration to Derive the Crystal Morphology of Hexamethylmelamine, Acta Crystallogr. Sect. A. 32 (1976) 751–767. https://doi.org/10.1023/A:1018927109487.

[40] M. Nakayama, M. Martin, First-principles study on defect chemistry and migration of oxide ions in ceria doped with rare-earth cations, Phys. Chem. Chem. Phys. 11 (2009) 3241–3249. https://doi.org/10.1039/B900162J.

[41] M. Mogensen, D. Lybye, N. Bonanos, P. V. Hendriksen, F.W. Poulsen, Factors controlling the oxide ion conductivity of fluorite and perovskite structured oxides, Solid State Ionics. 174 (2004) 279–286. https://doi.org/10.1016/j.ssi.2004.07.036.

[42] M. Coduri, S. Checchia, M. Longhi, D. Ceresoli, M. Scavini, Rare earth doped ceria: The complex connection between structure and properties, Front. Chem. 6 (2018) 1–23. https://doi.org/10.3389/fchem.2018.00526.

[43] R. Schmitt, A. Nenning, O. Kraynis, R. Korobko, A.I. Frenkel, I. Lubomirsky, S.M. Haile, J.L.M. Rupp, A review of defect structure and chemistry in ceria and its solid solutions, Chem. Soc. Rev. 49 (2020) 554–592. https://doi.org/10.1039/c9cs00588a.

[44] G.Y. Adachi, N. Imanaka, The binary rare earth oxides, Chem. Rev. 98 (1998) 1479–1514. https://doi.org/10.1021/cr940055h.

[45] P.A. Žguns, A. V. Ruban, N. V. Skorodumova, Phase diagram and oxygen–vacancy ordering in the CeO2 –Gd2O3 system: a theoretical study, Phys. Chem. Chem. Phys. 20 (2018) 11805–11818. https://doi.org/10.1039/C8CP01029C.

[46] G. Brauer, H. Gradinger, Über heterotype Mischphasen bei Seltenerdoxyden. I, Zeitschrift Für Anorg. Und Allg. Chemie. 276 (1954) 209–226. https://doi.org/10.1002/ZAAC.19542760502.

[47] T. Nakagawa, T. Osuki, T.A. Yamamoto, Y. Kitauji, M. Kano, M. Katsura, S. Emura, Study on local structure around Ce and Gd atoms in CeO2-Gd2O3 binary system, J. Synchrotron Radiat. 8 (2001) 740–742. https://doi.org/10.1107/S0909049500018148.

[48] Y. Ikuma, K. Takao, M. Kamiya, E. Shimada, X-ray study of cerium oxide doped with gadolinium oxide fired at low temperatures, in: Mater. Sci. Eng. B Solid-State Mater. Adv. Technol., Elsevier, 2003: pp. 48–51. https://doi.org/10.1016/S0921-5107(02)00546-9.

[49] D.J.M. Bevan, J. Kordis, Mixed oxides of the type MO2 (fluorite)-M2O3-I oxygen dissociation pressures and phase relationships in the system CeO2-Ce2O3 at high temperatures, J. Inorg. Nucl. Chem. 26 (1964) 1509–1523. https://doi.org/10.1016/0022-1902(64)80038-5.

[50] D.R. Ou, T. Mori, F. Ye, T. Kobayashi, J. Zou, G. Auchterlonie, J. Drennan, Oxygen vacancy ordering in heavily rare-earth-doped ceria, Appl. Phys. Lett. 89 (2006) 87–90. https://doi.org/10.1063/1.2369881.

[51] F. Ye, T. Mori, D.R. Ou, J. Zou, J. Drennan, A structure model of nano-sized domain in Gd-doped ceria, Solid State Ionics. 180 (2009) 1414–1420. https://doi.org/10.1016/j.ssi.2009.08.013.

[52] D.Y. Wang, D.S. Park, J. Griffith, A.S. Nowick, Oxygen-ion conductivity and defect interactions in yttria-doped ceria, Solid State Ionics. 2 (1981) 95–105. https://doi.org/10.1016/0167-2738(81)90005-9.

[53] H. Inaba, H. Tagawa, Ceria-based solid electrolytes, Solid State Ionics. 83 (1996) 1–16. https://doi.org/10.1016/0167-2738(95)00229-4.

[54] J.A. Purton, N.L. Allan, D.S.D. Gunn, Simulations of doped CeO2 at finite dopant concentrations, Solid State Ionics. 299 (2017) 32–37. https://doi.org/10.1016/J.SSI.2016.09.017.

[55] H.M. Rietveld, IUCr, A profile refinement method for nuclear and magnetic structures, Urn:Issn:0021-8898. 2 (1969) 65–71. https://doi.org/10.1107/S0021889869006558.

[56] J. Rodríguez-Carvajal, Recent advances in magnetic structure determination by neutron powder diffraction, Phys. B Phys. Condens. Matter. 192 (1993) 55–69. https://doi.org/10.1016/0921-4526(93)90108-I.

[57] A.C. Larson, R.B. Von Dreele, GSAS, 1994.

[58] F. Izumi, T. Ikeda, A Rietveld-Analysis Programm RIETAN-98 and its Applications to Zeolites, Mater. Sci. Forum. 321–324 (2000) 198–205. https://doi.org/10.4028/WWW.SCIENTIFIC.NET/MSF.321-324.198.

[59] ICSD, (n.d.). https://icsd.products.fiz-karlsruhe.de/ (accessed December 5, 2022).
[60] American Mineralogist Crystal Structure Database, (n.d.). http://rruff.geo.arizona.edu/AMS/amcsd.php (accessed December 5, 2022).
[61] Crystallography Open Database, (n.d.). http://www.crystallography.net/cod/ (accessed December 5, 2022).
[62] R.A. Young, The Rietveld Method IUCr: Oxford, Cambridge University Press, 1993.
[63] H.Y. Xiao, Y. Zhang, W.J. Weber, Ab initio molecular dynamics simulations of low-energy recoil events in ThO2, CeO2, and ZrO2, Phys. Rev. B - Condens. Matter Mater. Phys. 86 (2012) 054109. https://doi.org/10.1103/PhysRevB.86.054109.
[64] B.T. Kelly, Physics of Graphite, Applied Science, London, 1981.
[65] J. Wiiliam A. McKinley, H. Feshbach, The Coulomb Scattering of Relativistic Electrons by Nuclei, Phys. Rev. 74 (1948) 1759–1763.
[66] F. Esch, S. Fabris, L. Zhou, T. Montini, C. Africh, P. Fornasiero, G. Comelli, R. Rosei, Electron Localization Determines Defect Formation on Ceria Substrates, Science (80-.). 309 (2005) 752–755. https://doi.org/10.1126/science.1111568.
[67] N. V Skorodumova, S.I. Simak, B.I. Lundqvist, I.A. Abrikosov, B. Johansson, Quantum Origin of the Oxygen Storage Capability of Ceria, (2002) 14–17. https://doi.org/10.1103/PhysRevLett.89.166601.
[68] P. Jonnard, C. Bonnelle, G. Blaise, G. Rémond, C. Roques-Carmes, F+ and F centers in α-Al2O3 by electron-induced x-ray emission spectroscopy and cathodoluminescence, J. Appl. Phys. 88 (2000) 6413–6417. https://doi.org/10.1063/1.1324697.
[69] S. Aškrabić, Z.D. Dohčević-Mitrović, V.D. Araújo, G. Ionita, M.M. De Lima, A. Cantarero, F-centre luminescence in nanocrystalline CeO2, J. Phys. D. Appl. Phys. 46 (2013). https://doi.org/10.1088/0022-3727/46/49/495306.
[70] J.-M. Costantini, T. Ogawa, A.S.I. Bhuian, K. Yasuda, Cathodoluminescence induced in oxides by high-energy electrons: Effects of beam flux, electron energy, and temperature, J. Lumin. 208 (2019) 108–118. https://doi.org/10.1016/j.jlumin.2018.12.045.
[71] J.F. Ziegler, J.P. Biersack, The Stopping and Range of Ions in Matter, Treatise Heavy-Ion Sci. (1985) 93–129. https://doi.org/10.1007/978-1-4615-8103-1_3.
[72] A.Y. Konobeyev, U. Fischer, Y.A. Korovin, S.P. Simakov, Evaluation of effective threshold displacement energies and other data required for the calculation of

advanced atomic displacement cross-sections, Nucl. Energy Technol. 3 (2017) 169–175. https://doi.org/10.1016/j.nucet.2017.08.007.

[73] B.L. Henke, E.M. Gullikson, J.C. Davis, X-Ray Interactions: Photoabsorption, Scattering, Transmission, and Reflection at E = 50-30,000 eV, Z = 1-92, At. Data Nucl. Data Tables. 54 (1993) 181–342. https://doi.org/10.1006/ADND.1993.1013.

[74] P.D. Lesueur, Cascades de déplacement dam les solides polyatomiques, Philos. Mag. A Phys. Condens. Matter, Struct. Defects Mech. Prop. 44 (1981) 905–929. https://doi.org/10.1080/01418618108239557.

[75] M. Yamaga, P.I. Macfarlane, B. Henderson, K. Holliday, H. Takeuchi, T. Yosida, M. Fukui, Substitutional disorder and the ground state spectroscopy of gallogermanate crystals, J. Phys. Condens. Matter. 9 (1997) 569–578. https://doi.org/10.1088/0953-8984/9/2/024.

[76] M. Ghamnia, C. Jardin, M. Bouslama, Luminescent centres F and F+ in α-alumina detected by cathodoluminescence technique, J. Electron Spectros. Relat. Phenomena. 133 (2003) 55–63. https://doi.org/10.1016/j.elspec.2003.08.003.

[77] ICRU Report 37, Stopping Powers for Electrons and Positrons, 1984. http://physics.nist.gov/ PhysRefData/Star/Text/ESTAR.html.

[78] B.. G. Yacobi, D.. B. Holt, Cathodoluminescence scanning electron microscopy of semiconductors, J. Appl. Phys. 59 (1986). https://doi.org/10.1063/1.336491.

[79] V.I. Petrov, Cathodoluminescence microscopy, Physics-Uspekhi. 39 (1996) 807–818. https://doi.org/10.1070/PU1996v039n08ABEH000162.

[80] E. Wuilloud, B. Delley, W.-D. Schneider, Y. Baer, Spectroscopic Evidence for Localized and Extended f-Symmetry States in CeO2, Phys. Rev. Lett. 53 (1984) 202–205. https://doi.org/10.1103/PhysRevLett.53.202.

[81] E. Wuilloud, B. Delley, W.-D. Schneider, Y. Baer, SPECTROSCOPIC STUDY OF LOCALIZED AND EXTENDED f-SYMMETRY STATES IN CeO2, CeN AND CeSi2, J. Magn. Magn. Mater. 47–48 (1985) 197–199.

[82] P.O. Maksimchuk, V. V. Seminko, I.I. Bespalova, A.A. Masalov, Influence of CeO2 nanocrystals size on the vacancies formation processes determinded by spectroscopic techniques, Funct. Mater. 21 (2014) 254–259.

[83] V. Pankratov, L. Grigorjeva, D. Millers, T. Chudoba, R. Fedyk, W. Łojkowski, Time-Resolved Luminescence Characteristics of Cerium Doped YAG Nanocrystals, Solid State Phenom. 128 (2007) 173–178. https://doi.org/10.4028/www.scientific.net/ssp.128.173.

[84] B.A. Danja, A Review of Lanthanides As Activators In Luminecence, IOSR J. Appl. Chem. 9 (2016) 104–110. https://doi.org/10.9790/5736-090701104110.

[85] A.H. Morshed, M.E. Moussa, S.M. Bedair, R. Leonard, S.X. Liu, N. El-Masry, Violet / blue emission from epitaxial cerium oxide films on silicon substrates, Appl. Phys. Lett. 70 (1997) 1647–1649.

[86] H. Suzuki, T.A. Tombrello, C.L. Melcher, J.S. Schweitzer, Light Emission Mechanism of Lu2(SiO4)O:Ce, IEEE Trans. Nucl. Sci. 40 (1993) 380–383. https://doi.org/10.1109/23.256584.

[87] Y. Jia, A. Miglio, M. Mikami, X. Gonze, Ab initio study of luminescence in Ce-doped Lu 2 SiO 5 : The role of oxygen vacancies on emission color and thermal quenching behavior, Phys. Rev. Mater. 2 (2018) 1–11. https://doi.org/10.1103/PhysRevMaterials.2.125202.

[88] X. Han, J. Lee, H. Yoo, Oxygen-vacancy-induced ferromagnetism in CeO2 from first principles, Phys. Rev. B. 79 (2009) 100403(R). https://doi.org/10.1103/PhysRevB.79.100403.

[89] G. Blasse, A. Bril, Investigation of Some Ce 3+-Activated Phosphors ARTICLES YOU MAY BE INTERESTED IN A NEW PHOSPHOR FOR FLYING-SPOT CATHODE-RAY TUBES FOR COLOR TELEVISION, J. Chem. Phys. 47 (1967) 5139. https://doi.org/10.1063/1.1701771.

[90] T. Hoshina, 5d→4f Radiative Transition Probabilities of Ce3+ and Eu2+ in Crystals, J. Phys. Soc. Japan. 48 (1980) 1261–1268. https://doi.org/10.1143/JPSJ.48.1261.

[91] P. Dorenbos, 5d-level energies of Ce3+ and the crystalline environment. I. Fluoride compounds, Phys. Rev. B - Condens. Matter Mater. Phys. 62 (2000) 15640–15649. https://doi.org/10.1103/PhysRevB.62.15640.

[92] L. Guerbous, O. Krachni, The 4f-5d luminescence transitions in cerium-doped LuF3, J. Mod. Opt. 53 (2006) 2043–2053. https://doi.org/10.1080/09500340600792424.

[93] A.H. Krumpel, E. Van Der Kolk, D. Zeelenberg, A.J.J. Bos, K.W. Krämer, P. Dorenbos, Lanthanide 4f-level location in lanthanide doped and cerium-lanthanide codoped NaLaF4 by photo-and thermoluminescence, J. Appl. Phys. 104 (2008) 073505. https://doi.org/10.1063/1.2955776.

[94] N. V. Skorodumova, R. Ahuja, S.I. Simak, I.A. Abrikosov, B. Johansson, B.I. Lundqvist, Electronic, bonding, and optical properties of CeO2 and Ce2O3 from first principles , Phys. Rev. B. 64 (2001) 1–9. https://doi.org/10.1103/physrevb.64.115108.

[95] G. Pezzotti, K. Wan, M.C. Munisso, W. Zhu, Stress dependence of F+-center cathodoluminescence of sapphire, Appl. Phys. Lett. 89 (2006) 14–17. https://doi.org/10.1063/1.2234307.

[96] J. Costantini, S. Miro, N. Touati, L. Binet, G. Wallez, G. Lelong, W.J. Weber, Defects induced in cerium dioxide single crystals by electron irradiation Defects induced in cerium dioxide single crystals by electron irradiation, 025901 (2018). https://doi.org/10.1063/1.5007823.

[97] B.G. Draeger, G.P. Summers, Defects in unirradiated Al2O3, Phys. Rev. B. 19 (1979) 1172–1177. https://doi.org/10.1103/PhysRevB.19.1172.

[98] J.M. Costantini, G. Lelong, M. Guillaumet, W.J. Weber, S. Takaki, K. Yasuda, Color-center production and recovery in electron-irradiated magnesium aluminate spinel and ceria, J. Phys. Condens. Matter. 28 (2016) 325901. https://doi.org/10.1088/0953-8984/28/32/325901.

[99] A. Guglielmetti, A. Chartier, L. van Brutzel, J.P. Crocombette, K. Yasuda, C. Meis, S. Matsumura, Atomistic simulation of point defects behavior in ceria, Nucl. Instruments Methods Phys. Res. Sect. B. 266 (2008) 5120–5125. https://doi.org/10.1016/j.nimb.2008.09.010.

[100] D. CURIE, Luminescence in crystals, Students Q. J. 34 (1963) 1262–1262. https://doi.org/10.1049/sqj.1963.0049.

[101] W. Hergert, P. Reck, L. Pasemann, J. Schreiber, Cathodoluminescence measurements using the scanning electron microscope for the determination of semiconductor parameters, Phys. Status Solidi. 101 (1987) 611–618. https://doi.org/10.1002/pssa.2211010237.

[102] A. Djemel, R.J. Tarento, J. Castaing, Y. Marfaing, A. Nouiri, Study of electronic surface properties of GaAs in cathodoluminescence experiments, Phys. Status Solidi Appl. Res. 168 (1998) 425–432. https://doi.org/10.1002/(SICI)1521-396X(199808)168:2<425::AID-PSSA425>3.0.CO;2-N.

[103] I. Plante, F.A. Cucinotta, Ionization and excitation cross sections for the interaction of HZE particles in liquid water and application to Monte Carlo simulation of radiation tracks, New J. Phys. 10 (2008). https://doi.org/10.1088/1367-2630/10/12/125020.

[104] T. Liamsuwan, H. Nikjoo, A Monte Carlo track structure simulation code for the full-slowing-down carbon projectiles of energies 1 keV u-1-10 MeV u-1 in water, Phys. Med. Biol. 58 (2013) 673–701. https://doi.org/10.1088/0031-9155/58/3/673.

[105] S.T. Perkins, D.E. Cullen, S.M. Seltzer, Tables and graphs of electron-interaction cross-sections from 10 eV to 100 GeV derived from the LLNL evaluated electron data library (EEDL), Z= 1-100, UCRL-50400. 31 (1991) 21–24.

[106] I. Blanco, P. Molle, L.E. Sáenz de Miera, G. Ansola, Basic Oxygen Furnace steel slag aggregates for phosphorus treatment: Evaluation of its potential use as a substrate in constructed wetlands, Water Res. 89 (2016) 355–365. https://doi.org/10.1016/j.watres.2015.11.064.

[107] K.E. Sickafus, L. Minervini, R.W. Grimes, J.A. Valdez, M. Ishimaru, F. Li, K.J. McClellan, T. Hartmann, Radiation Tolerance of Complex Oxides, Science (80-.). 289 (2000) 748–751. https://doi.org/10.1126/science.289.5480.748.

[108] B.H. Toby, R factors in Rietveld analysis: How good is good enough? , Powder Diffr. 21 (2006) 67–70. https://doi.org/10.1154/1.2179804.

[109] B.D. Cullity, Elements of X-ray Diffraction, Addison-Wesley Publishing, 1956.

[110] J.B. Nelson, D.P. Riley, An experimental investigation of extrapolation methods in the derivation of accurate unit-cell dimensions of crystals, Proc. Phys. Soc. 57 (1945) 160–177. https://doi.org/10.1088/0959-5309/57/3/302.

[111] S.J. Hong, A. V. Virkar, Lattice Parameters and Densities of Rare-Earth Oxide Doped Ceria Electrolytes, J. Am. Ceram. Soc. 78 (1995) 433–439. https://doi.org/10.1111/j.1151-2916.1995.tb08820.x.

[112] G.K. Williamson, W.H. Hall, X-ray line broadening from filed aluminium and wolfram, Acta Metall. 1 (1953) 22–31. https://doi.org/10.1016/0001-6160(53)90006-6.

[113] N.C. Halder, C.N.J. Wagner, Separation of particle size and lattice strain in integral breadth measurements, Acta Crystallogr. 20 (1966) 312–313. https://doi.org/10.1107/s0365110x66000628.

[114] W.H. Weber, K.C. Bass, J.R. Mcbride, W. Graham, C.R. Peters, R. Usmen, J. Catalysis, Raman study of CeOz. Second-order scattering, lattice dynamics, and particle-size effects, Phys. Rev. B. 48 (1992) 178–185.

[115] J.R. McBride, K.C. Hass, B.D. Poindexter, W.H. Weber, Raman and x-ray studies of Ce1−xRExO2−y, where RE=La, Pr, Nd, Eu, Gd, and Tb, J. Appl. Phys. 76 (1994) 2435–2441.

[116] J.M. Costantini, S. Miro, G. Gutierrez, K. Yasuda, S. Takaki, N. Ishikawa, M. Toulemonde, Raman spectroscopy study of damage induced in cerium dioxide by swift heavy ion irradiations, J. Appl. Phys. 122 (2017) 205901. https://doi.org/10.1063/1.5011165.

[117] J.-M. Costantini, G. Gutierrez, G. Lelong, M. Guillaumet, P. Seo, K. Yasuda, Radiation damage in ion-irradiated CeO2 and (Ce, Gd)O2 sinters: Effect of the Gd content, J. Nucl. Mater. 564 (2022) 153667. https://doi.org/10.1016/j.jnucmat.2022.153667.

[118] C. Schilling, A. Hofmann, C. Hess, M.V. Ganduglia-Pirovano, Raman Spectra of Polycrystalline CeO2: A Density Functional Theory Study, J. Phys. Chem. C. 121 (2017) 20834–20849. https://doi.org/10.1021/acs.jpcc.7b06643.

[119] J.M. Costantini, G. Gutierrez, G. Lelong, M. Guillaumet, M.M. Rahman, K. Yasuda, Raman spectroscopy study of damage in swift heavy ion-irradiated ceramics, J. Raman Spectrosc. 53 (2022) 1–11. https://doi.org/10.1002/JRS.6414.

[120] M.H. Brodsky, M. Cardona, Local order as determined by electronic and vibrational spectroscopy: Amorphous semiconductors, J. Non. Cryst. Solids. 31 (1978) 81–108. https://doi.org/10.1016/0022-3093(78)90100-X.

[121] J. Buckeridge, D.O. Scanlon, A. Walsh, C.R.A. Catlow, A.A. Sokol, Dynamical response and instability in ceria under lattice expansion, Phys. Rev. B. 87 (2013) 214304. https://doi.org/10.1103/PhysRevB.87.214304.

[122] M. Coduri, M. Scavini, M. Pani, M.M. Carnasciali, H. Klein, C. Artini, From nano to microcrystals: effects of different synthetic pathways on the defect architecture in heavily Gd-doped ceria, Phys. Chem. Chem. Phys. 19 (2017) 11612–11630. https://doi.org/10.1039/C6CP08173H.

[123] A. Nakajima, A. Yoshihara, M. Ishigame, Defect-induced Raman spectra in doped CeO2, Phys. Rev. B. 50 (1994) 13297–13307. https://doi.org/10.1103/PhysRevB.50.13297.

[124] A. Banerji, V. Grover, V. Sathe, S.K. Deb, A.K. Tyagi, CeO2 - Gd2O3 system: Unraveling of microscopic features by Raman spectroscopy, Solid State Commun. 149 (2009) 1689–1692. https://doi.org/10.1016/j.ssc.2009.06.045.

[125] D.R. Ou, T. Mori, F. Ye, J. Zou, G. Auchterlonie, J. Drennan, Oxygen-vacancy ordering in lanthanide-doped ceria: Dopant-type dependence and structure model, Phys. Rev. B - Condens. Matter Mater. Phys. 77 (2008) 1–8. https://doi.org/10.1103/PhysRevB.77.024108.

[126] K. Yasuda, M. Etoh, K. Sawada, T. Yamamoto, K. Yasunaga, S. Matsumura, N. Ishikawa, Defect formation and accumulation in CeO2 irradiated with swift heavy ions, Nucl. Instrum. Methods Phys. Res. Sect. B. 314 (2013) 185–190. https://doi.org/10.1016/j.nimb.2013.04.069.

[127] S. Takaki, K. Yasuda, T. Yamamoto, S. Matsumura, N. Ishikawa, Structure of ion tracks in ceria irradiated with high energy xenon ions, Prog. Nucl. Energy. 92 (2016) 306–312. https://doi.org/10.1016/j.pnucene.2016.07.013.

[128] M. Tang, P. Lu, J.A. Valdez, K.E. Sickafus, Ion-irradiation-induced phase transformation in rare earth sesquioxides (Dy2O3,Er2O3,Lu2O3), J. Appl. Phys. 99 (2006) 063514. https://doi.org/10.1063/1.2184433.

[129] S.P. Ray, A.S. Nowick, D.E. Cox, X-ray and neutron diffraction study of intermediate phases in nonstoichiometric cerium dioxide, J. Solid State Chem. 15 (1975) 344–351. https://doi.org/10.1016/0022-4596(75)90290-X.

[130] H. Ohno, A. Iwase, D. Matsumura, Y. Nishihata, J. Mizuki, N. Ishikawa, Y. Baba, N. Hirao, T. Sonoda, M. Kinoshita, Study on effects of swift heavy ion irradiation in cerium dioxide using synchrotron radiation X-ray absorption spectroscopy, Nucl. Instrum. Methods Phys. Res. Sect. B. 266 (2008) 3013–3017. https://doi.org/10.1016/j.nimb.2008.03.155.

[131] C.L. Tracy, M. Lang, J.M. Pray, F. Zhang, D. Popov, C. Park, C. Trautmann, M. Bender, D. Severin, V.A. Skuratov, R.C. Ewing, Redox response of actinide materials to highly ionizing radiation, Nat. Commun. 6 (2015) 1–9. https://doi.org/10.1038/ncomms7133.

[132] T. Sonoda, M. Kinoshita, Y. Chimi, N. Ishikawa, M. Sataka, A. Iwase, high-energy ions of typical fission products, Nucl. Instrum. Methods Phys. Res. Sect. B. 250 (2006) 254–258. https://doi.org/10.1016/j.nimb.2006.04.120.

[133] N. Ishikawa, K. Takegahara, Radiation damages in CeO 2 thin films irradiated with ions having the same nuclear stopping and different electronic stopping powers, Nucl. Instrum. Methods Phys. Res. Sect. B. 272 (2012) 227–230. https://doi.org/10.1016/j.nimb.2011.01.071.

[134] S. Takaki, K. Yasuda, T. Yamamoto, S. Matsumura, N. Ishikawa, Atomic structure of ion tracks in Ceria, Nucl. Instrum. Methods Phys. Res. Sect. B. 326 (2014) 140–144. https://doi.org/10.1016/j.nimb.2013.10.077.

[135] D. Simeone, C. Dodane-Thiriet, D. Gosset, P. Daniel, M. Beauvy, Order–disorder phase transition induced by swift ions in MgAl2O4 and ZnAl2O4 spinels, J. Nucl. Mater. 300 (2002) 151–160. https://doi.org/10.1016/S0022-3115(01)00749-8.

[136] B.P. Mandal, V. Grover, M. Roy, A.K. Tyagi, X-ray diffraction and raman spectroscopic investigation on the phase relations in Yb2O3- and Tm2O 3-substituted

CeO2, J. Am. Ceram. Soc. 90 (2007) 2961–2965. https://doi.org/10.1111/j.1551-2916.2007.01826.x.

[137] D.J.M. Bevan, E. Summerville, Mixed rare earth oxides, in: Handb. Phys. Chem. Rare Earths, Elsevier, 1979: pp. 401–524. https://doi.org/10.1016/S0168-1273(79)03011-7.

[138] E.R. Andrievskaya, O.A. Kornienko, A. V. Sameljuk, A. Sayir, Phase relation studies in the CeO2–La2O3 system at 1100–1500 °C, J. Eur. Ceram. Soc. 31 (2011) 1277–1283. https://doi.org/10.1016/J.JEURCERAMSOC.2010.05.024.

[139] A. Kossoy, Q. Wang, R. Korobko, V. Grover, Y. Feldman, E. Wachtel, A.K. Tyagi, A.I. Frenkel, I. Lubomirsky, Evolution of the local structure at the phase transition in CeO 2-Gd2O3 solid solutions, Phys. Rev. B - Condens. Matter Mater. Phys. 87 (2013) 054101. https://doi.org/10.1103/PHYSREVB.87.054101/FIGURES/5/MEDIUM.

[140] M. Scavini, M. Coduri, M. Allieta, P. Masala, S. Cappelli, C. Oliva, M. Brunelli, F. Orsini, C. Ferrero, Percolating hierarchical defect structures drive phase transformation in Ce1-xGdxO2-x/2: A total scattering study, IUCrJ. 2 (2015) 511–522. https://doi.org/10.1107/S2052252515011641.

[141] C. Artini, G.A. Costa, M. Pani, A. Lausi, J. Plaisier, Structural characterization of the CeO2/Gd2O3 mixed system by synchrotron X-ray diffraction, J. Solid State Chem. 190 (2012) 24–28. https://doi.org/10.1016/J.JSSC.2012.01.056.

[142] V. Grover, A.K.K. Tyagi, Phase relations, lattice thermal expansion in CeO2–Gd2O3 system, and stabilization of cubic gadolinia, Mater. Res. Bull. 39 (2004) 859–866. https://doi.org/10.1016/j.materresbull.2004.01.007.

[143] W. Chen, A. Navrotsky, Thermochemical study of trivalent-doped ceria systems: CeO2–MO1.5 (M = La, Gd, and Y), J. Mater. Res. 21 (2011) 3242–3251. https://doi.org/10.1557/JMR.2006.0400.

[144] A. Atkinson, Chemically-induced stresses in gadolinium-doped ceria solid oxide fuel cell electrolytes, Solid State Ionics. 95 (1997) 249–258. https://doi.org/10.1016/S0167-2738(96)00588-7.

[145] N. Ishikawa, Y. Chimi, O. Michikami, Y. Ohta, K. Ohhara, M. Lang, R. Neumann, Study of structural change in CeO2 irradiated with high-energy ions by means of X-ray diffraction measurement, Nucl. Instrum. Methods Phys. Res. Sect. B. 266 (2008) 3033–3036. https://doi.org/10.1016/j.nimb.2008.03.159.

[146] M. Patel, J. Aguiar, K. Sickafus, G. Baldinozzi, Structure and radiation response of anion excess bixbyite Formula Presented, Phys. Rev. Mater. 6 (2022) 13610. https://doi.org/10.1103/PhysRevMaterials.6.013610.

[147] E. Ruiz-Trejo, The optical band gap of Gd-doped CeO2 thin films as function of temperature and composition, J. Phys. Chem. Solids. 74 (2013) 605–610. https://doi.org/10.1016/j.jpcs.2012.12.014.

[148] P. Dorenbos, Thermal quenching of Eu2+ 5d-4f luminescence in inorganic compounds, J. Phys. Condens. Matter. 17 (2005) 8103–8111. https://doi.org/10.1088/0953-8984/17/50/027.

[149] Baldassare Bartolo, Advances in Nonradiative Processes in Solids, Springer US, Erice, Italy, 1989.

[150] S. Poncé, Y. Jia, M. Giantomassi, M. Mikami, X. Gonze, Understanding Thermal Quenching of Photoluminescence in Oxynitride Phosphors from First Principles, J. Phys. Chem. C. 120 (2016) 4040–4047. https://doi.org/10.1021/acs.jpcc.5b12361.

Abstract

Ceramic oxide with fluorite structure, such as ceria (CeO_2), has been proposed as a surrogate of nuclear fuels (e.g. UO_2, PuO_2) and transmutation targets because of the excellent radiation resistance. Ceria has a redox effect between two charge states of cerium ions with localized *f* electrons, which induces oxygen vacancies (V_O) to compensate for charge neutrality. Gadolinia (Gd_2O_3) exhibits a bixbyite structure, and it has been doped in UO_2 fuel as a burnable poison due to the large absorption cross-section of thermal neutrons. Gd_2O_3-doped CeO_2 as expressed by $Ce_{1-x}Gd_xO_{2-x/2}$ also produces V_O since the Gd^{3+} substitutes into the Ce^{4+} site. The oxygen deficiency in $Ce_{1-x}Gd_xO_{2-x/2}$ is mainly controlled by the dopant concentration.

Moreover, V_O can be generated by elastic collisions with high-energy electrons by receiving energy above the threshold displacement energy of oxygen atoms. The V_O is a key factor to determine radiation tolerance since it enhances the recombination of interstitials and vacancies. The kinetic behavior of point defects in ceramics is known to depend on their charge states. However, there was only limited research on it since the *in-situ* techniques are needed to gain the production and charge state of point defects in ceramics during irradiation.

In this dissertation, radiation damage in $Ce_{1-x}Gd_xO_{2-x/2}$ was investigated for a wide range of Gd dopant concentrations ($0 \leq x \leq 0.5$). For this purpose, a unique facility of a high voltage electron microscope (HVEM) interfaced with cathodoluminescence (CL) facility at The Ultramicroscopy Research Center of Kyushu University was utilized to examine the production and charge state of point defects *in-situ* under high-energy electron irradiation. Further, microstructure change induced by heavy ion irradiation was studied comprehensively against dopant concentration by x-ray diffraction (XRD) analysis, micro-Raman spectroscopy, and transmission electron microscopy (TEM) to understand the role of oxygen vacancy on the microstructure stability. This dissertation consists of seven chapters.

Chapter 1 described the introduction and research goal of this study. At the end of this chapter, the structure of the dissertation was outlined.

Chapter 2 reviewed the theoretical and experimental background on structure in CeO_2 and $Ce_{1-x}Gd_xO_{2-x/2}$. Displacement damage, energy loss, diffraction analysis for structure evaluation, and CL emission mechanism were described in this chapter.

Chapter 3 explained the experimental methodology for the sample preparation, and the techniques of XRD, Raman spectroscopy, and TEM. Details for the synthesis of $Ce_{1-x}Gd_xO_{2-}$

$_{x/2}$ samples and ion irradiation conditions were described. *In-situ* CL measurement conditions were also described together with the data acquisition procedures.

Chapter 4 described point defect production under in-beam conditions in pure single crystal and polycrystalline ceria using the *in-situ* HVEM-CL technique. The CL spectra were obtained with 400 ~ 1250 keV electrons, and they were fitted into three CL bands. One band was assigned to be the F^+ center which is induced by electron-nuclear elastic collisions, and the other two bands were originated from charge-compensative Ce^{3+} ions caused by V_O formation. Localized atomic configurations between Ce^{3+} ions and charged V_O were suggested according to the CL spectra. The dependence of CL spectra against electron energy and irradiation temperature were also explained by taking the cross-sections of defect production and electronic excitation.

Chapter 5 discussed microstructure and radiation response in $Ce_{1-x}Gd_xO_{2-x/2}$ for a wide range of Gd_2O_3 concentrations ($0 \leq x \leq 0.5$). Microstructure characterization was carried out comprehensively by XRD, micro-Raman spectroscopy, and TEM. The formation of bixbyite structure with V_O ordering was observed for $x \geq 0.2$, associated with the saturation of lattice parameter and micro-strain relaxation. Those microstructure changes with values of x were found to influence the microstructure change induced by 200 MeV Xe ions. Ion track density and size were found to be depressed for samples with $x \geq 0.2$, and this was discussed with the ordering of V_O which attributes to the recovery process of radiation-induced defects.

Chapter 6 described the application of the *in-situ* HVEM-CL technique to $Ce_{1-x}Gd_xO_{2-x/2}$ samples. The CL bands for Ce^{3+}-V_O, Ce^{3+}, and F^+ center were observed from $Ce_{1-x}Gd_xO_{2-x/2}$ as same as pure ceria. The electronic configurations and energy dependence of CL spectra in $Ce_{1-x}Gd_xO_{2-x/2}$ were compared with those of pure ceria. Photon energy shifts and quenching of CL emission were observed in $Ce_{1-x}Gd_xO_{2-x/2}$, and the change was discussed with the generation of V_O induced by Gd_2O_3 doping, and the change of electrical configuration around Ce^{3+} ions and V_O. The band gap energy level of defects in $Ce_{1-x}Gd_xO_{2-x/2}$ was suggested in this chapter.

In chapter 7, all the experimental and simulation works done in the wake of this study are summarized as conclusions together with possible directions for future research.

Acknowledgements

The dissertation was able to be completed thanks to the support of many people, teachers, and institutions. Six years at Kyushu University have been a very valuable experience for me and I would like to express my gratitude to those who have helped me.

I would like to express my sincere gratitude to my supervisor, Prof. Kazuhiro Yasuda. Thanks to the professor's meticulous and accurate guidance, discussion, support, patience, and consideration, this dissertation can be completed. Besides research, he took care of my study abroad life in Japan and gave me warm encouragement and lots of advice whenever I had difficulties. I am very fortunate to have been taught by Prof. Yasuda, and I will continue to live as a good researcher remembering Prof. Yasuda.

I would like to appreciate Prof. Syo Matsumura, who retired in 2022, for giving me a chance to study at Kyushu University in a great environment. I was very impressed with the professor's competence, humility, and support for his students. I appreciate his precious guidance and discussion on this dissertation, as well as his detailed consideration and support for my study abroad life in Japan.

I would like to appreciate my collaborator, Prof. Jean-Marc Costantini at Université Paris-Saclay, CEA-Saclay, France for his valuable cooperation, detailed guidance, and idea to complete this dissertation. Thanks to online and on-site discussions, research collaborations, and encouragement, I could complete this study. The professor's curiosity and passion for research motivated me a lot.

I would like to appreciate Prof. Yasukazu Murakami for providing a great research environment and detailed discussions on this dissertation. His careful consideration and encouragement helped me study at Kyushu University.

I would like to appreciate Asst. Prof. Satoru Yoshioka for his valuable advice and discussion for this dissertation. Thanks to the professor's support, I was able to successfully conduct the experiment and obtain good results.

I would like to thank the co-chairs of this dissertation committee, Prof. Satoshi Hata and Prof. Yaohiro Inagaki.

I would like to express my gratitude to Asst. Prof. Tomokazu Yamamoto, Asst. Prof. Takehiro Tamaoka and all staff members at the Ultramicroscopy Research Center of Kyushu

University for their efforts in the development and maintenance of the electron microscope facilities and their technical support, guidance, and cooperation in using them.

I would like to thank the Center of Advanced Instrumental Analysis of Kyushu University and Asst. Prof. Midori Watanabe for her technical support to use analytical facilities.

I would like to thank Yasuda, Matsumura, and Murakami group members for their various support and cooperation. Sujin Lee gave me a lot of strength by my side. I appreciate alumni and staff members; Dr. AKM Saiful Islam Bhuian, Dr. Md. Majidur Rahman, Dr. Kohei Aso, Dr. Wenhui Yang, Dr. Youngji Cho, Mrs. Atsuko Sato, Mr. Youichiro Kawami for their help and support.

I would like to express my gratitude to Mrs. Hiromi Kumagai and Mrs. Mayumi Matsumoto for their support for comfortable study and research activities.

I would like to express my deep gratitude to my parents, brother, aunt, uncle, Hyunju, and his families, who gave me infinite love, prayer, and support. My friends at Kyushu University, Fukuoka vision church families, Bae's family, and Kkokkyo, I owe a debt of love and prayer to them.

Above all, I praise and thank the almighty God Jesus Christ for guiding and savior of my life. The fear of the Lord is the beginning of wisdom, and knowledge of the Holy One is understanding. Proverbs 9:10.

Table of Contents

List of Figures

List of Tables

List of Abbreviation

BF: Bright-field

CL: Cathodoluminescence

CSDA: Continuous slowing down approximation

E_d: Threshold displacement energy

EELS: Electron energy loss spectroscopy

EPR: Electron-paramagnetic resonance

fcc: Face-centered cubic

HRTEM: High-resolution transmission electron microscopy

HVEM: High-voltage electron microscopy

MOX: Mixed oxide

PKA: Primary knock on atom

PL: Photoluminescence

RE: Rare earth

SAED: Selected area electron diffraction

S_e: Electronic stopping power

SEM: Scanning electron microscope

S_n: Nuclear stopping power

STEM: Scanning transmission electron microscopy

TEM: Transmission electron microscope

URC: Ultramicroscopy Research Center

V_O: Oxygen vacancy

XRD: X-ray diffraction

YSZ: Yttria-stabilized cubic zirconia

ZA: Zone axis

σ_d: Displacement cross-section

Chapter 1

Introduction

A sufficient energy supply is as importance as a fast growing of world population in modern life society demanding safety, mobility and daily comfort life. For this reason, the energy industry has discussed and studied the energy generation and storage systems. To lead these technologies, it is necessary to develop superior materials for energy source applications, such as generation facilities for chemical and photo-physical energy, nuclear reaction energy, and thermomechanical energy. All of those industries need excellent materials, which generate high efficient energy for each environmental condition.

Ceramic oxide is one of the remarkable and fascinated materials, which have high strength, high insulation ability, low thermal expansion, and chemical stability. For those reasons, ceramic oxide has been used safely in many industrial fields, such as energy-supplement devices, auto motives, medical technology, and aerospace. Especially for nuclear applications, magnesia (MgO), sapphire (α-$Al_2O_{3)}$, and yttria-stabilized cubic zirconia (ZrO_2: Y) are promising ceramic materials to be used for the host of inert matrix fuels in nuclear fission reactors, transmutation targets, and functional materials in fusion devices under high-energy particle radiations. They can endure the exposure to extreme environments, for instance, high or low temperatures, and intense radiation. Therefore, it is necessary to understand their physical and chemical characteristics under harsh environment to prevent degradation of physical and chemical properties.

In particular, ceramics are used for nuclear fuel, and they are widely investigated for their safety and reliability. Typically, plutonium oxide (PuO_2) is actively developed for use in mixed oxide (MOX) fuel such as (U, Pu)O_2 for thermal reactors or fast reactor fuel. For the

safe use of MOX fuel, it is necessary to understand the drawbacks caused by the pile-up of damage for a long time. However, it might be hard to handle and study the radiative materials caused by irradiation. Therefore, cerium dioxide or ceria (CeO_2) with a fluorite structure can be considered as a surrogate of PuO_2 to avoid radioactive problems caused by its direct use of it.

Moreover, for the high performance of nuclear reactors to use in long-life power plants, the burnable poison has been used to control the initial reactivity. Fuel utilization has been introduced with additional neutron absorbers in fissile materials. Gadolinium (Gd) is one of the fission products forming solid solutions with uranium dioxide. Gd_2O_3 has been, therefore, used as a dopant for UO_2 fuel in boiling water reactors because Gd isotopes have a large absorption cross-section of 49,000 barns for thermal neutrons with taking the natural abundance of Gd isotopes into consideration [1]. The UO_2-Gd_2O_3 fuel has been used in the boiling water reactor (BWR) type since 1967, and the maximum concentration of Gd_2O_3 is around 4 wt% (i.e. ~6 at% Gd). Recently, the UO_2-Gd_2O_3 fuel is introduced in the pressurized water reactor (PWR) type up to high concentration of Gd_2O_3 around 10 wt% (i.e. ~14 at% Gd).

Nuclear fuel materials are exposed to various radiations such as high-energy fission fragments, high-energy neutrons, α-, β-, and γ-rays generated by nuclear fission reactions in nuclear reactors. Radiation with those high-energy particles has been known to induce the amorphization in ceramics and cause degradation of mechanical properties, and void swelling due to the atomic displacement damage [2]. Irradiation defects resulting from these various radiations form and accumulate in the heating-resisting materials. Also, accumulation of fission products and high-density electron excitation damage are also of importance for the stability of fuels. Detailed knowledge of the point defect production and kinetics are often required for the further understandings of radiation damage in ceramics. For example, electronic excitation is known to affect damage processes, such as the formation and migration of point defects, and

stability of point defect aggregates in ionic and covalently bonded ceramic materials [3–5]. Fission fragments arising from fuels and transmutation targets have high energies of 70 - 100 MeV and induce a high density of electronic excitation in materials. It has been reported that when such high-density electronic excitation is induced during crystallization, columnar irradiation defects called 'ion tracks' form along ion trails [6]. In nuclear fuel, such high-density electronic excitation damage is induced repeatedly to reach 10^4 to 10^5 times for the burn-up of 1% FIMA (% fissioned per initial metal atom). Therefore, evaluation of the ion track formation in the fluorite-structure oxide and the microstructure change due to its overlap is important for understanding the stability of the structure of nuclear reactor fuels and for the development of next-generation fuels.

To understand the basic process of irradiation damage, the threshold displacement energy (E_d) is indispensable physical quantity. Costantini et al. used an electron accelerator to irradiate electrons with a wide range of energies to yttria-stabilized cubic zirconia (YSZ), and anion electron trapping centers (F^+ centers) were investigated by electron spin resonance (EPR) method [7]. From the analysis of the electron-energy dependence of the point defect accumulation process, the value of E_d can be derived by *in-situ* observation in transmission electron microscopy (TEM). Yasunaga et al. irradiated electrons to CeO_2 for various energies by using TEM and observed the formation and growth process of the irradiation defect in-beam state [8,9]. They confirmed that the properties of the dislocation loop depended on the electron energy, and according to the results, they estimated the E_d of Ce and O ions as 44 ~ 58 eV and <33 eV, respectively [9]. Values of E_d in various ceramic materials, such as UO_2 (U: ~40 eV, O: ~20 eV), ThO_2 (Th: 48.5 ~ 61.5 eV, O: 17.5 ~ 100 eV), ZrO_2 (Zr: 54 ~ 68.5 eV, O: 14 ~ 100 eV), were summarized in references [10–12], although the reported values of E_d are not sufficient at the present moment.

Mostly, ceramics includes multielement and their crystal structures content multi-sublattices themselves. The atomic bonds also have ion-covalent bonding which depends on crystal. The electronic valence of point defects can be changed by electronic excitation that influences the migration dynamics and aggregation of point defects [13]. Under radiation irradiation conditions, it is, therefore, necessary to have a general idea of in-beam physical characteristics of defect behaviors.

Electron microscopy is one of the useful techniques to measure radiation damage in materials. High energy electrons generated in an electron microscope, such as a TEM, can be irradiated with a high-flux electron beam to a specimen and produce point defects in a short time. Namely, an *in-situ* TEM experiment has an advantage that one can observe the nucleation and accumulation of defects dynamically. The use of electron irradiation has an additional advantage since the target does not need to be cooled down unlike neutron or high-energy ion irradiation. Unfortunately, the defects recombination occurs during the cooling period, and it is hard to observe its effects *in-situ* right after neutrons/ions irradiation. Therefore, the *in-situ* TEM method has the characteristics of being able to conduct a systematic and precise study on the effects of fission product accumulation in-beam environment and high-density electron excitation.

0ptical absorption spectroscopy technique has an advantage to identify the defects in ceramics. Photoluminescence (PL) spectroscopy and UV-visible optical absorption spectroscopy were used to examine the defects in ceramics [14,15]. A photo-induced electron-hole pair indicates the localized defect level at photoexcitation energies within the bandgap energy. In particular, naturally present defects, such as F centers (electron centers) and V centers (hole centers), were demonstrated by PL spectroscopy in alkali halides and oxides [15]. In addition, thermo-stimulated luminescence (TSL) [16], optically stimulated luminescence

(OSL) [17], and radio-luminescence (RL) [18] were also used to identify nature or radiation-induced defects in ceramics.

Cathodoluminescence (CL) spectroscopy is one of the optical absorption techniques, and it has been used for the impurity analysis by using SEM under low-energy electron irradiation (≤ 40 keV). The first observation of discoloration was investigated by Goldstein [19] in alkali halides induced by electron irradiation. For several decades, F centers from oxygen vacancies were examined in various ceramic oxides, such as MgO, Al_2O_3, ZnO, and TiO_2 [20–23].

CL spectroscopy has also been utilized to study the radiation-induced defects. Recently, a study on point defect formation by elastic and inelastic collisions under high-energy electron irradiation was performed in ceramics by using *in-situ* CL spectroscopy under high-energy electron irradiation [24,25]. CL spectra emitted from impurities and F centers in sapphire (α-Al_2O_3), YSZ (ZrO_2:Y), spinel ($MgAl_2O_4$) were detected and revealed its electrical characteristics and formation of defects in-beam condition. It was revealed the point defects formation and aggregation with their charge states under electron irradiation [25].

Radiation response due to multi-particles collisions of electronic and nuclear stopping is also attracted for ceramics leading the annealing of radiation damage due to a synergetic effect. The synergetic effect of elastic (or nuclear) (S_n) and inelastic (or electronic) (S_e) energy loss is a key factor of nanostructure evolution and defect kinetics of ceramics [26,27]. The recovering and expansion delay of the defects due to ionization-induced diffusion and recombination of point defects lead the synergetic effect. These point defects in ceramic influence physical properties, such as thermal conductivity and diffusivity [28]. The kinetic behaviors of point defects are depending on their charge states. Therefore, it is important to understand the charge states of the defects under irradiation conditions, and thereby *in-situ* high

voltage electron microscopy (HVEM)-CL method can be a powerful technique for the radiation damage study in ceramics.

Based on the explanation above, the purpose of this dissertation is to gain insights into the radiation damage in the rare-earth (RE)-doped fluorite structure oxides. In particular, this dissertation has two objectives to elucidate the followings: i) understanding the on-site point defect production and its charge state during electron irradiation, and ii) examination of microstructure evaluation by RE doping and ion irradiation.

The dissertation consists of seven chapters.

Chapter 1 describes the introduction and research goal of this dissertation. At the end of this chapter, the orientation of each chapter is proposed.

Chapter 2 reviews the theoretical and experimental background of physical and chemical characteristics of the main material of Gd_2O_3 doped ceria, and diffraction analysis. Furthermore, fundamental knowledge of displacement damage, energy loss, and cathodoluminescence spectroscopy are described.

Chapter 3 explains experimental methodologies for the sample preparation, measurement, and analysis techniques. The sample preparation complies synthesis procedure, thinning for TEM observation, and ion irradiation. Experimental facility performances and conditions for x-ray diffraction (XRD), Raman spectroscopy, TEM, and *in-situ* HVEM-CL measurement are described with the explanation of data acquisition procedures.

Chapter 4 describes *in-situ* HVEM-CL measurement in pure ceria under electron irradiation by using the HVEM. This technique yields information on the instant Frenkel point defect formation under out-of-equilibrium conditions upon high-energy electron irradiation. CL spectra were obtained from single crystal and polycrystalline samples. Charge states of defects were interpreted by CL profiles and they related to oxygen vacancy localization. Moreover, energy and temperature dependence of CL emission was investigated.

Chapter 5 discusses the microstructure evaluation in Gd_2O_3 doped ceria upon the creation of oxygen vacancies in a wide range of dopant concentrations. Comprehensive microstructure characterization, such as phase, lattice parameter, and microstrain of the samples was carried out by XRD, micro-Raman spectroscopy, and TEM in virgin samples. Moreover, heavy ion radiation-induced microstructure evolution was followed in the same samples by comprehensive microstructure characterization techniques to understand the radiation resistance effect by Gd_2O_3 doping and intrinsic oxygen vacancy creation.

Chapter 6 presents the application of the *in-situ* HVEM-CL technique to the Gd_2O_3 doped ceria samples. Information on charge state and electronic configurations of *in-situ* defects generated during high-energy electron irradiation were investigated in the doped samples. The Gd_2O_3 concentration effect with the creation of oxygen vacancies by doping for CL emission from the defects varying accelerate energies of the HVEM was investigated. At the end of this chapter, the energy levels of defects in the bad gap of the Gd_2O_3 doped ceria were summarized by comparing the pure ceria.

In chapter 7, all the experimental and simulation works done in the wake of this study are summarized as conclusions. Possible directions of research for further understanding of the radiation recovery effect in electron/ion irradiated $Ce_{1-x}Gd_xO_{2-x/2}$ are also highlighted.

Chapter 2

Theoretical and Experimental background

2.1 Introduction

Ceramics are compounds of ionic and covalent bonds of cations and anions, and they are arranged regularly with the periodicity in crystalline solids. To understand the degradation of ceramics under ions and/or electrons irradiation, it often requires the analysis of physical properties under in-beam condition. Also, the background of the reference materials, ceria and Gd_2O_3 doped ceria which are used in this dissertation, need to be introduced especially for the structure and oxygen deficiency by trivalent cation doping. Fundamental knowledge of analytical methods in short and long ranges is important to understand physical and chemical property changes. Moreover, background of radiation dynamics should be introduced with an emphasis on complex displacement mechanism of ceramics with multi sublattices. In this chapter, the background of experimental techniques and fundamental displacement process relevant to this dissertation are described.

2.2 Crystals and ceramics

Crystals have a long-range order in periodic and they can be categorized into six crystal families and seven crystal systems according to the direction and magnitude (Table 2-1) [29,30]. The labels of a, b, c, and α, β, γ in Figure 2-1 are crystallographic axes and angles, respectively. Generally, ceramics are more complex than metals, which are usually contain two or more crystallographic sublattices with a combination of ionic and/or covalent bonds. These bonds give a high elastic modulus and hardness, high melting point, low thermal expansion, and excellent chemical resistance of ceramic materials [31,32]. The crystal structure of ceria (CeO_2),

Table 2-1. Crystal families and systems

Crystal family	Crystal system	Axis system	
Isomeric	Cubic	a = b = c	$\alpha = \beta = \gamma = 90°$
Tetragonal	Tetragonal	a = b ≠ c	$\alpha = \beta = \gamma = 90°$
Hexagonal	Hexagonal	a = b ≠ c	$\alpha = \beta = 90°, \gamma = 120°$
	Trigonal or Rhombohedral	a = b = c	$\alpha = \beta = \gamma \neq 90°$
Orthorhombic	Orthorhombic	a ≠ b ≠ c	$\alpha = \beta = \gamma = 90°$
Monoclinic	Monoclinic	a ≠ b ≠ c	$\alpha = \beta = 90°, \gamma \neq 90°$
Anorthic	Triclinic	a ≠ b ≠ c	$\alpha \neq \beta \neq \gamma \neq 90°$

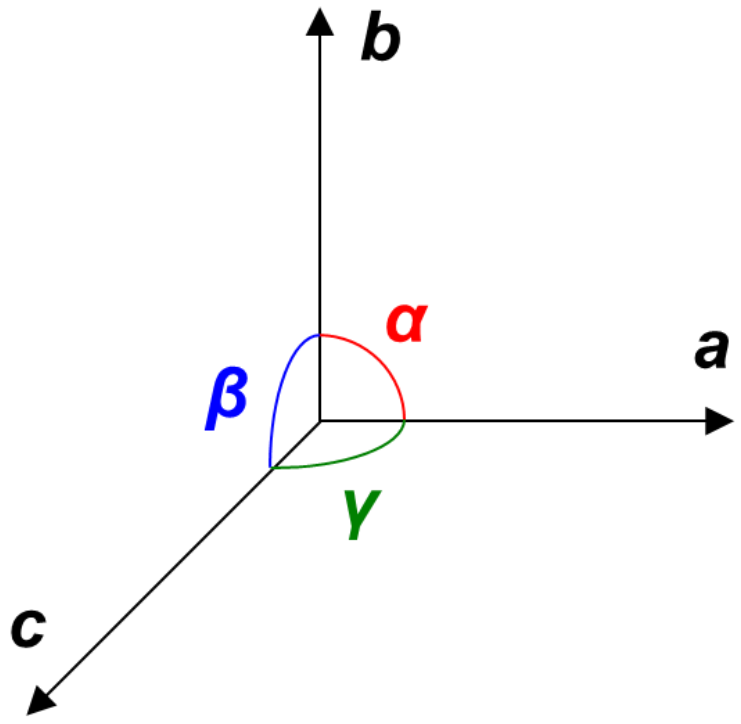

Figure 2-1. Crystallographic axes *a*, *b*, *c* and the angles α, β, γ in positive values.

which is the main compounds investigated in this dissertation, is shown in Figure 2-2 (a). As shown in Figure 2-2 (b), it forms the fluorite structure: the structure and stability of ceria will be discussed in the following section 2.2.1.

2.2.1 Cerium dioxide (CeO_2)

Cerium dioxide or ceria (CeO_2) is one of the prominent materials for a surrogate of PuO_2 and for an inert matrix fuel, such as rock-like oxide fuel [33]. It is noted that most oxide-based nuclear fuels have a fluorite structure. Ceria also possesses a stable cubic fluorite structure under ambient pressure from room temperature to the melting point (2477 °C) [Figure 2-2 (b)].

Ceria produces nature oxygen vacancies due to its non-stoichiometry occurring through the reduction and oxidization of cerium. Under the reducing condition, Ce (IV) is converted into Ce (III), and the reduced ceria is charge-balanced by forming oxygen vacancies. The composition of ceria can be expressed as CeO_{2-x}, where x in CeO_{2-x} represents the oxygen vacancy concentration. The reversible redox reaction in ceria is written in Kröger-Vink notation as below,

$$\mathrm{Ce(IV)} \leftrightarrow \mathrm{Ce(III)}, \tag{2-1}$$

$$2\mathrm{Ce}_{\mathrm{Ce}}^{\times} + \mathrm{O}_{\mathrm{O}}^{\times} \leftrightarrow 2\mathrm{Ce}_{\mathrm{Ce}}^{\prime} + 1/2\mathrm{O}_2(\mathrm{g}) + \mathrm{V}_{\mathrm{O}}^{\cdot\cdot}, \tag{2-2}$$

where the $\mathrm{Ce}_{\mathrm{Ce}}^{\times}$ and $\mathrm{O}_{\mathrm{O}}^{\times}$ are neutrally possessed Ce and O ions in their lattice sites (i.e., Ce^{4+} and O^{2-}), respectively. $\mathrm{Ce}_{\mathrm{Ce}}^{\prime}$ represents a Ce ion at a Ce ion lattice site with a localized mobile electron (i.e., Ce^{3+}), and $\mathrm{V}_{\mathrm{O}}^{\cdot\cdot}$ is positively charged oxygen vacancy (no electron localization). Ceria has a wide band gap energy (~ 6 eV) between 2*p* oxygen valence band and 5*d*, 6*s* cerium conduction band [34,35]. Between these two bands, there is an empty cerium 4*f* band, called $4f^0$ state, which is a narrow localized level in stoichiometric ceria [36]. As the oxygen atom is reduced, an electron is transferred to the empty 4*f* band and it is partially filled, leading the

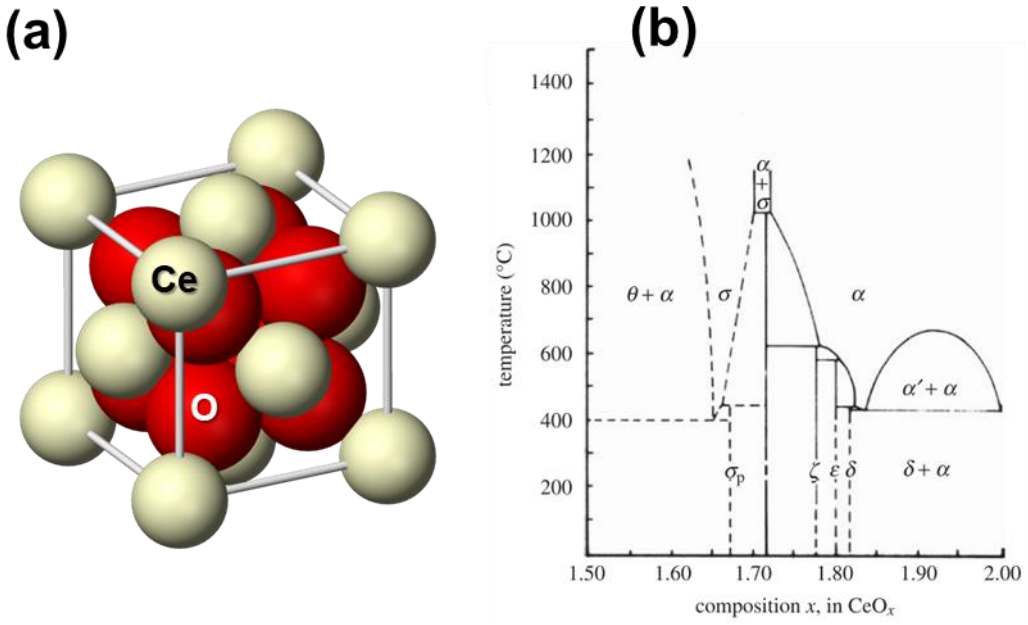

Figure 2-2. (a) Cubic fluorite-type crystal structure and (b) phase diagram of ceria [37].

band splitting into 4*f* full ($4f^1$) and 4*f* empty ($4f^0$) due to spin-orbit coupling of cerium ion [38].

2.2.2 Gd_2O_3 doped CeO_2

Gd_2O_3 doped CeO_2, as expressed by $Ce_{1-x}Gd_xO_{2-x/2}$, is expected to create oxygen vacancies by the substitution of Gd^{3+} into Ce^{4+} site since cations have similar Shannon ionic radius (i.e. Gd^{3+}: 1.053 Å, Ce^{4+}: 0.970 Å). However, due to the different valence states of Gd^{3+} into Ce^{4+} ions [39], a vacancy is created at an oxygen ion site as described by Kröger–Vink notation below,

$$2Ce_{Ce}^{\times} + O_O^{\times} + Gd_2O_3 \rightarrow 2Gd'_{Ce} + V_O^{\cdot\cdot} + 2CeO_2, \qquad (2\text{-}3)$$

where $Ce_{Ce}^{\times}$ and $O_O^{\times}$ represent the neutral charge state of Ce^{4+} on a cerium lattice site and O^{2-} on an oxygen lattice site, respectively. Gd'_{Ce} is a Gd^{3+} ion located at a cerium lattice site with -1 charge, and $V_O^{\cdot\cdot}$ is a vacancy at an oxygen lattice site with +2 charge [40]. In the $Ce_{1-x}Gd_xO_{2-x/2}$ system, the oxygen deficiency is mainly determined by the Gd_2O_3 content [41–43]. Besides, the Gd_2O_3 has a cubic bixbyite (C-type, Ia-3) structure as shown in Figure 2-3 (a) which is close to the fluorite (F-type, Fm-3m) structure. A unit cell of the C-type structure is built from eight-unit cells of the F-type structure, but the C-type structure includes 25% of ordered oxygen vacancies unless the F-type structure [44]. As a consequence of Gd_2O_3 doping, the crystal structure transforms from F-type to the double lattice parameter of C-type ordering oxygen vacancies. Figure 2-3 (b) is a phase diagram of Gd_2O_3 doped ceria examined by different authors. The temperature of ordering (T_{ord}), phase separation (T_{sep}), freezing transition (T_F), cation quenching (T_q), and ordering transition (T^q_{ord}) were evaluated by Monte Carlo (MC) modeling and density function theory (DFT) in $4 \times 4 \times 4$ supercells with 768 lattice sites by Žguns et al [45]. Also, the phase transition from fluorite (F) to C-type (C) was observed by experimental analysis such as XRD [46–48], XAFS [47], and gas analysis [49] at various

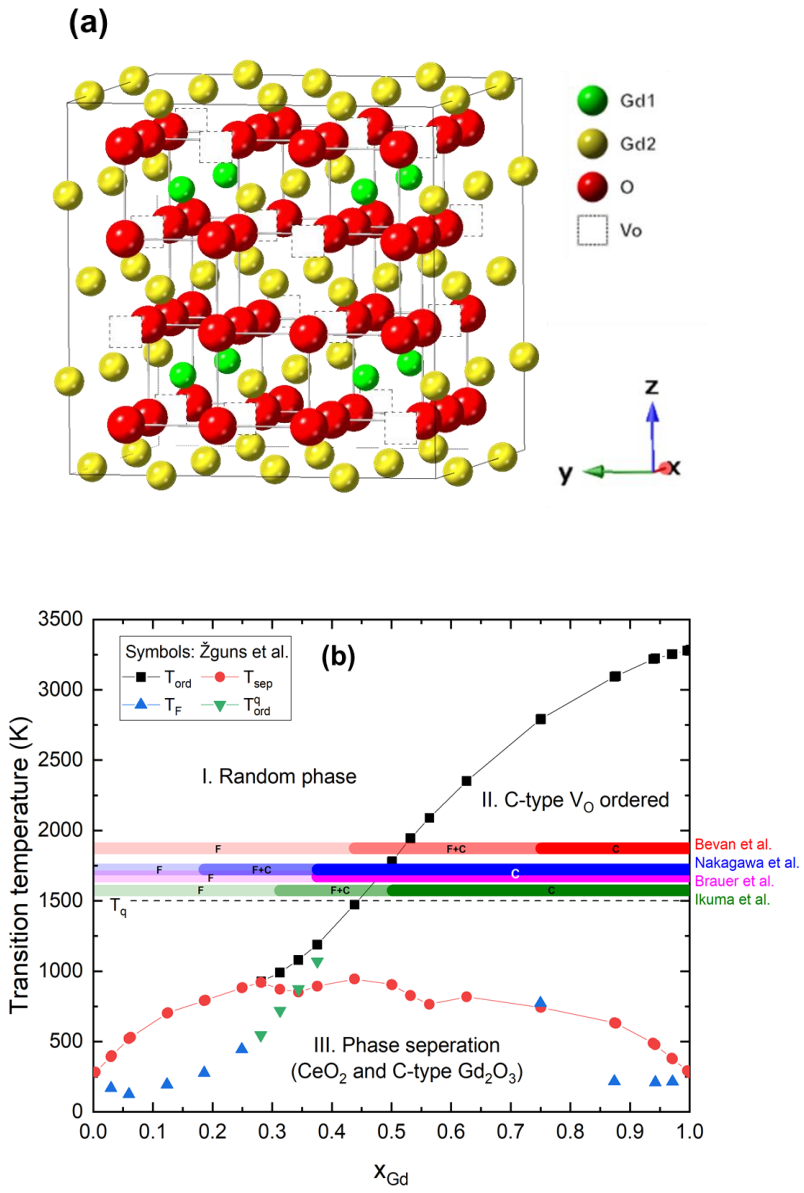

Figure 2-3. (a) Bixbyite (C-type) structure of Gd_2O_3 and (b) phase diagram of Gd_2O_3–CeO_2. Symbols represent the DFT calculation results conducted by Žguns et al. [45]. In the thermodynamic equilibrium, T_{ord} (black) and T_{sep} (red) are temperatures of ordering and phase separation, respectively. The ordering transition was hardly observed for $x_{Gd} < 0.3$, while the vacancy ordering occurred with phase transition for $x_{Gd} \gtrsim 0.3$. Cations were quenched at 1500 K (T_q) and ordering transition (T^q_{ord}) was observed for $0.27 \lesssim x_{Gd} \lesssim 0.4$. Oxygen freezing ($T_F$), which is the rearrangements of vacancies upon cooling are mostly stopped, was observed for $x_{Gd} \lesssim 0.27$ and $\gtrsim$ 0.75. The red, blue, magenta and green horizontal bars represented experimental data of phase transition between fluorite (F) to C-type (C) suggested by Bevan et al. [49], Nakagawa et al. [47], Brauer et al. [46], and Ikuma et al.[48]. F+C is a biphasic region.

quenching temperatures. The fluorite structure started to transform around x_{Gd} = 0.2 ~ 0.5 to the C-type structure but it strongly depends on T_q and analysis methods.

The oxygen vacancy ordering was observed in nano-sized domains formed by the aggregation of dopant Gd^{3+} ions and oxygen vacancies, as observed by electron energy loss spectroscopy (EELS) analysis [50], high-resolution transmission electron microscopy (HRTEM) and the selected area electron diffraction (SAED) patterns [51]. As a consequence of the oxygen vacancy ordering, the disordering is produced by the influence of electrostatic repulsion with oxygen vacancies in the C-type structure, while cations in fluorite keep their perfect cube with 8 coordinated oxygen ions [42]. In particular, it affects the distribution of the interatomic distance between cation-cation pairs rather than cation-oxygen pairs. In addition, the clustering of the dopants with associated oxygen vacancies is increasing with dopant concentration increasing. The clusters reduce the concentration of freely mobile oxygen vacancies that rather decreases conductivity at high concentrations of dopants [51–54].

2.3 X-ray diffraction (XRD) analysis and the Rietveld refinement

X-ray diffraction (XRD) technique helps the understanding of the physical properties of metals, ceramics, polymers, and other solids allowing one to understand the arrangement and distance of lattice planes in a form of crystals. W.H. Bragg and W. L. Bragg interpreted the crystal diffraction by using the wavelength of x-ray, and they expressed it as Bragg's law [Eq. (2-4)].

$$n\lambda = 2d \sin\theta. \qquad (2\text{-}4)$$

When the phase difference between two or more waves is half of the wavelength, the wave is offset and disappears, but when the phase difference is an integer (n) multiple of the wavelength (λ), the amplitude is amplified, and the intensity becomes greater. In Figure 2-4, the distance from A to B is $d \sin\theta$, where d is lattice distance, θ for Bragg's angle, which is

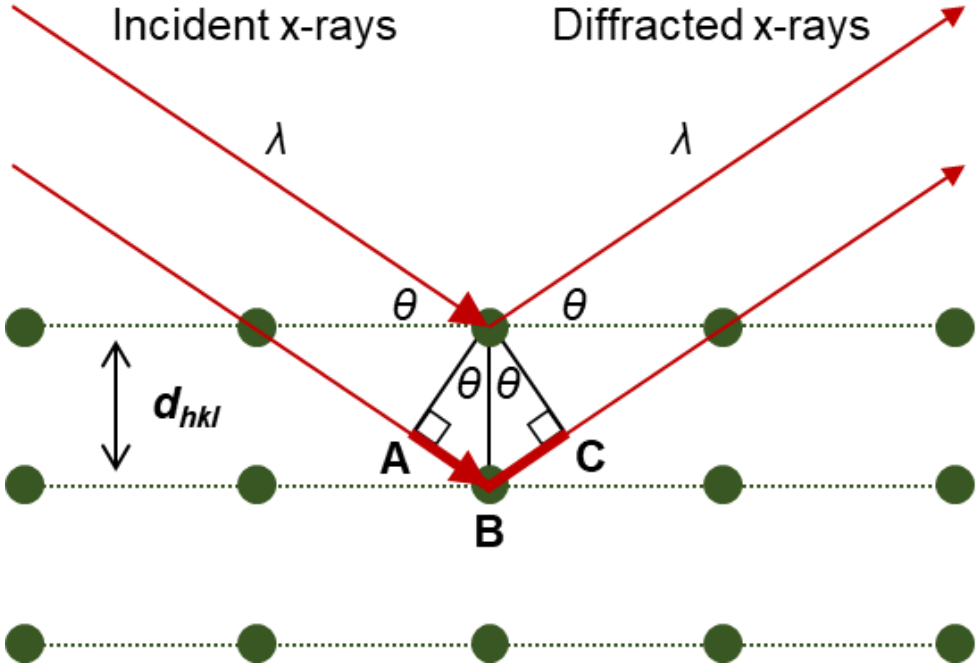

Figure 2-4. Braggs' law reflection

equal to the distance from B to C. Therefore, if AB = BC = $d \sin\theta$ and the following Eq. (2-4) is satisfied, x-rays are strongly diffracted.

In the microcrystalline powder sample, a number of crystalline are combined in random directions. Furthermore, one powder sample consists of more than one phase. In this multi-phase sample, the single Braggs' reflection is hard to examine the crystal structure with high symmetry refinement, since diffracted XRD intensities are overlapped in the XRD patterns. For the multi-phase sample XRD analysis, the Rietveld refinement can be used by fitting Gaussian, Lorentzian, or Pseudo-Voigt profiles using the least-square method, and this method can use for quantitative analysis [55]. The Rietveld refinement is conducted by a computer algorithm and free software programs are typically used for instance Fullprof [56], GSAS [57], and RIETAN [58]. For the operation of Rietveld refinement, it is important to determine crystal structure if the initial structure is known, unless it should be operated by *ab-initio* calculation. Reliable crystal structure models can obtain from the database such as 'Inorganic Crystal Structure Database' [59], 'American Mineralogist Crystal Structure Database' [60], and Crystallography Open Database [61].

The quality of Rietveld refinement is measured by parameters of goodness factor (χ^2), weighted profile factor (R_{WP}) and R expected (R_{EXP}). For the interpretation, values of observed and computed XRD peak intensity at the position of $2\theta_i$ are assigned to $y_{i,O}$ and $y_{i,C}$, respectively. The Rietveld algorithm targets to minimize the weighted sum of squared differences between the observed and computed intensity values [i.e., $\sum w_i\left(y_{i,O} - y_{i,C}\right)^2$], where w_i is $1/\sigma^2[y_{i,O}]$. $\sigma[y_{i,O}]$ is uncertainty estimate for $y_{i,O}$. R_{WP} is the most meaningful of the weighted profile R-factors because of the minimized residuals. It can be expressed by,

$$R_{WP}{}^2 = \frac{\sum w_i(y_{i,O} - y_{i,C})^2}{\sum w_i(y_{i,O})^2} \quad (2\text{-}5)$$

The best possible value of R_{WP} expected for the number of data points (N) can be represented as the expected R-factor, R_{EXP} [62]. R_{EXP} is described below,

$$R_{EXP}{}^2 = \frac{N}{\sum w_i (y_{i,O})^2} \quad (2\text{-}6)$$

The statistical quality of the refinement is explained by Chi-squared (χ^2). They are calculated through equations as written below,

$$\chi^2 = R_{WP}/R_{Exp} \quad (2\text{-}7)$$

A goodness of fit can be defined by χ^2, and its value of 1.3 or less is usually considered reasonable [62]. Too small χ^2 value means that the counting statistical errors are greater than the model errors either because of poor counting statistics or because of high background by slowly varied angle [62].

2.4 Displacement damage and Energy loss

A displacement cascade is induced by an elastic collision between a high-energy particle and a target atom. The initially displaced atom directly from an incident radiation particle is called as a primary knock-on atom (PKA). If the PKA has sufficient energy, the knocked lattice atom results to rest in an interstice of lattice, which generates an interstitial atom. Complementary, the original lattice site remains vacant to form a vacancy. This simple pair of interstitial and vacancy remaining stable is called as a Frenkel pair.

To initiate displacement from the lattice site, the transferred kinetic energy to the lattice atom should be higher than the threshold displacement energy (E_d). E_d is a material dependent physical quantity. In general, experimental measurement of E_d is difficult for ceramics due to their complex structure [11,63]. The values of E_d are also dependent on the crystallographic direction [64], and temperature.

In a collision between a charged particle and a target atom nucleus, the mean free path between these two-body collisions should be greater than the interatomic spacing. We can apply the law of conservation of energy and momentum in the elastic collision satisfied with nonrelativistic mechanics.

$$T = \frac{4M_1M_2}{(M_1+M_2)^2} E\sin^2(\frac{\theta}{2}), \quad (2\text{-}8)$$

where T is the transferred energy to the PKA, E is the incident particle energy, θ is the angle of deflection of the incident particle as a result of the collision, M_1 is incident particle mass and M_2 is struck atomic mass. When the θ = 0, the T shows the maximum value, T_m, which is written as,

$$T_m = \frac{4M_1M_2}{(M_1+M_2)^2} E \quad (2\text{-}9)$$

For the case of high-energy electrons, relativistic quantum mechanics should be used for the calculation. As assuming that M_1 is an electron (m_e), the rest energy is written by Eq. (2-10) with an approximation of $M_1 \ll M_2$ as follows,

$$M_1c^2 = m_ec^2 = 0.511 \text{ (MeV)}, \quad (2\text{-}10)$$

where c is the light velocity (2.998 × 10^8 m/s). By adding the relativistic correction, T_m given by the incident electron to the target atom is expressed as,

$$T_m = \left(\frac{2m_e}{M}\right)\left(\frac{E+2m_ec^2}{m_ec^2}\right)E, \quad (2\text{-}11)$$

where E is incident electron energy (MeV), M is mass of PKA (u).

To understand displacement damage generation by electron irradiation, E_d should be higher than T_m. The relationship between T and E_d can be explained by,

i) $T_m < E_d$: No displacement occurs,

ii) $T_m \geq E_d$: Displacement occurs displaced atoms remain as the Frenkel pairs producing defects such as displacement loop or voids.

iii) $T_m \gg E_d$ (i.e., T > ~1 keV): PKA produce displacement chain reaction to surrounding atoms, which is called as cascade collision.

The displacement cross-section (σ_d) for electron-nuclear collision can be measured for the range of angle between θ_m and π for the quantity of greatest interest in the interpretation of radiation damage. σ_d was evaluated by McKinley-Feshbach formula [65],

$$\sigma_d = \frac{\pi}{4}(b')^2\left\{\frac{T_m}{E_d} - 1 - \beta^2 \ln\frac{T_m}{E_d} + \pi\alpha\beta\left[2\left(\frac{T_m}{E_d}\right)^{1/2} - \ln\frac{T_m}{E_d} - 2\right]\right\}, \qquad (2\text{-}12)$$

where $b' = \frac{2Ze^2}{mv^2}(1-\beta^2)^{1/2}$, $\alpha = Ze^2/\hbar c$, $\beta = v/c$, v is velocity of the electron incident on a nucleus of charge Ze. The σ_d calculation for O and Ce sublattice in ceria as a function of incident electron energy will be shown in Chapter 4.

When a charged particle incident to a target material, it loses the kinetic energy through interaction with the nuclei or electrons in the target matter. The energy loss in a targeted matter determines the final distribution of defects. The energy loss which is referred to as stopping power is noted as

$$S(E) = -\frac{dE}{dx} = \left(-\frac{dE}{dx}\right)_n + \left(-\frac{dE}{dx}\right)_e, \qquad (2\text{-}13)$$

where the total stopping power $S(E)$ is defined as the differential of its energy (E) by the penetration depth, or $-\frac{dE}{dx}$. The total stopping power is the sum of nuclear (n) and electronic (e) stopping power. The electronic and nuclear stopping power calculation results for oxygen ions in CeO_2 are shown in Figure 2-5. The threshold displacement energy of oxygen ion ($E_{d,O}$) value was used as 14 eV for this calculation. The left y-axis is electronic stopping power (S_e) and the right one is nuclear stopping power (S_n). The S_e showed higher values than the values of S_n, and the energy loss mostly occurred by S_e with the increase of the primary electron energy. For the thin TEM samples (thickness: ~100 nm), S_e is negligible for the E ranging of 200 keV < E < 1500 keV as 5 ~ 6 eV, while the think samples for CL measurement (thickness: ~150

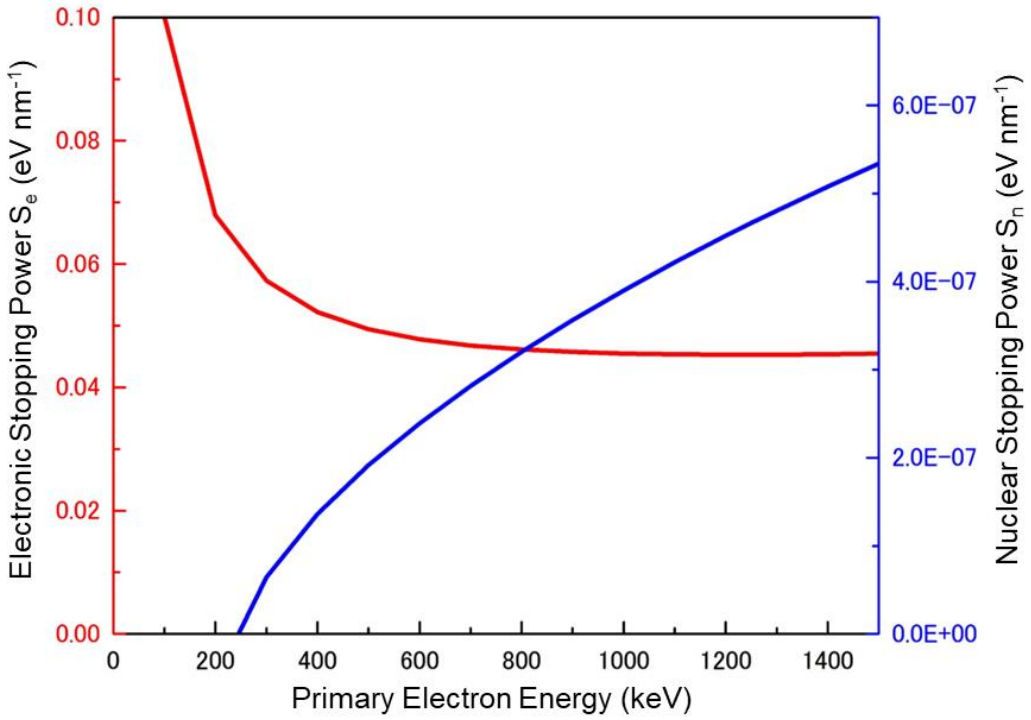

Figure 2-5. Oxygen ion electronic and nuclear stopping power in CeO_2 as a function of primary electron energy. The threshold displacement energy of oxygen ion ($E_{d,O}$) was 14 eV for this calculation.

μm) showed high S_e as 8 ~ 9 keV. Despite high S_e values for thick samples, the reduction of S_e is dominant only for E < 200 keV. Therefore, displacement is mainly depending on the increase of S_n versus primary electron energy.

2.5 F center and CL spectroscopy

Defect charge state and electronic structure is important properties of an ionic crystal. The defects located within band gap cause absorptions and emissions of visible light. This defect is called F center (Farbe center or color center). F centers are generated in laser-active metallic oxides. It is formed by as the anion is excited; one or more unpaired electrons are trapped by the anion vacancy site. F centers are designated according to its charge state, such as F^0, F^+ or F^{++} centers by the number of captured electrons of two, one, or zero, respectively.

Figure 2-6 illustrates F centers and Ce ions (Ce^{3+}, Ce^{4+}) in ceria. The distribution of oxidation number of Ce ion around the F center was involved in the charge state of the F center according to the number of electrons left behind at a vacancy or 4*f* level [66,67]. The conversion of F and F^+ centers is related to the excitation and ionization cross-section, the intensity of incident electrons, and the number of excited F^+ centers (F^{+*}) [68]. The energy level of F centers is ceria was interpreted by photoluminescence spectroscopy, electron paramagnetic resonance (EPR), and density functional theory (DFT) calculation [69].

Cathodoluminescence (CL) is an optical and electromagnetic phenomenon using pulses from high-energy electrons (cathode rays) as the means of excitation. The CL emission is generally collected for imaging or spectroscopy. CL image gives an important information on different phases, point defects or impurities localization. On the other hand, CL spectroscopy provides a specific wavelength emitted from impurities and defects in band gap materials giving its charge number.

The electron beam for CL measurement is generally produced from an electron microscope [e.g., SEM, scanning transmission electron microscope (STEM)], electron-prove microanalysis (EPMA), or cathodoluminescence microscope. These primary electron energies are generally too high to directly excite electrons. Therefore, the inelastic scattering of the primary electrons in the target leads to the emission of secondary electrons, and the secondary electrons excite the electrons with a kinetic energy higher than band gap of the target.

CL emission process can be explained by the electron and hole trapping and de-trapping in phosphor interaction. At first, the secondary electrons are produced by elastic and inelastic scattering process. They produce electron and hole pairs and give rise electron and hole trapping at defects or impurities levels in the band gap. The trapped electrons and holes are excited by primary and secondary electrons. Then, light emitted by radiative decay from excited states. Finally, the electrons and holes are recombined together, and CL light is emitted. The CL cross-section (σ_{CL}) can be shown schematically in Figure 2-7 and written as,

$$\sigma_{CL} = \sigma_i \sigma_t \sigma_e \sigma_r, \tag{2-14}$$

where σ_i is the ionization cross-section generating free electron hole pairs by elastic and inelastic collision, σ_t is the trapping cross-section for thermalized electrons or holes on electronic levels of defects or impurities, σ_e is the excitation cross-section of these levels by primary and secondary electrons, and σ_r is the radiative-decay cross-section from excites state [25]. Non-radiative recombination takes place from ground state to the valence band states [70].

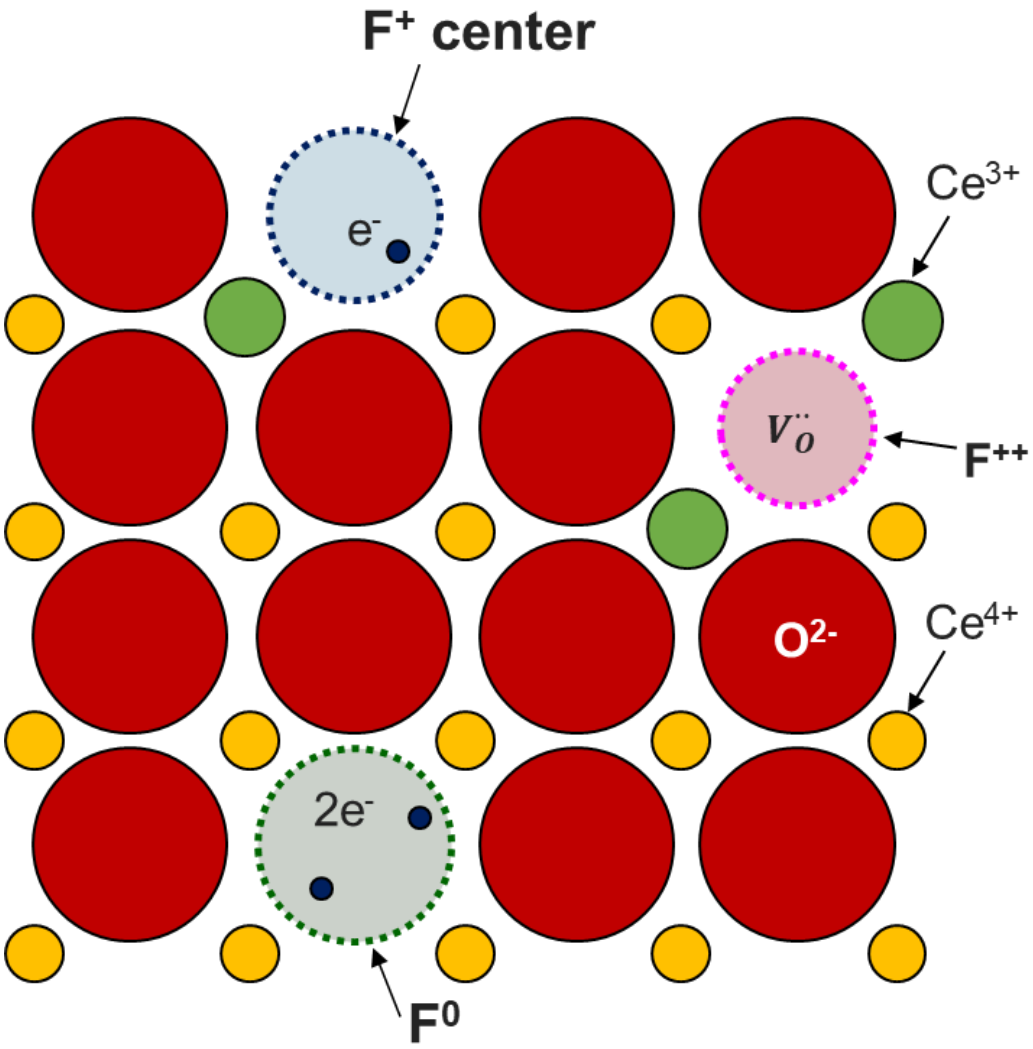

Figure 2-6. Scheme of F centers, cerium (Ce^{3+}, Ce^{4+}) and O^{2-} ions in ceria (100) plane.

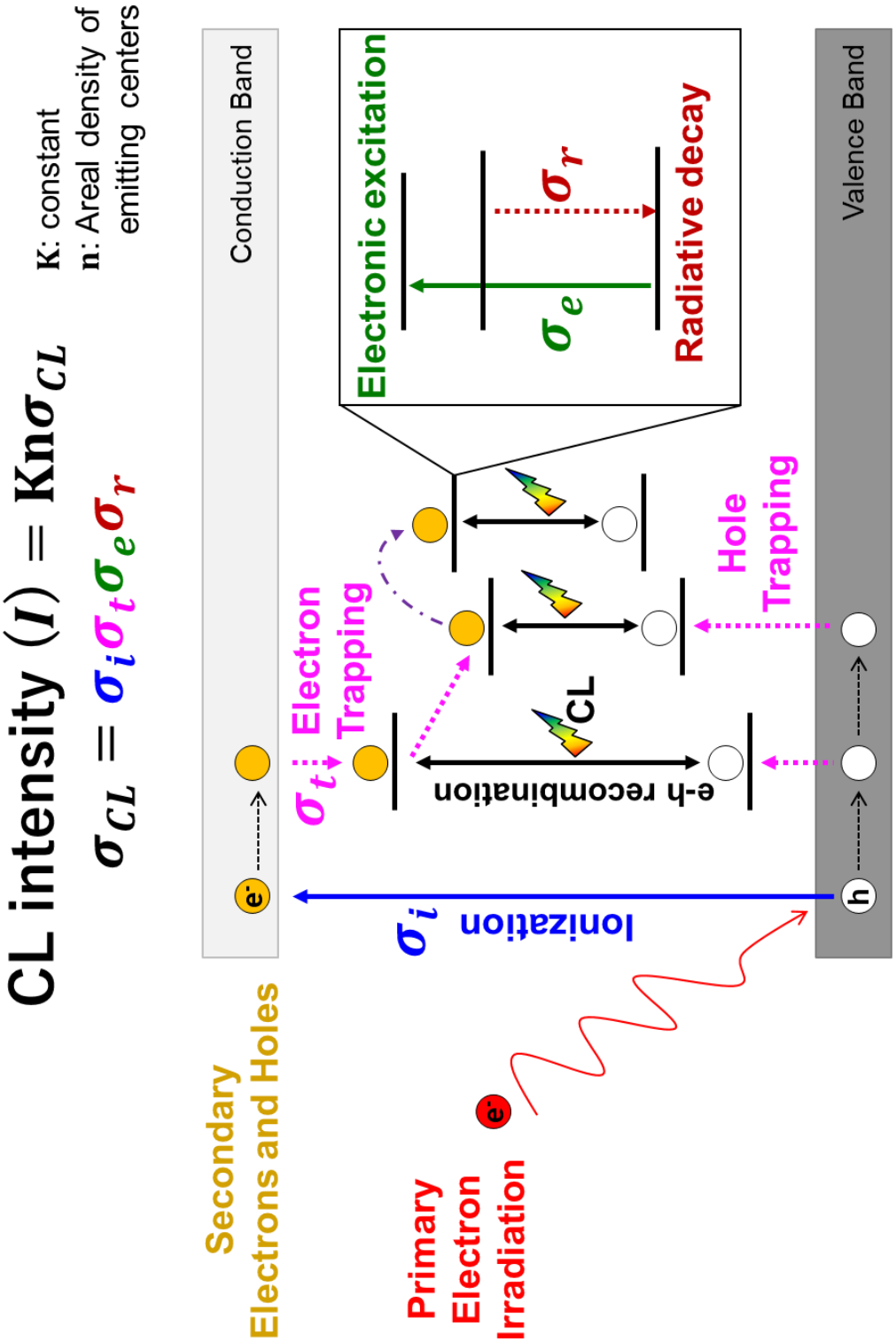

Figure 2-7. Scheme of cathodoluminescence (CL) emission process.

Chapter 3

Experimental detail

3.1 Introduction

In this dissertation, atomistic and electronic characteristics of radiation-induced displacements in ceramics and their crystal microstructure evaluation with heavy ion irradiation were elucidated in a wide range of scale analysis methods to understand the synergetic effect and kinetics of point defects under irradiation. In this chapter, the structural properties of virgin ceramics before the irradiation, and electron/ion irradiation experimental conditions were described in detail. Moreover, experimental techniques, for instance, XRD, Raman spectroscopy, TEM methods, *in-situ* CL spectroscopy under high-energy electron irradiation, and experiment conditions operated in this dissertation were described.

3.2 Specimens

Single crystal ceria, polycrystalline ceria and Gd_2O_3 doped ceria were used in this dissertation. The single crystal ceria was supplied from Dr. W. J. Weber in Oak Ridge National Laboratory in USA. The thickness of the specimen is around 1 mm. It was attached to half-disk shape of tungsten washer in diameter of 3 mm to adjust the specimen. The sample image is shown in Figure 3-1.

3.2.1 Synthesis

Polycrystalline ceria and Gd_2O_3 doped ceira ($Ce_{1-x}Gd_xO_{2-x/2}$) ($0.01 \leq x_{Gd} \leq 0.5$), were synthesized by solid state method. Ceria and Gd_2O_3 powders were supplied by Rare Metallic Co., Ltd., with 99.9% of purity. The impurities in ceria were shown in Table 3-1. Ceria and

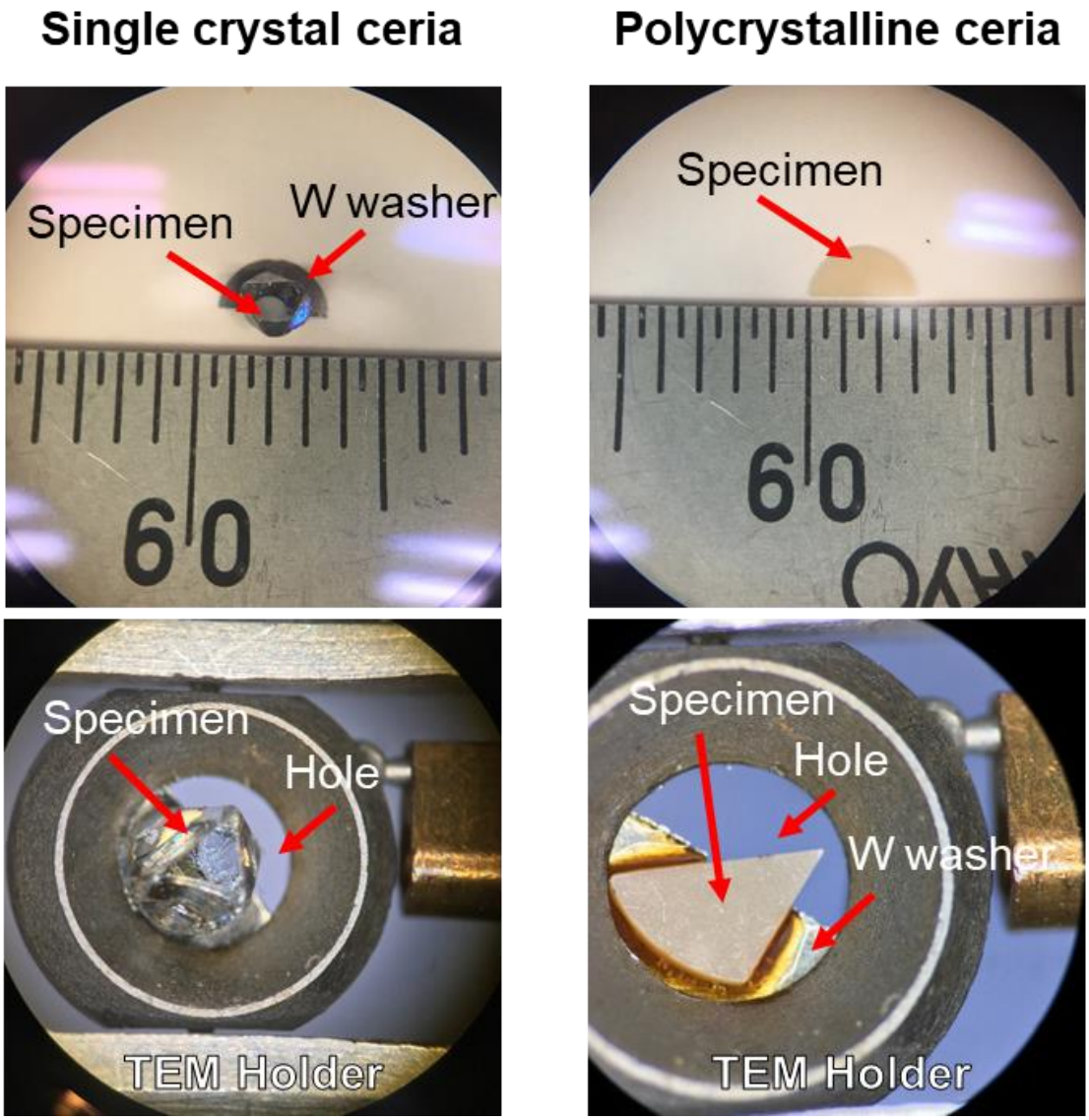

Figure 3-1. Single crystal and polycrystalline ceria specimen images.

Table 3-1. Impurities in ceria powder.

Element	Concentration (ppm)
Y_2O_3	< 5
La_2O_3	10
Pr_6O_{11}	< 5
Nd_2O_3	6
Sm_2O_3	< 5
Eu_2O_3	< 5
Gd_2O_3	< 5
Tb_4O_7	< 5
Dy_2O_3	< 5
Ho_2O_3	< 5
Er_2O_3	< 5
Tm_2O_3	< 5
Yb_2O_3	< 5
Lu_2O_3	< 5
CaO	< 5
Fe_2O_3	< 5
SiO_2	< 20

Gd_2O_3 powders were ball milled homogeneously with ethyl alcohol for 24 hours. The mixtures were compacted into a pellet by uniaxial pressure at 30 MPa for 15 minutes to make a condensed pellet type sample ($\varphi \approx 10$ mm, $t \approx 2$ mm). They were compressed again sealed in a plastic bag by hydraulic pressure at 150 MPa for 30 minutes. The compacted pellets were put in an alumina crucible within ceria powder and sintered in the air-atmosphere at a temperature of 1500 ℃ for 12 h followed by an additional annealing at 1000 ℃ for 3 h in the air. The sintered compact samples have ~95% of relative densities. The sintered samples were prepared as a disk type for ion irradiation in a diameter of 3 mm and a thickness of 150 μm. They were polished by diamond slurries in particles size of 9 μm, 3 μm and 0.5 μm (Masashino Denshi, inc., MP-1000(W)), and then removed distortion, deterioration layers and fine scratch marks using colloidal silica (Masashino Denshi, inc.).

3.2.2 Heavy ion irradiation

The thin disk-type samples in thickness of 150 μm were irradiated at ambient temperature with 200 MeV $^{131}Xe^{14+}$ ions using the Tandem accelerator at Tokai Research and Development Center, Japan Atomic Energy Agency (JAEA-Tokai) to fluence ranging from 3×10^{11} to 1×10^{13} cm^{-2}. The electronic (S_e) and nuclear (S_n) stopping power of the 200 MeV Xe^{14+} ion for CeO_2 and $Ce_{0.5}Gd_{0.5}O_{1.75}$ were calculated with the Stopping and Range of Ions in Matter (SRIM) code [71] with assumptions of displacement energies of 60 eV for Ce, 70 eV for Gd and 30 eV for O atoms, respectively [9,72]. Initial values of S_e at the surface were evaluated to be 27.3 and 26.5 keV nm^{-1} for CeO_2 and $Ce_{0.5}Gd_{0.5}O_{1.75}$, respectively, whereas values of S_n at the surface region were negligible, 0.07 and 0.05 keV nm^{-1} for CeO_2 and $Ce_{0.5}Gd_{0.5}O_{1.75}$, respectively, compared to S_e. The maximum of S_n for CeO_2 and $Ce_{0.5}Gd_{0.5}O_{1.75}$ is 0.96 and 0.89 keV nm^{-1} at a depth of 11.3 and 12.2 μm, respectively.

3.2.3 Ion thinning

For the thin-foil sample preparation suitable for TEM observation, the thin disk-type samples with a diameter of 3 mm were attached to a single-hole molybdenum TEM grid (Φ = 1.2 μm) to keep them from destruction during the dimpling process. The center of the sample was dimpled using diamond slurries from the opposite side of the irradiated surface, followed by an ion thinning using an ion-milling system (PIPSII M-695, Gatan Inc.) with 5 keV Ar ion beams at 8 deg. until a small hole was formed. A dual-beam mode for both side milling was followed to enlarge the hole size up to ~200 μm. Contamination and Ar-ion damaged layers were finally removed using 0.5 keV Ar ions for 30 min. A thin carbon film was coated on the irradiated samples to weaken the charge-up effect during TEM observations.

3.3 XRD measurement

XRD experiments were performed at room temperature by an XRD Rigaku. SmartLab® diffractometer with Cu-Kα ($K\alpha_1$ = 0.15406 nm, $K\alpha_2$ = 0.15444 nm) radiation x-ray source (30 mA, 40 kV) of monochromatic θ-2θ scans. The XRD facility is shown in Figure 3-2. XRD patterns were recorded under continuous rotation from 20 to 90 2θ deg. at a step size of 0.01 deg. A part of sintered virgin samples was ground to a powder and was mounted in a glass holder with a volume of 200 mm^3, and the pattern was obtained with a scan speed of 10 deg. min^{-1}.

On the other hand, XRD patterns of ion-irradiated samples were measured with a bulk type of samples. The Cu-Kα X-ray penetration depth in $Ce_{1-x}Gd_xO_{2-x/2}$ is 2.26 μm for 90 deg. [73], while the projected range of 200 MeV Xe^{14+} ions is 11 ~ 12 μm. Therefore, signals from ion-irradiated samples were generated from the irradiated surface region, including ion tracks caused by electronic stopping power [71], and the unirradiated layer beneath the ion-irradiated surface does not influence the XRD patterns. A non-reflective holder, made with single crystal

Figure 3-2. XRD measurement facility (SmartLab, Rigaku Co.) at the Center for Advanced Instrumental Analysis in Kyushu University

silicon in an orientation that does not satisfy the diffraction conditions, was used for holding ion-irradiated samples of a relatively small size of 3 mm in diameter with a scan speed of 3 deg. min^{-1} to enhance the intensity. The XRD patterns from thin disk-shaped samples were also obtained by the virgin samples in the same measurement conditions to compare the intensity with those of irradiated samples. The crystal structure of each sample was refined by the Rietveld method using FullProf suite software [56] based on the split Pseudo-Voigt function, and the XRD patterns from Cu-$K\alpha_1$ radiation were only used for the analysis.

3.4 Raman spectroscopy

Micro-Raman spectra were recorded at room temperature with 532 nm Nd-YAG laser excitation in the backscattering geometry using an Invia Reflex® Renishaw spectrometer coupled with an Olympus microscope containing a $x - y - z$ stage. The TO/LO peak of silicon wafer was used as a reference spectrum. Spectra were collected between 100 and 1100 cm^{-1} for virgin $Ce_{1-x}Gd_xO_{2-x/2}$ samples with a focal spot of 1×1 μm^2 inside a single grain and collected through a 100 times objective. The laser power was kept below 1-mW to avoid in-beam sample annealing. Raman spectra were obtained from virgin samples in CEA, France by Dr. Jean-Marc Costantini.

3.5 Transmission electron microscopy (TEM)

The SAED patterns and bright-field (BF) TEM images were taken by using a conventional TEM (JEM-2100HC, JEOL Ltd.) in the Ultramicroscopy Research Center (URC) of Kyushu University at an accelerating voltage of 200 kV. A photo of JEM-2100HC is shown in Figure 3-3. For the imaging, a parallel beam was used with the opened condenser lens aperture and spot size 2. A biaxial holder (JEOL EM-31630) was used to tilt the sample up to ± 38° and ± 30° to x and y-axis, respectively. JEM-2100HC performance is written below.

Figure 3-3. A conventional TEM (JEM-2100HC, JEOL Ltd.) in Kyushu University.

- Acceleration voltage: 100, 120, 200 kV
- Resolution: 0.31 nm for point, 0.14 nm for lattice
- Magnification: 1 k ~ 800 k
- Minimum probe diameter: 1~5 μm

3.6 High voltage electron microscope (HVEM)

The HVEM (JEM 1300NEF, JEOL Ltd.) of the URC was operated to detect *in-situ* CL under high-energy electron irradiation. A photo of JEM-1300NEF is shown in Figure 3-4. A scheme of it below the acceleration tube system is shown in Figure 3-5. The electrons are emitted from LaB_6 filament and accelerated by using the acceleration tube with certain energies. The intensity of the electron beam and parallel illumination is adjusted by the condenser lens and irradiated to the specimen. It is possible to observe and record a magnified image of the specimen on the fluorescent screen if the specimen is very thin where electrons transmit the specimen. High-resolution imaging by using an Omega-type energy filter, elemental mapping with SDD XEDS detector, or EELS system are available with the HVEM. The performance of the HVEM is written below.

- Acceleration voltage: 400 ~ 1250 kV
- Resolution: 0.12 nm for point, 0.10 nm for lattice
- Magnification: 0.2 k ~ 1200 k
- Minimum probe diameter: 1.6 nm

Figure 3-4. HVEM (JEM 1300NEF, JEOL Ltd.) – CL facility in Kyushu University.

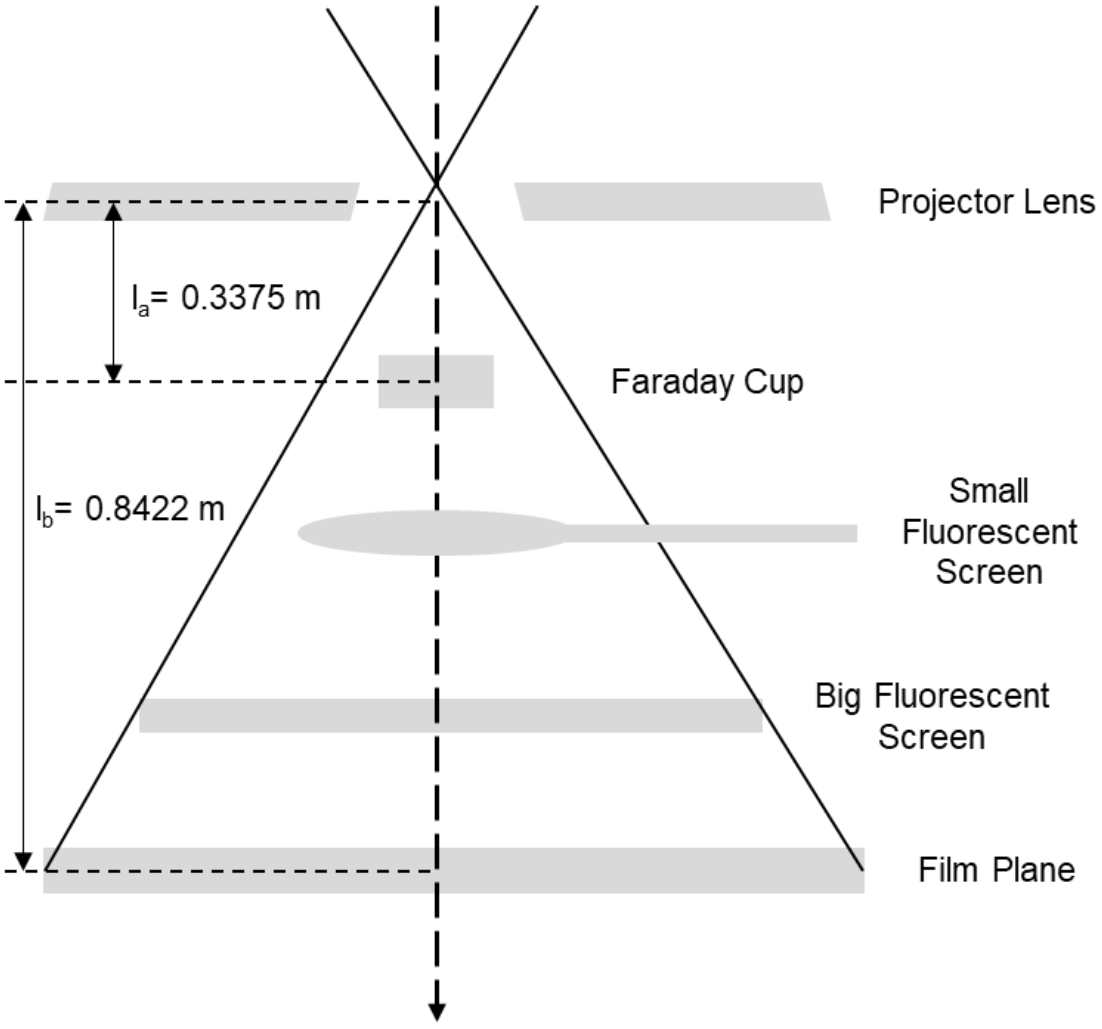

Figure 3-5. Scheme of JEM-1300NEF below projector lens.

3.7 Scanning electron microscope (SEM)

SEM produces images of a specimen by scanning a focused electron beam in a vacuum on a specimen. Secondary electrons, backscattered electrons, x-ray, lights, etc. are emitted from the specimen during the scanning of the electron beam. The SEM consists of an electron gun to emit electrons, the condenser lens and scanning coil to scan electrons, the specimen stage to put and arrange the specimen, detector to detect emitted from the specimen surface. The SEM (SU6600, Hitachi Ltd.) of the Center of Advanced Instrumental Analysis at Kyushu University was operated, and it is shown in Figure 3-6. The focused beams of electrons (0.5 ~ 30 keV) were used from the Schottky emission electron source. The SEM is interfaced with a CL system (Gatan Inc.) to collect CL spectra. The performance of the SEM is written below.

- Secondary electron resolution: 3.0 nm (1 kV), 1.2 nm (30 kV)
- Reflected electron resolution: 3.0 nm (30 kV)
- Vacuum level: 10 ~ 300 Pa (for low vacuum), ~10^{-4} Pa (for high vacuum)
- Magnification: 10 ~ 600 k
- Probe current: 1 ~ 200 nA

3.8 *In-situ* CL spectroscopy system and measurement conditions

3.8.1 High-energy electron irradiation

The CL emission was collected through an optical fiber probe system, which is installed near the specimen port in the HVEM as shown in Figure 3-7. An optical fiber probe was used to correct CL signals, which consist of an optical fiber probe with a 600 μm core diameter and copper coating, which is designed for high throughput in the 180 ~ 1200 nm wavelength range

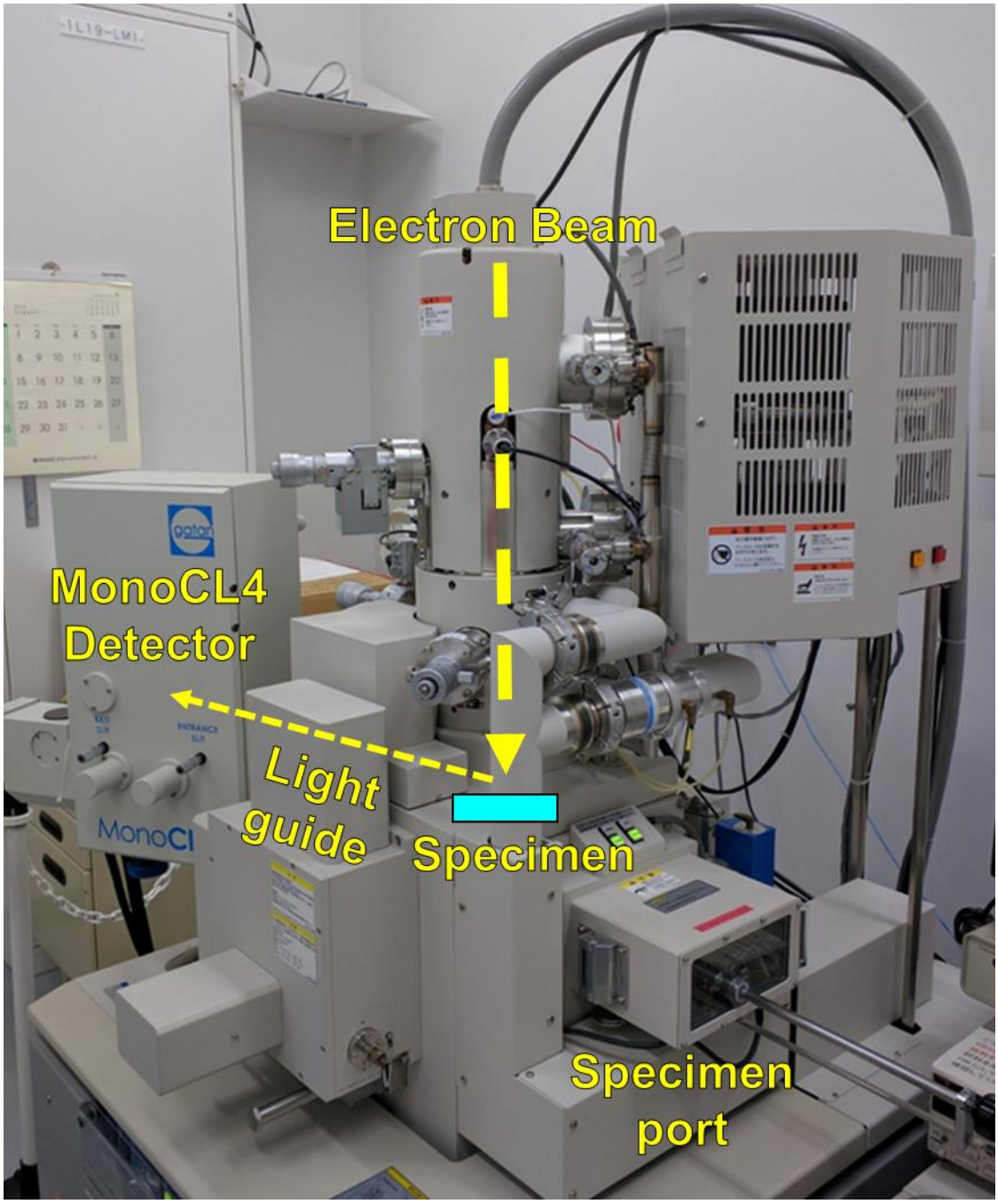

Figure 3-6. SEM-CL facility view of specimen port with CL detection guide lines and a detector.

(ref. 151-AC-AC-UV600, Chiyoda Electronics Co., Ltd). The fiber was inserted through a small hole in diameter of 2 mm and it was aligned at 44° from the electron beam direction without any disturbance for TEM observation. CL signals can be collected with the cooperation of various sample holders and other analyzing tools. CL spectra in the 200 ~ 950 nm wavelength were recorded with a Czerny-Tuner HAMAMATSU MCA spectrometer (PMA-12 C10027-1) equipped with a cooled CCD linear image sensor (1024 channels). The wavelength resolution of the spectrometer was 2 nm. Each spectrum can be taken under the electron beam.

The electron energy was changed during the CL measurement for 400, 600, 800, 1000, and 1250 keV. The electron beam-current density was also changed by changing the intensity of the condenser lens. The electron beam flux (φ) was adjusted in the range from 2.6×10^{21} to 7.7×10^{21} $m^{-2}s^{-1}$ with a beam diameter of 30 μm at the specimen position. The thickness of specimens is ~150 μm for CL measurement for the high number of counts from the electron irradiation. Therefore, the observation of microstructure using HVEM during CL measurement is not available. The half disk-shaped sample was used to adjust the shape, size, and current of the transmission electron beam at the hole in the specimen. The CL spectra were obtained in the magnification × 10k. The specimen holder was used for a biaxial cooling holder (GATAN636). The holder was equipped with a liquid-nitrogen cooling stage for temperature down to about 100 K and up to room temperature (300 K), preventing excessive in-beam heating of samples and temperature control and regulation. The CL spectra were detected for 30 seconds under electron beam in wavelength raging between 195 and 950 nm. The spectra were averaged out for 5 recordings and repeated 5 times for high reproducibility.

Table 3-2. Optical fiber probe performance used in HVEM (JEM-1300NEF).

Optical fiber	SiO_2, Cu coating, core φ = 600 μm, UV transmission
Wavelength range	180 ~ 1200 nm
Fiber protection	Stainless tube, φ = 1.8 mm
Connector	SMA905
Fiber optic application	Optical ball lens, φ = 1 mm
Loss in fiber	In the near the visible range (< 0.04 dBm^{-1} at 400 nm)
Remain in fiber	In the near UV range (< 0.3 dBm^{-1} at 300 nm)

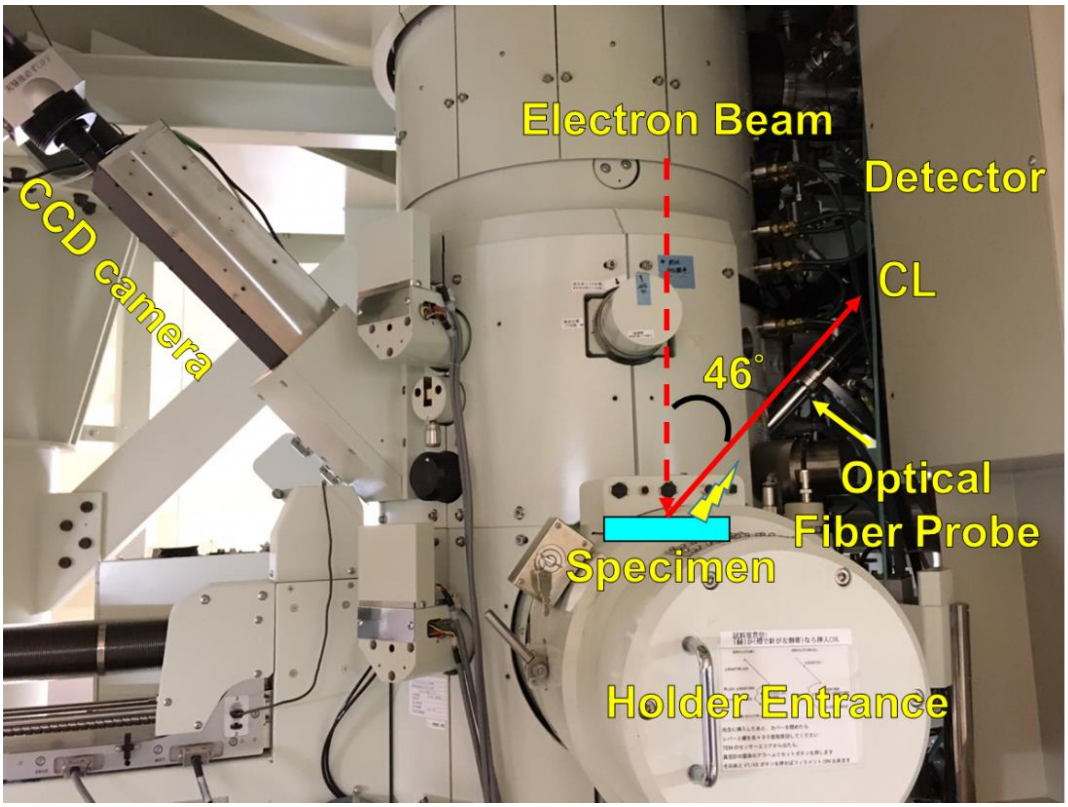

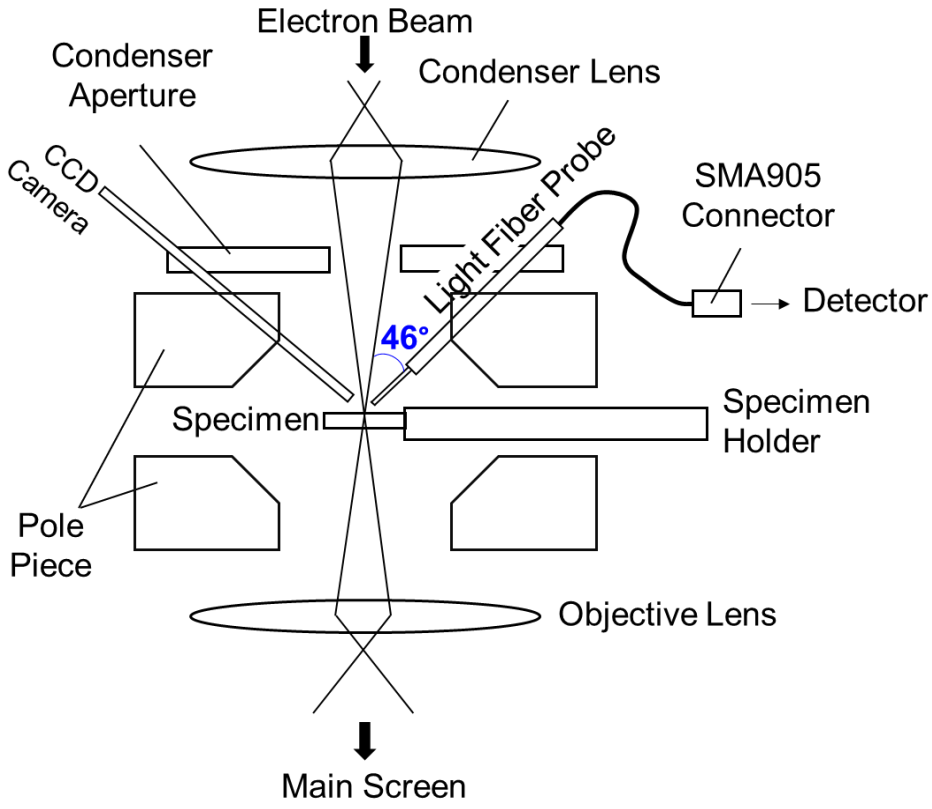

Figure 3-7. HVEM-CL facility view of specimen port, CL (optical fiber) probe and detector and its schematic image [24].

3.8.2 Evaluation of electron irradiation fluence

A Faraday cup, inserted between the specimen and fluorescent screen was used for HVEM to adjust electron irradiation fluence. Accurate electron beam current can be measured with correcting the loss of backscattered electrons and secondary electrons, with a cylindrical shape of a Faraday cup as shown in Figure 3-8. Figure 3-5 is a scheme of HVEM-CL (JEM-1300NEF) below projector lens. R_S was obtained by conversion of the diameter of the Faraday cup and factors below,

$$R_S = R_F \frac{l_b}{l_a} \frac{1}{M}, \tag{3-1}$$

where R_F, l_a, l_b, and M represent diameter of entrance aperture of Faraday up, distance between cross-over of projector lens and Faraday cup, distance between cross-over of projector lens and film plane, and magnification of image plane, respectively.

The total number of electrons incident on Faraday cup is equal to the number of electrons in the electron beam at specimen penetration position. The number of measured electrons per unit time was determined by dividing the current measured from Faraday cup by the elementary charge. The irradiation electron beam intensity (φ) can be calculated by dividing the number of electrons by the area of entrance aperture of Faraday cup as written below,

$$\varphi = \frac{I}{e\pi(R_S/2)^2}, \tag{3-2}$$

where I is current value measured by Faraday cup (A), e is elementary charge (1.602×10^{-19} C). For JEM-1300NEF, $R_F = 1.00 \times 10^{-3}$ m, $l_a = 0.3375$ m, $l_b = 0.8422$ m as shown in Figure 3-5.

3.8.3 Low-energy electron irradiation (MonoCL4 System)

The MonoCL4 system (Gatan Inc.) was used to lead and detect CL emission from the sample under 20 keV electron irradiation in the SEM. The MonoCL4 system consists of a parabolic mirror, light guide to use the emitted CL light, detector, and photomultiplier tube to count photons as shown in Figure 3-9. The parabolic mirror is located to cover the specimen stage. The CL photons are emitted from the specimen, which is generated by the electron beam illumination to the specimen after passing through an aperture with 1 mm in diameter. The CL photons were reflected by the mirror and collected at a detector. The CL photons are collected through light guide toward to the detector in every wavelength. Particular wavelength of CL light could be measured locating diffraction grating since dispersion of the light depends on an angle and variety of the grating.

Electrons with an energy of 20 keV were used in this dissertation. Electron beam current of I = ~1.67 nA was obtained in the magnification ×10k. *In-situ* CL spectra were measured at monochromatic mode in wavelength ranging from 200 nm to 950 nm in a step size 2 nm and dwell time 2 seconds.

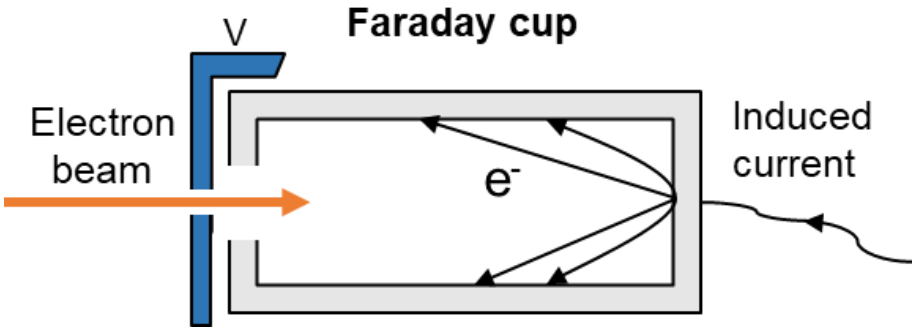

Figure 3-8. Faraday cup for measurement of electron irradiation dose installed in HVEM.

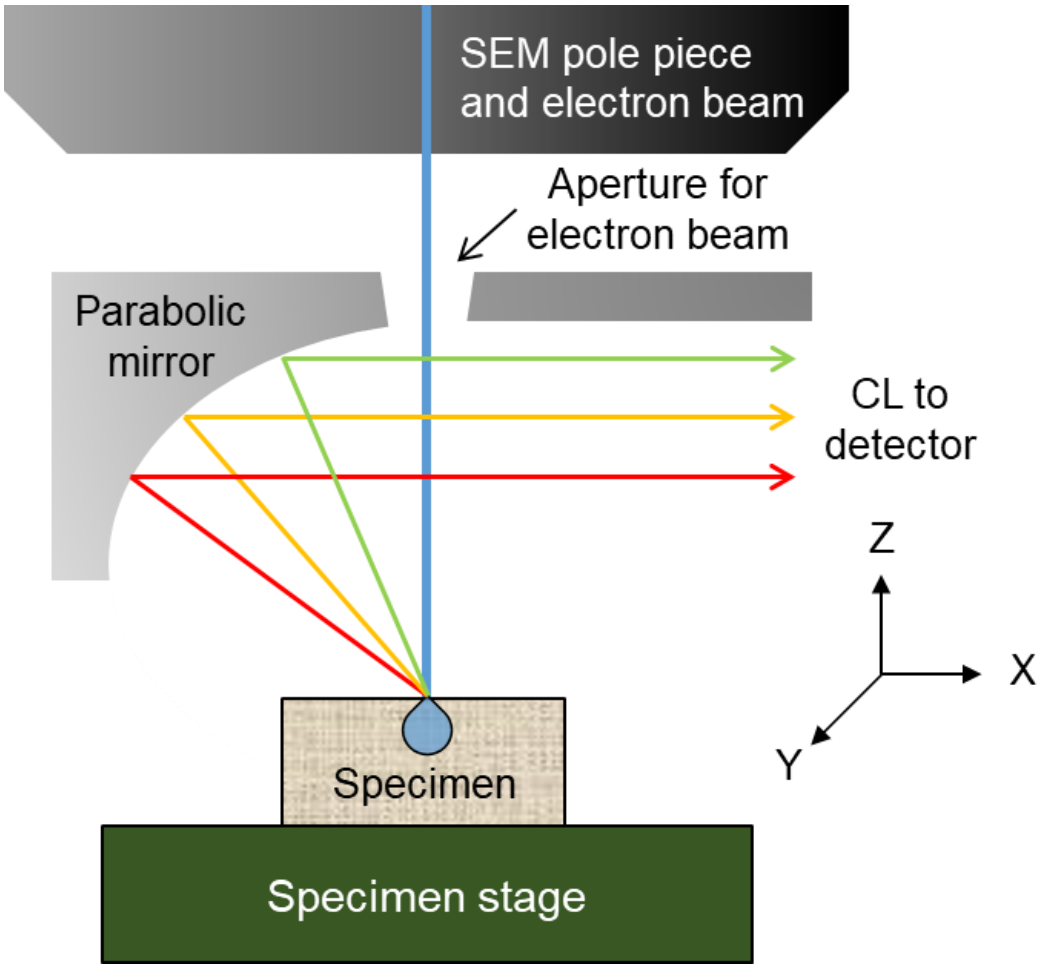

Figure 3-9. CL emission in MonoCL4 system through parabolic mirror.

Chapter 4

Development of *in-situ* CL technique in ceria under electron irradiation

4.1 Introduction

Ceria is a surrogate of fuels and transmutation targets for a nuclear reactor. Therefore, understanding the production and growth of radiation-induced defects during irradiation is of importance for the safe use of nuclear reactors. In this chapter, the point defects production and its charge states were investigated to understand the kinetics of displacement in-beam state. For this purpose, the *in-situ* CL spectroscopy technique was operated during high-energy electron irradiation using the HVEM. Complementary CL spectra were also obtained for low-energy electron irradiation by using the SEM. The electrical configurations of ceria under high-energy electron irradiation and CL emission from the point defects were evaluated depending on electron energy temperature.

4.2 Materials and Experimental Procedure

In-situ CL spectra were measured from pure single crystal and polycrystalline ceria samples under high- and low-energy electron irradiation. A single crystal ceria supplied by Dr. W. J. Weber of Oak Ridge National Laboratory and the polycrystalline sintered ceria samples were used in this study. The detail of sample information is described in Chapter 3.

For high-energy electron irradiation, the HVEM-CL facility (Figure 3-7) operated electron energies from 400 keV to 1250 keV at temperatures of 100, 200, and 300 K.

Meanwhile, the CL spectra under low-energy electron irradiation were obtained from the SEM-CL facility (Figure 3-6) at 300 K. The energy was 20 keV which is out of $E_{d,O}$ bound. All the obtained spectra were fitted with a Gaussian function and the intensity of bands were integrated to interpret energy and temperature dependence of CL emission. The details of equipment and experimental conditions are described in Chapter 3.

4.3 Results

4.3.1 Displacement cross-section calculation

The displacement cross-section (σ_d) in ceria induced by energetic electrons through elastic collisions was calculated by using SMOTT/POLY computer code [74] based on Eq. (2-12). The threshold displacement energies (E_d) were assumed based on the reported values of E_d for Ce ($E_{d,Ce}$: 44 ~ 58 eV) and O ($E_{d,O}$: < 33 eV) sublattices [9].

The calculated total σ_d is shown in Figure 4-1. The threshold electron energy to induce elastic displacement was evaluated where the cross-section exceed 1 barn: those were 150 ~ 200 keV for oxygen sublattice ($E_{0,O}$) and 1300 ~ 1600 keV for Ce sublattice ($E_{0,Ce}$), respectively. These results indicate that the electron irradiation by using a HVEM in the energies range of 400 ~ 1250 keV generates displacement damage only for oxygen sublattice. Therefore, the CL spectra obtained by using HVEM would include an additional band induced by F centers. On the other hand, atomic displacement will not be induced with 20 keV electrons. Therefore, one can hypothesize that the CL spectra obtained using SEM are induced by ionization or natural defects by energy transfer to electrons at Ce 4*f* level.

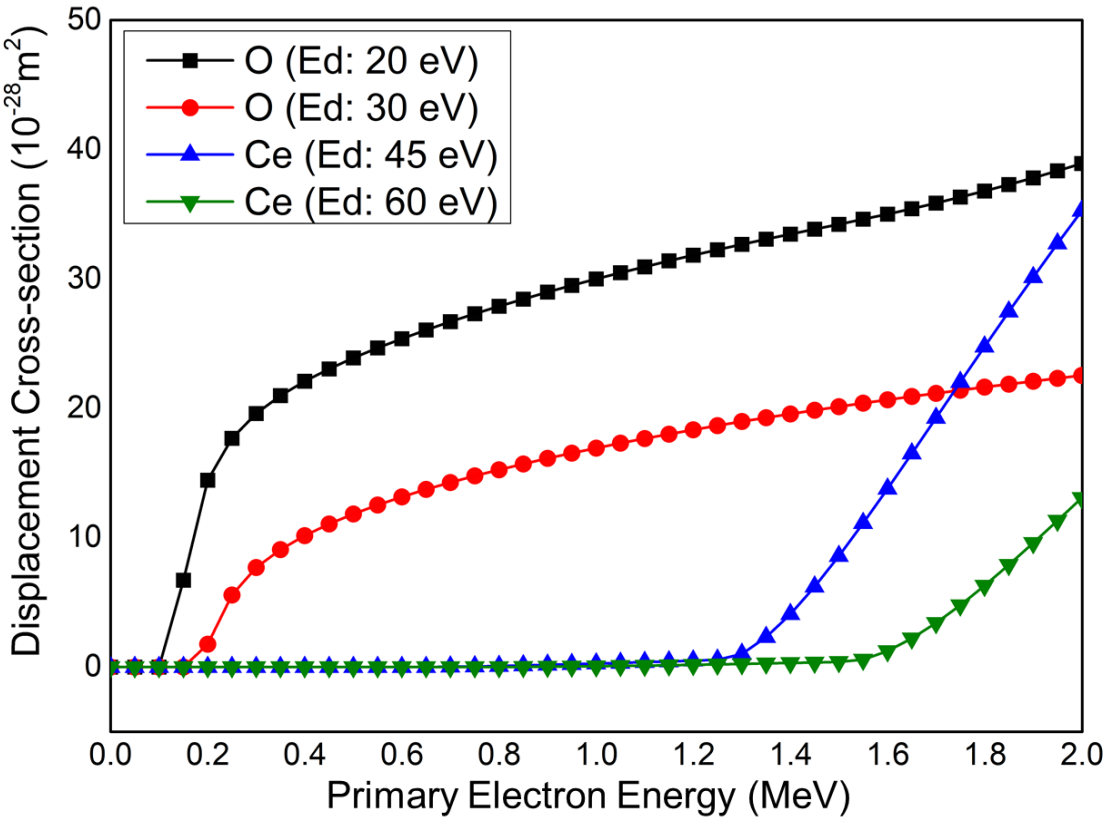

Figure 4-1. Oxygen and cerium atoms displacement cross section in ceria by electron-nucleus collisions calculated by SMOTT/POLY computer code [74].

4.3.2 CL spectra in single crystal ceria

CL spectra under high- and low-energy electron irradiation in single crystal ceria were obtained. For high-energy electron irradiation, one spectrum was taken under electron irradiation for 30 seconds at 300 K ~ 100 K, and the spectra were averaged out for 5 recordings for 400 keV ~ 1250 keV electrons. The spectra were fit with Gaussian profiles. Figure 4-2 shows an example of *in-situ* CL spectrum for 600 keV electron irradiation together with fitted curves by Gaussian function. 4 Gaussian bands were appeared at photon energies of 1.6 eV, 2.4 eV, 2.9 eV, and 4.2 eV with full-width at half-maximum (FWHM) of 0.4 eV, 0.8 eV, 0.5 eV, and 1.1 eV, respectively. A sharp and intense unresolved line was seen at 1.79 eV (probably R-lines of Cr^{3+} impurities). Cr^{3+} exhibits narrow-band emission at around 700 nm because of spin-forbidden $^2E \rightarrow {}^4A_2$ transition or broadband emission ranging from 650 nm to 1600 nm because of the spin-allowed $^4T_2 \rightarrow {}^4A_2$ transition [75] and a small doublet at 1.73 ~ 1.75 eV, and another broader impurity line at 1.85 eV were observed.

CL spectra were also measured for electrons with 20 keV at a constant beam current of 1.7 nA at room temperature, and they are shown in Figure 4-3. The CL band characteristics for 20 keV electrons are described in Table 4-1. Only one broad CL band at 2.4 eV was observed and this band was divided into two bands at 2.37 eV and 2.84 eV by Gaussian fitting.

For high-energy electron irradiation, CL spectra were measured at different electron energies of 400, 600, 800, 1000, and 1250 keV at constant beam-flux of 3.8×10^{21} $m^{-2}s^{-1}$. The CL spectra were obtained by averaging out the recordings after 0 ~ 150 seconds at 300, 200, and 100 K as shown in Figure 4-4. Further, the average CL band characteristics in single crystal ceria were summarized in Table 4-1 for electron irradiation with 400 keV ~ 1250 keV. The CL intensity for F^+ center band is dependent on electron energy, and it showed a maximum at 600 keV electrons.

4.3.3 CL spectra in polycrystalline ceria

CL spectra under high- and low-energy electron irradiation in polycrystalline ceria were obtained. For high-energy electron irradiation, one spectrum was taken under electron irradiation for 30 seconds at 300 ~ 100 K and the spectra were averaged out for 5 recordings for 400 keV ~ 1250 keV electrons. The spectra were fit with Gaussian profiles. Similar to the spectrum with 600 keV electrons [Figure (4-2)], spectra with 400 keV ~ 1250 keV electrons were fitted with 4 Gaussian bands, which were recorded at photon energies of 1.6 eV, 2.1 eV, 2.7 eV, and 4.2 eV with full-width at half-maximum (FWHM) of 0.4 eV, 0.8 eV, 0.6 eV, and 1.2 eV, respectively. A sharp and intense unresolved line was seen at 1.79 eV (probably R-lines of Cr^{3+} impurities [75]) and a small doublet at 1.73 ~ 1.75 eV and another broader impurity line was observed at 1.85 eV.

CL spectra were also measured for electrons with 20 keV at a constant beam current of 1.7 nA at room temperature, and they are shown in Figure 4-3. The CL bands characteristics for 20 keV electrons are described in Table 4-2. Only one broad CL band at 2.5 eV was observed and this band was divided into two bands at 2.35 eV and 2.80 eV by Gaussian fitting.

For high-energy electron irradiation, CL spectra were measured at different electron energies of 400, 600, 800, 1000, and 1250 keV at constant electron beam-flux of 3.8×10^{21} $m^{-2}s^{-1}$. The CL spectra were obtained by averaging out the recordings after 0 ~ 150 seconds as shown in Figure 4-5. Further, the average CL band characteristics in polycrystalline ceria were summarized in Table 4-2 for electron irradiation with 400 keV ~ 1250 keV. The CL intensity for F^+ center band is dependent on electron energy, and it showed a faint maximum for 600 keV electrons.

Table 4-1. CL band characteristics and defect assignments for the ceria single crystal samples.

	Band center (eV)	FWHM (eV)	Defect
HVEM (300 K)	4.2	1.1	F^+ center
	2.9	0.5	Ce^{3+}_{I}
	2.4	0.8	Ce^{3+}_{II}
	1.7	0.4	Impurity
HVEM (200 K)	4.2	1.2	F^+ center
	2.9	0.5	Ce^{3+}_{I}
	2.5	0.9	Ce^{3+}_{II}
	1.6	0.4	Impurity
HVEM (100 K)	4.2	1.1	F^+ center
	3.0	0.4	Ce^{3+}_{I}
	2.6	0.9	Ce^{3+}_{II}
	1.6	0.5	Impurity
SEM (300 K)	2.7	0.7	Ce^{3+}_{I}
	2.3	0.6	Ce^{3+}_{II}

Table 4-2. CL band characteristics and defect assignments for the ceria polycrystalline samples.

	Band center (eV)	FWHM (eV)	Defect
HVEM (300 K)	4.2	1.2	F^+ center
	2.7	0.6	Ce^{3+}_{I}
	2.1	0.8	Ce^{3+}_{II}
	1.5	0.4	Impurity
HVEM (200 K)	4.3	1.3	F^+ center
	2.9	0.5	Ce^{3+}_{I}
	2.2	0.9	Ce^{3+}_{II}
	1.7	0.6	Impurity
HVEM (100 K)	4.3	1.4	F^+ center
	2.8	0.7	Ce^{3+}_{I}
	2.1	0.7	Ce^{3+}_{II}
	1.6	0.6	Impurity
SEM (300 K)	2.8	0.7	Ce^{3+}_{I}
	2.4	0.6	Ce^{3+}_{II}

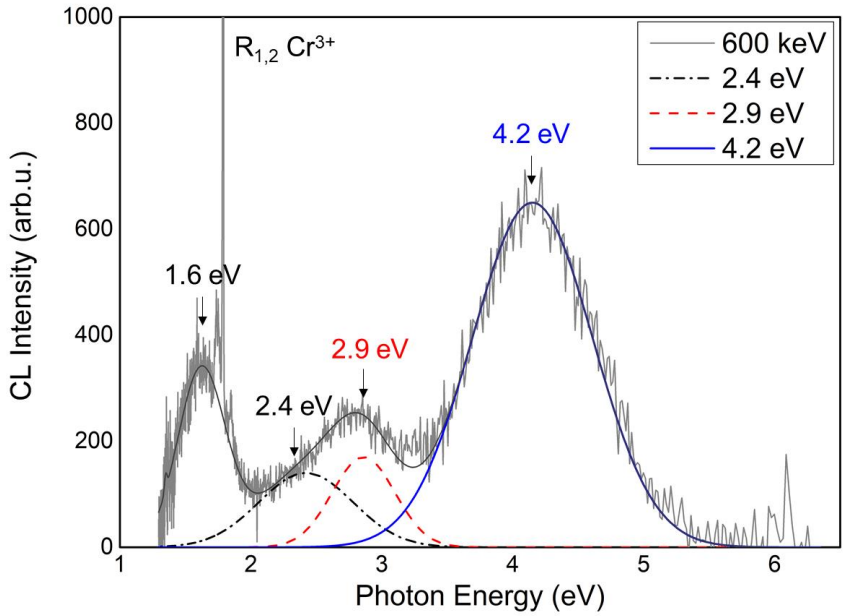

Figure 4-2. Assignment of CL bands at 300 K of the ceria single crystal for 600 keV electron excitation. Dotted, dashed, and dotted-dashed lines are fitted spectra and solid line is the Gaussian curve used for fits of spectrum.

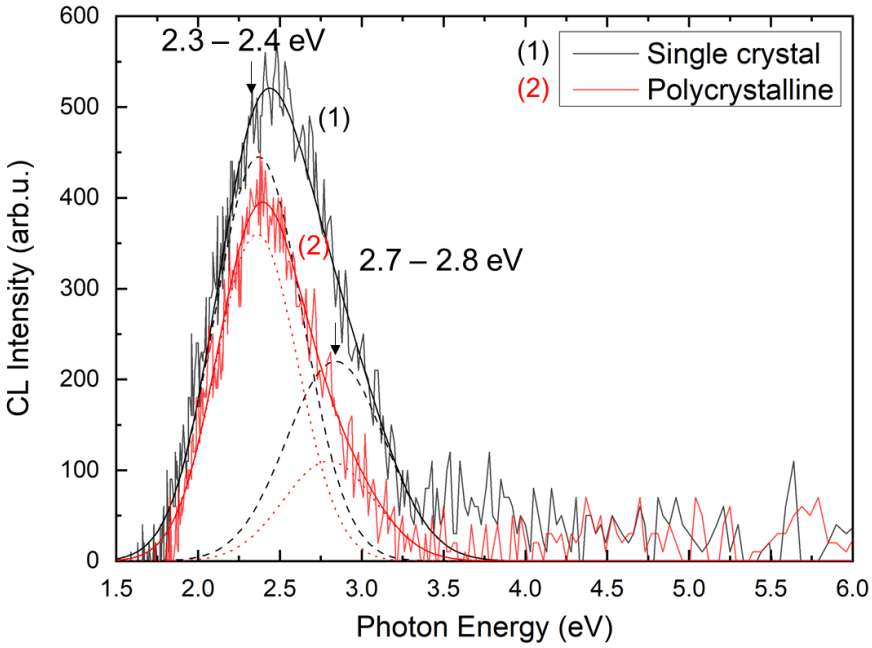

Figure 4-3. CL spectra at 300 K of the ceria single crystal and polycrystalline sample for 20 keV electron excitation. Dashed and dotted lines are the fitted spectra and solid lines are the Gaussian curves used for least-square fits.

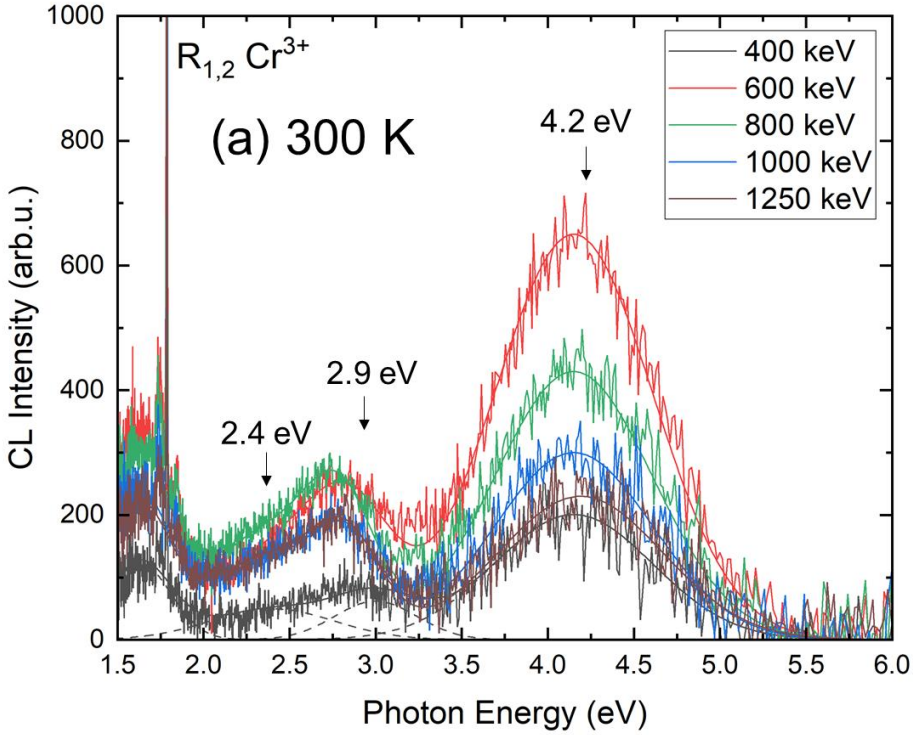
$R_{1,2}$ Cr^{3+}
(a) 300 K
400 keV
600 keV
800 keV
1000 keV
1250 keV
4.2 eV
2.9 eV
2.4 eV
CL Intensity (arb.u.)
Photon Energy (eV)

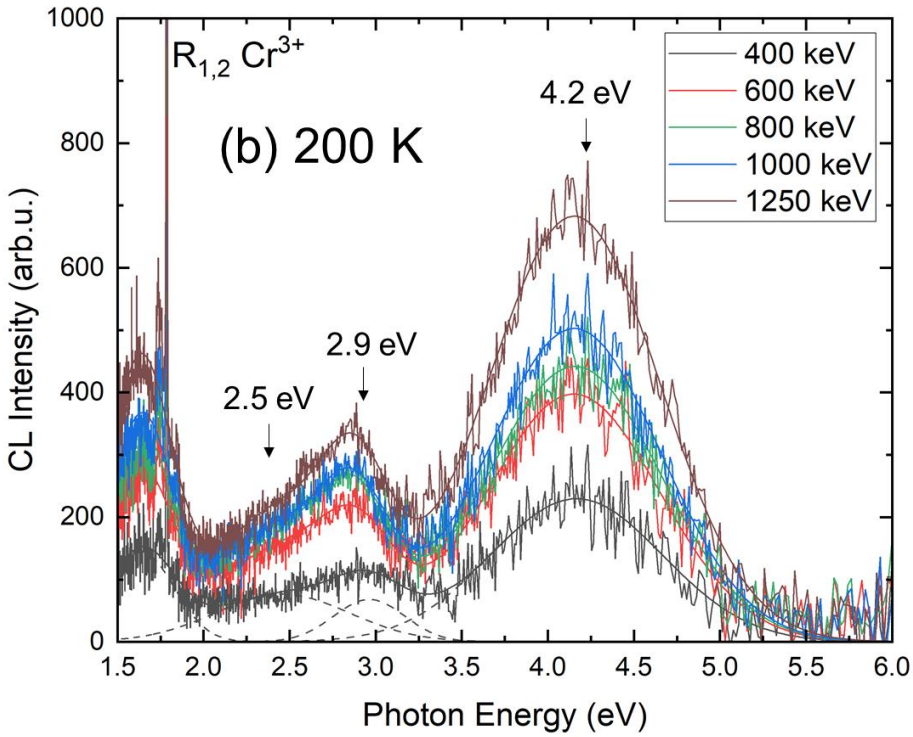
$R_{1,2}$ Cr^{3+}
(b) 200 K
400 keV
600 keV
800 keV
1000 keV
1250 keV
4.2 eV
2.9 eV
2.5 eV
CL Intensity (arb.u.)
Photon Energy (eV)

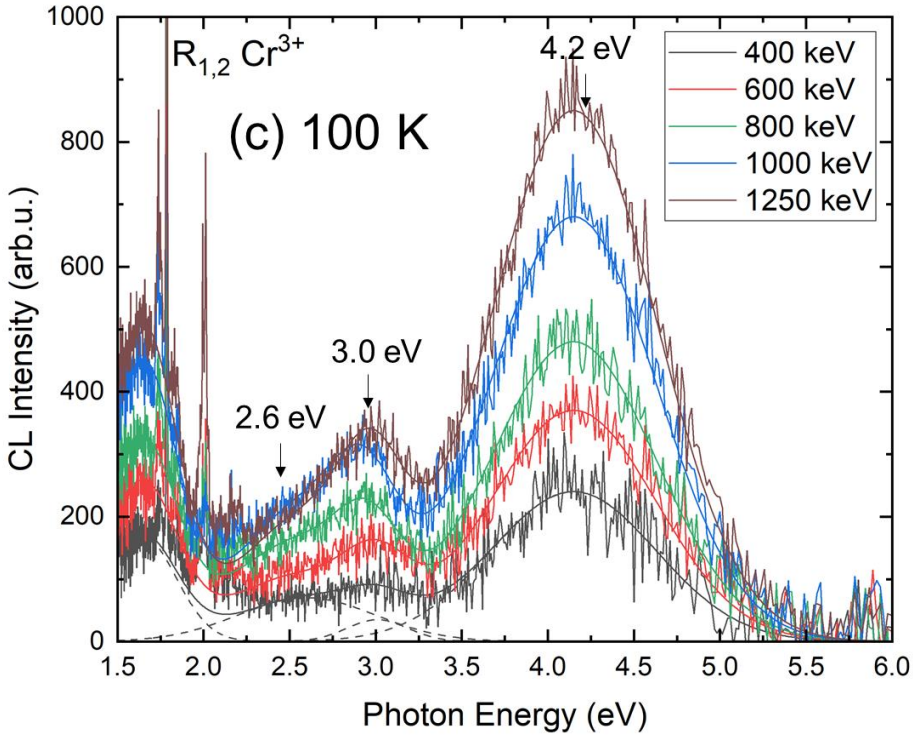

Figure 4-4. CL spectra at (a) 300 K, (b) 200 K, and (c) 100 K of the ceria single crystal sample for electrons of variable energy at fluences of 5.74×10^{23} m^{-2}. Dashed lines are the fitted spectra and solid lines are the Gaussian curves used for least-square fits.

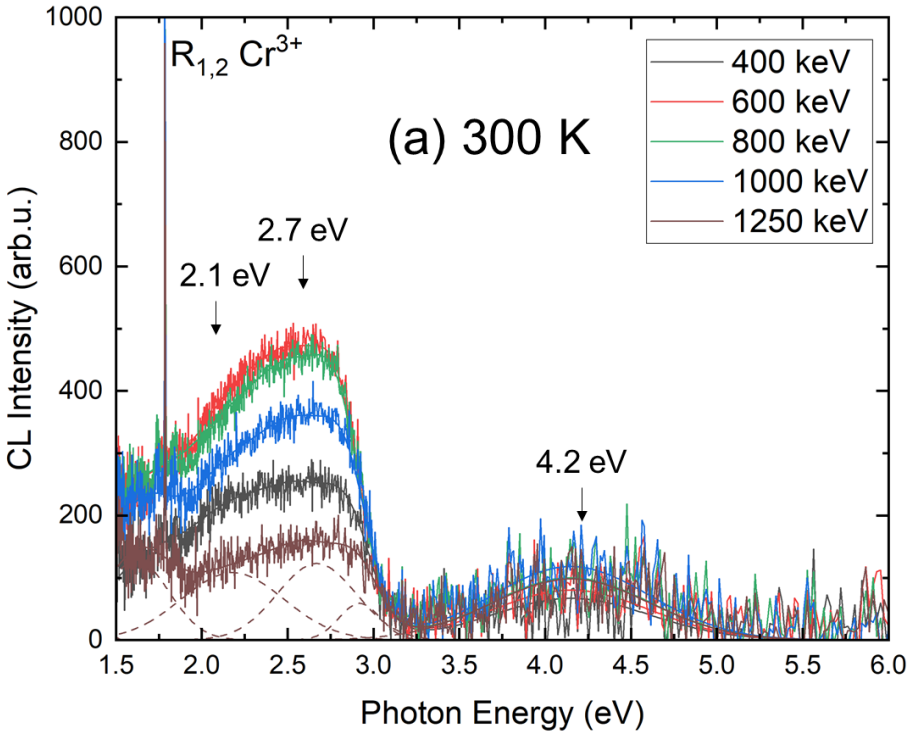
R1,2 Cr3+
(a) 300 K
400 keV
600 keV
800 keV
1000 keV
1250 keV
2.7 eV
2.1 eV
4.2 eV
CL Intensity (arb.u.)
Photon Energy (eV)

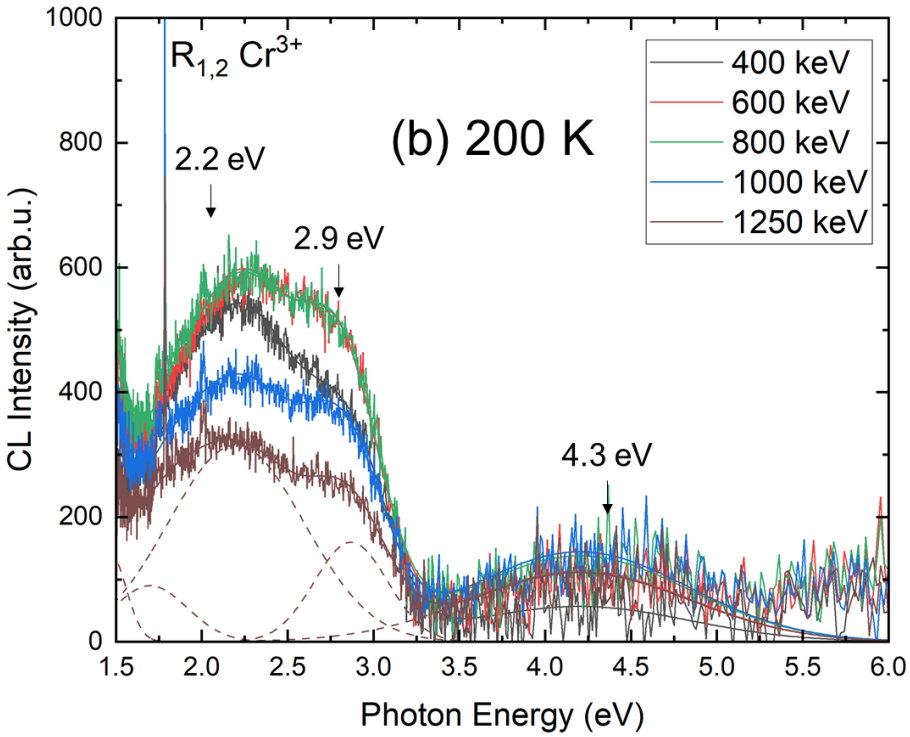
R1,2 Cr3+
(b) 200 K
400 keV
600 keV
800 keV
1000 keV
1250 keV
2.2 eV
2.9 eV
4.3 eV
CL Intensity (arb.u.)
Photon Energy (eV)

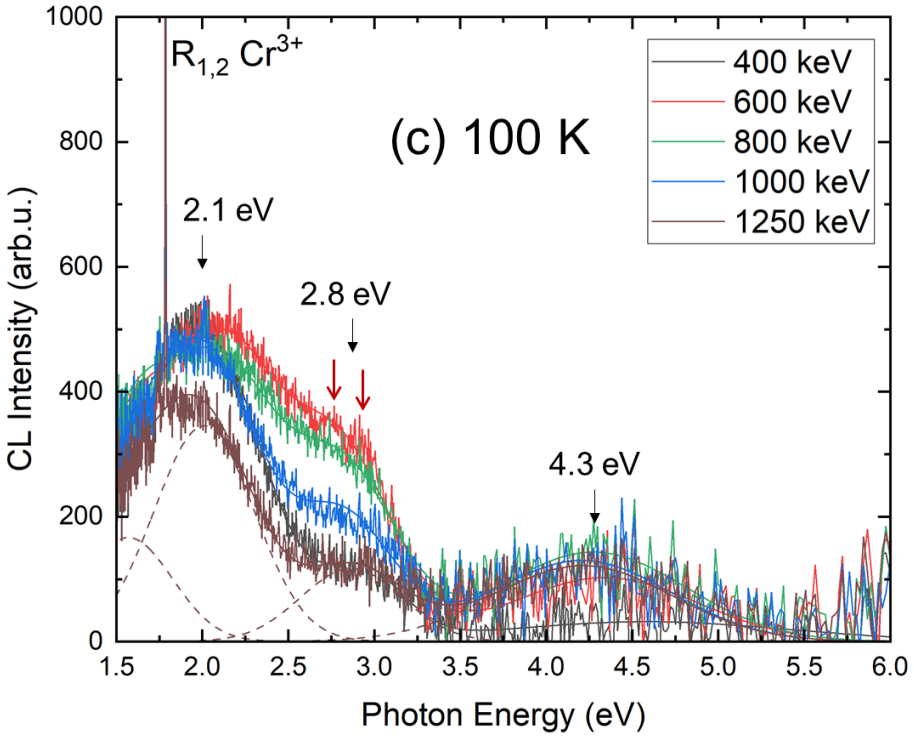

Figure 4-5. CL spectra at (a) 300 K, (b) 200 K, and (c) 100 K of the ceria polycrystalline sample for electrons of variable energy at fluences of 5.74 x 10^{23} m^{-2}. Dashed lines are the fitted spectra and solid lines are the Gaussian curves used for least-square fits.

4.4 Discussion

CL in oxides is emitted by thermalized secondary electrons (SEs) and holes generated by elastic and inelastic collisions with energetic electrons [70]. The CL signal is usually proportional to the volume density of the carriers, and it is produced during the trapping of these thermalized SEs by defect and impurity levels in the band gap [68,76]. It indicates that CL emission in thin samples is not proportional to the energy of primary electrons since they are mostly transmitted through the targets as indicated by simulations by the ESTAR code [77] (Table 4-3).

The extrinsic CL is assumed that it results from electronic excitation and radiative decay from the defect and impurity levels by thermalized SEs [70]. At 300 K, most shallow levels created by impurities and defects are fully ionized while deep levels created by charged point defects are partially filled. The CL cross-section consists of four independent steps as described in Eq. (2-14) i.e. ($\sigma_{CL} = \sigma_i \sigma_t \sigma_e \sigma_r$) [70]. Trapping of thermalized carriers may also occur directly on excited states rather than on the ground state of the defect levels. In that case, the CL process is reduced to three steps only. Thermal quenching by phonon-assisted non-radiative channels reduces the CL yield at a high temperature [78,79]. For the temperature effect in CL intensity, σ_t increases with temperature, whereas σ_r decreases with temperature [70]. However, the quenching effect by other non-radiative decay to the defect and impurity levels is still puzzling and difficult to explain in detail [79]. The radiative decay of exciton across the band gap is quenched at a high temperature (< 55 K) which can be assumed as intrinsic CL emission [78]. The CL spectra at 5.5 ~ 6 eV were not observed in ceria which was deduced by EELS [80,81].

Table 4-3. Characteristics of electron irradiations of CeO_2 (mass density = 7.215 g cm^{-3}), computed with the ESTAR code [77] for different primary electron energies (E) and mean ionization energy I = 407.6 eV: CSDA range, and total inelastic stopping power ($(-dE/dx)_{inel}$)

E (keV)	20	400	600	800	1000	1250
Range (µm)	2.3	289	500	720	943	1221
(-dE/dx)inel. (MeV μm^{-1})	52×10^{-4}	9.9×10^{-4}	9.2×10^{-4}	9.0×10^{-4}	9.0×10^{-4}	9.1×10^{-4}

4.4.1 Analysis of CL spectra

The CL spectra observed in this study showed three broad bands. These bands were centered at photon energies of around 1.6 eV, 2.1 ~ 2.5 eV, 2.8 ~ 3.0 eV, and 4.2 eV. Interpretation of the CL bands was referred to the literature of PL data in ceria, although they suggested various energy levels for each defect. For example, Aškrabič et al. assigned the PL band centered at 1.7 eV results from the charge transfer transitions from F^+ centers ($V_O^{\cdot}$) to the oxygen 2*p* states, and the band at 2 ~ 2.5 eV is F^0/F^+ centers [69]. Alternatively, the same bands at 2 ~ 2.5 eV were associated to $5d^1 \rightarrow 4f^1$ transitions of Ce^{3+} ions in non-stoichiometric nano-crystalline ceria (nc-CeO_2) by Maksimchuk et al. [82]. Generally, PL bands at ~2 eV are considered to attribute to Ce^{3+} luminescence, for example in the case of YAG: Ce^{3+} [83] and ZrO_2: Ce^{3+} [84]. Finally, the bands at 3.1 ~ 3.15 eV were ascribed by Morshed et al. to $4f \rightarrow 2p$ charge transfer transitions for CeO_2 films on a silicon substrate [85] and nc-CeO_2 [82]. Also, the band at 2.9-3.0 eV was also assigned by Aškrabič et al. to charge transfer transitions from the F^{2+} center ($V_O^{\cdot\cdot}$) level to Ce^{3+} ($4f^1$) for nc-CeO_2 [69]. The emission band at 3.18 eV in Lu_2SiO_5:Ce^{3+} (LSO: Ce^{3+}) was attributed to Ce^{3+} in Lu site by Suzuki et al. [86]. However, Jia et al. suggested two PL bands for each Ce^{3+} level for LSO: Ce^{3+} by *ab initio* calculations; Ce^{3+} in a crystallographic site occurs at higher photon energy (~ 3.2 eV) than that of a Ce^{3+} adjacent to an oxygen vacancy (~ 2.6 eV) [87].

It seems confusing with the variety of interpretations, but it was overlooked that two Ce^{4+} ions are connected with two O^{2-} ions as shown in Figure 4-6. Let us consider a cluster of neutral oxygen vacancy ($V_O^{\times}$) at one oxygen site connecting the two Ce^{4+} ions (Ce^{4+}-$V_O^{\times}$-Ce^{4+}) where the other connecting O^{2-} ion is not shown in the cluster for clarity. According to first principle calculations, the two electrons of $V_O^{\times}$ are primarily localized on the two Ce^{4+} ions that are next to each other, generating a Ce^{3+}-$V_O^{\cdot\cdot}$-Ce^{3+} cluster with more than 0.9 electrons localized on each

Ce and just around 0.1 electron remaining on the vacancy site [88]. The high electron density at cerium sites promotes the interpretation of CL data in terms of Ce^{3+} optical transitions rather than V_O-type (or F-type in spectroscopic notation) transitions, notwithstanding the partial electron delocalization. As a result, it can be taken into consideration that the various electronic configurations of the neutral oxygen vacancy $V_O^{\times}$, described in terms of a Ce^{4+}-$V_O^{\times}$-Ce^{4+} cluster rather of adopting the description of oxygen vacancies in terms of F, F^+ and F^{2+} centers.

Thereby, three different electronic configurations for this cluster can be assumed considering the electro-neutrality, leading to two or three types of Ce^{3+} ions (Figure 4-6): (i) Neutral configuration (Ce^{3+}-$V_O^{\cdot\cdot}$-Ce^{3+}) with two neighboring Ce^{3+} ions, (ii) One positive configuration (Ce^{3+}-$V_O^{\cdot\cdot}$-Ce^{4+}) with the other electron trapped in the form of a Ce^{3+} at undistorted substitution location further from the vacancy, and (iii) Two positive configuration (Ce^{4+}-$V_O^{\cdot\cdot}$-Ce^{4+}) with the two electrons trapped at two undistorted Ce^{3+} sites farther away from the vacancy. Configurations (i), (ii) and (iii) correspond to the F center ($V_O^{\times}$), F^+ center ($V_O^{\cdot}$) and F^{2+} center ($V_O^{\cdot\cdot}$), respectively. In configurations (i) and (ii), CL detects only the Ce^{3+} ions where the compensating electrons are trapped. Only the Ce^{3+} ions in configurations (i) and (ii) where the compensating electrons are confined are detected by CL. As will be explained later, in the case of configuration (iii), CL comprises both the emission of Ce^{3+} and of a traditional F^+ center.

In the present results, two broad CL bands were fitted regardless of primary electron energies centered at 2.1-2.5 eV and 2.7-3.0 eV with FWHM of ~0.5 eV at 300 K (Figures 4-3 ~ 4-5). For the polycrystalline sample, they have more intense emission for Ce^{3+} ions in than in the single crystal. Those two CL bands arise from spin and parity-allowed $5d^1 \rightarrow 4f^1$ electric-dipole transitions with large oscillator strengths. The $4f^1$ (^2F) level of Ce^{3+} is split into $^2F_{5/2}$ and $^2F_{7/2}$ sub-levels by the spin-orbit coupling interaction, with an energy difference of ~0.25 eV (~2,000 cm^{-1}) [89–93]. The spin-orbit coupling is shown in Figure 4-5 (c) with the red arrows.

It might be tempting to attribute the two prominent CL bands to the two $5d^1 \rightarrow 4f^1$ ($^2F_{7/2}$, $^2F_{5/2}$) transitions. However, there are several arguments against this interpretation. In the case of the polycrystalline sample: a) the splitting of 0.5 eV at 300 K to 0.9 eV at 100 K between these bands is larger than the theoretical value 0.25 eV for the spin-orbit splitting of Ce^{3+}; b) the observed splitting increases from 0.5 to 0.9 eV, whereas the spin-orbit coupling should be independent of temperature; c) the low energy CL band shifts to lower temperature (2.3 to 2.0 eV) upon decreasing the temperature from 300 K to 100 K; d) the intensities of the two transitions differ by a factor ~5 (~1.5 for the single crystal).

Ce_I (2.8 – 3.0 eV) and Ce_{II} (2.1 – 2.5 eV) are assigned to the two types of CL bands from Ce^{3+} emitting centers compared to the empirical and theoretical analysis in LSO: Ce^{3+} [87]. The CL band Ce_I can be attributed to a Ce^{3+} at an unperturbed crystallographic site of CeO_2, and the CL band Ce_{II} to a Ce^{3+} adjacent to an oxygen vacancy. These CL bands have two characteristics that support this interpretation: a) the low energy CL band (~2 eV) exhibits a temperature quenching effect as it is weaker at 300 K than at 100 K (Figure 4-5 (c), marked with arrows in red color), suggesting that the band ~3 eV may be composed of two components separated by about 0.25 eV, corresponding to the spin-orbit splitting of Ce^{3+}. These two characteristics were also seen in LSO:Ce^{3+} [87] for Ce^{3+} at an undistorted crystallographic position and for a Ce^{3+} next to an oxygen vacancy, respectively. Assuming a 5.5 ~ 6 eV energy gap between the conduction band (Ce-5*d*) and the valence band (O-2*p*), the schematic energy levels of Ce_I and Ce_{II} centers are shown in Figure 4-8 [80,81,93,94]. In Figure 4-6, configurations (ii) and (iii) of the oxygen vacancy correspond to the Ce_I center (2.8 ~ 3.0 eV), attributed to a Ce^{3+} at an undistorted crystallographic site, while configurations (i) and (ii) of the oxygen vacancy correspond to the Ce_{II} center (2.1 ~ 2.5 eV), attributed to a Ce^{3+} adjacent to an oxygen vacancy.

The broad CL emission band around ~4 eV was observed for 400 keV ~ 1250 keV electron irradiation (Figures 4-4 and 4-5) unlike 20 keV (Figure 4-3). The broad 4.2 eV band is more intense in the single crystal (Figures 4-4) than in the polycrystalline sample (Figures 4-5). It is also represented in Figure 4-2 for the CL spectrum of the single crystal irradiated at the electron energy of 600 keV. Previously, the F^+ center for sapphire (α-Al_2O_3) and YSZ were assigned to similar CL bands with centers at 3.8 eV and 4.1 eV, respectively [25,70]. The schematic model of oxygen vacancy (Figure 4-6) suggests that the 4.2 eV band could be related to configuration (iii), in which the vacancy is represented by an F^{2+} center ($V_O^{\cdot\cdot}$) and two nearby Ce^{4+} ions. As a result, this center loses the Ce^{3+} feature. The 4.2 eV band may be the result of an electron being captured by the vacancy (the Ce^{4+}-$V_O^{\cdot\cdot}$-Ce^{4+} cluster) and emitting from the F^+ center. The caught electron is concentrated just before emission on the oxygen vacancy site, which corresponds to an excited F^+ core, at the center of this symmetric cluster. The Frank-Condon principle states that during the emission, the electron is still localized at the V_O site. This final state corresponds to an unrelaxed (transient) state of the F^+ ground state. Immediately after the emission, the electron is then shifted to one of the two Ce^{4+}, giving a Ce^{3+}-$V_O^{\cdot\cdot}$-Ce^{4+} cluster. This center corresponds to the relaxed state of the F^+ center. The F^+ center CL emission is described in a schematic configuration as shown in Figure 4-7. Almost all of CL bands have a FWHM of about 0.5 eV, except for the 4.2-eV band having a width of ~1 eV as the other F^+ centers in sapphire and YSZ [25,36,70,95]. The assignment of the CL bands is summarized in Figure 4-8 and Tables 4-1 ~ 4-2.

For the previous EPR results, information only for the Ce^{3+} were observed after electron irradiation without detection of F^+ center [96]. However, CL showed F^+ center emission at 4.2 eV during irradiation which indicates relaxed state of F^+ center has a short lifetime and the electron is immediately transferred to ground state of Ce_{II} forming the Ce^{3+}-$V_O^{\cdot\cdot}$-Ce^{4+} cluster.

Moreover, it suggests that relaxed state of F^+ center located a higher energy level from the valence band (~1.8 eV) than that of Ce_{II}, which is corresponding to the first principle calculations results suggested by Han et al., that Ce 4*f* sate is located at ~1.4 eV from the valence band [88]. A schematic diagram of energy level in ceria is proposed in Figure 4-8.

In addition, the CL band at 4.2 eV was not observed in both single and poly crystal samples for 20 keV electron irradiation (Figure 4-3). The oxygen atom displacement cross-section [97] was calculated by using SMOTT/POLY code [74,98] devised for polyatomic targets (Figure 4-1). These calculations take into account the primary electron-nucleus collisions and small atomic displacement cascade contribution, and the admitted value of threshold displacement energy of $E_{d,O}$ = 35 eV based on the upper boundary value (33 eV) deduced from experiments at the HVEM [74]. Note that molecular dynamics simulations gave smaller values of 27 eV [9], and 20 to 35 eV [99]. A larger value of $E_{d,Ce}$ = 58 eV is admitted for cerium [74]. Our data show that oxygen displacement by elastic electron-nucleus collisions can only occur for electron energies higher than ~200 keV [97]. This explains the lack of 4.2 eV CL band in CeO_2 irradiated by 20 keV electrons (Figure 4-3). However, it must be noticed that the Ce_I (~2.7 eV) and Ce_{II} (~2.3 eV) CL bands are present even after 20 keV electron irradiation and may originate from two possible processes: (a) excitation of Ce^{3+} at lattice position (Ce_I) and Ce^{3+} adjacent to preexisting oxygen vacancies (Ce_{II}), and (b) the production of oxygen vacancies in configurations (i) and (ii) by electronic excitations. Hypothesis (b) is not totally unlikely as the inelastic stopping power $(-dE/dx)_{inel}$ is 4 to 6 times larger for 20 keV electrons than for 400 keV to 1250 keV, where it is nearly constant (Table 4-3).

The 4.2 eV band is substantially smaller in the sintered sample than in the single crystal (Figures 4-4 ~ 4-5) when their CL spectra are compared, regardless of temperature, whereas the Ce^{3+} ion signal is stronger even though the sintered sample is thinner. Due to the short

lifetime of the excited state and low temperatures, this effect cannot result from defect diffusion to the grain boundaries of the sintered sample, as could be expected. The contaminants [79,100] separated at grain boundaries may be more closely related to athermal non-radiative channels. Because of thermal quenching at temperatures of 100 K and above, the emission lines of these contaminants could not be seen. Such a reduction could potentially be caused by the prompt recombination/annihilation of oxygen Frenkel pairs at grain boundaries.

Finally, a 3d-transition element impurity, such as Ti^{3+} in sapphire [68,76], is likely the cause for the rather broad CL band at 1.7 eV (FWHM = 0.4 eV) observed for high energy electron irradiation (Figures 4-4 ~ 4-5). This band has previously been observed for oxide systems with different band gap energies [25,70]. The extremely narrow peaks in this 1.7 eV band are caused by Cr^{3+} impurities in oxide hosts and their ^2E - $^4A_2$ emission bands ($R_{1,2}$ lines) [63].

4.4.2 Effect of electron energy

Diffusion and recombination processes at the surface of excess free minority carriers were taken into account to model the electron-energy dependence of the CL signal in the case of semiconductors, where the effect of electron energy was previously addressed for low-energy electron excitations ($E \leq 40$ keV) of n-doped GaAs in a SEM [101,102]. The depth dependence of the light emission yield brought on by self-absorption results in a maximum. In the presence of a dominant surface recombination, the maximum changes to a higher voltage [102]. The primary electrons are shot through the targets in the current work on CeO_2, however, and the secondary electron distribution can be thought of as homogeneous across the sample thickness regardless of the source electron energy [70]. Unlike to low-energy electron irradiation of semiconductors [101], the maximum in CL intensity (Figure 4-9) cannot result

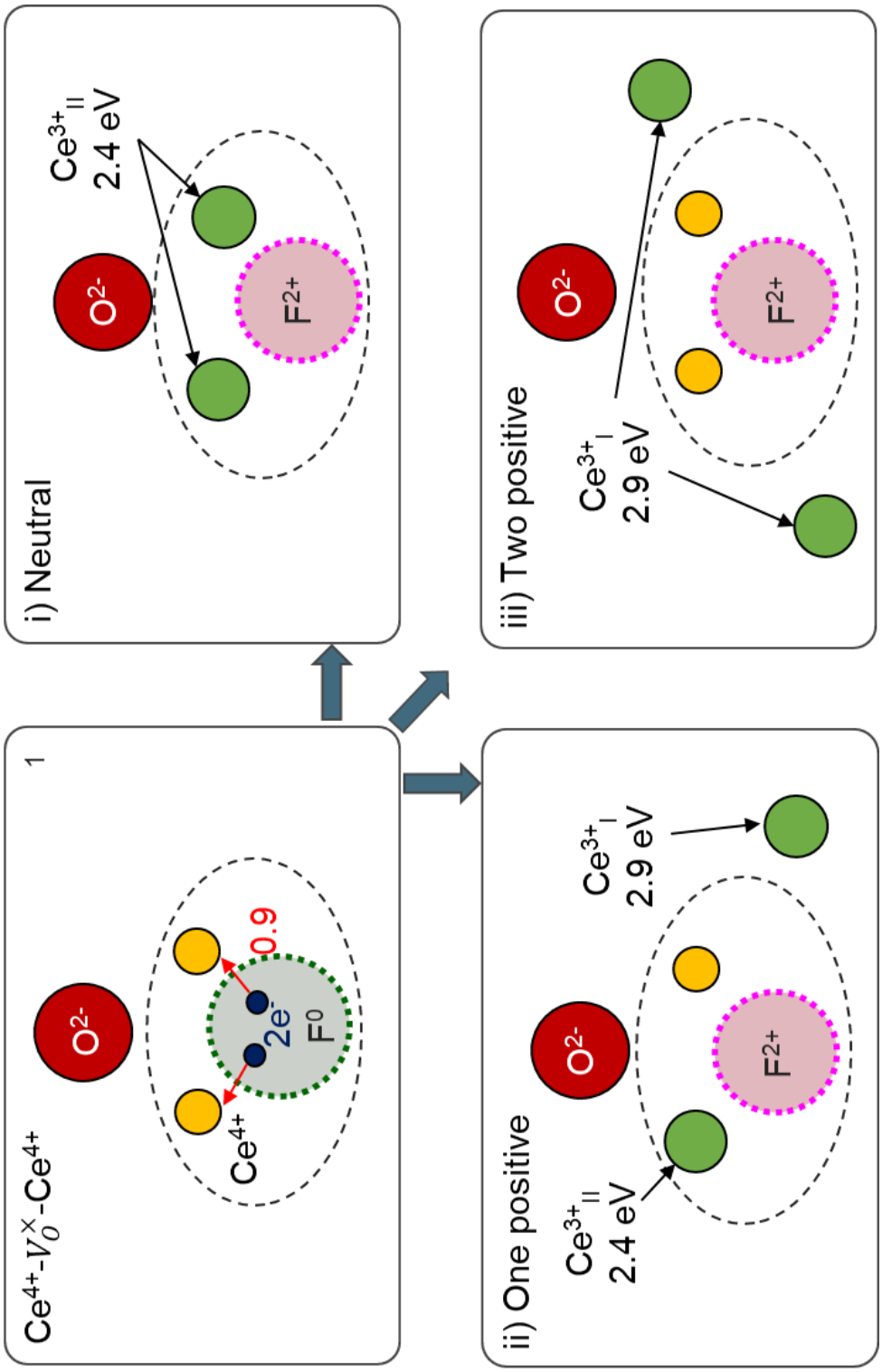

Figure 4-6. Schematic representation of different electronic configuration of a neutral oxygen vacancy in ceria.

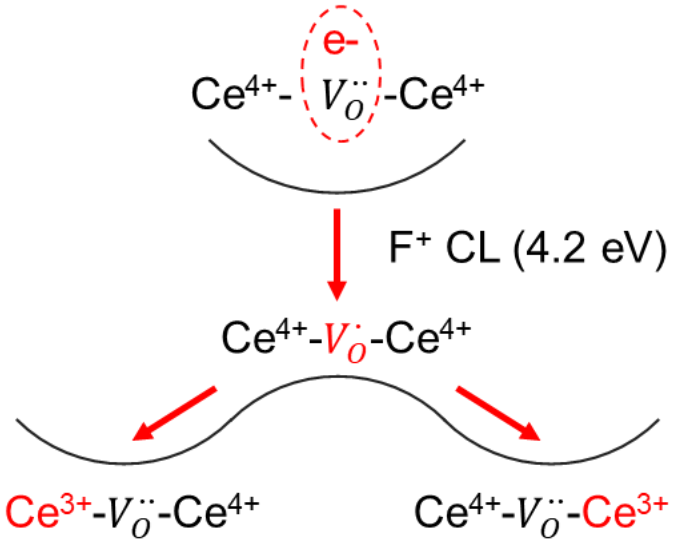

Figure 4-7. Schematic configuration coordinate representation of the F^+ center emission. The site of the unpaired electron is represented in red.

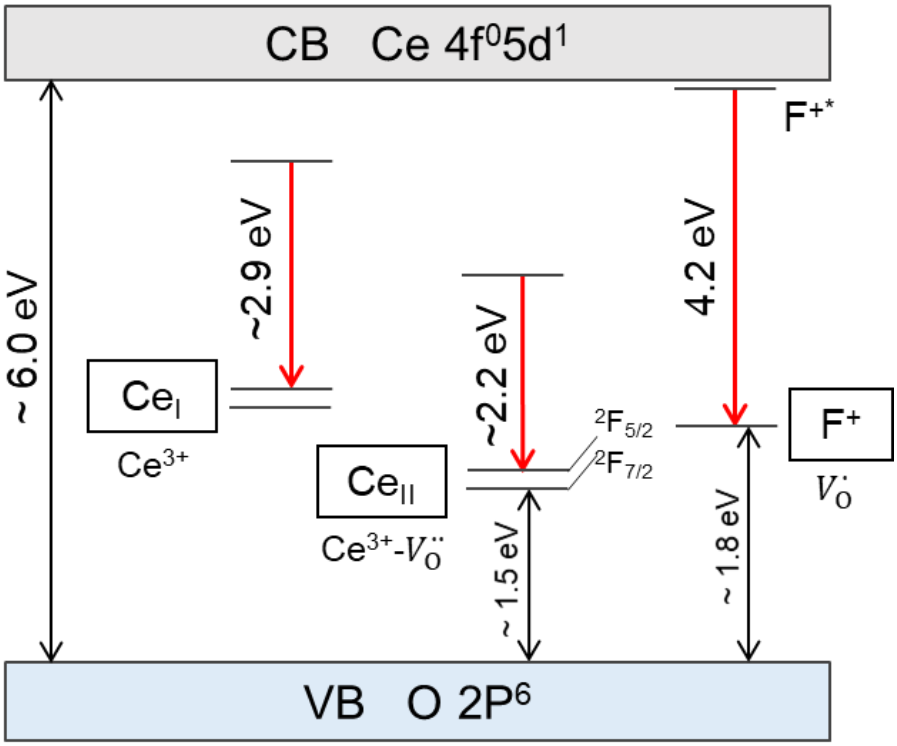

Figure 4-8. Sketch of electronic levels in the band gap of ceria possessing oxygen vacancies.

from inhomogeneity of the depth profile of secondary electrons and drift of excess carriers to the insulator surface.

For the various primary electron energies, little variation in cross-sections was seen at low cut-off energies ($E_s = E_{cut}$) values [70]. This translates into minor variations in $(dE/dx)_{inel}$ (Table 4-3), which are mostly driven by the input of low-energy secondary electrons [103]. Noting that $(dE/dx)_{inel}$ has its minimal value in this energy range (400 keV ~ 1250 keV), the highest CL intensity as a function of primary electron energy (Figure 4-9) cannot be explained by the minor fluctuations in $(dE/dx)_{inel}$ by just 10 % (Table 4-3). As a result, between 400 keV and 1250 keV, the sample produces almost the same amount of electron-hole pairs [104].

E_{cut}, which is the energy corresponding to an electron range equal to the sample thickness as calculated by the ESTAR computer code [77], was utilized as previously to choose the range of efficient secondary electrons yielding the maximum light emission yield. This number is obviously higher for the single crystal that is 0.5 mm thick (E_{cut} = 600 keV) than it is for the sintered sample that is 150 µm thick (E_{cut} = 250 keV). According to calculations of the survival probability of secondary electrons inside a 150 µm thick YSZ target vs E_s for E = 400 keV and E = 1250 keV, secondary electrons' spatial distributions were used to support this rough approximation [70].

However, we anticipate that the excitation cross-section (σ_e) will decline more quickly than the main electron energy. Upon electron irradiation up to 1 GeV above a maximum at low energy (< 100 eV), this type of decline was in fact seen for the apparent cross section for fluorescence of molecular levels of nitrogen N_2 [105]. Such phenomenon is also possible when a secondary electron is trapped on an excited state rather than the defect level's ground state.

Moreover, the displacement cross-section (σ_d) should increase with the CL integrated intensity (I_{CL}) for point defects caused by elastic collisions. We therefore suppose that I_{CL} can written as follows

$$I_{CL} = \mathrm{K}\sigma_{CL}\sigma_d, \quad (4\text{-}1)$$

where K is a constant that includes all elements of the experimental setup and conditions. According to the presumption, the cross-section for electron/hole trapping can be roughly calculated as $(E - E_0)^{\beta}$, for $E \geq E_0$, where E_0 is the electron energy threshold for atomic displacement. However, it is possible to believe that σ_t just depends on temperature and not directly on E as a characteristic of the defective electronic levels [70]. On the other hand, the radiative decay cross-section (σ_r) decreases with E, since the luminescence can be quenched by increasing the point defect concentration [79,100]. Therefore, a dependence of $E^{-\alpha}$stands for the product of σ_r and σ_e. Thus, the primary electron energy dependence of I_{CL} can be surmised as

$$I_{CL} = \mathrm{K}'E^{-\alpha}(E - E_0)^{\beta}, \quad (4\text{-}2)$$

where K' is another constant. A strong decay of I_{CL} versus E due to a large α exponent is required to counteract the steep increase of the total displacement per atom (dpa) induced inside a 150 µm thick sample by the primary electrons and the secondary electron cascade versus E. Due to the lesser E_d value of oxygen atoms (35 eV) compared to cerium atoms (58 eV), those dpa values solely result from oxygen displacement [74].

Such kind of function yields a maximum of I_{CL} versus E for both samples at 300 K (Figure 4-9) whereas I_{CL} is expected to increase steadily if σ_d is only considered. A limiting factor must be included to account for this maximum. Least-square fits with Eq. (4-2) give values of E_0 and α and β exponents for the various bands (Table 4-4). The value of E_0 ~400 keV for the F^+ center 4.2 eV band of the single crystal and polycrystalline sample at 300 K is

rather consistent with the data of oxygen displacement by elastic electron-nucleus collisions. The threshold E_0 value is comprised of between 200 keV and 400 keV in agreement with the CL data. The α exponent (~2) agrees with previous results for F^+ center bands in sapphire and YSZ single crystals with values of ~3 [70]. A smaller exponent (~0.6) is deduced for the 4.2 eV band of the polycrystalline sample at 300 K (Table 4-4). The behavior of CL bands assigned to the luminescence of Ce^{3+} at 300 K is quite similar for both kinds of samples with α exponents of ~1.5 (Table 4-4). Fitted parameters for the polycrystalline sample at 100 K and 200 K show similar consistent data versus electron energy. The behavior of CL bands related to Ce^{3+} luminescence at 300 K show that these ions are definitely produced with a similar threshold electron energy as the F^+ centers by charge compensation of the 2+ oxygen vacancies for the high-energy electrons. In contrast, the same CL bands for the 20 keV electron excitation likely derive from ionization effects [106].

Such an analysis, however, is not applicable to the F^+ center data of the single crystal at 100 K and 200 K, which indicate a constant increase against electron energy above the E_0 400 keV threshold energy rather than a maximum [Figures 4-9 (b-c)]. The 100 K values are extrapolated linearly to get an E_0 value of about 100 keV [Figure 4-9(c)]. It appears that Eq. (4-2) is solely left with the $(E - E_0)^\beta$ a term for σ_d. According to Draeger et al., the increase in I_{CL} is roughly in line with the rise in d from 400 keV to 1250 keV [97]. Table 4-4 contains the three bands' fitted values.

The relationship between an increase in electron energy and a drop in temperature depends on the corresponding evolutions of σ_{CL} and σ_d: reducing the sample temperature can result in either a maximum or an ongoing increase in I_{CL}. This is comparable to the temperature effect, which produces either a maximum or a continuous increase for a given electron energy [70]. Remember that σ_r decays with temperature owing to thermal quenching, as was

Table 4-4. Fitting parameters for the electron-energy dependence of CL bands of ceria

Temp.	Crystal		Band	E_0 (MeV)	α	β
300 K	Single	4.2 eV	F^+ center	399	2.20	0.37
		2.9 eV	Ce^{3+}_{I}	396	1.39	0.39
		2.4 eV	Ce^{3+}_{II}	396	1.11	0.39
	Poly	4.2 eV	F^+ center	388	0.61	0.37
		2.7 eV	Ce^{3+}_{I}	398	1.41	0.25
		2.1 eV	Ce^{3+}_{II}	398	1.57	0.25
200 K	Single	4.2 eV	F^+ center	287	0	0.36
		2.9 eV	Ce^{3+}_{I}	250	0	0.34
		2.5 eV	Ce^{3+}_{II}	250	0	0.34
	Poly	4.3 eV	F^+ center	385	0.67	0.38
		2.9 eV	Ce^{3+}_{I}	375	0.96	0.27
		2.2 eV	Ce^{3+}_{II}	375	1.23	0.27
100 K	Single	4.2 eV	F^+ center	355	0	0.36
		3.0 eV	Ce^{3+}_{I}	371	0	0.45
		2.6 eV	Ce^{3+}_{II}	340	0.03	0.43
	Poly	4.3 eV	F^+ center	396	1.22	0.32
		2.8 eV	Ce^{3+}_{I}	397	1.10	0.28
		2.1 eV	Ce^{3+}_{II}	387	0.41	0.28

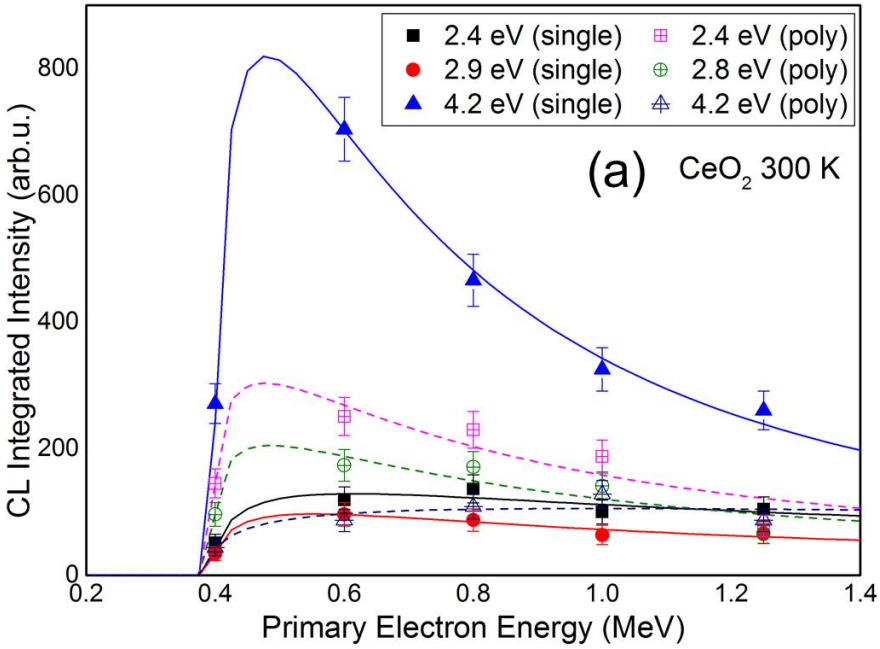
2.4 eV (single)
2.9 eV (single)
4.2 eV (single)
2.4 eV (poly)
2.8 eV (poly)
4.2 eV (poly)
(a) CeO2 300 K
CL Integrated Intensity (arb.u.)
Primary Electron Energy (MeV)
0
200
400
600
800
0.2
0.4
0.6
0.8
1.0
1.2
1.4

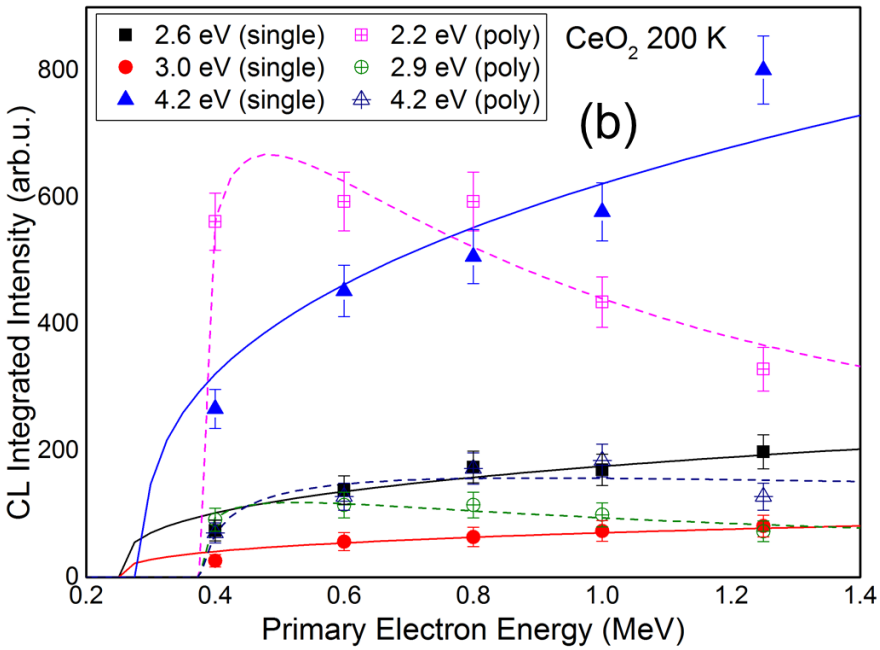
2.6 eV (single)
3.0 eV (single)
4.2 eV (single)
2.2 eV (poly)
2.9 eV (poly)
4.2 eV (poly)
CeO2 200 K
(b)
CL Integrated Intensity (arb.u.)
Primary Electron Energy (MeV)
0
200
400
600
800
0.2
0.4
0.6
0.8
1.0
1.2
1.4

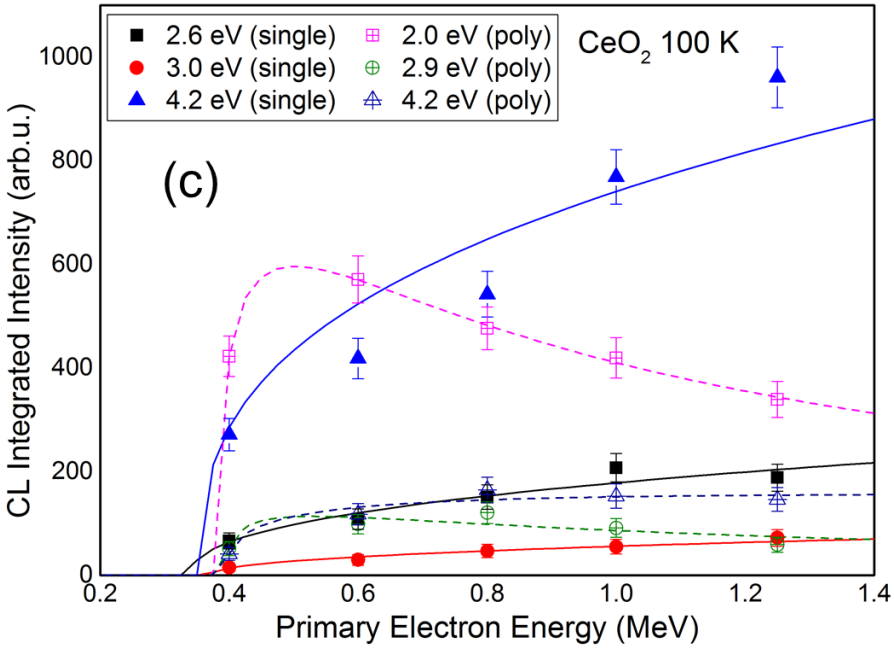

Figure 4-9. CL integrated intensities of the CL bands at (a) 300 K, (b), 200 K, and (c) 100 K versus electron energy for the ceria single crystal (full symbols) and polycrystalline sample (open symbols). Each set of data was recorded for a similar flux and fluence. Solid and dashed lines are least-square fits with Eq. (4-2) for the single crystal and polycrystalline sample, respectively.

previously mentioned [70,78,79,100]. According to the fits, this implies that the exponent should be temperature dependent (Table 4-4). This could explain why a maximum is observed in the sintered sample for a distinct thermal quenching behavior of the luminescence, whereas an almost linear increase of I_{CL} for F^+ centers is observed in the single crystal at 100 K and 200 K.

4.5 Conclusions

In an HVEM, the CL of cerium dioxide was investigated for electron energies ranging from 400 keV to 1250 keV at 100 K, 200 K, and 300 K, as well as for 20 keV electrons at 300 K in a SEM. Only the high-energy electrons (> 200 keV) show a broad, noticeable CL band that is centered at photon energy of 4.2 eV, whereas all electron energies show smaller bands at 2.3 ~ 2.6 eV and 2.8 ~ 3.0 eV. The emission of F^+ centers due to elastic electron-nucleus collisions over a threshold electron energy equivalent to the oxygen displacement energy is attributed to the 4.2 eV band. The charge compensation of oxygen vacancies for the high-energy (400 ~ 1250 keV) electrons and ionization effects for the low-energy (20 keV) electron excitation with a larger inelastic stopping power are attributed to the lower energy CL bands, respectively. At 100 K and 200 K, similar spectra are obtained, but with larger and slightly shifted emission bands. Regardless of temperature, the effects of grain boundaries cause the F^+ center CL signal for the polycrystalline sample to be weaker than the single crystal under the identical circumstances. The interaction between the oxygen displacement cross-section and the luminescence cross-section is used to explain the dependency of CL integrated intensities as a function of primary electron energy for both types of targets.

Chapter 5

Microstructure and radiation response of ceria and Gd_2O_3 doped ceria

5.1 Introduction

The point defects are important for lattice stability and subsequent damage accumulation/annihilation [107]. The trivalent doped ceria, such as Gd_2O_3 doped ceria, generates oxygen vacancies for the compensation of charge neutrality, and the oxygen deficiency of Gd_2O_3 doped ceria is generally higher than pure ceria. In the nuclear reactor, Gd_2O_3 dopant concentration in Gd_2O_3-UO_2 fuel is not high (i.e., < 6 Gd at% for BWR and < 14 Gd at% for PWR). However, the concentration of natural oxygen vacancies is mainly controlled by dopant concentration, and knowledge of the radiation response in high- and wide-concentration of Gd_2O_3 doped ceria is rather limited. In this chapter, the microstructure of virgin and heavy-ion irradiated Gd_2O_3 doped ceria ($Ce_{1-x}Gd_xO_{2-x/2}$) was evaluated in a wide range of Gd dopant concentrations ($0 \leq x_{Gd} \leq 0.5$) to gain insight into the fundamental understanding of radiation response in oxygen-deficient ceramics. For this purpose, a variety of analytical techniques with a wide-scale range was operated, such as XRD, micro-Raman spectroscopy, and TEM.

5.2 Materials and Experimental procedure

Sintered CeO_2 and $Ce_{1-x}Gd_xO_{2-x/2}$ ($0.01 \leq x_{Gd} \leq 0.5$) were used in this chapter and the details of sample preparation methods were described in Chapter 3. The virgin samples were analyzed by XRD measurements in powder type and thin bulk samples prepared from the same

bulk sinters. Raman spectroscopy and TEM observation were also utilized with bulk samples. The thin bulk samples were irradiated at ambient temperature with 200 MeV $^{131}Xe^{14+}$ ions from the JAEA-Tokai to fluence ranging from 3×10^{11} to 1×10^{13} cm^{-2}. They were also analyzed by XRD and TEM observation. The details of experimental conditions are also described in Chapter 3.

5.3 Results

5.3.1 Virgin samples

Figure 5-1 shows the powder XRD patterns of sintered virgin $Ce_{1-x}Gd_xO_{2-x/2}$ (x_{Gd} = 0, 0.01, 0.05, 0.1, 0.2, 0.3, 0.4, and 0.5) samples and unsintered as-received Gd_2O_3 powder. For low Gd concentrations ($x_{Gd} \leq 0.3$), the samples exhibit a single F-type structure, as same as CeO_2. As the Gd_2O_3 doping concentration increases, the C-type characteristic peaks start to be detected from $x_{Gd} = 0.4$, and the intensity of the C-type peaks is increased at $x_{Gd} = 0.5$, as shown in the inset magnified figure in Figure 5-1.

Examples of Rietveld refinement results are shown in Figures 5-2(a) and 5-2(b) for CeO_2 and $Ce_{0.5}Gd_{0.5}O_{1.75}$, respectively. The analysis revealed that a sintered CeO_2 sample has the F-type structure and $Ce_{0.5}Gd_{0.5}O_{1.75}$ has both the F-type and C-type structures by Gd_2O_3 doping. The Rietveld refinement's goodness of fit (χ^2) was defined as the ratio of the expected (R_{EXP}) to weighted (R_{WP}) R-factors as $\chi^2 = (R_{WP}/R_{EXP})^2$. The R_{WP}, R_{EXP}, and χ^2 results for all virgin powder samples are summarized in Table 5-1. CeO_2 and $Ce_{1-x}Gd_xO_{2-x/2}$ samples with values of x_{Gd} in the range of $0.01 \leq x_{Gd} \leq 0.3$ were refined only using the Fm-3m phase since the C-type characteristics peaks did not appear in the patterns, while $Ce_{0.6}Gd_{0.4}O_{1.80}$ and $Ce_{0.5}Gd_{0.5}O_{1.75}$ samples were refined using two phases of fluorite (Fm-3m) and bixbyite (Ia-3) structure. The phase fractions obtained by Rietveld refinement was 71% (fluorite) and 29% (bixbyite) for

$Ce_{0.6}Gd_{0.4}O_{1.80}$ sample, 59% (fluorite) and 41% (bixbyite) for $Ce_{0.5}Gd_{0.5}O_{1.75}$ sample. The value of χ^2 is usually considered reasonable if the value of χ^2 is less than 1.3 [62]. In the present analyses, χ^2 is close to 1.3 for samples of $0.1 \leq x_{Gd} \leq 0.5$. However, the values of χ^2 for $0 \leq x_{Gd} \leq 0.05$ show slightly higher values than the criterion. This is due to the large number of XRD counts that may attribute to the increase in the differences between R_{EXP} and R_{WP}, even with minor imperfections of fitting in the peak shapes and positions [108].

The lattice parameter (a) and microstrain (ε) were evaluated using the Braggs' angles and full-width half-maximum (FWHM) results derived from the Rietveld refinement [109]. The lattice parameter for each sample was determined by the Nelson-Riley plot [110]. The lattice parameter for each Bragg reflection plane of a cubic cell is given by the equation:

$$a_{hkl} = d\sqrt{h^2 + k^2 + l^2}, \quad (5\text{-}1)$$

where d is the d-spacing obtained from the Braggs' equation, hkl the Miller indices of the crystal. The Nelson-Riley function $f(\theta)$ is given by:

$$f(\theta) = (\cos^2\theta/\sin\theta) + (\cos^2\theta/\theta), \quad (5\text{-}2)$$

where θ is the Braggs' angle. The lattice parameter for each sample was calculated from the y-intercept of linear regression on a plot of a_{hkl} versus $f(\theta)$, as an example shown in Figure 5-3(a). The evaluated lattice parameter is plotted in Figure 5-4 as a function of Gd concentration with error bars representing the standard deviation of the linear regression fitting results. The results show that the lattice parameter based on the F-type structure Miller indices ($a_{F\text{-type}}$) increases from 0.5411 to 0.5430 nm for $0 \leq x_{Gd} \leq 0.3$, and saturates to 0.5432 nm for $x_{Gd} > 0.3$. In addition, the lattice parameters for x_{Gd} = 0.4 and 0.5 samples were calculated using the Nelson-Riley plot based on the C-type structure Miller indices ($a_{C\text{-type}}$). The lattice parameter for the C-type structure is double of the F-type structure. Hence, the $a_{F\text{-type}}$ for x_{Gd} = 0.4 and 0.5 is almost similar to half of the values of $a_{C\text{-type}}$ (i.e. $a_{F\text{-type}} \approx 1/2a_{C\text{-type}}$).

The theoretical lattice parameter (a_{Vegard}) was deduced from Vegard's law based on a model of rare-earth (RE) doped CeO_2 [111], which is given by:

$$a_{\mathrm{Vegard}} = 4/\sqrt{3}\left[x_{\mathrm{Gd}}r_{\mathrm{Gd}} + (1 - x_{\mathrm{Gd}})r_{\mathrm{Ce}} + (1 - 0.25x_{\mathrm{Gd}})r_{\mathrm{O}} + 0.25x_{\mathrm{Gd}}r_{\mathrm{V_O}}\right] \times 0.9971, \quad (5\text{-}3)$$

where the ideal ionic radius of Gd^{3+} (r_{Gd}), Ce^{4+} (r_{Ce}), O^{2-} (r_{O}), and V_O ($r_{\mathrm{V_O}}$) are assigned to r_{Gd}= 0.1053 nm, r_{Ce} = 0.0970 nm, r_{O} = 0.1380 nm, and $r_{\mathrm{V_O}}$ = 0.1164 nm, respectively. The constant 0.9971 is a ratio of the actual lattice parameter of CeO_2 from the JCPDS card (0.5411 nm) to the calculated lattice parameter derived from the ionic radii of Ce^{3+} and O^{2-} (0.5427 nm). The $r_{\mathrm{V_O}}$ for RE doped CeO_2 is 0.1164 nm regardless of dopant cation concentration and radius [111]. The calculated a_{Vegard} is shown as a solid line in Figure 5-4, which fairly coincides with small discrepancies ($\Delta a \leq 0.0001$ nm) for $0 \leq x_{Gd} \leq 0.3$, and deviates from the data due to the saturation.

The microstrain can be derived from Braggs' angle and FWHM of the diffraction peaks from XRD refinement results [109]. The microstrain is estimated by the y-intercept extrapolation and the slope of the Williamson-Hall [$\beta\cos\theta = K\lambda/D + 4\varepsilon\sin\theta$] and Halder-Wagner [$(\beta/\tan\theta)^2 = (K\lambda/D)\cdot(\beta/\tan\theta\sin\theta) + 16\varepsilon^2$] plots, where θ is Braggs' angle, β is FWHM, K is a shape constant which is taken into 0.94, and λ is the wavelength of Cu-Kα_1 radiation (0.15406 nm) [112,113]. The corresponding example plots are shown in Figures. 5-3(b) and 5-3(c) for a sample of $Ce_{0.8}Gd_{0.2}O_{1.90}$. The mean values of the microstrain are plotted against Gd dopant concentrations in Figure 5-4. The values of the microstrain increase with Gd concentration and show significant relaxation around x_{Gd} = 0.2, followed by a constant value within the experimental errors beyond x_{Gd} > 0.3.

Micro-Raman spectra between 220 and 700 cm^{-1} with fluorescence background corrections were shown in Figure 5-5. For pure CeO_2, a prominent peak at around 465 cm^{-1},

Table 5-1. XRD and TEM analysis results of $Ce_{1-x}Gd_xO_{2-x/2}$ samples for each Gd concentration (x_{Gd}). The Rietveld refinement performed using FullProf Suite software [67] and its results; weighted profile factor (R_{WP}), expected factor (R_{EXP}), goodness of fit (χ^2). Empirical lattice parameters (a) calculated by the Nelson-Riley plot [105] for virgin and irradiated samples (fluence = 3×10^{12} and 1×10^{13} cm^{-2}), damage cross-section (σ) and track radius (R) deduced from XRD profiles, and track-core radius (R_0) and cross sections (σ_0) deduced from BF-TEM images.

x_{Gd}	R_{WP} (%)	R_{EXP} (%)	χ^2	a (nm)			σ (cm^2)	R (nm)	σ_0 (cm^2)	R_0 (nm)
				Virgin	$3x10^{12}$ cm^{-2}	$1x10^{13}$ cm^{-2}				
0	16.9	9.1	3.4	0.5411	0.5412	0.5413	$23.7x10^{-13}$	8.7	$0.4x10^{-13}$	1.1
0.01	16.8	9.6	3.0	0.5412						
0.05	14.6	9.7	2.3	0.5415						
0.1	16.8	13.0	1.7	0.5419	0.5420	0.5420	$19.9 x10^{-13}$	8.0		
0.2	17.1	14.1	1.5	0.5426	0.5425	0.5426	$1.4 x10^{-13}$	6.6	$0.2x10^{-13}$	0.7
0.3	17.2	14.7	1.4	0.5430	0.5430	0.5430	$8.9 x10^{-13}$	5.3		
0.4	16.3	15.6	1.1	0.5432	0.5432	0.5432	$8.9 x10^{-13}$	5.3		
0.5	8.6	6.5	1.0	0.5432	0.5433	0.5432	$7.5 x10^{-13}$	4.9	$0.09x10^{-13}$	0.5

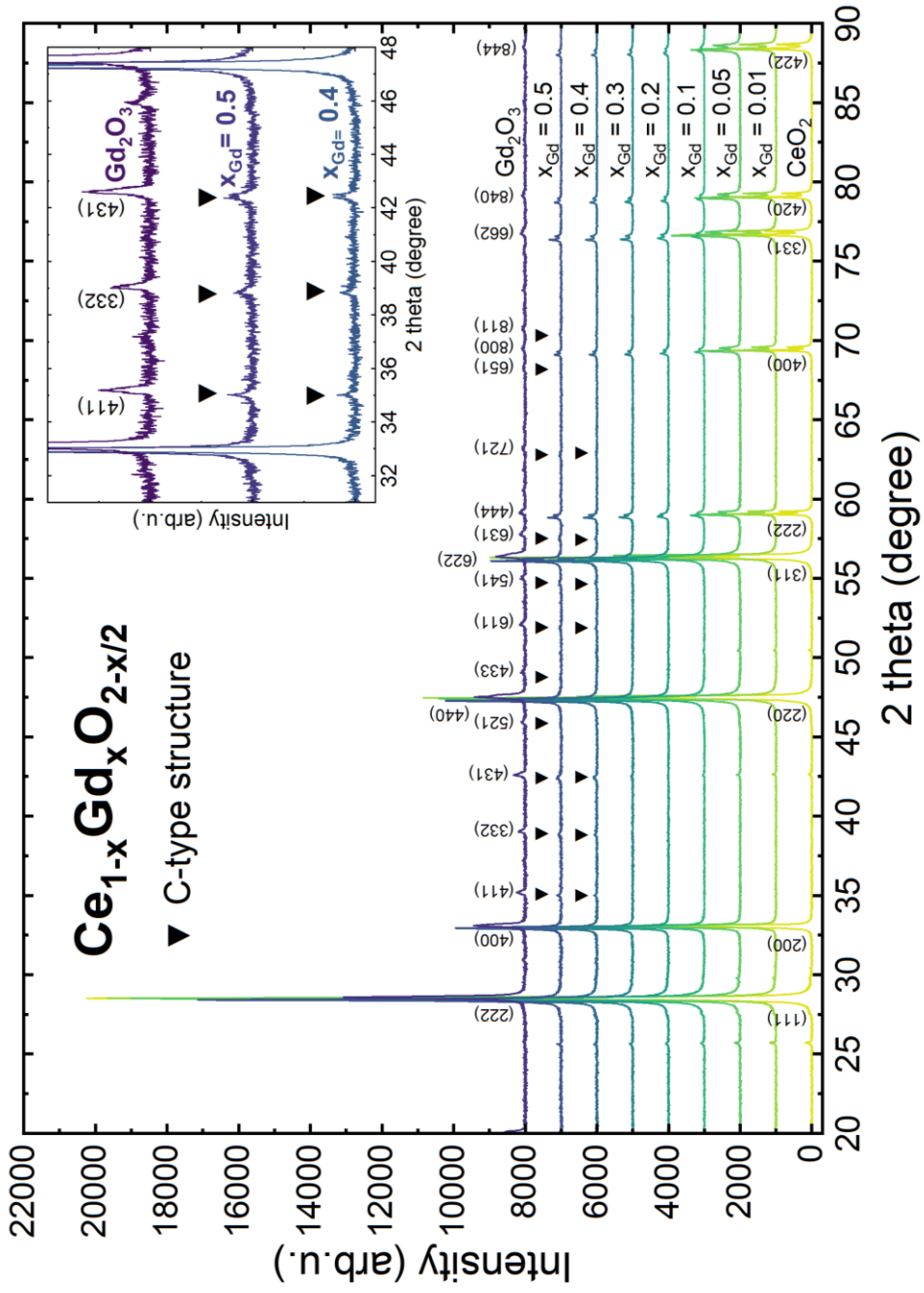

Figure 5-1. Powder XRD patterns of virgin $Ce_{1-x}Gd_xO_{2-x/2}$ and as-received Gd_2O_3 (x_{Gd} = 1). The (*hkl*) planes of the F-type and C-type structures are noticed on the CeO_2 and Gd_2O_3 profiles, respectively. The characteristics of the C-type structure are indicated on the peaks (▼). Inset shows magnified XRD patterns for $Ce_{0.6}Gd_{0.4}O_{1.80}$, $Ce_{0.5}Gd_{0.5}O_{1.75}$ and Gd_2O_3 samples.

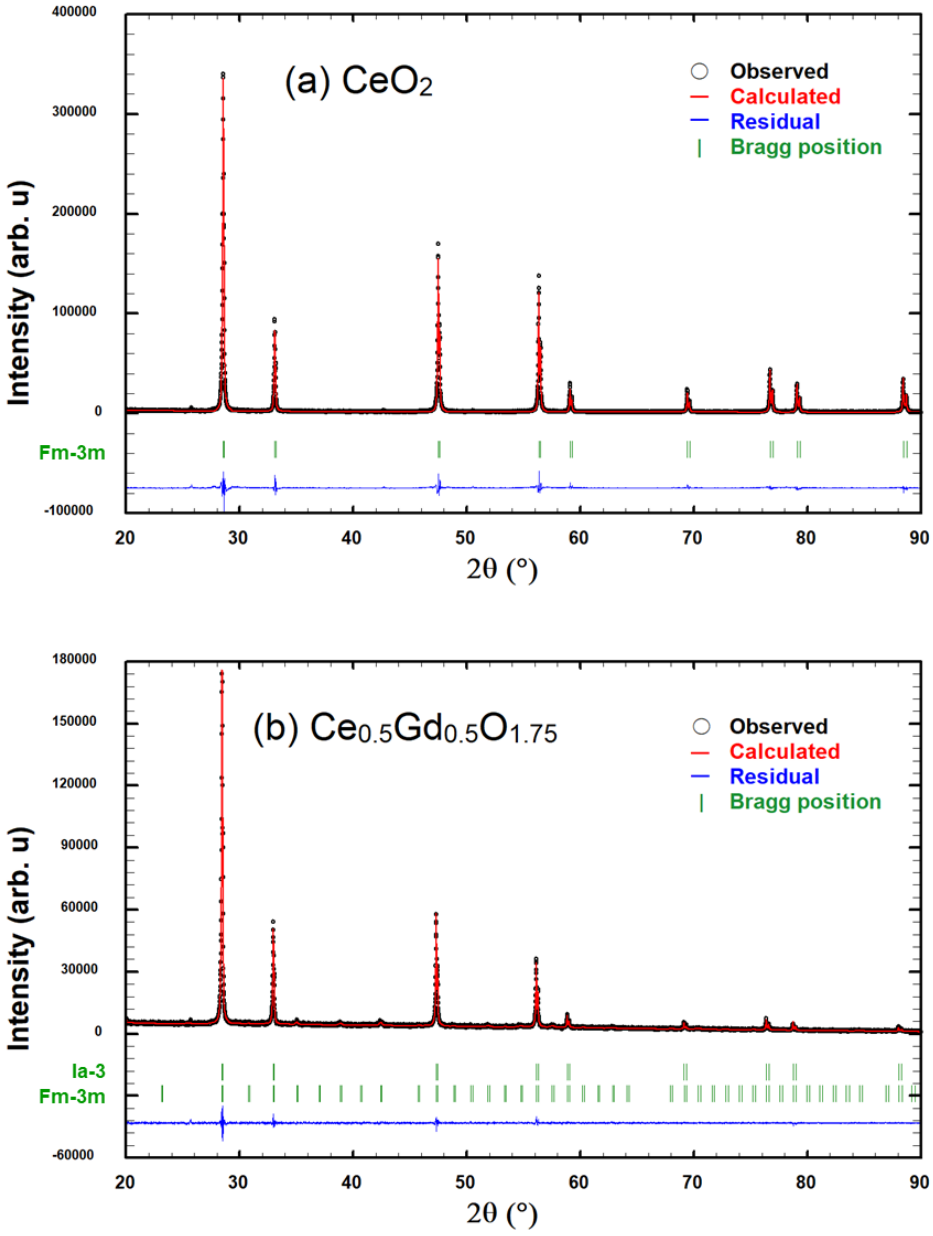

Figure 5-2. Observed (open circles) and Rietveld refinement calculated (red) XRD patterns of (a) CeO_2 and (b) $Ce_{0.5}Gd_{0.5}O_{1.75}$ with the residuals below (blue). The characteristics (*hkl*) of fluorite and cubic plane indices are noticed with Bragg reflection position (green).

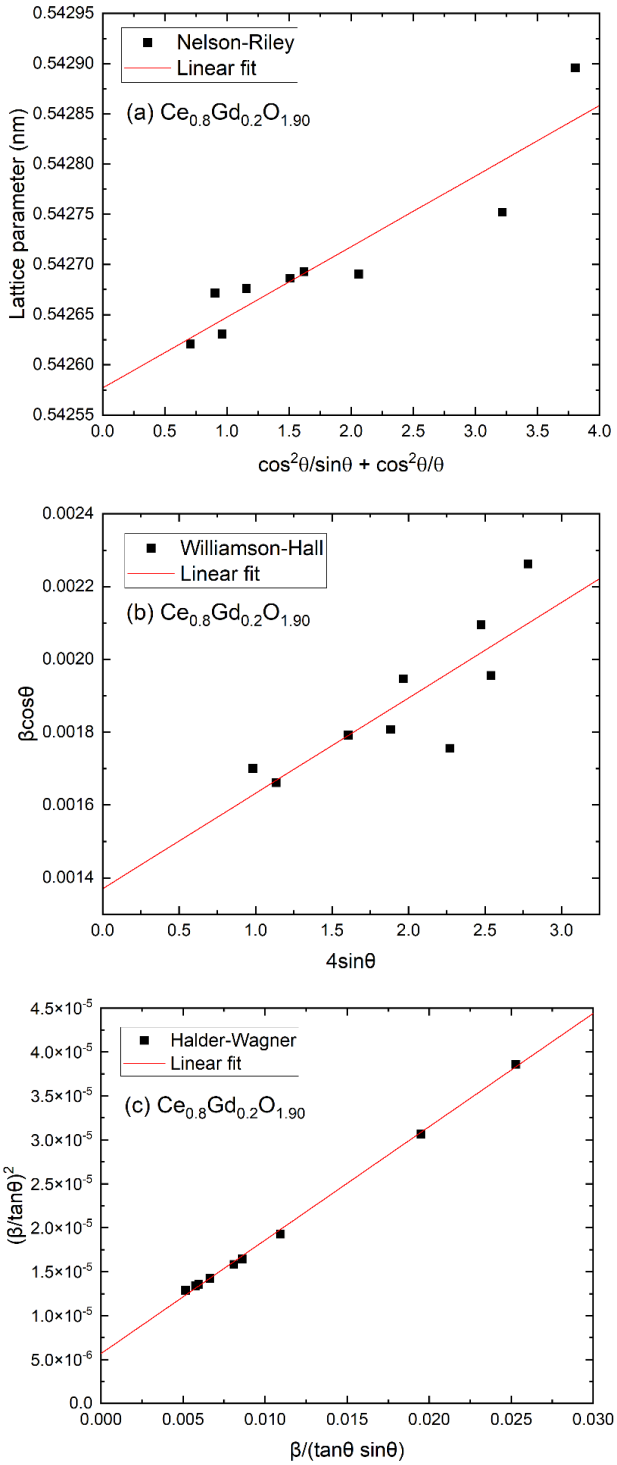

Figure 5-3. Examples of plots of (a) Nelson-Riley, (b) Willamson-Hall, and (c) Halder-Wagner for $Ce_{0.8}Gd_{0.2}O_{1.90}$ and the linear regression fits (red line).

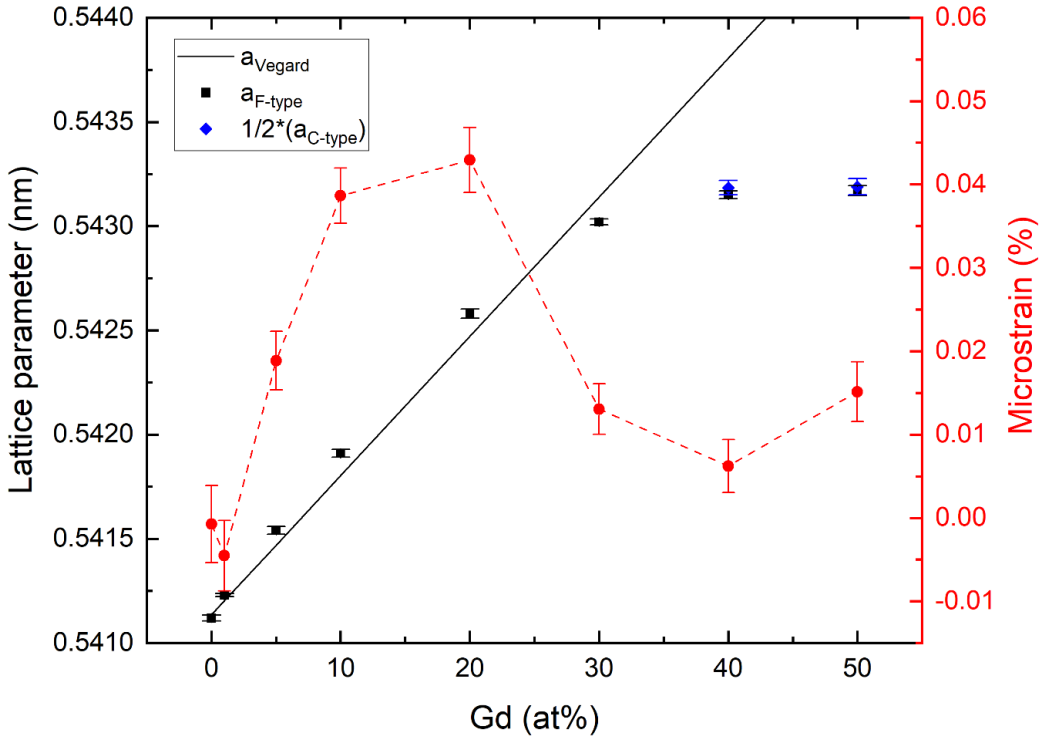

Figure 5-4. The lattice parameter (black, blue, left) and microstrain (red, right) in virgin $Ce_{1-x}Gd_xO_{2-x/2}$ samples as a function of Gd atomic concentration. Dashed and dotted lines are guides to the eyes. A solid line is the theoretical lattice parameter based on Vegard's law (a_{Vegard}), or Eq. (5-3).

five narrow satellites (490 ~ 555 cm^{-1}), and broad bands at around 250, 330, 365, 410 and 670 cm^{-1} were observed. Those peaks were fitted by Lorentzian function at 467 cm^{-1}, and Gaussian function at 251, 334, 365, 410, 493, 513, 523, 537, 555 and 670 cm^{-1}. The signal at 467 cm^{-1} is attributed to the F_{2g} symmetric vibration mode of Ce-O bond in 8-coordination ($Ce^{4+}O_8$) in the F-type structure [114,115]. The five satellites were discussed to native oxygen deficiency with 8-coordination cubes around Ce^{4+} and Ce^{3+} ions in CeO_{2-x} [116–119]. The bands centered at 251 cm^{-1} are assigned to the folded $E_g(X)$ (in directions of [00ζ]) [117,120,121]. The weak and broad bands at 334, 365, and 410 cm^{-1} are assigned to the folded $E_g(L)$, $E_u(L)$ and $A_{1g}(L)$ modes, respectively, in the [ζζζ] directions [121]. The sharp peak at 670 cm^{-1} could be attributed to the combination mode of the F_{2g} mode (467 cm^{-1}) with the A_{1u} mode (227 cm^{-1}) [121].

As a consequence of Gd_2O_3 doping, the F_{2g} mode was broadened, and it merged with the shifted first satellite (487 cm^{-1}) that appeared in the Gd_2O_3 doped samples. The last four satellites (513 ~ 555 cm^{-1}) were broadened and decayed by Gd_2O_3 doping, as well as the bands at 250 ~ 410, and 670 cm^{-1}. Meanwhile, new broadband has appeared at 600 cm^{-1} growing with Gd concentration, which was induced by intrinsic oxygen vacancy formation due to partial reduction of Ce^{4+} ions to Ce^{3+} ions [122].

For samples with high concentration Gd in the range of $0.3 \leq x_{Gd} \leq 0.5$, the latter four satellites disappeared, while broad bands were newly observed at 265, 375, and 565 cm^{-1}, and they are growing with Gd concentration. The bands at 265 and 565 cm^{-1} were ascribed to the interaction between the oxygen vacancies and the six next-nearest neighbor O^{2-} ions [123]. The band at 375 cm^{-1} originated from C-type Gd^{3+} in 6-coordination [124]. The two bands at 565 and 600 cm^{-1} were merged at $x_{Gd} = 0.5$.

The microstructure of $Ce_{1-x}Gd_xO_{2-x/2}$ samples was evaluated by conventional TEM. Figure 5-6 represents SAED patterns from virgin samples of CeO_2, $Ce_{0.8}Gd_{0.2}O_{1.90}$, and

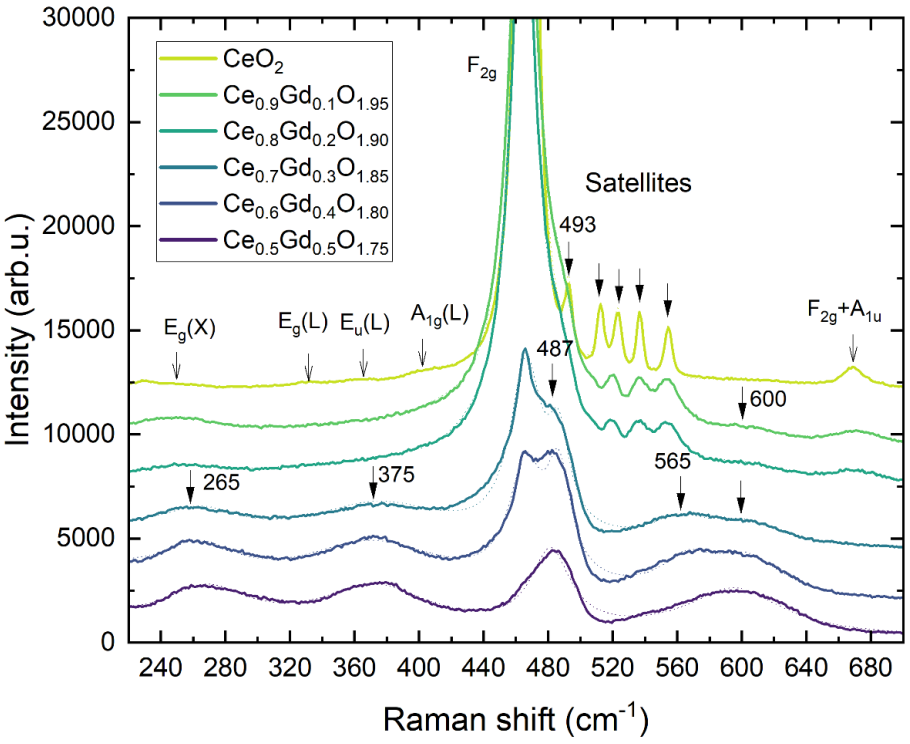

Figure 5-5. Micro-Raman spectra of virgin $Ce_{1-x}Gd_xO_{2-x/2}$ samples. Dotted lines are the sum of Lorentzian or Gaussian fitted curves.

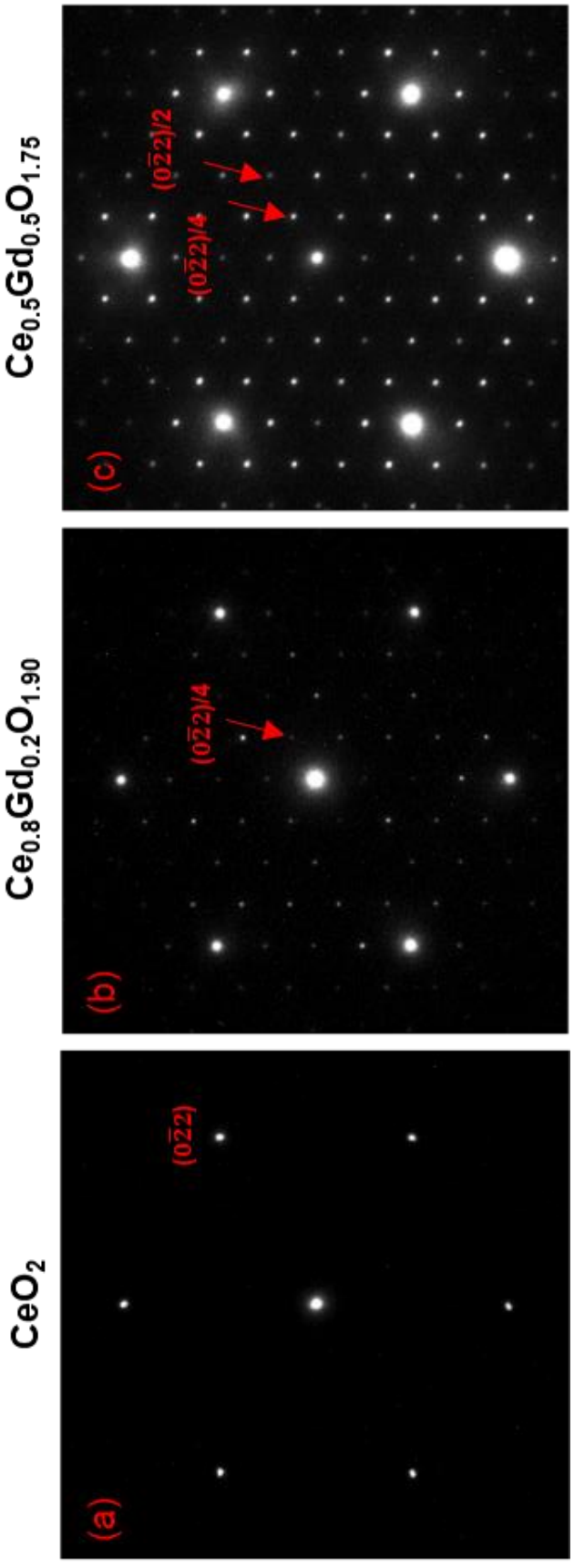

Figure 5-6. SAED patterns of virgin (a) CeO_2, (b) $Ce_{0.8}Gd_{0.2}O_{1.90}$, and (c) $Ce_{0.5}Gd_{0.5}O_{1.75}$ samples along the [111] zone axis.

$Ce_{0.5}Gd_{0.5}O_{1.75}$ taken along the [111] direction. The pure F-type structure reflections (reciprocal vector: $\boldsymbol{G_F}$) are seen in the virgin CeO_2 sample [Figure 5-6(a)]. For the Gd_2O_3 doped CeO_2 samples, extra spots have appeared at $\boldsymbol{G_F \pm \{220\}^*/4}$ and $\boldsymbol{G_F \pm \{220\}^*/2}$, and their intensity increases with increasing Gd concentration. The extra spots are induced by the formation of the domain and/or phase of C-type structure in the F-type phase [125], which will be discussed in section 5.4.1.

In this section, the microstructure in virgin $Ce_{1-x}Gd_xO_{2-x/2}$ samples was observed against to Gd_2O_3 dopant concentration on a wide range of scales. The XRD patterns showed the C-type structure creation in a high concentration of dopant. The XRD refinement results showed the saturation of lattice parameters and the relaxation of the microstrain at dopant concentrations higher than $x_{Gd} = 0.3$. Furthermore, the C-type characteristic Raman band at 375 cm^{-1} appeared for $x_{Gd} \geq 0.3$ with the decay and broadening of F_{2g} mode and satellites. According to TEM-SAED analysis, extra spots at $\boldsymbol{G_F \pm \{220\}^*/4}$ and $\boldsymbol{G_F \pm \{220\}^*/2}$ were observed for $x_{Gd} \geq 0.2$. These comprehensive experimental results provide the information on nucleation-and-growth of the C-type structure in the F-type matrix and a threshold of gadolinium dopant concentration in CeO_2 for the microstructure evaluation.

5.3.2 Irradiated samples with 200 MeV Xe^{14+} ions

The microstructure of $Ce_{1-x}Gd_xO_{2-x/2}$ samples evaluated after ion irradiation at room temperature. XRD patterns of thin bulk type virgin and irradiated $Ce_{1-x}Gd_xO_{2-x/2}$ (x_{Gd} = 0, 0.2, 0.5) samples are shown in Figure 5-7 for the 2θ angle range corresponding to (331) and (420) peaks to ion fluence of 3×10^{12} and 1×10^{13} cm^{-2}. The XRD profiles were fitted by the Pseudo-Voigt function based on the fluorite structure. All samples clearly show the F-type structure peaks, showing that no amorphization was induced by 200 MeV Xe ion irradiation as observed

in references [126,127]. For the irradiated samples, the C-type XRD peaks were diminished by irradiation (see the inset in Figure 5-7). Phase transition to the monoclinic structure was not observed, as reported in an ion-irradiated C-type structure of sesquioxide [128]. In addition, new asymmetric peaks appeared at approximately 0.1 deg. lower than the F-type structure peaks of $K\alpha_1$. The asymmetric peaks were grown and broadened with increasing ion fluence without any splitting of peaks. A new phase reported in reduced CeO_{2-x} samples ($CeO_{1.71} - CeO_2$) [129], which is featured by splitting of F-type structure peaks, was not recognized. The peaks are, therefore, considered to be induced by lattice distortion of the F-type structure by ion irradiation, and they were assigned to the peak of Damage-$K\alpha_1$ hereafter. The Damage-$K\alpha_1$ decays with increasing Gd concentration, and it almost completely disappeared for $x_{Gd} > 0.3$.

The lattice parameters of irradiated samples were deduced from the $K\alpha_1$ and Damage-$K\alpha_1$ peaks using the Nelson-Riley analysis based on the F-type structure. Results are shown in Figure 5-8 for ion fluence of 3×10^{12} and 1×10^{13} cm^{-2}, together with the lattice parameter of virgin samples ($a_{F\text{-type}}$) and the theoretical one (a_{Vegard}). Both $a_{K\alpha1}$ and $a_{Damage\text{-}K\alpha1}$ are seen to increase with x_{Gd} to reach saturation for $x_{Gd} > 0.3$, as observed in virgin samples ($a_{F\text{-type}}$). Further, the values of $a_{K\alpha1}$ show slight change after irradiation regardless of ion fluence. On the other hand, the values of $a_{Damage\text{-}K\alpha1}$ revealed higher values than $a_{F\text{-type}}$. The difference between $a_{K\alpha1}$ and $a_{Damage\text{-}K\alpha1}$ was greater for high fluence (1×10^{13} cm^{-2}) than low fluence (3×10^{12} cm^{-2}). The estimated lattice expansion of $\Delta a_{K\alpha1}/a_{F\text{-type}}$ in CeO_2 at a fluence of 1×10^{13} cm^{-2} was 0.04%. This is consistent with reported values of 0.06 ~ 0.07% by Ohno et. al. and Tracy et. al. obtained in CeO_2 with 200 MeV and 167 MeV Xe, and 950 MeV Au irradiation [130,131]. A slightly smaller value than the previous reports might be due to the lower ion fluence (1×10^{13} cm^{-2}) than references (1×10^{14} cm^{-2}). On the other hand, the change in the lattice parameter of the new shoulder peak, $\Delta a_{Damage\text{-}K\alpha1}/a_{F\text{-type}}$ showed rather large values of

0.12 ~ 0.14 % for CeO_2 and $Ce_{0.9}Gd_{0.1}O_{1.95}$. It is also noted that the value of $\Delta a_{\text{Damage-K}\alpha 1}/a_{\text{F-type}}$ was remarkably observed for low Gd concentration, and the lattice expansion became small for high Gd concentration samples above $x_{Gd} = 0.2$.

Figure 5-9 shows plane-view BF-TEM images of $Ce_{1-x}Gd_xO_{2-x/2}$ (x_{Gd} = 0, 0.2, 0.5) samples irradiated to a fluence of 1×10^{13} cm^{-2}, which were taken in a kinematical over-focus condition with a defocus value of $\Delta f = +1.0$ μm. As examples are noted with arrows in Figures 5-9(a) ~ 5-9(c), black dot contrast is observed as Fresnel contrast. The contrast represents the cylindrical defects of ion tracks observed at an end-on condition [126]. The ion-track radius (R_0) was evaluated to be 1.1 nm for CeO_2 and it gradually decreases to 0.7 and 0.5 nm for $Ce_{0.8}Gd_{0.2}O_{1.90}$ and $Ce_{0.5}Gd_{0.5}O_{1.75}$, respectively. They are reported in Table 5-1 with the cross-section values (σ_0) deduced by $\sigma_0 = \pi R_0^2$. These sizes are significantly smaller than the reported values obtained by XRD and TEM [117,132,133]. Since ion tracks in this study were observed as Fresnel contrast, the contrast represents the core region of ion tracks including a high concentration of vacancies [10,134], but not the strained regions around ion tracks. It is also noted that the size of Fresnel contrast varies with the defocus condition, or Δf [116], and the value of Δf = +1 gives a small and sharp contrast of ion tracks. The areal density of ion tracks for CeO_2, $Ce_{0.8}Gd_{0.2}O_{1.90}$, and $Ce_{0.5}Gd_{0.5}O_{1.75}$ was evaluated to be 5.9×10^{11}, 5.9×10^{11}, and 2.8×10^{11} cm^{-2}, respectively, and the density decreased at the high Gd content sample. It is reported that the density of ion tracks induced by 200 MeV Xe ions in CeO_2 increases linearly with ion fluence and saturates at high fluence higher than around 1×10^{12} cm^{-2}, which was discussed due to the balance between the formation and recovery of the core damage region of ion tracks [126,135]. The ion track density of the CeO_2 sample, which was obtained at a fluence of 1×10^{13} cm^{-2} in this study, seems to be saturated since the ion fluence is sufficiently higher than the reported fluence. Although there have been no data for the accumulation of ion tracks

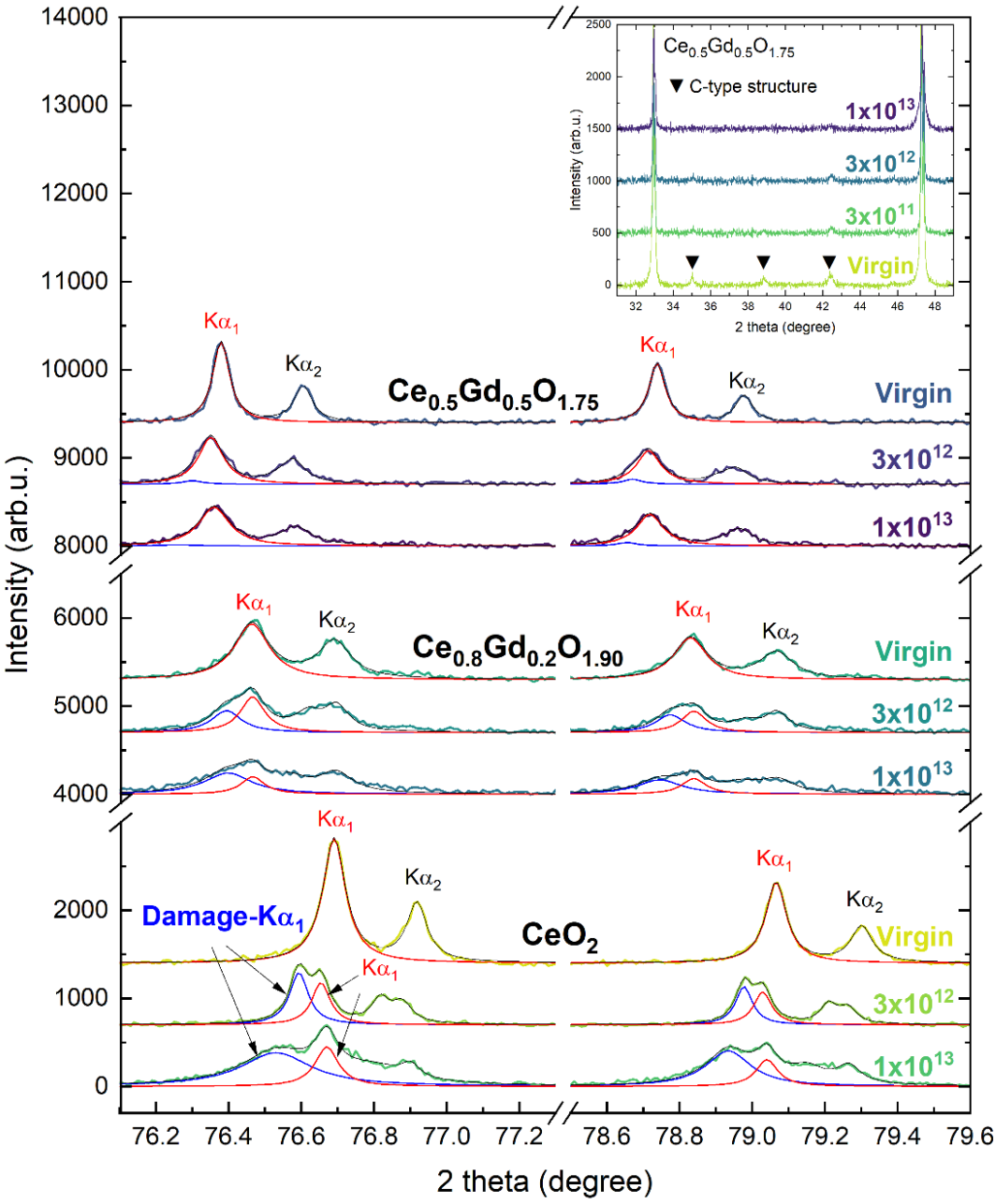

Figure 5-7. XRD patterns of (331) and (420) planes from virgin and irradiated $Ce_{1-x}Gd_xO_{2-x/2}$ samples (x_{Gd} = 0, 0.2, 0.5) with 200 MeV Xe^{14+} ions to fluence of 3×10^{12} cm^{-2} and 1×10^{13} cm^{-2}. $K\alpha_1$ (red) and Damage-$K\alpha_1$ (blue) peaks were fitted by the Pseudo-Voigt function. Inset shows the C-type characteristic peaks (▼) for virgin and irradiated $Ce_{0.5}Gd_{0.5}O_{1.75}$ samples at fluences ranging from 3×10^{11} to 1×10^{13} cm^{-2}.

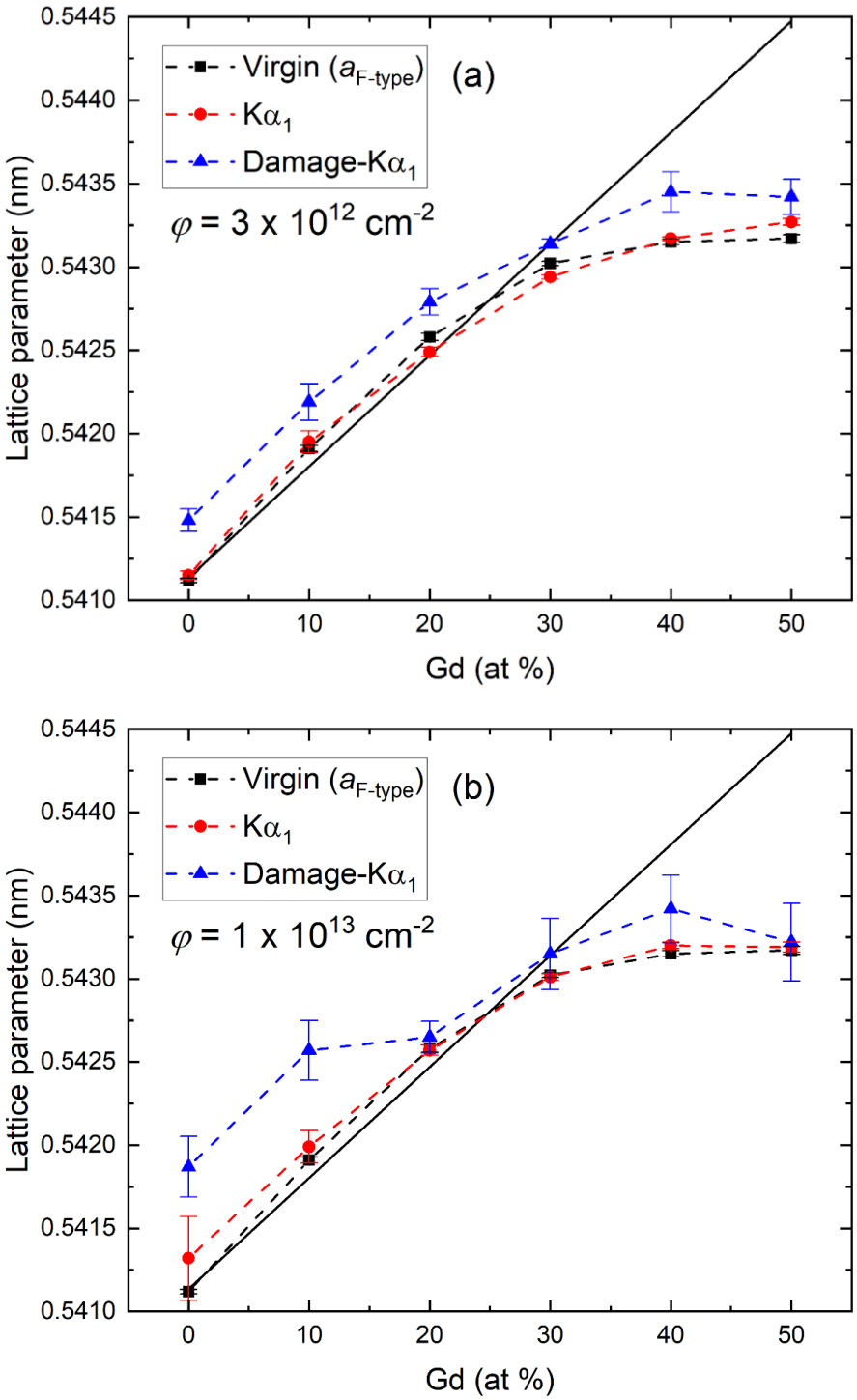

Figure 5-8. The lattice parameters of $Ce_{1-x}Gd_xO_{2-x/2}$ after ion irradiation to fluences of (a) 3×10^{12} cm^{-2} and (b) 1×10^{13} cm^{-2} comparing to virgin samples ($a_{F\text{-}type}$). Dashed lines are guides to the eyes. A solid line is the theoretical lattice parameter of virgin samples (a_{Vegard}) obtained from Eq. (5-3).

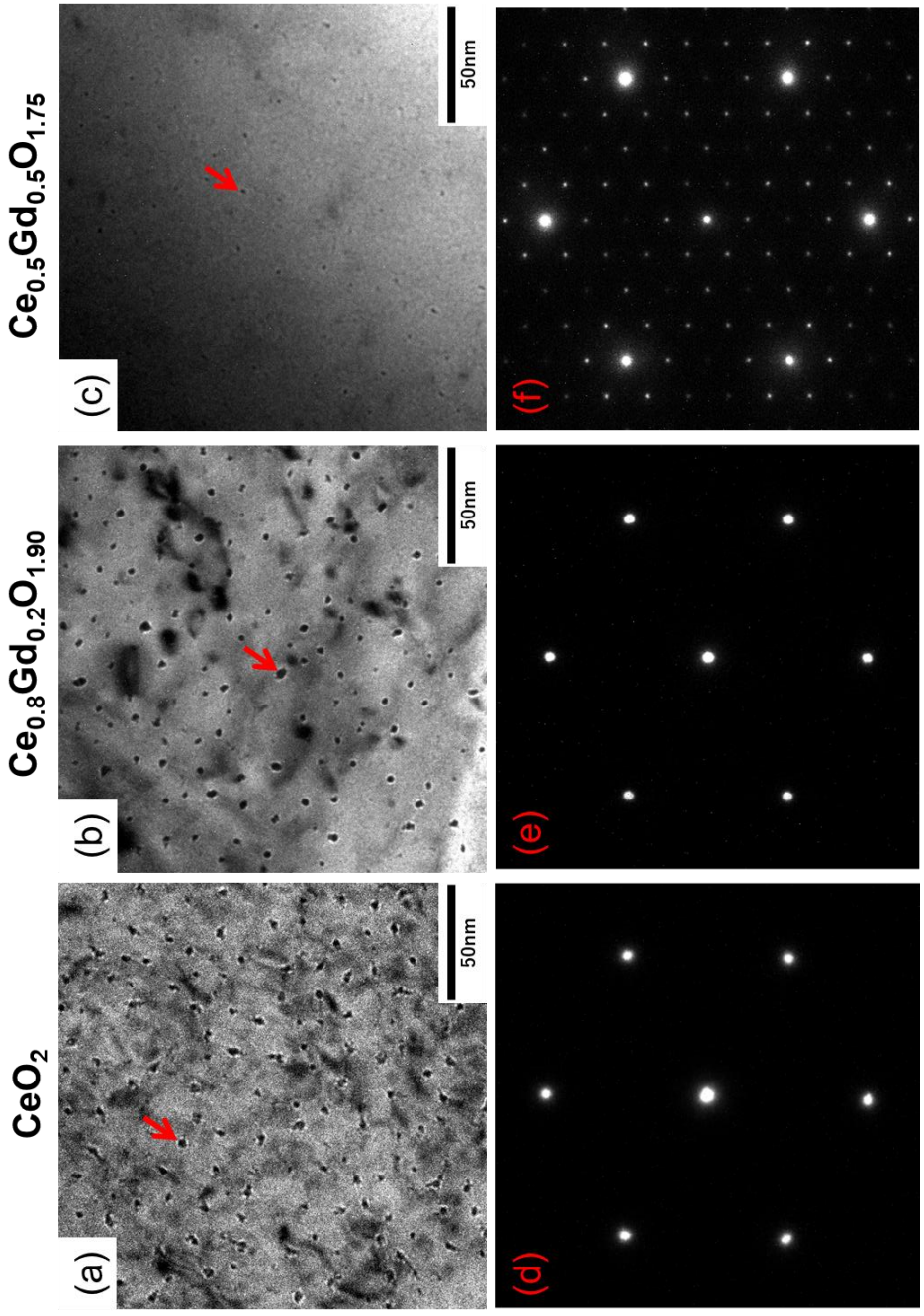

Figure 5-9. BF-TEM images showing Fresnel contrast taken from the direction along the incident ions in (a) CeO_2, (b) $Ce_{0.8}Gd_{0.2}O_{1.90}$, and (c) $Ce_{0.5}Gd_{0.5}O_{1.75}$ with 200 MeV Xe^{14+} ions to a fluence of 1×10^{13} cm^{-2}. BF images were taken in a kinematical over-focus condition with a defocus value of $\Delta f = +1.0$ µm. The corresponding SAED patterns along the [111] zone axis are shown in (d) – (f).

in Gd_2O_3 doped CeO_2, the density of ion tracks for high concentration $Ce_{1-x}Gd_xO_{2-x/2}$ samples might be depressed under an assumption that a fluence of 1×10^{13} cm^{-2} is in the saturation range as same as CeO_2. Figures 5-9(d) ~ 5-9(f) show the corresponding SAED patterns taken along the [111] zone axis. The F-type reflections are clearly visible in all samples, whereas the extra spots were eliminated for $Ce_{0.8}Gd_{0.2}O_{1.90}$ [Figure 5-9(e)]. The intensity of the $\boldsymbol{G_F \pm \{220\}^*/2}$ reflections for the $Ce_{0.5}Gd_{0.5}O_{1.75}$ sample is reduced significantly due to the ion irradiation [Figure 5-9(f)], and the SAED pattern of $Ce_{0.8}Gd_{0.2}O_{1.90}$ is similar to the $Ce_{0.5}Gd_{0.2}O_{1.90}$ sample without ion-irradiation [Figure 5-6(b)].

5.4 Discussion

5.4.1 C-type structure formation in $Ce_{1-x}Gd_xO_{2-x/2}$

The phase transition in the miscibility gap has been discussed in trivalent Ln doped ceria-based oxides solutions in literature, such as $Ce_{1-x}Yb_xO_{2-x/2}$ [136], $Ce_{1-x}Y_xO_{2-x/2}$ [137], and $Ce_{1-x}La_xO_{2-x/2}$ [138]. The amount of Ln dopant for the phase transition depends especially on its ionic radii [42]. The phase transition in $Ce_{1-x}Gd_xO_{2-x/2}$ was observed in a wide range scale by Raman spectroscopy [123,124], EXAFS [47,139], XRD [137,140–142], and oxidative drop solution calorimetry [143]. However, the reported value of x_{Gd} for the phase transition was different in literature in the range from $x_{Gd} = 0.13$ to 0.54. Such a wide range of x_{Gd} values is related to the similarity of the F-type and C-type structures, and different synthesis methods of materials. The average value of x_{Gd} from the above literature is 0.34. In the present study, the C-type structure was observed by XRD patterns without peak splitting for $x_{Gd} > 0.3$, which coincides with the average value deduced from the literature.

As shown in Figure 5-4, the lattice parameter of the virgin sample ($a_{F\text{-type}}$) increased following Vegard's law to saturate at $x_{Gd} > 0.3$, where the formation of the C-type structure

was observed. High resolution TEM observation of $Ce_{1-x}Gd_xO_{2-x/2}$ samples has found the formation of nano-scale domains of the C-type structure at $x_{Gd} = 0.2$ in the F-type matrix, and the size of the C-type nanodomain increased with Gd concentration [51]. Ou et al. suggested from the analysis and simulation of SAED patterns that the ordering of oxygen vacancies was initiated in the C-type nanodomains [125]. The SAED patterns of the virgin $Ce_{0.8}Gd_{0.2}O_{1.90}$ sample shown in Figure 5-6(b) clearly demonstrated extra spots at $\boldsymbol{G_F \pm \{220\}^*/4}$ and $\boldsymbol{G_F \pm \{220\}^*/2}$, despite the XRD pattern revealing single F-type structure (Figure 5-1). This implies that the ordering of oxygen vacancies occurred in the stable F-type structure at $x_{Gd} = 0.2$, and it grows to the C-type precipitates in the F-type matrix at the concentration of $x_{Gd} > 0.2$.

The above interpretation of the formation of the C-type structure at $x_{Gd} > 0.2$ coincides with the Raman spectroscopy result. For pure CeO_2, Raman shifts related to Ce^{4+}-O and Ce^{3+}-O bonds in the F-type structure were observed at the F_{2g} mode and at the first satellite (493 cm^{-1}), respectively, due to the reversible redox in CeO_{2-x} [118]. For Gd_2O_3 doped CeO_2, the F_{2g} mode sharply decayed with the increase of Gd concentration especially for higher values of $x_{Gd} > 0.2$ (Figure 5-5), due to the loss of symmetry of Ce^{4+}-O. Furthermore, a shift of the first satellite to 487 cm^{-1} was observed by Gd_2O_3 doping from $x_{Gd} = 0.1$. The shifted peak, which is assigned to Gd^{3+}-O bond in the F-type structure with 8-fold coordination [124], was growing gradually with Gd concentration compared to the change in the F_{2g} mode. On the other hand, for $x_{Gd} = 0.3$, a new broad Raman band appeared at 375 cm^{-1} and grew with Gd concentration, which was assigned to the 6-coordinated Gd^{3+}-O bond in the C-type structure [124]. Those results and interpretation imply that the growth of the C-type structure with Gd^{3+}-O bonds in the F-type structure started to grow at $x_{Gd} = 0.1$ and those in the C-type structure generated at $x_{Gd} = 0.3$.

The formation of the C-type structure is also linked to the microstrain relaxation. The microstrain was observed to increase with x_{Gd} while it was relaxed at around x_{Gd} = 0.2 – 0.3 (Figure 5-4). The microstrain was induced by the substitution of Gd^{3+} ions with a large ionic radius into the Ce^{4+} sites and the associated creation of oxygen vacancies [141,144]. Kossoy et al. observed a sharp decrease in the distance of Ce-O bond at x_{Gd} = 0.2 – 0.25 by EXAFS and XRD analysis. The structural distortion is influenced strongly by the change in the distance of the first shell (Ce-O and Gd-O) rather than that of the second shell (Ce-Ce and Gd-Ce) [139]. Therefore, the sharp relaxation of the microstrain observed at around x_{Gd} = 0.2 – 0.3 is attributed to the reduction of the coordination number of Ce ions, together with the development of oxygen vacancy ordering in the formation of the C-type precipitates in the F-type matrix.

5.4.2 Disappearance of C-type structure and damage recovery induced by heavy ion irradiation in $Ce_{1-x}Gd_xO_{2-x/2}$

The microstructure change of $Ce_{1-x}Gd_xO_{2-x/2}$ was evaluated after heavy ion irradiation by XRD and TEM analysis. The XRD patterns revealed a non-amorphized F-type structure after 200 MeV Xe ion irradiation. Slight changes in the lattice parameters of $a_{K\alpha1}$ (Table 5-1) indicate the F-type matrix is not largely expanded by irradiation. Xe ion irradiation, however, induced Damage-$K\alpha_1$ peaks at the shoulder of each $K\alpha_1$ peak, and those peaks were broadened with the increase of ion fluence whereas $K\alpha_1$ peaks decrease their intensities. The larger value of the lattice parameter of $a_{Damage\text{-}K\alpha1}$ than $a_{K\alpha1}$ indicates that the lattice of the damaged region was expanded by ion irradiation. The peaks of damage-$K\alpha_1$ were, therefore, understood caused by the lattice distortion of the F-type structure around the core region of ion tracks. The difference in the $a_{K\alpha1}$ and $a_{Damage\text{-}K\alpha1}$ values for the samples irradiated to low fluence (3×10^{12} cm^{-2}) is

almost constant regardless of x_{Gd} values [Figure 5-8(a)]. On the other hand, the discrepancy of the high fluence sample (1×10^{13} cm^{-2}) depends on Gd concentration. A larger discrepancy appeared for $x_{Gd} < 0.2$, while the discrepancy showed a low constant value above $x_{Gd} = 0.2$ within the experimental errors. This indicates that the lattice distortion is remarkable for $x_{Gd} < 0.2$ where the concentration of oxygen vacancies is relatively low without a fully ordered condition in the C-type structure.

To analyze the damage cross-section of 200 MeV Xe ions against the Gd concentration, the XRD peaks shown in Figure 5-1 were fitted by the Pseudo-Voigt function and the intensities were integrated. For the damage kinetics analysis, using the peak area parameter is much more accurate than the peak intensity since it contains strain and size information of the crystal induced by ion irradiation. In the following analysis, the damaged region was assumed to have no contributions to the original XRD peaks [145]. The area of $K\alpha_1$ peaks (A) at the (331) plane of an ion-irradiated sample was normalized to that of the corresponding virgin sample (A_0), and it was plotted in Figure 5-10 as a function of ion fluence (φ). As expected, the normalized value of A/A_0 decreases as a function of fluence to saturation at high fluence. The fraction of damaged regions (δ) can be estimated as

$$\delta = (S/\sigma)[1 - \exp(-\sigma\varphi)], \quad (5\text{-}4)$$

where S is the cross-section for recovery induced by ion-track over-lapping, σ is the damage cross-section. Assuming a linear dependence of A on δ, A is given by a decay function of

$$A = A_0 + (A_\infty - A_0)[1 - \exp(-\sigma\varphi)], \quad (5\text{-}5)$$

where A_∞ is the saturated area value. Fitting results are shown in Figure 5-10 as dashed lines for each sample. The values of A_∞/A_0 were found to increase with x_{Gd}: those were evaluated to be 0.26 for CeO_2 and 0.71 for $Ce_{0.5}Gd_{0.5}O_{1.75}$. The ratio of A_∞/A_0 for CeO_2 was saturated at $\varphi = 1 \times 10^{12}$ cm^{-2}, which shows a good agreement with the areal density saturation trends

versus φ determined by TEM and STEM observations [126,127]. For Gd_2O_3 doped CeO_2 samples at x_{Gd} = 0.4 and 0.5, the values of A_∞/A_0 were saturated at a rather higher fluence of ~5×10^{12} cm^{-2}. The values of σ were deduced by Eq. (5-5), and they showed to decrease with x_{Gd}. Particularly for $x_{Gd} > 0.2$, the values of σ show rapid reduction versus Gd concentration. The values of σ and track radii (R) deduced by $R = (\sigma/\pi)^{1/2}$ are reported in Table 5-1, together with the cross-section (σ_0) and the track radii (R_0) evaluated by Fresnel contrast of BF-TEM images.

The track radius deduced from XRD and TEM is plotted in Figure 5-11. The evaluated value of the ion track radius of the CeO_2 sample was 8.7 nm and it is significantly larger than the size obtained by Fresnel contrast of BF-TEM, or 1.1 nm. The evaluated size by XRD analysis reveals a good agreement with the recovery size (8.4 nm) evaluated based on the modeling of the accumulation process of ion tracks, where a saturation regime is interpreted on a balanced condition between the formation of a new ion track and the elimination of preexisting tracks within the recovery region [126,127]. It suggests that the obtained size by the present XRD study possesses the same physical meaning of recovery from the thermal spike regime. Figure 5-11 also shows that the radius of the ion track decreases with the increase of Gd concentration, showing a saturation at values of $x_{Gd} > 0.3$. This is a clear indication that the recovery cross-section of the ion track damage is influenced by the concentration of the oxygen vacancies and their ordering.

At the same time, the C-type XRD peaks (see the inset in Figure 5-7) and the extra spots in the SAED patterns (Figure 5-9) disappeared with 200 MeV Xe ion irradiation, indicating the destruction of the ordering structure of oxygen vacancies and the C-type structure. The ordered structure of oxygen vacancies is considered to be disappeared through the recombination with interstitial oxygens induced by ion irradiation. Patel et al. [146] also observed the reduction of

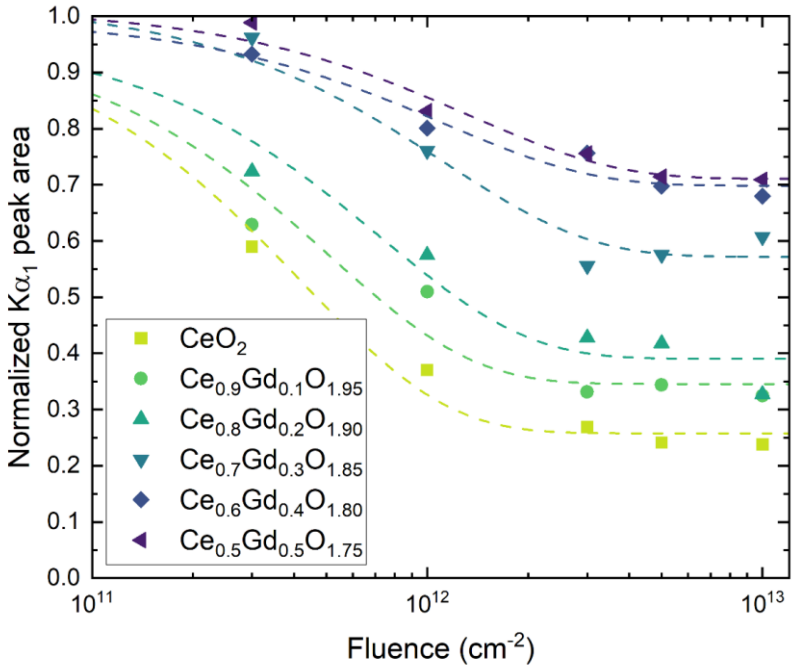

Figure 5-10. Area of normalized $K\alpha_1$ peaks fitted by the Pseudo-Voigt function as a function of fluence. Dashed lines are fits of area data with Eq. (5-5).

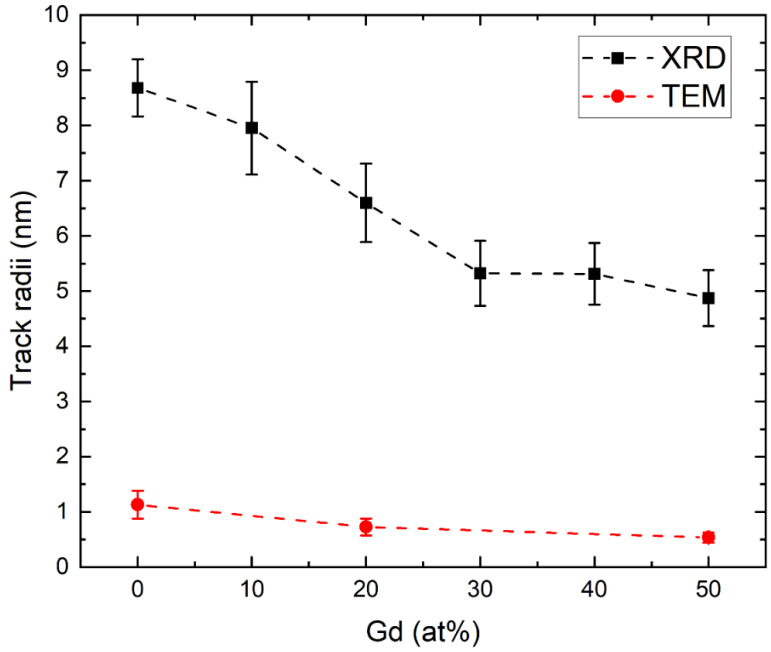

Figure 5-11. Track radius in $Ce_{1-x}Gd_xO_{2-x/2}$ against Gd atomic concentration deduced by from XRD analysis using Eq. (5-5), and Fresnel contrast BF-TEM images. Dashed lines are guides to the eyes.

lattice strain by XRD analysis in $Ce_2Gd_2O_7$ or $Ce_{0.5}Gd_{0.5}O_{1.75}$ irradiated with 92 MeV Xe^{26+} ions, and they suggested the radiation damage recovery occurred through the ordered oxygen vacancies in the C-type domain walls. The SAED pattern of $Ce_{0.5}Gd_{0.5}O_{1.75}$ irradiated to a fluence of 1×10^{13} cm^{-2} showed a partial elimination of extra spots [Figure 5-9(f)] compared to the unirradiated condition [Figure 5-6(c)], and the pattern and intensity of extra spots in the SAED pattern in Figure 5-9(f) resemble that of the virgin $Ce_{0.8}Gd_{0.2}O_{1.90}$ sample [Figure 5-6(b)]. Since the microstructure of $Ce_{0.8}Gd_{0.2}O_{1.90}$ is considered to contain nano-sized domains of the C-type structure in the F-type matrix [125], the SAED result suggests that the elimination of the C-type structure under ion irradiation might be proceeded gradually passing through the ordering condition of oxygen vacancies with nano-sized domains, but not directly from the C-type precipitates to the F-type matrix. This is consistent with the remarkable change in the recovery process observed in Figures 5-10 and 5-11 at $x_{Gd} = 0.2 \sim 0.3$, and this implies an important role in the ordering of oxygen vacancies for the recovery process during ion irradiation with 200 MeV Xe ions.

5.5 Conclusions

We have studied the microstructure evolution of virgin and 200 MeV Xe^{14+} ion irradiated $Ce_{1-x}Gd_xO_{2-x/2}$ samples for a wide range of Gd concentrations ($0 \leq x_{Gd} \leq 0.5$) at room temperature through comprehensive structural analysis of XRD, micro-Raman spectroscopy and TEM. The lattice parameter increased with the increase of Gd concentration and simultaneous creation of charge-compensation oxygen vacancies. The lattice parameter was saturated at $x_{Gd} > 0.3$ due to the formation of the C-type structure in the F-type matrix. The reduction in the F-type symmetry with the formation of the C-type structure associated with

ordered oxygen vacancies was observed at $x_{Gd} \geq 0.2$ consistently from the experimental techniques used in the present study.

The XRD and TEM results showed that all the compositions of $Ce_{1-x}Gd_xO_{2-x/2}$ samples were resistant to amorphization and sustained the F-type structure with 200 MeV Xe ion irradiation. In the XRD patterns, asymmetrical peaks (Damage-$K\alpha_1$) were observed on the shoulders of F-type peaks ($K\alpha_1$), and the asymmetry was decreased with the increase of Gd concentration. The asymmetric peaks are caused by the lattice distortion in the F-type structure due to the formation of damaged regions induced by ion tracks. On the other hand, the C-type structure has disappeared with ion irradiation because of the loss of the ordered oxygen vacancy structure in the C-type domain. Analysis of the radiation-induced recovery by XRD patterns with ion irradiation showed track radii, or recovery radii, decreases with the Gd concentration. Besides, the XRD analysis showed rapid recovery of radiation damage for values of $x_{Gd} = 0.2 \sim 0.3$, suggesting an important role of oxygen vacancy ordering in the C-type structure for the recovery process in Gd_2O_3 doped CeO_2.

Chapter 6

Application of *in-situ* HVEM - CL technique to CeO_2 doped with Gd_2O_3

6.1 Introduction

Ceria is an oxygen-deficient material since Ce^{4+} reversibly reduces to Ce^{3+} ion generating intrinsic oxygen vacancies for charge neutrality. As mentioned in Chapter 1, ceria has been used as a surrogate of nuclear fuel and it is doped with Gd_2O_3 for a burnable poison. Doping of Gd_2O_3 also produces oxygen vacancies as described $Ce_{1-x}Gd_xO_{2-x/2}$ by the substitution of Gd^{3+} into Ce^{4+} ion sites due to their similar ionic radii (i.e. r_{Gd}= 0.1053 nm, r_{Ce} = 0.0970 nm). The oxygen deficiency in $Ce_{1-x}Gd_xO_{2-x/2}$ is mostly controlled with the concentration of Gd dopant.

Oxygen point defects are also produced by high-energy electron irradiation. Frenkel defects are created by elastic collisions transferring energies over threshold displacement energy (E_d) of oxygen atoms. In Chapter 4, it was found that F^+ centers (1+ charged oxygen vacancies) were generated in pure CeO_2 in a short time under high-energy electron irradiation (400 ~ 1250 keV) by using the HVEM-CL facility. The in-beam charge states of defects and their electronic configurations were modeled through *in-situ* CL spectroscopy.

As described in Chapter 5, oxygen vacancies were shown to have an important role for the radiation recovery in $Ce_{1-x}Gd_xO_{2-x/2}$. Ordered oxygen vacancies were observed in the C-type structure in $Ce_{1-x}Gd_xO_{2-x/2}$ for the composition of $x_{Gd} > 0.2$, and this attributed for the reduction of the density and size of ion tracks induced by 200 MeV Xe ion irradiation. Those results suggest that oxygen vacancies act as a sink of irradiation-induced interstitials.

The displacement damage of O ions was found to influence the charge states of cation and F^+ center, and those strongly depend on the localized position in their lattice site. It is, therefore, interesting and indispensable to investigate the electronic states of ions and F^+ centers under electron irradiation during the production of oxygen vacancies. In this chapter, the oxygen point defects creation in $Ce_{1-x}Gd_xO_{2-x/2}$ under high-energy electron irradiation was evaluated by *in-situ* CL spectroscopy for a wide range of Gd dopant concentrations in the samples. Energy levels and energy dependence of F center and impurities were investigated regarding of dopant concentration.

6.2 Materials and experimental procedure

Sintered thin (~150 μm) half disk-shaped polycrystalline $Ce_{1-x}Gd_xO_{2-x/2}$ samples ($0.01 \leq x_{Gd} \leq 0.5$) were used to obtain *in-situ* CL spectra using the HVEM-CL facility (Figures 3-4 and 3-7) at electron energies from 400 keV to 1250 keV at the temperature of 300 K. Also, the CL spectra under low-energy (20 keV) electron irradiation were corrected by using the SEM-CL facility (Figure 3-6) at the temperature of 300 K. All obtained spectra were fitted by a Gaussian function and the intensity of CL bands were integrated to interpret CL emission dependence with electron energy and Gd dopant concentration. The detailed information for sample preparation, the HVEM-CL facility together with the *in-situ* measurement conditions were described in Chapter 3.

6.3 Results

6.3.1 Displacement cross-section calculation

The displacement cross-sections (σ_d) of oxygen, cerium, and gadolinium atoms in $Ce_{1-x}Gd_xO_{2-x/2}$ induced by electron-nuclear elastic collisions were calculated by using SMOTT/

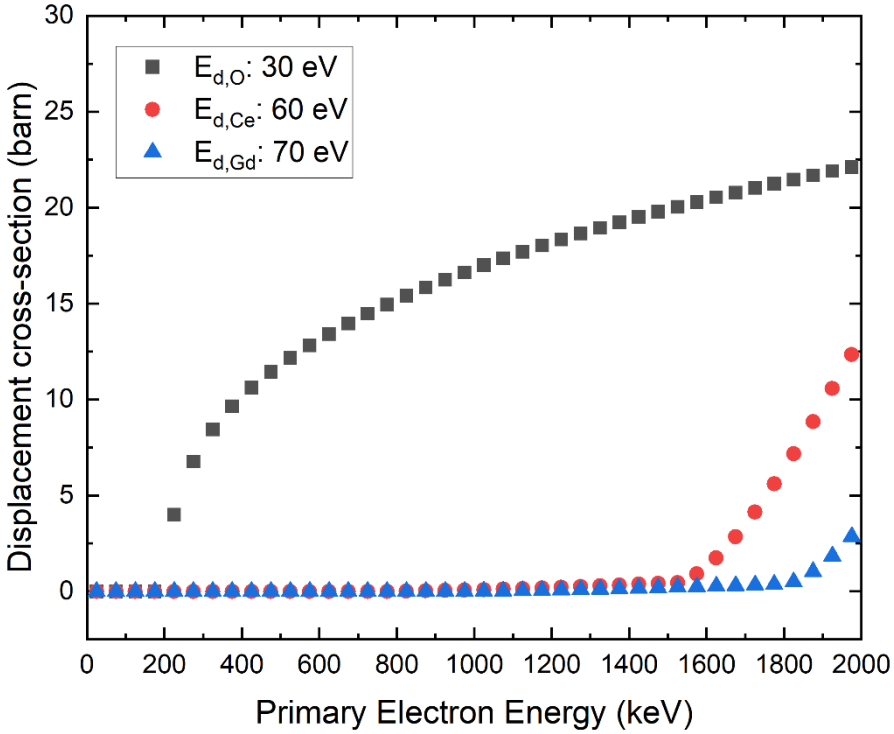

Figure 6-1. Oxygen, cerium, gadolinium atoms displacement cross section in Gd_2O_3 doped ceria by electron-nucleus collisions calculated by SMOTT/POLY computer code [74]. The values of E_d for each atom were referred to literature proposed by Yasunaga et al. [9] and Konobeyev et al. [72]

POLY computer code [74] based on Eq. (2-12). The threshold displacement energies (E_d) for each atom were assumed based on the reported values of Ce ($E_{d,Ce}$: 44 ~ 58 eV), O ($E_{d,O}$: < 33 eV) [9], and Gd ($E_{d,Gd}$: 71 ± 16 eV) [72] sublattices. The calculated total σ_d is shown in Figure 6-1 as a function of electron energy. The threshold electron energies in ceria where the cross-sections exceed 1 barn were evaluated in Chapter 4 for oxygen ($E_{0,O}$: 150 ~ 200 keV) and cerium ($E_{0,Ce}$: 1300 ~ 1600 keV) sublattices. The value of $E_{0,Gd}$ was evaluated in Fig.6-1 to be 1700 ~ 1900 keV. The selective oxygen displacement using HVEM in its energy range (400 ~ 1250 keV) was deduced for $Ce_{1-x}Gd_xO_{2-x/2}$ the total σ_d calculation results, while 20 keV electron irradiation hardly induces displacements of lattice atoms as same as the case of ceria described in Chapter 4.

6.3.2 CL spectra in polycrystalline Gd_2O_3 doped CeO_2

CL spectra in sintered polycrystalline $Ce_{1-x}Gd_xO_{2-x/2}$ (x_{Gd} = 0, 0.01, 0.05, 0.1, 0.2, 0.3, 0.4, 0.5) were obtained under high- and low-energy electron irradiation. For high-energy electron irradiation, one spectrum was taken under electron irradiation for 30 seconds at 300 K, and the spectra were averaged out for 5 recordings for 400 keV ~ 1250 keV electrons. The spectra were fitted using the Gaussian function. Figure 6-2 shows an example of *in-situ* CL spectrum for 1250 keV electron irradiation in ceria and $Ce_{0.5}Gd_{0.5}O_{1.75}$ together with fitted Gaussian profiles. 4 Gaussian bands were recorded at photon energies of ~1.7 eV, 2.2 ~ 2.4 eV, 2.4 ~ 2.8 eV, and ~4.3 eV with full-width at half-maximum (FWHM) of 0.6 ~ 0.9 eV, 0.5 ~ 0.7 eV, 0.3 ~ 0.6 eV, and 1.6 eV, respectively. A sharp and intense unresolved line was observed at 1.79 eV (probably R-lines of Cr^{3+} impurities [75]) for all samples, and a small doublet at 1.73 ~ 1.75 eV and another broader impurity line was observed at 1.85 eV.

CL spectra were measured at different electron energies of 400, 600, 800, 1000, and 1250 keV for all Gd_2O_3 doped samples at a constant electron beam-flux of 3.8×10^{21} $m^{-2}s^{-1}$. The CL spectra were obtained by averaging out the recordings after 0 ~ 150 seconds, and they are shown in Figure 6-3 with the Gaussian fitted profiles (dashed lines). Further, the average CL band characteristics, such as the band center (eV), FWHM (eV), and the types of defects in all samples of $Ce_{1-x}Gd_xO_{2-x/2}$ (x_{Gd} = 0, 0.1, 0.2, 0.3, 0.4, 0.5) were summarized in Table 6-1.

CL spectra were also measured for electrons with 20 keV at a constant beam current of 1.7 nA at the temperature of 300 K. The measured CL spectra are shown in Figure 6-4 with the Gaussian fitted profiles (dashed and dotted lines) for x_{Gd} = 0, 0.2, 0.3, 0.5 samples. The CL band characteristics for 20 keV electron irradiation are described in Table 6-2. Only one broad CL band centered at ~2.5 eV was observed in the samples for $x_{Gd} \leq 0.2$, and this band was divided into two bands centered at 2.3 eV and 2.6 ~ 2.7 eV by Gaussian fitting. It is noted here that the CL band was reduced for the samples with high Gd dopant concentration for $x_{Gd} > 0.2$, which is caused by the quenching of CL emission and will be discussed later.

6.4 Discussion

6.4.1 Cation CL emission with point defects production

CL from oxides under high energy electron irradiation is emitted by recombination of thermalized secondary electrons and holes while most of primary electrons are transmitted [70]. It is shown in Table 6.3 by the values of range and electronic stopping power of ceria and Gd_2O_3 doped ceria (x_{Gd} = 0.5) samples simulated by using the ESTAR code [77].

For sufficient CL intensity detection, a large volume of sample was used in the HVEM-CL measurements to increase the electron and hole carriers. To this end, CL spectra were obtained from thick (~150 μm) $Ce_{1-x}Gd_xO_{2-x/2}$ samples under 400 keV ~ 1250 keV electron

Table 6-1. CL band characteristics and defect assignments for $Ce_{1-x}Gd_xO_{2-x/2}$ (x_{Gd} = 0, 0.1, 0.2, 0.3, 0.4, 0.5) under high-energy (400 keV ~ 1250 keV) electron irradiation.

x_{Gd}	Band center (eV)	FWHM (eV)	Type of defect	x_{Gd}	Band center (eV)	FWHM (eV)	Type of defect
0	4.3	1.6	F^+ center	0.3	4.3	1.6	F^+ center
	2.8	0.4	Ce^{3+}_{I}		2.6	0.3	Ce^{3+}_{I}
	2.4	0.5	Ce^{3+}_{II}		2.3	0.7	Ce^{3+}_{II}
	1.8	0.6	Impurity		1.8	0.7	Impurity
0.1	4.3	1.6	F+ center	0.4	4.3	1.6	F+ center
	2.8	0.6	Ce3+I		2.6	0.3	Ce3+I
	2.4	0.6	Ce3+II		2.3	0.7	Ce3+II
	1.7	1.0	Impurity		1.7	0.8	Impurity
0.2	4.3	1.6	F+ center	0.5	4.2	1.6	F+ center
	2.6	0.3	Ce^{3+}_{I}		2.4	0.3	Ce^{3+}_{I}
	2.4	0.7	Ce^{3+}_{II}		2.2	0.7	Ce^{3+}_{II}
	1.7	0.8	Impurity		1.7	0.9	Impurity

Table 6-2. CL band characteristics and defect assignments for $Ce_{1-x}Gd_xO_{2-x/2}$ (x_{Gd} = 0, 0.1, 0.2) under low-energy (20 keV) electron irradiation.

x_{Gd}	Band center (eV)	FWHM (eV)	Type of defect
0	2.6	0.6	Ce^{3+}_{I}
	2.3	0.7	Ce^{3+}_{II}
0.1	2.8	0.8	Ce^{3+}_{I}
	2.2	0.7	Ce^{3+}_{II}
0.2	2.7	0.8	Ce^{3+}_{I}
	2.3	0.7	Ce^{3+}_{II}

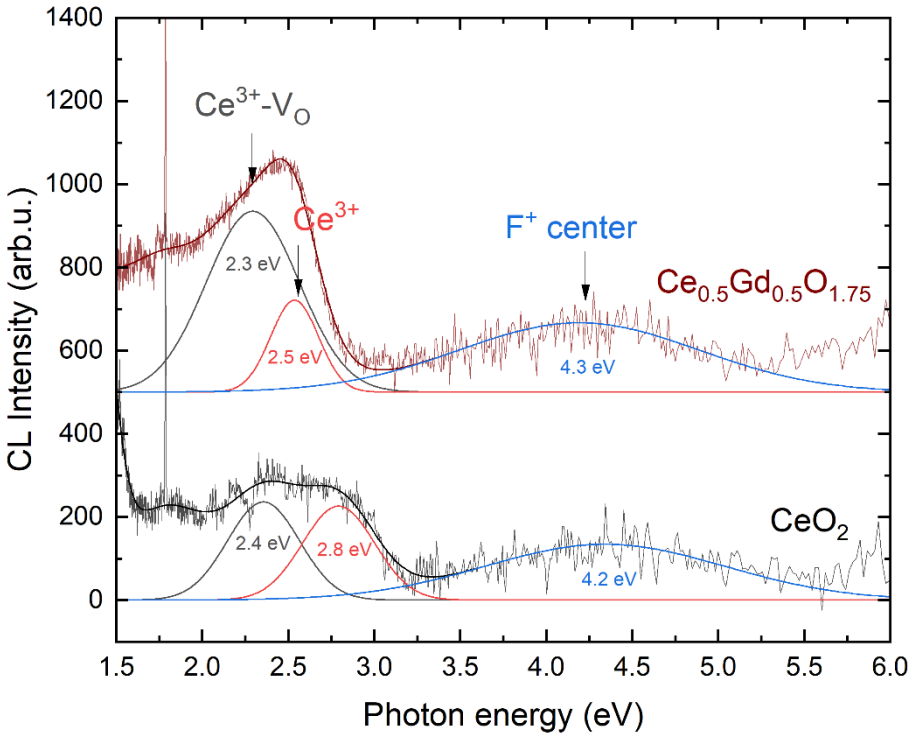

Figure 6-2. *In-situ* CL spectra for 1250 keV electron irradiation in ceria and Gd_2O_3 doped ceria at 300 K.

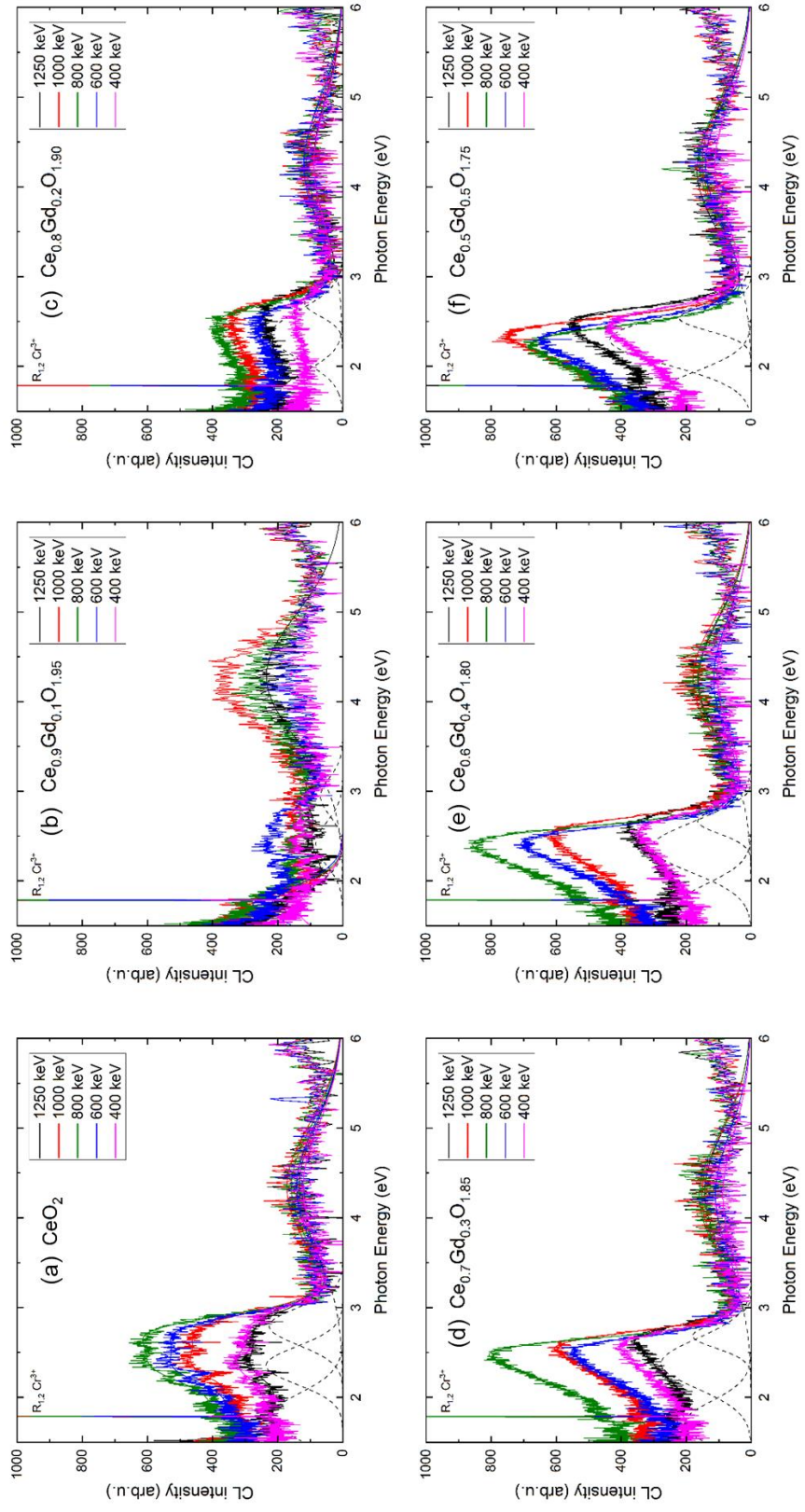

Figure 6-3. CL spectra at 300 K of polycrystalline ceria and Gd_2O_3 doped ceria ($Ce_{1-x}Gd_xO_{2-x/2}$) for $0.1 \leq x_{Gd} \leq 0.5$ at fluences of 5.7 x 10^{23} m^{-2}. Dashed lines are the fitted spectra and dotted lines are the Gaussian curves used for least-square fits.

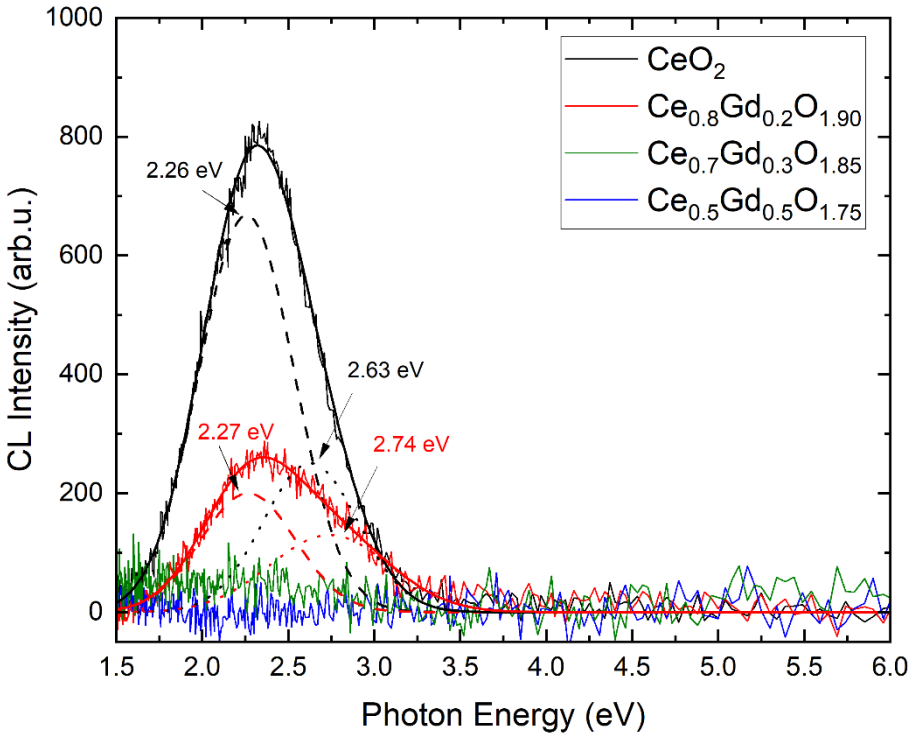

Figure 6-4. *In-situ* CL spectra for 20 keV electron irradiation in ceria and Gd_2O_3 doped ceria at 300 K. Dashed and dotted lines are fitted spectra and solid lines are Gaussian curves for least-square fits.

irradiation as same as pure CeO_2 samples, and the CL spectra showed enough intensity (Figure 6-3) as observed in pure polycrystalline ceria samples (Figure 4-5). The spectra were fitted by the Gaussian function, and the CL bands appeared at 2.2 ~ 2.4 eV, 2.4 ~ 2.8 eV, and 4.3 eV. These CL band positions are mostly similar to pure ceria results, which were measured at the temperature of 300 K [Figure 4-5(a) or Figure 6-3(a)].

In Chapter 4, CL bands for pure ceria were interpreted by experimental and theoretical methods. The CL emission was found to strongly link with oxygen vacancies, which form localized cation-V_O clusters. Namely, for pure ceria, CL bands centered at 2.1 eV, 2.7 eV, and 4.2 eV were assigned to i) Ce_I: Ce^{3+}, ii) Ce_{II}: Ce^{3+}-V_O, and iii) F^+ center, respectively. CL emission from Ce_I (2.7 eV) is induced by Ce^{3+} ions located in a site of cation sublattice far from V_O, while Ce_{II} is Ce^{3+} ions localized in a caton site near oxygen vacancy (V_O) that emits low energy (2.1 eV). On the other hand, CL emission from F^+ center at 4.2 eV was induced by a $(Ce_{Ce}^{\times} - V_O^{\cdot\cdot} - Ce_{Ce}^{\times})^{\cdot\cdot}$ trimer capturing an electron in ane oxygen vacancy $(Ce_{Ce}^{\times} - V_O^{\cdot} - Ce_{Ce}^{\times})^{\cdot\cdot}$, and immediately shifting the electron to one of the two Ce^{4+} (i.e. $Ce_{Ce}^{\times}$), resulting a $(Ce_{Ce}^{\times} - V_O^{\cdot\cdot} - Ce_{Ce}^{\prime})^{\cdot}$ trimer.

In the Gd_2O_3 doped ceria sample, the creation of extrinsic oxygen vacancies (denoted as $V_{O,ext}^{\cdot\cdot}$ hereafter) induced by charge compensation with Gd_2O_3 doping should be discussed before electronic excitation-induced point defects production. $V_{O,ext}^{\cdot\cdot}$ is generated in a dimer equilibrium process associating with the Gd dopant as expressed by $[Gd_{Ce}^{\prime} + V_{O,ext}^{\cdot\cdot} \leftrightarrow (Gd_{Ce}^{\prime} - V_{O,ext}^{\cdot\cdot})^{\cdot}]$. Trimer equilibrium equation $[2Gd_{Ce}^{\prime} + V_{O,ext}^{\cdot\cdot} \leftrightarrow (Gd_{Ce}^{\prime} - V_{O,ext}^{\cdot\cdot} - Gd_{Ce}^{\prime})^{\times}]$ can be also proposed. However, the low cation mobility rarely drives this reaction at low temperatures [43]. This trimer equilibrium equation in Gd_2O_3 doped ceria is similar to the defects creation in pure ceria induced by electronic excitation. It can be assumed that the Gd^{3+} dopants change not only the Ce^{3+}/Ce^{4+} redox equilibrium but also the excitation-induced defects equilibrium

by fixing the oxygen deficiency and reducing the number of Ce^{3+} ions. Therefore, (Gd'_{Ce}-V_O) cluster can be expressed as Ce_{II} or Ce^{3+}-V_O instead.

The photon energies of three CL bands (Ce^{3+}, Ce^{3+}-V_O, and F^+ center) observed in Gd_2O_3 doped ceria are plotted in Figure 6-5 as a function of Gd dopant concentration. Energies of Ce^{3+}-V_O and F^+ center showed constant regardless of the dopant concentration, while the peak of Ce^{3+} ion is seen to shift to lower energy (2.8 eV → 2.4 eV) with the increase of the Gd dopant concentration. The Ce^{3+} ion is localized far from oxygen vacancy, theirby this enegry shift is attributed to the increase of the direct band gap energy (E_G) between O 2*p* and Ce 4*f* bands. UV-visible absorption spectroscopy showed an increase of E_G in thin film samples from 3.6 eV for CeO_2 to 3.72 eV $Ce_{0.7}Gd_{0.3}O_{1.85}$ at 0 K since the lower overlapping capacity of 4*f* orbitals in the doped sample makes narrow 4*f* band [147]. On the other hand, for the low Gd dopant concentration ($x_{Gd} \leq 0.1$), no clear changes in E_G were observed [117]. For Gd_2O_3 doped ceria, Gd^{3+} has half-filed $4f^7$ orbital. Exciting an electron breaks the stabilization, and the excited electrons are more likely to be accommodated in the empty Ce $4f^0$ orbitals [147]. Therefore, the high Gd_2O_3 dopant concentration is considered to induce a narrow $4f^1$ band and decrease the value of E_G.

6.4.2 Auto-ionization thermal quenching model for CL emission

The CL bands were integrated versus Gd concentrations and primary electron energies, and they are shown in Figure 6-6 and Figure 6-8, respectively. The energy dependence will be discussed later. For the high energy electron irradiation, the CL emission dependence becomes clearer that shows a minimum for Ce^{3+} ion CL bands at x_{Gd} = 0.05, while F^+ center shows a maximum at x_{Gd} = 0.1. Beyond the x value, the CL emissions are observed to increase with the increase of the Gd dopant concentration for all electron energies. The quenching of CL bands

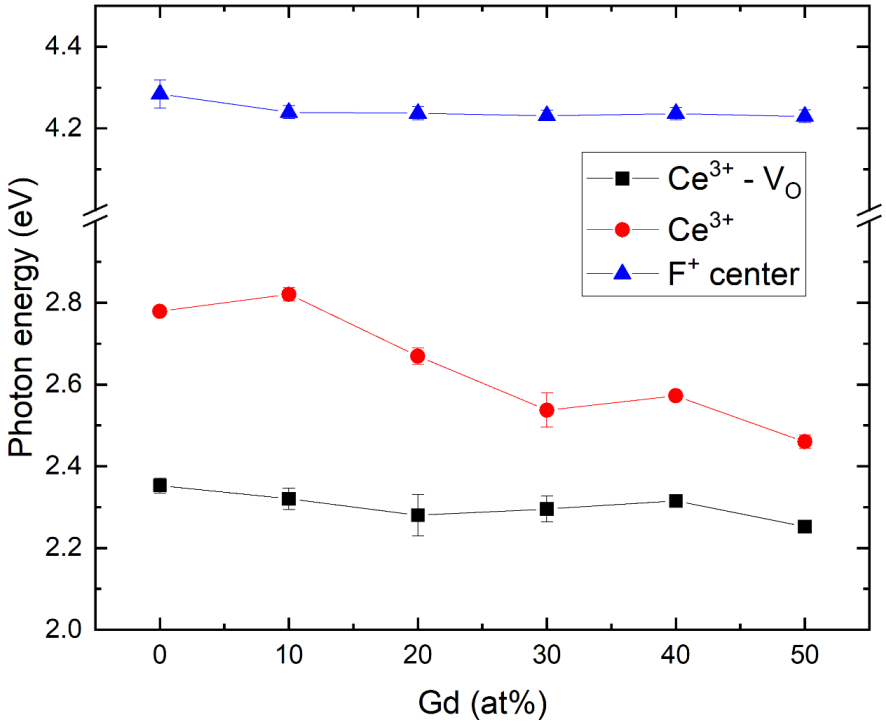

Figure 6-5. Photon energy for Ce^{3+} ions and F^{+} center in Gd_2O_3 doped ceria under high-energy electron irradiation versus Gd dopant atomic concentrations.

for Ce^{3+} ion at low Gd concentrations can be induced by the auto-ionization theory proposed by Dorenbos [148]. As an alternate explanation, a cross-over thermal quenching model has been suggested for 4*f*-5*d* system that induces non-radiative decay from the crossing point (X) between 4*f*-5*f* bands when the excited electron of 5*d* band overcomes the activation energy barrier (E_X) [149]. The CL emission and quenching model is described schematically in Figure 6-7. Figure 6-7(a) describes the luminescence emission for the case $E_X < E_R$, where E_R is an energy difference between the excited 5*d* level and the minimum 5*d* level. For the cross-over thermal quenching model, E_X should be smaller than 0.2 eV. However, it has been reported that ceria has a high value of $E_X > 1{,}5$ eV for Ce_{II} (i.e. Ce^{3+}-V_O) CL emission, which cannot induce CL emission due to the strong thermal quenching [87]. Thereby, auto-ionization theory has been suggested by Dorenbos for the thermal quenching of 4*f*-5*d* CL emission, whose schematic image is illustrated in Figure 6-7(c). 5*d* electron is transferred to the conduction band and becomes delocalized and mobile. Auto-ionization dissipates energy through other non-radiative mechanisms such as trapping or killer centers such as defects [150]. The increase of V_O concentration by Gd_2O_3 doping induces the 4*f*-5d thermal quenching by transferring electrons from V_O to Ce_{II} level, which results in the decrease in the recombination of e-h pairs.

In Figure 6-6, CL integrated intensities were growing versus Gd dopant concentration for $x_{Gd} > 0.05$. Let us consider the redox equilibrium equation. For electronic charge neutrality, the total oxygen vacancies concentration ($[V_O^{\cdot\cdot}]$) follows the equation below,

$$[V_O^{\cdot\cdot}] = \left[V_{O,int}^{\cdot\cdot}\right] + \left[V_{O,ext}^{\cdot\cdot}\right] = 1/4[Ce'_{Ce}] + 1/4[Gd'_{Ce}] \qquad (6\text{-}1)$$

However, $[V_O^{\cdot\cdot}]$ is mainly controlled by the Gd concentration for high dopant concentration [43]. The equation of (6-2) can be, therefore, rewritten as

$$[V_O^{\cdot\cdot}] = 1/2[Gd'_{Ce}]. \qquad (6\text{-}2)$$

Therefore, 4*f*-5*d* thermal quenching is reduced due to the rather low $V_O^{\cdot\cdot}$ creation comparing to Gd'_{Ce} creation for the high Gd_2O_3 concentration.

F^+ center CL emission in Gd_2O_3 doped ceria is indued by capturing electrons in a trimer as same as pure ceria. F^+ center CL emission is more likely to occur in a neutral cluster of $(Ce_{Ce}^{\times} - V_O^{\cdot\cdot} - Ce_{Ce}^{\times})^{\cdot\cdot}$ that includes no 3+ charged cations. However, for the high Gd_2O_3 concentration, $(Gd'_{Ce} - V_O^{\cdot\cdot} - Gd'_{Ce})^{\cdot\cdot}$ and $(Ce_{Ce}^{\times} - V_O^{\cdot\cdot} - Gd'_{Ce})^{\cdot\cdot}$ trimers are also growing together with $(Ce_{Ce}^{\times} - V_O^{\cdot\cdot} - Ce_{Ce}^{\times})^{\cdot\cdot}$. Despite of the increase of $[V_O]$ by Gd_2O_3 doping, F^+ center emission could have non-radiative decay or auto-ionization of the excited electron to 4*f* level.

6.4.3 Energy dependence of CL emission

The energy dependence of CL emission from the defects in pure ceria was discussed in Chapter 4. Electron energy dependence of I_{CL} results in a competitive process between the displacement cross-section (σ_d) with positive dependence against energy and the CL emission cross-section (σ_{CL}) with negative dependence [Eq. (4-1)]. For the Gd_2O_3 doped ceria samples, the I_{CL} for Ce^{3+} ions (i.e., $I_{CL,Ce-V_O}$ and $I_{CL.Ce}$) showed a maximum at ~800 keV. I_{CL} for F^+ center (i.e., $I_{CL,Fcenter}$) showed a maximum for $x_{Gd} \leq 0.1$, however, $I_{CL,Fcenter}$ gradually increased versus the energy for $x_{Gd} > 0.1$ (Figure 6-8). The competitive effect appeared strongly for the low Gd_2O_3 concentration samples, while the negative effects on the σ_{CL} was negligible for $I_{CL,Fcenter}$. The reduction of effect on σ_{CL} for low Gd_2O_3 concentration samples can be related to the thermal quenching due to the auto-ionization. Moreover, the CL spectra for the 20 keV electron irradiation (Figure 6-4) also showed a strong thermal quenching for the Ce^{3+} ion band since intrinsic oxygen vacancies are induced by the auto-ionization. However, the energy dependence in the doped samples is complex due to other parameters, such as strain

effect, and lattice size contraction, and it needs a more comprehensive theoretical or computational study to conclude the energy dependence equation.

For the summary, the schematic illustration of the energy band gap in Gd_2O_3 doped ceria can be suggested in Figure 6-9. The charge states of the defects in Gd_2O_3 doped ceria under electron irradiation were evaluated by using the *in-situ* HVEM-CL method compared to pure ceria. The charge states of cation defects and F^+ centers are highly close to that of pure ceria due to the similar point defect production mechanism with doped and non-doped samples. However, the rare-earth content Gd^{3+} was found to induce an energy shift in the CL spectrum due to the overlapping 4*f* orbitals in Gd^{3+} level. Also, high-dopant concentration samples showed strong 4*f*-5*d* CL thermal quenching by the auto-ionization due to the existence of oxygen vacancies.

6.5 Conclusions

In-situ HVEM-CL measurement technique was applied to yield charge state of point defects in polycrystalline Gd_2O_3 doped ceria ($Ce_{1-x}Gd_xO_{2-x/2}$) for a wide range of Gd dopant concentrations ($x_{Gd} = 0 \sim 0.5$). The CL spectra were obtained by 400 keV ~ 1250 keV electron irradiation in the HVEM, and 20 keV irradiation in the SEM. The CL bands appeared at 2.2 ~ 2.4 eV, 2.4 ~ 2.8 eV, and 4.3 eV were assigned to Ce^{3+}-V_O, Ce^{3+}, and F^+ center, respectively, which were qualitatively the same with pure ceria. The photon energy shift of Ce^{3+} ion band was induced by narrow $4f^1$ orbitals in the Gd^{3+} doped samples. Also, the high natural oxygen vacancy concentration in the doped samples derived thermal quenching of 4*f*-5*d* CL emission. The CL integrated intensities as function of primary electron energy is interpreted by the competitive interplay of displacement and CL emission cross-sections, but the energy

dependence for Ce^{3+} ions CL emission is much more affected by CL quenching effect than that of F^{+} center.

Table 6-3. Characteristics of electron irradiations of CeO_2 (mass density = 7.215 g cm^{-3}) and $Ce_{0.5}Gd_{0.5}O_{1.75}$ (mass density = 7.35 g cm^{-3}) computed with the ESTAR code [77] for different primary electron energies (E) and mean ionization energy I = 407.6 eV: CSDA range, and total inelastic stopping power ($(-dE/dx)_{inel}$).

E (keV)	20	400	600	800	1000	1250
CeO_2						
Range (μm)	2.1	265	460	663	869	1126
$(-dE/dx)_{inel}$ (MeV μm^{-1})	57×10^{-4}	11×10^{-4}	10×10^{-4}	9.8×10^{-4}	9.7×10^{-4}	9.7×10^{-4}
$Ce_{0.5}Gd_{0.5}O_{1.75}$						
Range (μm)	2.1	262	454	655	859	1113
$(-dE/dx)_{inel}$ (MeV μm^{-1})	57×10^{-4}	11×10^{-4}	10×10^{-4}	9.9×10^{-4}	9.8×10^{-4}	9.8×10^{-4}

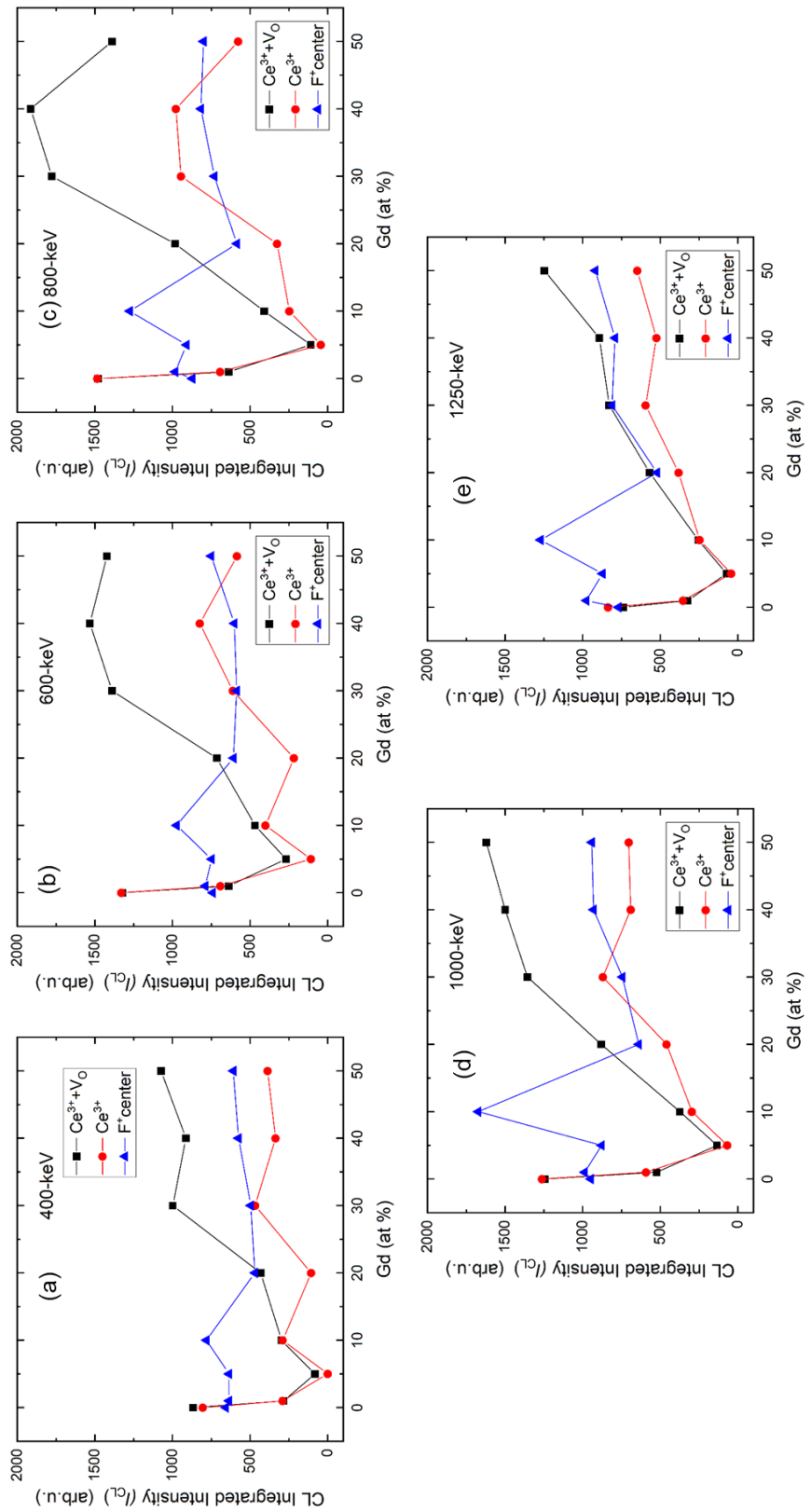

Figure 6-6. Gd dopant dependence versus integrated CL intensity in polycrystalline ceria and Gd_2O_3 doped ceria ($Ce_{1-x}Gd_xO_{2-x/2}$) for 400 keV ~ 1250 keV electron irradiation at 300 K.

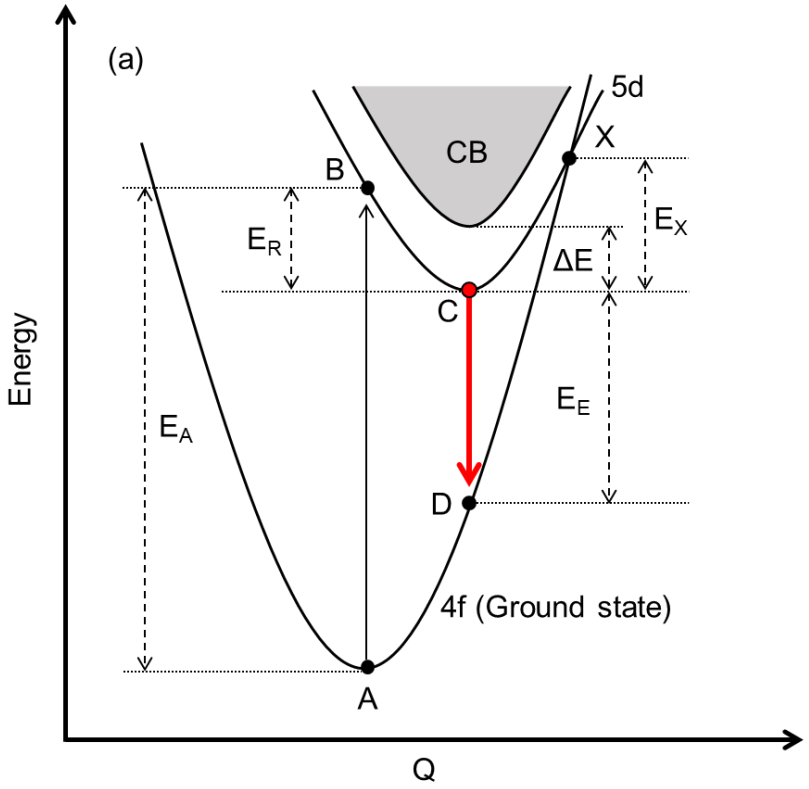
(a)
5d
CB
X
B
E_X
E_R
ΔE
C
Energy
E_E
E_A
D
4f (Ground state)
A
Q

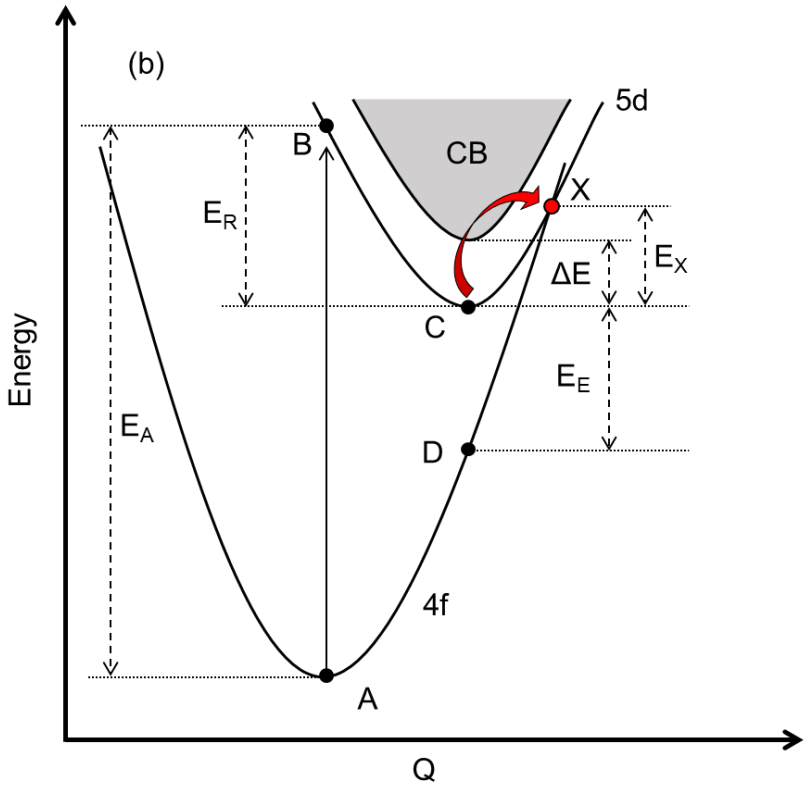
(b)
5d
B
CB
X
E_R
E_X
ΔE
C
Energy
E_E
E_A
D
4f
A
Q

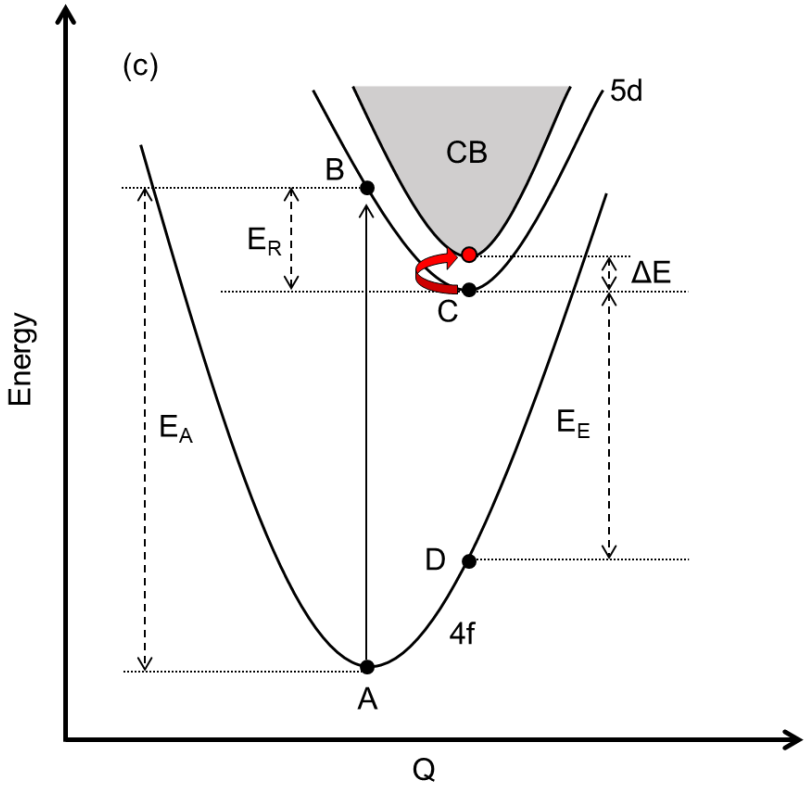

Figure 6-7. (a) The 4*f*-5*d* luminescence emission process for $E_x > E_R$ and comparison of thermal quenching models; (b) cross-over model ($E_x < E_R$) [149], (c) Dorenbos auto-ionization model [148].

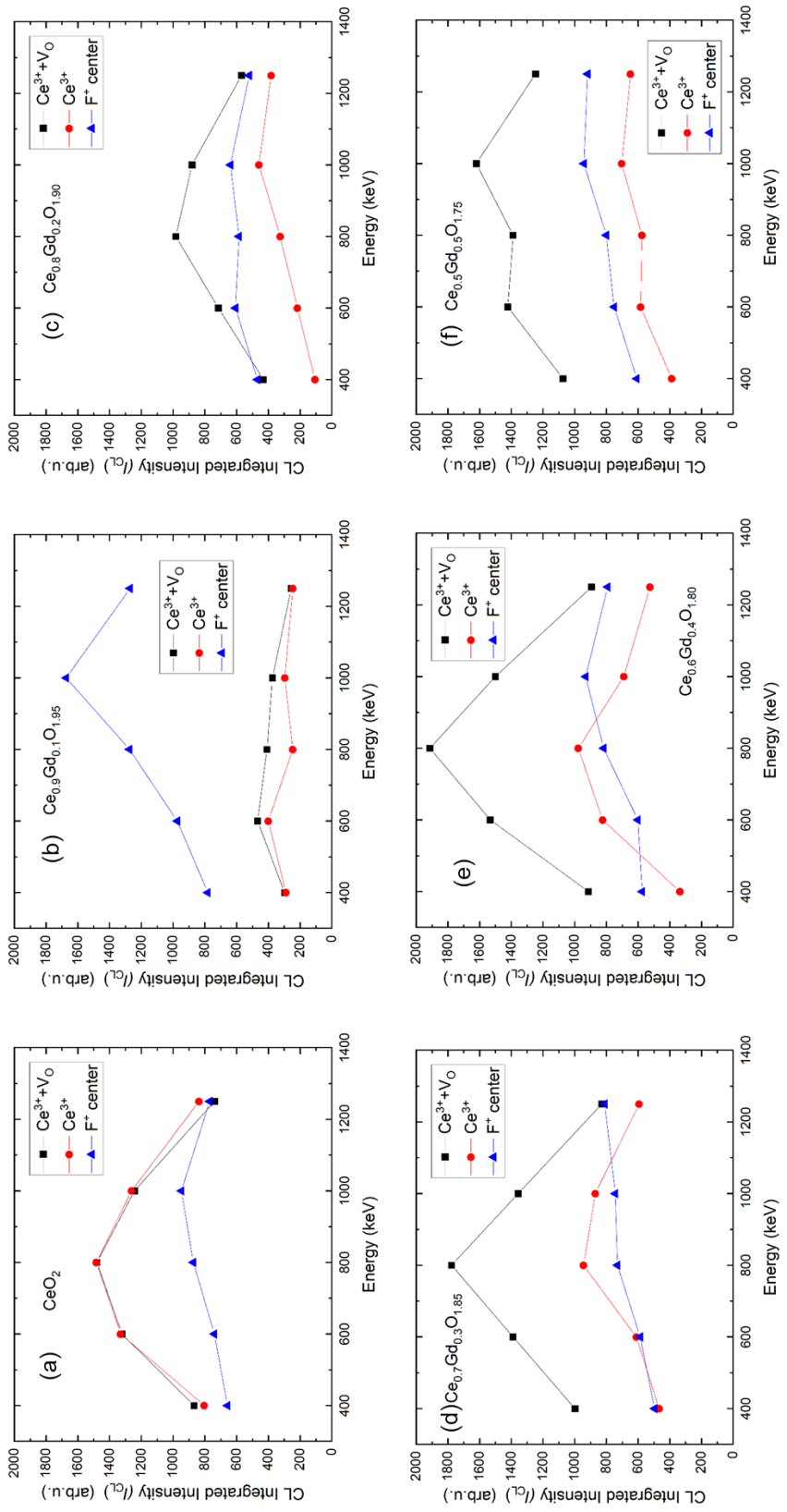

Figure 6-8. Energy dependence versus integrated CL intensity in polycrystalline ceria and Gd_2O_3 doped ceria ($Ce_{1-x}Gd_xO_{2-x/2}$) for $0.1 \leq x_{Gd} \leq 0.5$ at 300 K.

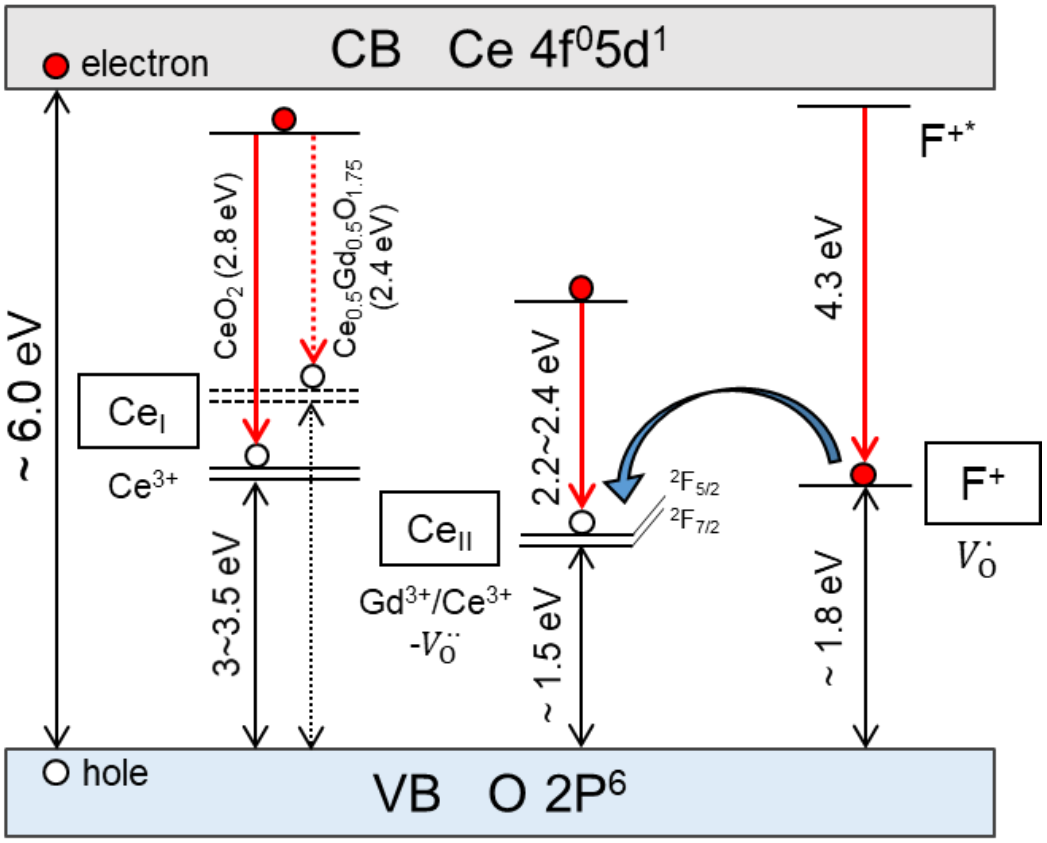

Figure 6-9. Sketch of electronic levels in the band gap of Gd_2O_3 doped ceria possessing oxygen vacancies.

Chapter 7

Concluding Remarks

7.1 General conclusions

CeO_2 or ceria is a considerable ceramic oxide as a surrogate and transmutation target for a nuclear reactor that has a radiation-resistant fluorite structure. Nuclear fuels, such as UO_2 are used to dope with Gd_2O_3, which is a burnable poison with a high thermal neutron absorption cross-section. Ceramic oxides have radiation damage by exposure to not only heavy ions but also electrons in the reactors. Therefore, understanding radiation response and damage production by ion/electron irradiation in the fuel materials is important for the safe use of the nuclear reactor. Information on the in-beam damage production is of importance since the defects are mobile during irradiation and the charge states of the defects are remarkable for the damage recovery kinetics. Moreover, the structural stability of the oxides as fuel materials is influenced by rare-earth doping and irradiation.

In this dissertation, the radiation-induced point defects and structural evaluation were investigated in ceria and Gd_2O_3 doped ceria. Point defects were produced by electronic excitation using the HVEM, and their charge state was interpreted by using *in-situ* CL spectroscopy. CL spectroscopy is a powerful technique to detect point scale defects, and the HVEM can produce oxygen point defects by accelerating voltages over the threshold displacement energy of oxygen atoms. In Chapter 4, the total displacement cross-section in ceria was calculated by using the SMOTT/POLY computer code [74] and CSDA range, and total inelastic stopping power ($(-dE/dx)_{inel}$) was computed with the ESTAR code [77] for different primary electron energies (E). CL spectra were obtained from pure ceria by electrons irradiation energy ranging from 400 keV to 1250 keV at the temperatures of 100 K, 200 K, and

300 K. Complementary CL spectra were measured as well as for 20 keV electrons at 300 K in the SEM. This chapter gave information on the charge state and electronic configurations of ceria under high-energy electron irradiation, and the CL emission from defects was evaluated depending on energy and temperatures.

In Chapter 5, ceria and Gd_2O_3 doped ceria ($Ce_{1-x}Gd_xO_{2-x/2}$) samples were studied to evaluate the microstructure evolution by Gd_2O_3 doping and heavy ion irradiation. The microstructure of virgin $Ce_{1-x}Gd_xO_{2-x/2}$ samples was investigated for a wide range of Gd concentrations ($0 \leq x_{Gd} \leq 0.5$) through comprehensive structural analysis of XRD, micro-Raman spectroscopy, and TEM. Thereafter, the samples were irradiated by 200 MeV Xe^{14+} ion at room temperature. The radiation damage and response, such as lattice parameter and phase changes in the samples were examined regarding the dopant concentration and irradiation conditions.

Finally, the *in-situ* HVEM-CL measurement technique was applied to yield information from point defects in $Ce_{1-x}Gd_xO_{2-x/2}$ under electron irradiation for a wide range of Gd dopant concentrations ($x_{Gd} = 0 \sim 0.5$). The CL spectra were obtained by 400 keV ~ 1250 keV electron irradiation in the HVEM, and 20 keV irradiation in the SEM. The CL spectra and charge states of point defects in $Ce_{1-x}Gd_xO_{2-x/2}$ were compared with pure ceria as interpreted in Chapter 4.

Based on the *in-situ* HVEM-CL analysis and microstructure evaluation experiment in virgin and swift heavy-ion (200 MeV Xe) irradiated Gd_2O_3 doped ceria, the contributions of this dissertation are summarized below the followings:

- The prominent CL emission centered at 4.2 eV was assigned to F^+ centers which were induced by elastic electron-nucleus collisions over a threshold electron energy (> 200 keV) equivalent to the oxygen displacement energy.
- CL bands centered at 2.3 ~ 2.6 eV and 2.8 ~ 3.0 eV were measured for all electron energies

(> 20 keV) which were induced by the charge compensation of oxygen vacancies for the high-energy (400 keV ~ 1250 keV) electrons and ionization effects for the low-energy (20 keV) electron excitation with a larger inelastic stopping power are attributed to the lower energy CL bands, respectively.

- At low temperatures (100 K and 200 K), similar CL spectra were obtained, but with larger and slightly shifted emission bands. Regardless of temperature, the effects of grain boundaries cause the F^+ center CL signal for the polycrystalline sample to be weaker than the single crystal under identical circumstances.

- The interaction between the oxygen displacement cross-section and the luminescence cross-section is used to explain the dependency of CL integrated intensities as a function of primary electron energy for both types of targets.

- The lattice parameter increased with the increase of Gd concentration and the simultaneous creation of charge-compensation oxygen vacancies. The lattice parameter was saturated at $x_{Gd} > 0.3$ due to the formation of the C-type structure in the F-type matrix.

- The reduction in the F-type symmetry with the formation of the C-type structure associated with ordered oxygen vacancies was observed at $x_{Gd} \geq 0.2$ consistently from the experimental techniques used in the present study.

- The XRD and TEM results showed that all the compositions of $Ce_{1-x}Gd_xO_{2-x/2}$ samples were resistant to amorphization and sustained the F-type structure with 200 MeV Xe ion irradiation. In the XRD patterns, asymmetrical peaks (Damage-$K\alpha_1$) were observed on the shoulders of F-type peaks ($K\alpha_1$), and the asymmetry was decreased with the increase of Gd concentration. The asymmetric peaks are caused by the lattice distortion in the F-type structure due to the formation of damaged regions induced by ion tracks.

- The C-type structure has disappeared with ion irradiation because of the loss of the ordered oxygen vacancy structure in the C-type domain.
- Analysis of the radiation-induced recovery by XRD patterns with ion irradiation showed track radii, or recovery radii decreases with the Gd concentration. Besides, the XRD analysis showed rapid recovery of radiation damage for values of x_{Gd} = 0.2 ~ 0.3, suggesting an important role of oxygen vacancy ordering in the C-type structure for the recovery process in Gd_2O_3 doped CeO_2.
- The CL bands appeared at 2.2 ~ 2.4 eV, 2.4 ~ 2.8 eV, and 4.3 eV, and they were assigned to Ce^{3+}-V_O, Ce^{3+}, and F^+ center, respectively, as well as pure ceria.
- The photon energy shift of the Ce^{3+} ion was induced by narrow $4f^1$ orbitals in the Gd^{3+} doped samples. Also, the high natural oxygen vacancy concentration in the doped samples derived thermal quenching of 4*f*-5*d* CL emission.
- The CL integrated intensities as function of primary electron energy were interpreted by the competitive interplay of displacement and CL emission cross-sections, but the energy dependence for Ce^{3+} ions CL emission is much more affected by CL quenching effect than that of F^+ center.

7.2 Directions for future research

Fluorite structure ceramics such as ceria and YSZ is remarkable materials for radiation-resistant materials, and study on their stability under irradiation is of importance for the long-term use of nuclear reactor. According to this dissertation, the *in-situ* HVEM-CL methods were developed to investigate the charge state of point defects. However, the reactor condition is not only exposure to electrons but also heavy ions at the same time. Recently, a synergetic effect of electron (S_e) and nuclear (S_n) stopping power is attracted for radiation recovery system in

the fluorite oxides. To understand the kinetics of the recovery system, the *in-situ* HVEM-CL technique was conducted with the ion irradiated oxides.

The CL emission obtained from the specimen is strongly dependent on parameters such as energy, temperature, beam flux, and quenching effects. Understanding the relationship between the CL intensity and these parameters, computational investigation and the other optical experimental system, such as photoluminescence should be followed together. In particular, the quenching effect on luminescence is much more complex due to a lot of ways to lose energy through transferring carriers, luminescence killer centers, or non-radiative decays. Thereby, more systematic experimental and theoretical calculations should be followed to understand CL emission from the defects.

Also, the RE-doped oxides showed structure evolution by RE doping and radiation. However, there are several methods to synthesize the RE-dopes oxides and characterization techniques of microstructure, which show different results despite of same composition samples. Therefore, more wide characterization techniques and dopant concentrations should be conducted for the structure evaluation experimental.

Moreover, radiation damage recoveries were confirmed at the high concentration of RE-doped oxides with the changes in phase and structure. The nano-domains and ordered oxygen vacancies induced by RE doping act as key properties for the recovery. These properties are on the nanoscale and their production and annihilation should be followed by high-resolution TEM methods such as STEM analysis to understand accurate radiation recovery phenomena. The strain/stress changes by RE-doping or irradiation in the domain boundaries are also noticeable properties to understand radiation response.

References

[1] S.F. Mughabghab, THERMAL NEUTRON CAPTURE CROSS SECTIONS RESONANCE INTEGRALS AND G-FACTORS I N D C INTERNATIONAL NUCLEAR DATA COMMITTEE, Vienna, 2003.

[2] S.J. Zinkle, Radiation-induced effects on microstructure, 1st ed., Elsevier Inc., 2012. https://doi.org/10.1016/B978-0-08-056033-5.00003-3.

[3] S.J. Zinkle, Microstructure of ion irradiated ceramic insulators, Nucl. Instrum. Methods B. 91 (1994) 234–246. https://doi.org/10.1016/0168-583X(94)96224-3.

[4] K. Yasuda, C. Kinoshita, R. Morisaki, H. Abe, Role of irradiation spectrum in the microstructural evolution of magnesium aluminate spinel, Philos. Mag. A Phys. Condens. Matter, Struct. Defects Mech. Prop. 78 (1998) 583–598. https://doi.org/10.1080/01418619808241924.

[5] K. Yasuda, C. Kinoshita, M. Ohmura, H. Abe, Production and stability of dislocation loops in an MgO-Al2O3 system under concurrent irradiation with ions and electrons, Nucl. Instrum. Methods Phys. Res. Sect. B. 166 (2000) 107–114. https://doi.org/10.1016/S0168-583X(99)00738-7.

[6] T. Sonoda, M. Kinoshita, Y. Chimi, N. Ishikawa, M. Sataka, A. Iwase, Electronic excitation effects in CeO2 under irradiations with high-energy ions of typical fission products, Nucl. Instrum. Methods Phys. Res. Sect. B. 250 (2006) 254–258. https://doi.org/10.1016/J.NIMB.2006.04.120.

[7] J.M. Costantini, F. Beuneu, Threshold displacement energy in yttria-stabilized zirconia, Phys. Status Solidi Curr. Top. Solid State Phys. 4 (2007) 1258–1263. https://doi.org/10.1002/pssc.200673752.

[8] K. Yasunaga, K. Yasuda, S. Matsumura, T. Sonoda, Nucleation and growth of defect clusters in CeO2 irradiated with electrons, Nucl. Instrum. Methods Phys. Res. Sect. B. 250 (2006) 114–118. https://doi.org/10.1016/J.NIMB.2006.04.091.

[9] K. Yasunaga, K. Yasuda, S. Matsumura, T. Sonoda, Electron energy-dependent formation of dislocation loops in CeO2, Nucl. Instrum. Methods Phys. Res. Sect. B. 266 (2008) 2877–2881. https://doi.org/10.1016/j.nimb.2008.03.204.

[10] K. Yasuda, J.-M. Costantini, G. Baldinozzi, Radiation-Induced Effects on Materials Properties of Ceramics: Mechanical and Dimensional Properties, in: Compr. Nucl.

Mater. Second Ed., 2nd ed., 2020: pp. 153–185. https://doi.org/10.1016/B978-0-12-803581-8.12052-1.

[11] S.J. Zinkle, C. Kinoshita, Defect production in ceramics, J. Nucl. Mater. 251 (1997) 200–217. https://doi.org/10.1016/S0022-3115(97)00224-9.

[12] D. Simeone, J.M. Costantini, L. Luneville, L. Desgranges, P. Trocellier, P. Garcia, Characterization of radiation damage in ceramics: Old challenge new issues?, J. Mater. Res. 30 (2015) 1495–1515. https://doi.org/10.1557/jmr.2015.77.

[13] E.A. Kotomin, A.I. Popov, Radiation-induced point defects in simple oxides, Nucl. Instrum. Methods Phys. Res. Sect. B. 141 (1998) 1–15. https://doi.org/10.1016/S0168-583X(98)00079-2.

[14] W. Hayes, A.M. Stoneham, Defects and Defect Processes in Nonmetallic Solids, Courier Corporation, 2012.

[15] F. Agulló-López, C.R.A. Catlow, P.D. Townsend, Point defects in materials, Academic press, 1988.

[16] J.M. Costantini, F. Beuneu, M. Fasoli, A. Galli, A. Vedda, M. Martini, Thermo-stimulated luminescence of ion-irradiated yttria-stabilized zirconia, J. Phys. Condens. Matter. 23 (2011). https://doi.org/10.1088/0953-8984/23/11/115901.

[17] V. Pagonis, M.L. Chithambo, R. Chen, A. Chruścińska, M. Fasoli, S.H. Li, M. Martini, K. Ramseyer, Thermal dependence of luminescence lifetimes and radioluminescence in quartz, J. Lumin. 145 (2014) 38–48. https://doi.org/10.1016/j.jlumin.2013.07.022.

[18] T. Yanagida, K. Kamada, Y. Fujimoto, H. Yagi, T. Yanagitani, Comparative study of ceramic and single crystal Ce:GAGG scintillator, Opt. Mater. (Amst). 35 (2013) 2480–2485. https://doi.org/10.1016/J.OPTMAT.2013.07.002.

[19] E. Goldstein, Arbeiten der wissenschaftlichen Gäste der Abtheilung I. Professor Goldstein's Untersuchungen über Kathodenstrahlen, Zeits. f. Instrumentenk. 16 (1896).

[20] L.A. Kappers, R.L. Kroes, E.B. Hensley, F+ and F′ centers in magnesium oxide, Phys. Rev. B. 1 (1970) 4151–4157. https://doi.org/10.1103/PhysRevB.1.4151.

[21] K. H. Lee, J. J. H. Crawford, Electron centers in single-crystal Al2O3, Phys. Rev. B. 15 (1977) 4065–4070. http://prb.aps.org/abstract/PRB/v15/i8/p4065_1.

[22] D.M. Hofmann, D. Pfisterer, J. Sann, B.K. Meyer, R. Tena-Zaera, V. Munoz-Sanjose, T. Frank, G. Pensl, Properties of the oxygen vacancy in ZnO, Appl. Phys. A Mater. Sci. Process. 88 (2007) 147–151. https://doi.org/10.1007/s00339-007-3956-2.

[23] N. Serpone, Is the band gap of pristine TiO2 narrowed by anion- and cation-doping of titanium dioxide in second-generation photocatalysts?, J. Phys. Chem. B. 110 (2006) 24287–24293. https://doi.org/10.1021/jp065659r.

[24] K. Furumoto, T. Tanabe, N. Yamamoto, T. Daio, S. Matsumura, K. Yasuda, Development of Novel Optical Fiber System for Cathodoluminescence Detection in High Voltage Transmission Electron Microscope, Mater. Trans. 54 (2013) 854–856.

[25] J.M. Costantini, Y. Watanabe, K. Yasuda, M. Fasoli, Cathodo-luminescence of color centers induced in sapphire and yttria-stabilized zirconia by high-energy electrons, J. Appl. Phys. 121 (2017) 153101. https://doi.org/10.1063/1.4980111.

[26] K. Yasuda, C. Kinoshita, S. Matsumura, Effects of Simultaneous Displacive and Ionizing Radiation in Ionic and Covalent Crystals, Defect Diffus. Forum. 206–207 (2002) 53–74. https://doi.org/10.4028/www.scientific.net/DDF.206-207.53.

[27] W.J. Weber, E. Zarkadoula, O.H. Pakarinen, R. Sachan, M.F. Chisholm, P. Liu, H. Xue, K. Jin, Y. Zhang, Synergy of elastic and inelastic energy loss on ion track formation in SrTiO3, Sci. Rep. 5 (2015) 1–6. https://doi.org/10.1038/srep07726.

[28] P.G. Klemens, Phonon scattering by oxygen vacancies in ceramics, Phys. B Condens. Matter. 263–264 (1999) 102–104. https://doi.org/10.1016/S0921-4526(98)01202-2.

[29] R.J. Tilley, Crystal Structure, 2006.

[30] C.R. Barrett, W.D. Nix, W.D. Nix, A.S. Tetelman, The principles of engineering materials, Prentice hall, 1973.

[31] R.W. Grimshaw, A.B. Searle, The chemistry and physics of clays and allied ceramic materials, 1971.

[32] C.B. Carter, M.G. Norton, Ceramic materials: science and engineering, Springer, 2007.

[33] N. Nitani, K. Kuramoto, T. Yamashita, Y. Nihei, Y. Kimura, In-pile irradiation of rock-like oxide fuels, J. Nucl. Mater. 319 (2003) 102–107. https://doi.org/10.1016/S0022-3115(03)00140-5.

[34] Z. Crnjak, B. Orel, Optical Properties of Pure CeO2 and Mixed CeO2/SnO2 Thin Film Coatings, Phys. Stat. Sol. 186 (1994) 33–36. https://doi.org/10.1002/pssb.2221860135.

[35] F. Marabelli, P. Wachter, Covalent insulator CeO2: Optical reflectivity measurements, Phys. Rev. B. 36 (1987) 1238–1243. https://doi.org/10.1103/PhysRevB.36.1238.

[36] P.J. Hay, R.L. Martin, J. Uddin, G.E. Scuseria, Theoretical study of CeO2 and Ce 2O3 using a screened hybrid density functional, J. Chem. Phys. 125 (2006). https://doi.org/10.1063/1.2206184.

[37] L. Eyring, The Binary Lanthanide Oxides: Synthesis and Identification, in: G. Meyer, L.R. Morss (Eds.), Synth. Lanthan. Actin. Compd. Top. f-Element Chem. Vol 2., Springer, Dordrecht, 1991: pp. 187–224. https://doi.org/10.1007/978-94-011-3758-4_8.

[38] P.N. Hazin, J.W. Bruno, H.G. Brittain, Luminescence Spectra of a Series of Cerium(III) Halides and Organometallics: Probes of Bonding Properties Using 4f-5d Excited States, Organometallics. 6 (1987) 913–918. https://doi.org/10.1021/om00148a002.

[39] R.D. Shannon, Application of the Periodic Bond Chain (PBC) Theory and Attachment Energy Consideration to Derive the Crystal Morphology of Hexamethylmelamine, Acta Crystallogr. Sect. A. 32 (1976) 751–767. https://doi.org/10.1023/A:1018927109487.

[40] M. Nakayama, M. Martin, First-principles study on defect chemistry and migration of oxide ions in ceria doped with rare-earth cations, Phys. Chem. Chem. Phys. 11 (2009) 3241–3249. https://doi.org/10.1039/B900162J.

[41] M. Mogensen, D. Lybye, N. Bonanos, P. V. Hendriksen, F.W. Poulsen, Factors controlling the oxide ion conductivity of fluorite and perovskite structured oxides, Solid State Ionics. 174 (2004) 279–286. https://doi.org/10.1016/j.ssi.2004.07.036.

[42] M. Coduri, S. Checchia, M. Longhi, D. Ceresoli, M. Scavini, Rare earth doped ceria: The complex connection between structure and properties, Front. Chem. 6 (2018) 1–23. https://doi.org/10.3389/fchem.2018.00526.

[43] R. Schmitt, A. Nenning, O. Kraynis, R. Korobko, A.I. Frenkel, I. Lubomirsky, S.M. Haile, J.L.M. Rupp, A review of defect structure and chemistry in ceria and its solid solutions, Chem. Soc. Rev. 49 (2020) 554–592. https://doi.org/10.1039/c9cs00588a.

[44] G.Y. Adachi, N. Imanaka, The binary rare earth oxides, Chem. Rev. 98 (1998) 1479–1514. https://doi.org/10.1021/cr940055h.

[45] P.A. Žguns, A. V. Ruban, N. V. Skorodumova, Phase diagram and oxygen–vacancy ordering in the CeO2 –Gd2O3 system: a theoretical study, Phys. Chem. Chem. Phys. 20 (2018) 11805–11818. https://doi.org/10.1039/C8CP01029C.

[46] G. Brauer, H. Gradinger, Über heterotype Mischphasen bei Seltenerdoxyden. I, Zeitschrift Für Anorg. Und Allg. Chemie. 276 (1954) 209–226. https://doi.org/10.1002/ZAAC.19542760502.

[47] T. Nakagawa, T. Osuki, T.A. Yamamoto, Y. Kitauji, M. Kano, M. Katsura, S. Emura, Study on local structure around Ce and Gd atoms in CeO2-Gd2O3 binary system, J. Synchrotron Radiat. 8 (2001) 740–742. https://doi.org/10.1107/S0909049500018148.

[48] Y. Ikuma, K. Takao, M. Kamiya, E. Shimada, X-ray study of cerium oxide doped with gadolinium oxide fired at low temperatures, in: Mater. Sci. Eng. B Solid-State Mater. Adv. Technol., Elsevier, 2003: pp. 48–51. https://doi.org/10.1016/S0921-5107(02)00546-9.

[49] D.J.M. Bevan, J. Kordis, Mixed oxides of the type MO2 (fluorite)-M2O3-I oxygen dissociation pressures and phase relationships in the system CeO2-Ce2O3 at high temperatures, J. Inorg. Nucl. Chem. 26 (1964) 1509–1523. https://doi.org/10.1016/0022-1902(64)80038-5.

[50] D.R. Ou, T. Mori, F. Ye, T. Kobayashi, J. Zou, G. Auchterlonie, J. Drennan, Oxygen vacancy ordering in heavily rare-earth-doped ceria, Appl. Phys. Lett. 89 (2006) 87–90. https://doi.org/10.1063/1.2369881.

[51] F. Ye, T. Mori, D.R. Ou, J. Zou, J. Drennan, A structure model of nano-sized domain in Gd-doped ceria, Solid State Ionics. 180 (2009) 1414–1420. https://doi.org/10.1016/j.ssi.2009.08.013.

[52] D.Y. Wang, D.S. Park, J. Griffith, A.S. Nowick, Oxygen-ion conductivity and defect interactions in yttria-doped ceria, Solid State Ionics. 2 (1981) 95–105. https://doi.org/10.1016/0167-2738(81)90005-9.

[53] H. Inaba, H. Tagawa, Ceria-based solid electrolytes, Solid State Ionics. 83 (1996) 1–16. https://doi.org/10.1016/0167-2738(95)00229-4.

[54] J.A. Purton, N.L. Allan, D.S.D. Gunn, Simulations of doped CeO2 at finite dopant concentrations, Solid State Ionics. 299 (2017) 32–37. https://doi.org/10.1016/J.SSI.2016.09.017.

[55] H.M. Rietveld, IUCr, A profile refinement method for nuclear and magnetic structures, Urn:Issn:0021-8898. 2 (1969) 65–71. https://doi.org/10.1107/S0021889869006558.

[56] J. Rodríguez-Carvajal, Recent advances in magnetic structure determination by neutron powder diffraction, Phys. B Phys. Condens. Matter. 192 (1993) 55–69. https://doi.org/10.1016/0921-4526(93)90108-I.

[57] A.C. Larson, R.B. Von Dreele, GSAS, 1994.

[58] F. Izumi, T. Ikeda, A Rietveld-Analysis Programm RIETAN-98 and its Applications to Zeolites, Mater. Sci. Forum. 321–324 (2000) 198–205. https://doi.org/10.4028/WWW.SCIENTIFIC.NET/MSF.321-324.198.

[59] ICSD, (n.d.). https://icsd.products.fiz-karlsruhe.de/ (accessed December 5, 2022).
[60] American Mineralogist Crystal Structure Database, (n.d.). http://rruff.geo.arizona.edu/AMS/amcsd.php (accessed December 5, 2022).
[61] Crystallography Open Database, (n.d.). http://www.crystallography.net/cod/ (accessed December 5, 2022).
[62] R.A. Young, The Rietveld Method IUCr: Oxford, Cambridge University Press, 1993.
[63] H.Y. Xiao, Y. Zhang, W.J. Weber, Ab initio molecular dynamics simulations of low-energy recoil events in ThO2, CeO2, and ZrO2, Phys. Rev. B - Condens. Matter Mater. Phys. 86 (2012) 054109. https://doi.org/10.1103/PhysRevB.86.054109.
[64] B.T. Kelly, Physics of Graphite, Applied Science, London, 1981.
[65] J. Wiiliam A. McKinley, H. Feshbach, The Coulomb Scattering of Relativistic Electrons by Nuclei, Phys. Rev. 74 (1948) 1759–1763.
[66] F. Esch, S. Fabris, L. Zhou, T. Montini, C. Africh, P. Fornasiero, G. Comelli, R. Rosei, Electron Localization Determines Defect Formation on Ceria Substrates, Science (80-.). 309 (2005) 752–755. https://doi.org/10.1126/science.1111568.
[67] N. V Skorodumova, S.I. Simak, B.I. Lundqvist, I.A. Abrikosov, B. Johansson, Quantum Origin of the Oxygen Storage Capability of Ceria, (2002) 14–17. https://doi.org/10.1103/PhysRevLett.89.166601.
[68] P. Jonnard, C. Bonnelle, G. Blaise, G. Rémond, C. Roques-Carmes, F+ and F centers in α-Al2O3 by electron-induced x-ray emission spectroscopy and cathodoluminescence, J. Appl. Phys. 88 (2000) 6413–6417. https://doi.org/10.1063/1.1324697.
[69] S. Aškrabić, Z.D. Dohčević-Mitrović, V.D. Araújo, G. Ionita, M.M. De Lima, A. Cantarero, F-centre luminescence in nanocrystalline CeO2, J. Phys. D. Appl. Phys. 46 (2013). https://doi.org/10.1088/0022-3727/46/49/495306.
[70] J.-M. Costantini, T. Ogawa, A.S.I. Bhuian, K. Yasuda, Cathodoluminescence induced in oxides by high-energy electrons: Effects of beam flux, electron energy, and temperature, J. Lumin. 208 (2019) 108–118. https://doi.org/10.1016/j.jlumin.2018.12.045.
[71] J.F. Ziegler, J.P. Biersack, The Stopping and Range of Ions in Matter, Treatise Heavy-Ion Sci. (1985) 93–129. https://doi.org/10.1007/978-1-4615-8103-1_3.
[72] A.Y. Konobeyev, U. Fischer, Y.A. Korovin, S.P. Simakov, Evaluation of effective threshold displacement energies and other data required for the calculation of

advanced atomic displacement cross-sections, Nucl. Energy Technol. 3 (2017) 169–175. https://doi.org/10.1016/j.nucet.2017.08.007.

[73] B.L. Henke, E.M. Gullikson, J.C. Davis, X-Ray Interactions: Photoabsorption, Scattering, Transmission, and Reflection at E = 50-30,000 eV, Z = 1-92, At. Data Nucl. Data Tables. 54 (1993) 181–342. https://doi.org/10.1006/ADND.1993.1013.

[74] P.D. Lesueur, Cascades de déplacement dam les solides polyatomiques, Philos. Mag. A Phys. Condens. Matter, Struct. Defects Mech. Prop. 44 (1981) 905–929. https://doi.org/10.1080/01418618108239557.

[75] M. Yamaga, P.I. Macfarlane, B. Henderson, K. Holliday, H. Takeuchi, T. Yosida, M. Fukui, Substitutional disorder and the ground state spectroscopy of gallogermanate crystals, J. Phys. Condens. Matter. 9 (1997) 569–578. https://doi.org/10.1088/0953-8984/9/2/024.

[76] M. Ghamnia, C. Jardin, M. Bouslama, Luminescent centres F and F+ in α-alumina detected by cathodoluminescence technique, J. Electron Spectros. Relat. Phenomena. 133 (2003) 55–63. https://doi.org/10.1016/j.elspec.2003.08.003.

[77] ICRU Report 37, Stopping Powers for Electrons and Positrons, 1984. http://physics.nist.gov/ PhysRefData/Star/Text/ESTAR.html.

[78] B.. G. Yacobi, D.. B. Holt, Cathodoluminescence scanning electron microscopy of semiconductors, J. Appl. Phys. 59 (1986). https://doi.org/10.1063/1.336491.

[79] V.I. Petrov, Cathodoluminescence microscopy, Physics-Uspekhi. 39 (1996) 807–818. https://doi.org/10.1070/PU1996v039n08ABEH000162.

[80] E. Wuilloud, B. Delley, W.-D. Schneider, Y. Baer, Spectroscopic Evidence for Localized and Extended f-Symmetry States in CeO2, Phys. Rev. Lett. 53 (1984) 202–205. https://doi.org/10.1103/PhysRevLett.53.202.

[81] E. Wuilloud, B. Delley, W.-D. Schneider, Y. Baer, SPECTROSCOPIC STUDY OF LOCALIZED AND EXTENDED f-SYMMETRY STATES IN CeO2, CeN AND CeSi2, J. Magn. Magn. Mater. 47–48 (1985) 197–199.

[82] P.O. Maksimchuk, V. V. Seminko, I.I. Bespalova, A.A. Masalov, Influence of CeO2 nanocrystals size on the vacancies formation processes determinded by spectroscopic techniques, Funct. Mater. 21 (2014) 254–259.

[83] V. Pankratov, L. Grigorjeva, D. Millers, T. Chudoba, R. Fedyk, W. Łojkowski, Time-Resolved Luminescence Characteristics of Cerium Doped YAG Nanocrystals, Solid State Phenom. 128 (2007) 173–178. https://doi.org/10.4028/www.scientific.net/ssp.128.173.

[84] B.A. Danja, A Review of Lanthanides As Activators In Luminecence, IOSR J. Appl. Chem. 9 (2016) 104–110. https://doi.org/10.9790/5736-090701104110.

[85] A.H. Morshed, M.E. Moussa, S.M. Bedair, R. Leonard, S.X. Liu, N. El-Masry, Violet / blue emission from epitaxial cerium oxide films on silicon substrates, Appl. Phys. Lett. 70 (1997) 1647–1649.

[86] H. Suzuki, T.A. Tombrello, C.L. Melcher, J.S. Schweitzer, Light Emission Mechanism of Lu2(SiO4)O:Ce, IEEE Trans. Nucl. Sci. 40 (1993) 380–383. https://doi.org/10.1109/23.256584.

[87] Y. Jia, A. Miglio, M. Mikami, X. Gonze, Ab initio study of luminescence in Ce-doped Lu 2 SiO 5 : The role of oxygen vacancies on emission color and thermal quenching behavior, Phys. Rev. Mater. 2 (2018) 1–11. https://doi.org/10.1103/PhysRevMaterials.2.125202.

[88] X. Han, J. Lee, H. Yoo, Oxygen-vacancy-induced ferromagnetism in CeO2 from first principles, Phys. Rev. B. 79 (2009) 100403(R). https://doi.org/10.1103/PhysRevB.79.100403.

[89] G. Blasse, A. Bril, Investigation of Some Ce 3+-Activated Phosphors ARTICLES YOU MAY BE INTERESTED IN A NEW PHOSPHOR FOR FLYING-SPOT CATHODE-RAY TUBES FOR COLOR TELEVISION, J. Chem. Phys. 47 (1967) 5139. https://doi.org/10.1063/1.1701771.

[90] T. Hoshina, 5d→4f Radiative Transition Probabilities of Ce3+ and Eu2+ in Crystals, J. Phys. Soc. Japan. 48 (1980) 1261–1268. https://doi.org/10.1143/JPSJ.48.1261.

[91] P. Dorenbos, 5d-level energies of Ce3+ and the crystalline environment. I. Fluoride compounds, Phys. Rev. B - Condens. Matter Mater. Phys. 62 (2000) 15640–15649. https://doi.org/10.1103/PhysRevB.62.15640.

[92] L. Guerbous, O. Krachni, The 4f-5d luminescence transitions in cerium-doped LuF3, J. Mod. Opt. 53 (2006) 2043–2053. https://doi.org/10.1080/09500340600792424.

[93] A.H. Krumpel, E. Van Der Kolk, D. Zeelenberg, A.J.J. Bos, K.W. Krämer, P. Dorenbos, Lanthanide 4f-level location in lanthanide doped and cerium-lanthanide codoped NaLaF4 by photo-and thermoluminescence, J. Appl. Phys. 104 (2008) 073505. https://doi.org/10.1063/1.2955776.

[94] N. V. Skorodumova, R. Ahuja, S.I. Simak, I.A. Abrikosov, B. Johansson, B.I. Lundqvist, Electronic, bonding, and optical properties of CeO2 and Ce2O3 from first principles , Phys. Rev. B. 64 (2001) 1–9. https://doi.org/10.1103/physrevb.64.115108.

[95] G. Pezzotti, K. Wan, M.C. Munisso, W. Zhu, Stress dependence of F+-center cathodoluminescence of sapphire, Appl. Phys. Lett. 89 (2006) 14–17. https://doi.org/10.1063/1.2234307.

[96] J. Costantini, S. Miro, N. Touati, L. Binet, G. Wallez, G. Lelong, W.J. Weber, Defects induced in cerium dioxide single crystals by electron irradiation Defects induced in cerium dioxide single crystals by electron irradiation, 025901 (2018). https://doi.org/10.1063/1.5007823.

[97] B.G. Draeger, G.P. Summers, Defects in unirradiated Al2O3, Phys. Rev. B. 19 (1979) 1172–1177. https://doi.org/10.1103/PhysRevB.19.1172.

[98] J.M. Costantini, G. Lelong, M. Guillaumet, W.J. Weber, S. Takaki, K. Yasuda, Color-center production and recovery in electron-irradiated magnesium aluminate spinel and ceria, J. Phys. Condens. Matter. 28 (2016) 325901. https://doi.org/10.1088/0953-8984/28/32/325901.

[99] A. Guglielmetti, A. Chartier, L. van Brutzel, J.P. Crocombette, K. Yasuda, C. Meis, S. Matsumura, Atomistic simulation of point defects behavior in ceria, Nucl. Instruments Methods Phys. Res. Sect. B. 266 (2008) 5120–5125. https://doi.org/10.1016/j.nimb.2008.09.010.

[100] D. CURIE, Luminescence in crystals, Students Q. J. 34 (1963) 1262–1262. https://doi.org/10.1049/sqj.1963.0049.

[101] W. Hergert, P. Reck, L. Pasemann, J. Schreiber, Cathodoluminescence measurements using the scanning electron microscope for the determination of semiconductor parameters, Phys. Status Solidi. 101 (1987) 611–618. https://doi.org/10.1002/pssa.2211010237.

[102] A. Djemel, R.J. Tarento, J. Castaing, Y. Marfaing, A. Nouiri, Study of electronic surface properties of GaAs in cathodoluminescence experiments, Phys. Status Solidi Appl. Res. 168 (1998) 425–432. https://doi.org/10.1002/(SICI)1521-396X(199808)168:2<425::AID-PSSA425>3.0.CO;2-N.

[103] I. Plante, F.A. Cucinotta, Ionization and excitation cross sections for the interaction of HZE particles in liquid water and application to Monte Carlo simulation of radiation tracks, New J. Phys. 10 (2008). https://doi.org/10.1088/1367-2630/10/12/125020.

[104] T. Liamsuwan, H. Nikjoo, A Monte Carlo track structure simulation code for the full-slowing-down carbon projectiles of energies 1 keV u-1-10 MeV u-1 in water, Phys. Med. Biol. 58 (2013) 673–701. https://doi.org/10.1088/0031-9155/58/3/673.

[105] S.T. Perkins, D.E. Cullen, S.M. Seltzer, Tables and graphs of electron-interaction cross-sections from 10 eV to 100 GeV derived from the LLNL evaluated electron data library (EEDL), Z= 1-100, UCRL-50400. 31 (1991) 21–24.

[106] I. Blanco, P. Molle, L.E. Sáenz de Miera, G. Ansola, Basic Oxygen Furnace steel slag aggregates for phosphorus treatment: Evaluation of its potential use as a substrate in constructed wetlands, Water Res. 89 (2016) 355–365. https://doi.org/10.1016/j.watres.2015.11.064.

[107] K.E. Sickafus, L. Minervini, R.W. Grimes, J.A. Valdez, M. Ishimaru, F. Li, K.J. McClellan, T. Hartmann, Radiation Tolerance of Complex Oxides, Science (80-.). 289 (2000) 748–751. https://doi.org/10.1126/science.289.5480.748.

[108] B.H. Toby, R factors in Rietveld analysis: How good is good enough? , Powder Diffr. 21 (2006) 67–70. https://doi.org/10.1154/1.2179804.

[109] B.D. Cullity, Elements of X-ray Diffraction, Addison-Wesley Publishing, 1956.

[110] J.B. Nelson, D.P. Riley, An experimental investigation of extrapolation methods in the derivation of accurate unit-cell dimensions of crystals, Proc. Phys. Soc. 57 (1945) 160–177. https://doi.org/10.1088/0959-5309/57/3/302.

[111] S.J. Hong, A. V. Virkar, Lattice Parameters and Densities of Rare-Earth Oxide Doped Ceria Electrolytes, J. Am. Ceram. Soc. 78 (1995) 433–439. https://doi.org/10.1111/j.1151-2916.1995.tb08820.x.

[112] G.K. Williamson, W.H. Hall, X-ray line broadening from filed aluminium and wolfram, Acta Metall. 1 (1953) 22–31. https://doi.org/10.1016/0001-6160(53)90006-6.

[113] N.C. Halder, C.N.J. Wagner, Separation of particle size and lattice strain in integral breadth measurements, Acta Crystallogr. 20 (1966) 312–313. https://doi.org/10.1107/s0365110x66000628.

[114] W.H. Weber, K.C. Bass, J.R. Mcbride, W. Graham, C.R. Peters, R. Usmen, J. Catalysis, Raman study of CeOz. Second-order scattering, lattice dynamics, and particle-size effects, Phys. Rev. B. 48 (1992) 178–185.

[115] J.R. McBride, K.C. Hass, B.D. Poindexter, W.H. Weber, Raman and x-ray studies of Ce1−xRExO2−y, where RE=La, Pr, Nd, Eu, Gd, and Tb, J. Appl. Phys. 76 (1994) 2435–2441.

[116] J.M. Costantini, S. Miro, G. Gutierrez, K. Yasuda, S. Takaki, N. Ishikawa, M. Toulemonde, Raman spectroscopy study of damage induced in cerium dioxide by swift heavy ion irradiations, J. Appl. Phys. 122 (2017) 205901. https://doi.org/10.1063/1.5011165.

[117] J.-M. Costantini, G. Gutierrez, G. Lelong, M. Guillaumet, P. Seo, K. Yasuda, Radiation damage in ion-irradiated CeO2 and (Ce, Gd)O2 sinters: Effect of the Gd content, J. Nucl. Mater. 564 (2022) 153667. https://doi.org/10.1016/j.jnucmat.2022.153667.

[118] C. Schilling, A. Hofmann, C. Hess, M.V. Ganduglia-Pirovano, Raman Spectra of Polycrystalline CeO2: A Density Functional Theory Study, J. Phys. Chem. C. 121 (2017) 20834–20849. https://doi.org/10.1021/acs.jpcc.7b06643.

[119] J.M. Costantini, G. Gutierrez, G. Lelong, M. Guillaumet, M.M. Rahman, K. Yasuda, Raman spectroscopy study of damage in swift heavy ion-irradiated ceramics, J. Raman Spectrosc. 53 (2022) 1–11. https://doi.org/10.1002/JRS.6414.

[120] M.H. Brodsky, M. Cardona, Local order as determined by electronic and vibrational spectroscopy: Amorphous semiconductors, J. Non. Cryst. Solids. 31 (1978) 81–108. https://doi.org/10.1016/0022-3093(78)90100-X.

[121] J. Buckeridge, D.O. Scanlon, A. Walsh, C.R.A. Catlow, A.A. Sokol, Dynamical response and instability in ceria under lattice expansion, Phys. Rev. B. 87 (2013) 214304. https://doi.org/10.1103/PhysRevB.87.214304.

[122] M. Coduri, M. Scavini, M. Pani, M.M. Carnasciali, H. Klein, C. Artini, From nano to microcrystals: effects of different synthetic pathways on the defect architecture in heavily Gd-doped ceria, Phys. Chem. Chem. Phys. 19 (2017) 11612–11630. https://doi.org/10.1039/C6CP08173H.

[123] A. Nakajima, A. Yoshihara, M. Ishigame, Defect-induced Raman spectra in doped CeO2, Phys. Rev. B. 50 (1994) 13297–13307. https://doi.org/10.1103/PhysRevB.50.13297.

[124] A. Banerji, V. Grover, V. Sathe, S.K. Deb, A.K. Tyagi, CeO2 - Gd2O3 system: Unraveling of microscopic features by Raman spectroscopy, Solid State Commun. 149 (2009) 1689–1692. https://doi.org/10.1016/j.ssc.2009.06.045.

[125] D.R. Ou, T. Mori, F. Ye, J. Zou, G. Auchterlonie, J. Drennan, Oxygen-vacancy ordering in lanthanide-doped ceria: Dopant-type dependence and structure model, Phys. Rev. B - Condens. Matter Mater. Phys. 77 (2008) 1–8. https://doi.org/10.1103/PhysRevB.77.024108.

[126] K. Yasuda, M. Etoh, K. Sawada, T. Yamamoto, K. Yasunaga, S. Matsumura, N. Ishikawa, Defect formation and accumulation in CeO2 irradiated with swift heavy ions, Nucl. Instrum. Methods Phys. Res. Sect. B. 314 (2013) 185–190. https://doi.org/10.1016/j.nimb.2013.04.069.

[127] S. Takaki, K. Yasuda, T. Yamamoto, S. Matsumura, N. Ishikawa, Structure of ion tracks in ceria irradiated with high energy xenon ions, Prog. Nucl. Energy. 92 (2016) 306–312. https://doi.org/10.1016/j.pnucene.2016.07.013.

[128] M. Tang, P. Lu, J.A. Valdez, K.E. Sickafus, Ion-irradiation-induced phase transformation in rare earth sesquioxides (Dy2O3,Er2O3,Lu2O3), J. Appl. Phys. 99 (2006) 063514. https://doi.org/10.1063/1.2184433.

[129] S.P. Ray, A.S. Nowick, D.E. Cox, X-ray and neutron diffraction study of intermediate phases in nonstoichiometric cerium dioxide, J. Solid State Chem. 15 (1975) 344–351. https://doi.org/10.1016/0022-4596(75)90290-X.

[130] H. Ohno, A. Iwase, D. Matsumura, Y. Nishihata, J. Mizuki, N. Ishikawa, Y. Baba, N. Hirao, T. Sonoda, M. Kinoshita, Study on effects of swift heavy ion irradiation in cerium dioxide using synchrotron radiation X-ray absorption spectroscopy, Nucl. Instrum. Methods Phys. Res. Sect. B. 266 (2008) 3013–3017. https://doi.org/10.1016/j.nimb.2008.03.155.

[131] C.L. Tracy, M. Lang, J.M. Pray, F. Zhang, D. Popov, C. Park, C. Trautmann, M. Bender, D. Severin, V.A. Skuratov, R.C. Ewing, Redox response of actinide materials to highly ionizing radiation, Nat. Commun. 6 (2015) 1–9. https://doi.org/10.1038/ncomms7133.

[132] T. Sonoda, M. Kinoshita, Y. Chimi, N. Ishikawa, M. Sataka, A. Iwase, high-energy ions of typical fission products, Nucl. Instrum. Methods Phys. Res. Sect. B. 250 (2006) 254–258. https://doi.org/10.1016/j.nimb.2006.04.120.

[133] N. Ishikawa, K. Takegahara, Radiation damages in CeO 2 thin films irradiated with ions having the same nuclear stopping and different electronic stopping powers, Nucl. Instrum. Methods Phys. Res. Sect. B. 272 (2012) 227–230. https://doi.org/10.1016/j.nimb.2011.01.071.

[134] S. Takaki, K. Yasuda, T. Yamamoto, S. Matsumura, N. Ishikawa, Atomic structure of ion tracks in Ceria, Nucl. Instrum. Methods Phys. Res. Sect. B. 326 (2014) 140–144. https://doi.org/10.1016/j.nimb.2013.10.077.

[135] D. Simeone, C. Dodane-Thiriet, D. Gosset, P. Daniel, M. Beauvy, Order–disorder phase transition induced by swift ions in MgAl2O4 and ZnAl2O4 spinels, J. Nucl. Mater. 300 (2002) 151–160. https://doi.org/10.1016/S0022-3115(01)00749-8.

[136] B.P. Mandal, V. Grover, M. Roy, A.K. Tyagi, X-ray diffraction and raman spectroscopic investigation on the phase relations in Yb2O3- and Tm2O 3-substituted

CeO2, J. Am. Ceram. Soc. 90 (2007) 2961–2965. https://doi.org/10.1111/j.1551-2916.2007.01826.x.

[137] D.J.M. Bevan, E. Summerville, Mixed rare earth oxides, in: Handb. Phys. Chem. Rare Earths, Elsevier, 1979: pp. 401–524. https://doi.org/10.1016/S0168-1273(79)03011-7.

[138] E.R. Andrievskaya, O.A. Kornienko, A. V. Sameljuk, A. Sayir, Phase relation studies in the CeO2–La2O3 system at 1100–1500 °C, J. Eur. Ceram. Soc. 31 (2011) 1277–1283. https://doi.org/10.1016/J.JEURCERAMSOC.2010.05.024.

[139] A. Kossoy, Q. Wang, R. Korobko, V. Grover, Y. Feldman, E. Wachtel, A.K. Tyagi, A.I. Frenkel, I. Lubomirsky, Evolution of the local structure at the phase transition in CeO 2-Gd2O3 solid solutions, Phys. Rev. B - Condens. Matter Mater. Phys. 87 (2013) 054101. https://doi.org/10.1103/PHYSREVB.87.054101/FIGURES/5/MEDIUM.

[140] M. Scavini, M. Coduri, M. Allieta, P. Masala, S. Cappelli, C. Oliva, M. Brunelli, F. Orsini, C. Ferrero, Percolating hierarchical defect structures drive phase transformation in Ce1-xGdxO2-x/2: A total scattering study, IUCrJ. 2 (2015) 511–522. https://doi.org/10.1107/S2052252515011641.

[141] C. Artini, G.A. Costa, M. Pani, A. Lausi, J. Plaisier, Structural characterization of the CeO2/Gd2O3 mixed system by synchrotron X-ray diffraction, J. Solid State Chem. 190 (2012) 24–28. https://doi.org/10.1016/J.JSSC.2012.01.056.

[142] V. Grover, A.K.K. Tyagi, Phase relations, lattice thermal expansion in CeO2–Gd2O3 system, and stabilization of cubic gadolinia, Mater. Res. Bull. 39 (2004) 859–866. https://doi.org/10.1016/j.materresbull.2004.01.007.

[143] W. Chen, A. Navrotsky, Thermochemical study of trivalent-doped ceria systems: CeO2–MO1.5 (M = La, Gd, and Y), J. Mater. Res. 21 (2011) 3242–3251. https://doi.org/10.1557/JMR.2006.0400.

[144] A. Atkinson, Chemically-induced stresses in gadolinium-doped ceria solid oxide fuel cell electrolytes, Solid State Ionics. 95 (1997) 249–258. https://doi.org/10.1016/S0167-2738(96)00588-7.

[145] N. Ishikawa, Y. Chimi, O. Michikami, Y. Ohta, K. Ohhara, M. Lang, R. Neumann, Study of structural change in CeO2 irradiated with high-energy ions by means of X-ray diffraction measurement, Nucl. Instrum. Methods Phys. Res. Sect. B. 266 (2008) 3033–3036. https://doi.org/10.1016/j.nimb.2008.03.159.

[146] M. Patel, J. Aguiar, K. Sickafus, G. Baldinozzi, Structure and radiation response of anion excess bixbyite Formula Presented, Phys. Rev. Mater. 6 (2022) 13610. https://doi.org/10.1103/PhysRevMaterials.6.013610.

[147] E. Ruiz-Trejo, The optical band gap of Gd-doped CeO2 thin films as function of temperature and composition, J. Phys. Chem. Solids. 74 (2013) 605–610. https://doi.org/10.1016/j.jpcs.2012.12.014.

[148] P. Dorenbos, Thermal quenching of Eu2+ 5d-4f luminescence in inorganic compounds, J. Phys. Condens. Matter. 17 (2005) 8103–8111. https://doi.org/10.1088/0953-8984/17/50/027.

[149] Baldassare Bartolo, Advances in Nonradiative Processes in Solids, Springer US, Erice, Italy, 1989.

[150] S. Poncé, Y. Jia, M. Giantomassi, M. Mikami, X. Gonze, Understanding Thermal Quenching of Photoluminescence in Oxynitride Phosphors from First Principles, J. Phys. Chem. C. 120 (2016) 4040–4047. https://doi.org/10.1021/acs.jpcc.5b12361.